β-adrenergic stimulation and cardiac arrhythmogenesis in the infarct border zone



Jakub Tomek

St Catherine's College

University of Oxford

A thesis submitted for the degree of

Doctor of Philosophy

Trinity 2017

Jakub Tomek, St. Catherine's College; thesis submitted for the DPhil degree in Trinity 2017

β-adrenergic stimulation and cardiac arrhythmogenesis in the infarct border zone (ABSTRACT)

Sudden cardiac death due to ventricular arrhythmias after myocardial infarction (MI) is a major cause of mortality worldwide. Following a MI, the heart undergoes considerable remodelling; however, the precise mechanisms of how the changes induce arrhythmia have not been fully elucidated. The role of sympathetic innervation in the infarct border zone (BZ) is particularly controversial: while historical evidence posits a strongly proarrhythmic role, recent clinical studies report that it is the lack of such innervation which is associated with future arrhythmic events. In this thesis, we aim to improve the understanding of the sympathetic nervous system after MI, focussing predominantly at how neurally mediated β-adrenergic stimulation affects cardiac alternans, an arrhythmic precursor which often affects post-MI hearts and is frequently observed before fibrillation. Using *ex vivo* rat hearts with a healed myocardial infarction, we demonstrate that infarcted hearts are vulnerable to alternans in the BZ. Pharmacological β-adrenergic stimulation, which emulates sympathetic nervous activation, powerfully attenuates alternans, supporting the view that the border zone innervation may play an important role in prevention of fibrillation. Furthermore, we develop a computer model of a ventricular myocyte which allows representation of the BZ phenotype, as well as β-adrenergic stimulation. The model behaves consistently with the experimental data obtained and its analysis reveals a mechanistic explanation for alternans attenuation via β-adrenergic stimulation. Finally, we provide a set of software tools for high-throughput processing of cardiac imaging data that we hope to be useful to be to the community.

Our work helps resolve the controversy of the role of sympathetic innervation after myocardial infarction. It suggests a dual role for the cardiac sympathetic nervous system after MI: anti-arrhythmic via alternans attenuation, but pro-arrhythmic by increasing the heart rate. The results of this thesis have implications both for understanding of cardiac physiology, as well as for existing and future therapies.

To my ancestors, whose genetic, epigenetic, and memetic information made me.

Acknowledgements

I'd like to thank my three wonderful supervisors who guided me throughout this thesis and together exposed me to a fantastic array of techniques, approaches, and collaborators. Prof. Gil Bub's importance for this thesis may be hardly overstated, as it was him who introduced me to the world of cardiac physiology, supported me in the pursuit of my own project, was an endless fountain of positive energy, and always provided me with deep insight and understanding. I thank Prof. Blanca Rodriguez who took over my day-to-day supervision when Prof. Bub moved to Canada, and made sure I made it to the end of the DPhil focussed on the topic and in one piece. With her, I learned about the principles and utility of computer modelling and she also provided me with invaluable advice on how to adjust my writing style. Her human and warm approach to research and supervision is a beacon of light in the world, as testified by the amazing atmosphere in her group - also thank you, all the members of the group; it's great to work and chat with you. I thank Prof. David J. Paterson for high-level guidance throughout this project, as well as for allowing me to stray away from the original topic and approaches. He provided me with great advices on the literature on cardiac sympathetic system and with suggestions pertaining to our experimental designs.

Reaching our goals in this thesis would be impossible without the aid of multiple superb collaborators. I thank A/Prof. Carolyn Carr for providing us with infarcted hearts and their MRI scanning. At the stage of transfer of status, it appeared that we would have to use model systems with much lower relevance, and obtaining real infarcted hearts was a dream come true. Second, I owe great thanks to A/Prof. Neil Herring and Dr. Guoliang Hao, who taught me the Langendorff heart preparation, aided me with experimental design, and helped with its implementation. With them, I understood much of the hardship of lab work and it was transformational also for the computer-science facet of myself. Third, I thank Dr. Jordi Heijman from Maastricht. Our collaboration was started with me e-mailing him, asking for an advice regarding his model of ventricular myocyte and I could not have hoped for more enthusiastic and helpful response. The subsequent long (sorry, Jordi!) exchange of e-mails was critical for my understanding of the model's principles and for being able to modify the model to suit our needs. Fourth, I thank Dr. Rebecca Burton and Dr. Hege Larsen who taught me about culturing of cardiomyocyte monolayers. Even though we did not pursue this model system in the end, I have learned a lot nevertheless.

On both personal and scientific level, I would be entirely incomplete without my dear wife Markéta. Unfortunately, the word limit of this thesis does not allow listing of all her positive qualities, so I can only say to her "thank you – you know how deep it is".

I thank my family who led me through life in a way that gave me the opportunity to pursue this work and who made me happy. During the DPhil study, they supported me with constructive debates, optimism, and kept showing me that working myself to death is not an ideal way of doing it. I also thank Markéta's family, who are fantastic people (and cardiologists) and who treated me always so well. In the context of my Oxford studies, the crucial role of Markéta's grandparents Miluška (sadly recently deceased) and František must be acknowledged: One afternoon, when visited by me and Markéta, they locked us in the room and refused to let us out until we'd promise we'll consider and explore the opportunity of studying abroad. We kept the promise and ultimately got here – and it was well worth it!

I thank the funder of my study programme, EPSRC, and the Bakala foundation which funded my living costs.

I thank the Oxford University Ceilidh Band and the traditional music session scene in Oxford - we've had so many good times together, and playing music with you is a constant source of positive mood, stress relief, and enjoyment.

I thank all the Oxford friends we made for the happy moments we spent together – I'm now a bit sorry we didn't have more of them. You are lovely people and our debates and laughs were among the best in my life.

I thank the existence of pu-erh tea... and Dan Cong and Wu Yi oolongs... and Darjeelings... there are too many, but you'll be always in my heart and you were very important for getting me to the meditative state where novel ideas happen, and you helped me keep my focus through the boring stages of my work.

Finally, I thank music that I listened to during the project (minor excerpts of the work of several key bands head the chapters of this thesis), for music is crucial to me, both as a player and a listener. Most of the work on my doctorate was performed in the fantastic amalgam of night-time, Markéta (working on her project), tea, and music – a perfect combination for science and for life.

Publications

Journal articles

1. RAB Burton, A Klimas, CM Ambrosi, **J Tomek**, A Corbett, E Entcheva, G Bub. Optical control of excitation waves in cardiac tissue. *Nature Photonics* 9 (12): 813, 2015

2. JR Popelová, K Kotaška, M Tomková, **J Tomek**. Usefulness of N-terminal Pro-brain natriuretic peptide to predict mortality in adults with congenital heart disease. *The American Journal of Cardiology* 116 (9): 1425-1430, 2015

3. RAB Burton, **J Tomek**, S Aslam, S Bilton, HE Larsen, A Sharkey, G Stephens, E Mann, DJ Paterson, G Bub. Sympathetic stellate neurons increases cardiac conduction velocity and alters wave patterns in a myocyte-neuron co-culture model system. *Autonomic Neuroscience: Basic and Clinical* 192: 72-73, 2015

4. M Kalla, M Chotalia, C Coughlan, G Hao, MJ Crabtree, **J Tomek**, G Bub, DJ Paterson, N Herring. Protection against ventricular fibrillation via cholinergic receptor stimulation and the generation of nitric oxide. *The Journal of Physiology* 594 (14): 3981-3992, 2016

5. **J Tomek**, RAB Burton, G Bub. Ccoffinn: Automated Wave Tracking in Cultured Cardiac Monolayers. *Biophysical Journal* 111 (8): 1595-1599, 2016

6. JR Popelova, M Tomkova, **J Tomek**. NT-proBNP predicts mortality in adults with transposition of the great arteries late after Mustard or Senning correction. *Congenital Heart Disease* 12: 448–457, 2017

7. **J Tomek**, G Bub. Hypertension-induced remodelling: On the interactions of cardiac risk factors. *The Journal of Physiology* 595(12): 4027–4036, 2017

8. **J Tomek**, B Rodriguez, G Bub, J Heijman. β-adrenergic receptor stimulation inhibits proarrhythmic alternans in post-infarction border zone cardiomyocytes: a computational analysis. *American Journal of Physiology-Heart and Circulatory Physiology* 313 (2): 338-353, 2017,

9. F Pini, AK East, C Appia-Ayme, **J Tomek**, R Karunakaran, M Mendoza-Suarez, A Edwards, J Terpolili, J Roworth, JA Downie, PS Poole. Lux bacterial biosensors for in vivo spatiotemporal mapping of root secretion. *Plant Physiology* 174: 1289-1306, 2017

10. **J Tomek**, X Zhou, G Bub, B Rodriguez. Alternans driven by sarcoplasmic reticulum refractoriness: modulation by calcium release magnitude and dynamics. *In preparation*

11. **J Tomek**, G Hao, M Tomkova, C Carr, A Lewis, DJ Paterson, B Rodriguez, N Herring, G Bub. Suppression of alternans in the border zone of healed infarcts via β-adrenergic stimulation. *In preparation*

Sections of the article 11 are reused in Chapter 3. Sections of the articles 8, 10, and 11 are reused in Chapter 4. The article 5 comprises Chapter 5. All reuse of already published contents is approved by the respective publisher.

Conferences

1. Oxford Medical Science DPhil day, 2015 (poster)

2. Gordon Research Seminar (talk, poster) and Conference (blast talk, poster) on Cardiac Arrhythmia Mechanisms, 2017

3. Oxford BHF CRE Symposium 2017 (poster)

4. In Silico Drug Safety and Efficacy Symposium, 2017 (poster)

Statement of contribution

I am the author of this thesis and the work described in it with the following exceptions:

- The work described in section 3.2.1 was carried out and written up by A/Prof. Carolyn Carr and Dr. Andrew Lewis.
- Anaesthesia and excision of rat hearts was performed by Dr. Guoliang Hao; I performed the subsequent imaging and analysis.

List of abbreviations

- AM: alternans mapping
- AMI: acute myocardial infarction
- AMP: adenosine monophosphate
- AP: action potential
- APD: action potential duration
- ATP: adenosine triphosphate
- AV: atrioventricular
- β-AR: β-adrenoreceptor
- β-ARS: β-adrenoreceptor stimulation
- bcl: base cycle length
- BZ: border zone (of an infarct)
- CaMKII: Ca^{2+}/calmodulin-dependent protein kinase II
- cAMP: cyclic adenosine monophosphate
- CaT: calcium transient
- CaTA: calcium transient amplitude
- CaTD: calcium transient duration
- CCM: cultured cardiac monolayer
- CI: coupling interval
- CSNS: cardiac sympathetic nervous system
- CV: conduction velocity
- DFS: depth-first search

- DI: diastolic interval
- ECG: electrocardiogram
- ED: end-diastolic
- EDV: end-diastolic volume
- EF: ejection fraction
- ES: end-systolic
- ESV: end-systolic volume
- FOV: field of view
- HeRd: Heijman-Rudy model
- IQ: interquartile
- IQR: interquartile range
- ISO: isoproterenol
- JSR: junctional sarcoplasmic reticulum
- LAD: left anterior descending coronary artery
- LED: light emitting diode
- LV: left ventricular
- LVEF: left ventricular ejection fraction
- MCMF: minimum cost maximum flow
- ME: metoprolol
- MI: myocardial infarction
- MR: magnetic resonance
- MRI: magnetic resonance imaging
- NAM: normalised alternans magnitude
- NCX: sodium-calcium exchanger
- NE: norepinephrine

- NPUV: normalised peak upstroke velocity
- NPY: neuropeptide Y
- NSR: network sarcoplasmic reticulum
- NZ: normal zone
- ORd: O'Hara-Rudy model
- PKA: protein kinase A
- PLB: phospholamban
- PVC: premature ventricular complex
- REC: recovery curve measurement
- RyR: Ryanodine receptor
- SA: sinoatrial
- SCD: sudden cardiac death
- sCMOS: scientific complementary metal–oxide–semiconductor
- SD: Sprague-Dawley
- SERCA: sarco/endoplasmic reticulum Ca^{2+} ATPase
- SNR: signal-to-noise ratio
- SR: sarcoplasmic reticulum
- SV: stroke volume
- VF: ventricular fibrillation
- VT: ventricular tachycardia

Contents

1 Introduction **7**

1.1 Basics of cardiac physiology 8

1.1.1 Organ level 8

1.1.2 Cellular level 9

1.1.2.1 Myocyte electrophysiology 9

1.1.2.2 Myocyte calcium handling and contraction 14

1.1.2.3 Key species differences in cardiac electrophysiology and calcium handling 15

1.2 Ventricular fibrillation and sudden cardiac death 17

1.3 Myocardial infarction and ventricular fibrillation 19

1.4 Cardiac alternans 21

1.4.1 Alternans driven by steep restitution of APD 22

1.4.2 Alternans driven by calcium oscillations 24

1.4.3 T-wave alternans 25

1.5 The role of cardiac sympathetic nervous system in arrhythmogenesis . 25

1.6 Model systems in arrhythmia research 29

1.6.1 Ex vivo Langendorff heart 29

1.6.2 In vitro cultured cardiomyocytes 30

1.6.3 Computer modelling 32

1.7 Thesis aims and structure 35

2 General methods **37**

2.1 Langendorff heart 37

2.1.1 Myocardial infarction in Langendorff hearts 38

2.1.2 Common pacing protocols in Langendorff hearts 40
2.2 Computational modelling of ventricular myocytes 41
2.2.1 A model of β-adrenergic stimulation and and post-infarction remodelling in a ventricular myocyte 41
2.2.1.1 Model compartments 41
2.2.1.2 Electrophysiology and calcium handling in the Heijman-Rudy model 42
2.2.1.3 β-AR signalling in the HeRd model 44
2.2.1.4 Simplified activation of RyR via β-AR stimulation . . 44
2.2.2 Infarct border zone remodelling 45
2.2.3 Numerical solutions of systems of differential equations 46

3 β-adrenergic stimulation and alternans in post-infarction hearts 49
3.1 Introduction 49
3.2 Methods 50
3.2.1 Cryoinfarction procedure and magnetic resonance imaging . . 50
3.2.2 Langendorff heart preparation and imaging 51
3.2.3 Pacing protocols 52
3.2.4 Image processing methods 54
3.2.4.1 Calcium alternans mapping 55
3.2.4.2 Repolarisation alternans mapping 56
3.2.4.3 Membrane potential upstroke recovery 58
3.2.4.4 Calcium upstroke recovery 58
3.3 Results 59
3.3.1 Development of healed myocardial infarction 59
3.3.2 Rapid pacing induces calcium alternans in hearts 60
3.3.3 The infarct border zone is more prone to alternans than noninfarcted myocardium 62
3.3.4 Norepinephrine perfusion attenuates alternans 64
3.3.5 S1-S2 protocol and β-adrenergic stimulation 65
3.3.6 Other arrhythmia markers 68

3.4 Discussion . . . 69
3.4.1 Infarct border zone is vulnerable to alternans formation . . . 69
3.4.2 β-adrenergic stimulation attenuates formation of alternans in post-infarction hearts . . . 70
3.4.3 β-adrenergic stimulation normalises upstroke velocity and reduces arrhythmia incidence during S1-S2 protocol . . . 70
3.4.4 Sympathetic nervous system and arrhythmia after myocardial infarction . . . 71
3.5 Limitations . . . 72
3.6 Conclusions . . . 73

4 Computer simulations of infarct border zone remodelling and β-adrenergic stimulation 75
4.1 Introduction . . . 75
4.2 Methods . . . 76
4.2.1 Single-cell pacing protocols for alternans simulations . . . 76
4.2.2 Modulation of RyR under β-AR stimulation in the O'Hara-Rudy human model . . . 77
4.2.3 Multicellular simulations . . . 78
4.2.4 Implementation notes . . . 79
4.3 Results . . . 79
4.3.1 Alternans formation in the HeRd model . . . 79
4.3.2 β-adrenergic stimulation abolishes APD and CaT alternans . . . 84
4.3.3 Electrophysiological mechanisms underlying alternans inhibition via β-AR stimulation . . . 84
4.3.4 Biophysical RyR properties regulating CaT alternans . . . 89
4.3.4.1 SR release clamping to study impact of release dynamics on alternans vulnerability . . . 93
4.3.5 Difference in alternans vulnerability between NZ and BZ . . . 94
4.3.6 Alternans and RyR activation in O'Hara-Rudy model . . . 95
4.3.7 Arrhythmia precursors in a simulated myocardial fibre . . . 96

4.3.7.1 Discordant alternans promotes conduction block . . 98
4.3.7.2 Alternans increases vulnerability to premature ventricular complex propagation 100
4.4 Discussion 102
4.4.1 Alternans in HeRd model is driven by SR cycling refractoriness 102
4.4.2 β-adrenergic stimulation attenuates alternans via accelerated SR release dynamics. 104
4.4.3 Slow SR release dynamics increase vulnerability to alternans . 106
4.4.4 Alternans and arrhythmia in a fibre model 107
4.5 Limitations 108
4.6 Conclusions 109

5 Ccoffinn: a toolkit for processing high-resolution optical mapping data in cardiac cell cultures 111

5.1 Introduction 111
5.2 Materials and Methods 113
5.2.1 Wave segmentation and tracking 114
5.2.1.1 Blob segmentation 114
5.2.1.2 Determining times of blob activity 116
5.2.1.3 Wave segmentation 119
5.2.1.4 Wavefront tracking 122
5.2.2 Feature extraction 126
5.2.2.1 Number of blobs 127
5.2.2.2 Sparseness of blobs 127
5.2.2.3 Wavefront speed 127
5.2.2.4 Interspike duration 128
5.2.2.5 APD 128
5.2.2.6 Wavefront roughness 129
5.2.2.7 Beat frequency 129
5.2.2.8 Entropy 129
5.2.2.9 Perimeter-to-area ratio 131

5.2.3 Data description . . . 133
5.2.3.1 Cell culture data . . . 133
5.2.3.2 Synthetic data . . . 133
5.2.4 Implementation notes . . . 134
5.3 Results . . . 134
5.3.1 Analysing behaviour of cell cultures . . . 134
5.3.2 Evaluation of Ccoffinn using synthetic data . . . 136
5.3.2.1 Syn1: Results . . . 136
5.3.2.2 Syn2: Results . . . 137
5.3.2.3 Syn3: Results . . . 138
5.3.3 Comparison of MCMF and Bayly algorithms . . . 141
5.3.4 Slow band in a straight wave . . . 143
5.3.5 Near wavefronts in a single wave . . . 146
5.3.6 Wave shape affects CV and direction estimation . . . 146
5.3.7 Wavefront jaggedness yields overestimation of CV . . . 147
5.3.8 Heterogeneously spreading target waves and changing wavefront size . . . 148
5.4 Discussion . . . 152
5.5 Limitations . . . 154
5.6 Conclusions . . . 154

6 Concluding discussion **155**
6.1 Key findings and contributions . . . 155
6.2 Clinical perspective . . . 156
6.3 Future work . . . 159

Bibliography **163**

A Appendix:Experimental **197**

B Appendix:Computational investigation of alternans **199**

C Appendix:Ccoffinn **203**

C.1 Parameter values 203

What a beautiful day,
What a beautiful day,
And nothing is impossible
In my all powerful mind

Levellers – Beautiful Day

1 Introduction

Sudden cardiac death (SCD), defined as death due to cardiac causes within an hour from the onset of symptoms, is one of the most frequent causes of death worldwide, claiming 300,000–400,000 deaths annually in the USA alone (Zipes and Wellens, 1998; Katritsis et al., 2016). A hallmark of SCD is that it frequently manifests in otherwise low-risk patients, or it is a first clinical expression of an underlying heart disease, which, combined with survival rate of mere 31% in out-of-hospital cases, makes it an extremely serious event (Katritsis et al., 2016). Ventricular fibrillation (VF) remains the leading cause of sudden cardiac death, although its incidence is somewhat decreasing, with pulseless electrical activity and asystole increasing in prominence (Cobb, 2002; Väyrynen et al., 2011; Keller and Halperin, 2015; Area, 2005); we discuss potential causes of this phenomena in (Tomek and Bub, 2017). Despite the advances in research and prevention of VF, our understanding of the causes of this disease remains incomplete. This is especially true in patients after myocardial infarction (MI), who comprise the majority of cases manifesting VF (Israel, 2014; Deo and Albert, 2012). In particular, we find that in post-MI patients, the evidence on the role of cardiac sympathetic nervous system is unclear and conflicting. Historically, peri-infarct innervation was viewed as purely pro-arrhythmic (Shen and Zipes, 2014), however, the opposite finding was shown by multiple recent clinical studies (Malhotra et al., 2015; Fallavollita et al., 2014, 2017), suggesting the lack of peri-infarct innervation as pro-arrhythmic. This area of

arrhythmia study thus requires further research and understanding of the underlying patophysiology, which is the main aim of this thesis.

Below, we provide a brief overview of cardiac physiology, followed by an overview of origins of ventricular fibrillation and sudden cardiac death. Subsequently, several critical contributors to fibrillation formation which are a focus of this thesis (myocardial infarction, cardiac alternans, cardiac sympathetic nervous system) are described, followed by an overview of relevant research methodology, culminating in the formulation of precise thesis aims.

1.1 Basics of cardiac physiology

1.1.1 Organ level

The heart is a double pump responsible for blood flow in the body. Figure 1.1 shows the organisation of the organ and its division into four chambers: an atrium and a ventricle for the left and right side of the heart, each side acting as a single pump. Blood with low oxygen content arrives to the right atrium via inferior and superior venae cavae and upon the atrial contraction, it is transported to the right ventricle. From the right ventricle, blood is directed to the pulmonary circuit where it is oxygenated, and then flows to the left atrium, left ventricle, and is ultimately pushed back to the systemic circuit.

A single cardiac cycle of contraction and relaxation starts with atrial contraction (both atria contract in synchrony). This transports additional blood from the atria to the ventricles via atrioventricular valves. In the second phase, the ventricles start contracting. When ventricular pressure exceeds the atrial pressure, the atrioventricular valves shut down and a phase labelled “isovolumic contraction” starts. At this stage, blood is trapped in the ventricles, given that both atrioventricular valves and aortic/pulmonary valves (the valves between the ventricles and circulation) are shut. When the ventricular pressures exceed the respective aortic pressures, blood is ejected to the pulmonary and systemic circuit. Following the contraction, the ventricles start relaxing, decreasing ventricular pressure, with the effect of closure of the aortic and pulmonary valve. As the relaxation progresses, the ventricular pressures become lower than their respective atrial pressures, the atrioventricular valves open and blood in the atria, amassed during the

ventricular contraction, flows to the ventricle, concluding the cardiac cycle. Interestingly, most of ventricular refilling is achieved via passive filling; only a minor proportion of ventricular volume is transported via active filling due to an atrial contraction.

The synchronised contraction is driven by an underlying electrical activation of the cardiac tissue (Hall and Guyton, 2006). Here we overview the high-level pattern of electrical activation with cellular-level details of the electromechanical coupling detailed in the next section. The electrical activation starts in the sinoatrial (SA) node, close to the opening of superior vena cava, and provides periodic pacemaking. The stimulus then spreads through both atria, causing a contraction. The next stage of propagation is the atrioventricular (AV) node, which passes the signal to the ventricles, delaying it slightly in order to provide enough time to the atria for contraction. From the AV node, the Bundle of His conducts the stimulus along the septal wall to Purkinje[1] fibers, which then stimulate the ventricles, allowing their contraction.

1.1.2 Cellular level

1.1.2.1 *Myocyte electrophysiology*

The action potential of a ventricular myocyte involves a complex interplay of multiple ionic currents, visualised in Figure 1.2. Upon electrical stimulation via the activation of neighbouring cells coupled via gap junctions, the fast sodium current (I_{Na}) rapidly depolarises the cell. Consequently, the voltage-gated L-type calcium current (I_{CaL}) opens and enables the flow of calcium ions into the cell. Soon after the depolarisation, transient outward potassium current (I_{To}) opens, responsible for the "notch" in the membrane potential between the peak and the plateau. Ultimately, potassium outflow causes the cell to repolarise via slow and rapid delayed rectifier currents (I_{Ks}, I_{Kr}). The slope of the final phase of repolarisation, as well as resting membrane potential, are controlled by inward rectifier current (I_{K1}). A specific role is played by the sodium-calcium exchanger (NCX) which exchanges three sodium ions for a single calcium ion;

[1] This is an English-friendly spelling of the name of Jan Evangelista Purkyně, which, however, leads to different-than-original pronunciation of "Purkin-zhee"; the Czech pronunciation is close to Purkin-yee. I believe this mutation of pronunciation is probably due to some Czech writer who substituted "Purkyně" with "Purkinje" for a foreign publication (given that in Czech, "ě" is pronounced exactly the same as "je".), not realising that other nations pronounce "je" differently.

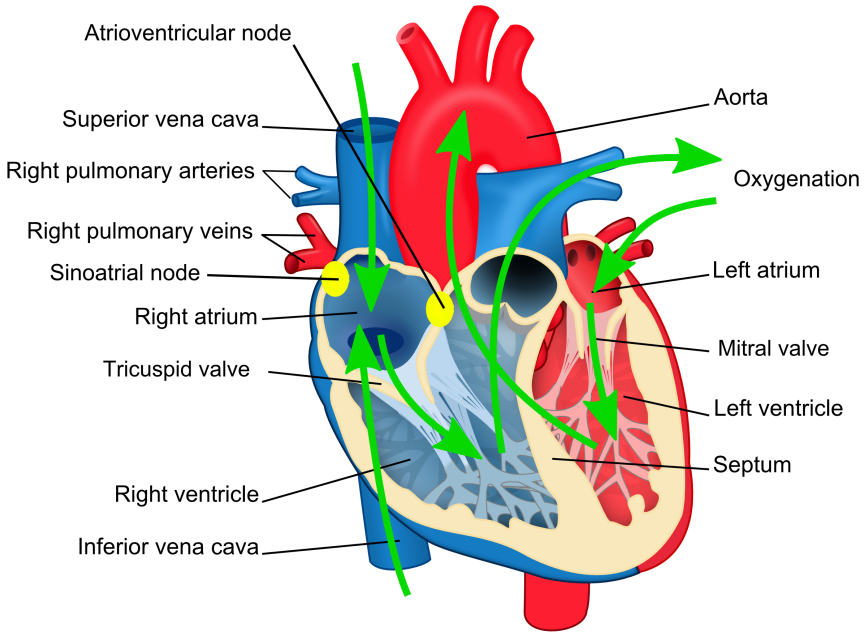


Figure 1.1: A diagram of key heart structures and blood flow. The green arrows show the direction of blood flow through the heart (the flow via right pulmonary artery is not shown and it is symmetrical to the left pulmonary artery). Not shown in the diagram, but present in the heart are valves between the ventricles and the arteries. The diagram is based on a figure from Wikimedia Commons: https://commons.wikimedia.org/wiki/File:Heart_diagram-en.svg

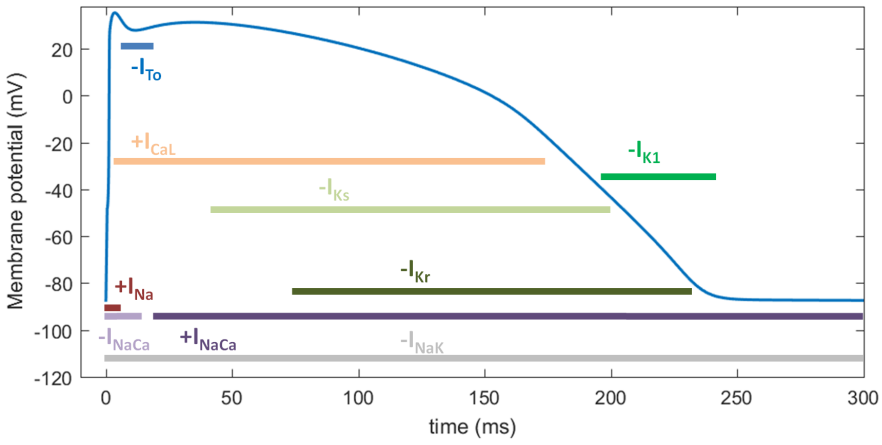


Figure 1.2: An overview of key myocyte currents in a mammalian action potential. Shown is the shape of a human action potential with coloured bands highlighting when the respective currents are predominantly active. The signs in current labels represent a net influx of positive ions (+) or a net outflow of positive ions (-). In the case of NCX current, I_{NaCa}, the exchanger operates in both forward (+) and backward (-) mode, which is why two lines and labels are given.

however, the direction of this transport is reversed within an action potential. At the start of the action potential, after the large influx of sodium, the NCX works in the reverse mode, exporting sodium, bringing calcium within the cell. However, with the subsequent elevation of calcium via I_{CaL} and release of intracellular calcium reserves from the sarcoplasmic reticulum (discussed further in the next section on contractility), the forward mode of NCX is engaged, exporting calcium and bringing sodium inside the cell. The second crucial ionic exchange is performed via the sodium-potassium pump (I_{NaK}), removing three sodium ions from the cell in exchange for two potassium ions entering. Given that this transport goes against the concentration gradient of both ions, the process requires ATP to proceed.

A specific type of current which is typically not highly expressed in ventricular cells, but abundant in SA node pacemaker cells, is the "funny current"[2]. This current activates when a cell is hyperpolarised (such as at the end of an action potential), triggering an influx of positively charged ions, depolarising the cell again, providing a mechanism of periodic activation.

What drives the ions across the membrane, allowing the ATP-independent currents to operate? Provided that the membrane is permeable to an ion, two main forces affect the ion: electrical driving force based on charge, and chemical diffusion based on ionic concentration. The membrane potential (the difference in electrical potential between the intracellular and extracellular space) required to counteract the chemical diffusion is named the "Nernst potential" and is informative for understanding the net ionic diffusion. The equation giving the Nernst equilibrium potential for an ion is:

$$E = \frac{RT}{zF} \ln \frac{concentration_{extracellular}}{concentration_{intracellular}},$$

where $R \approx 8.314$ is the gas constant, T is the temperature in kelvins, $F \approx 9648$ is the Faraday constant, and z is the valence of the ion. Approximate cardiac ionic concentrations and the respective equilibrium potentials for three key ions are given in Table 1.1. For example, given that the membrane potential of a myocyte is higher

[2]The name is supposedly derived from a mixed ionic conductance, slow kinetics and activation with hyperpolarisation rather than depolarisation as most other currents. I conclude that certain people have a strange sense of humor.

Ion	Extracellular c. (mM)	Intracellular c. (mM)	Equilibrium potential (mV)
K	4	150	-96
Ca	2.5	0.0001	134
Na	145	20	52

Table 1.1: Ionic concentrations and equilibrium potentials.

than the potassium equilibrium potential, the potassium ions travel outside the cell when the potassium-permeable membrane channels are open. Conversely, sodium and calcium flow into the cell, as the potential that would repel them is above usual membrane potential range (ca. -87 to 40 mV).

What is the structure of ionic channels? The channels allowing the formation of the above-described currents are usually complexes of transmembrane proteins, composed of several subunits. Each subunit can then span multiple transmembrane segments. For example, the complex underlying I_{Na} consists of a large α subunit (which alone can conduct sodium through the membrane) and two smaller subunits, β_1 and β_2. The transmembrane segment S4 of the α subunit is thought to provide the voltage-dependence of activation via a mechanism based on *helical screw* model of voltage sensing (Catterall, 2014). The other important property of the channel, selectivity to sodium, relies on a configuration of side-chains of four glutamate residues with internal diameter 4.6 Å (Payandeh et al., 2011). After opening, the fast sodium channels inactivate rapidly; the fast inactivation appears to be mediated via an intracellular loop connecting segments S3 and S4, which is put over the channel as a lid, preventing further conduction (Vassilev et al., 1988). In addition to the fast inactivation, a slow inactivation on the scale of up to seconds was observed and while not yet fully understood, it is assumed to be linked to conformational changes to the selectivity filter and the S6 segment (Catterall, 2014). The β subunits of the channel complex are not a required component of sodium conduction, but they both powerfully modulate the channel behaviour: the co-expression of either subunit with the α subunit resulted in considerably improved function (increased current density and altered gating properties) of the channel compared to a sole α subunit (Marban et al., 1998).

The voltage-sensitive L-type calcium current channels consist of α_1, α_2/δ, β, and in some tissues γ subunits. The α_1 subunit contains the pore, voltage sensor, and gating machinery, with the other subunits playing a more supporting and modulating role (Bodi et al., 2005). An important feature of the L-type calcium current is that its inactivation is mediated both by membrane depolarisation and intracellular calcium levels, with the latter playing a larger role (Lacinová and Hofmann, 2005). At the same time, the current is indirectly potentiated by chronically elevated intracellular calcium levels via the CaMKII signalling which serves to adapt the cell to rapid heart rate (Bodi et al., 2005).

Cardiac I_{to} channels are macromolecular protein complexes consisting of four α subunits and multiple accessory subunits which allow regulation and modulate channel dynamics (Niwa and Nerbonne, 2010). While I_{to} was traditionally considered to be a single current underlying the notch following peak membrane potential, it became clear that there are two distinct channels underlying it, depending on the gene encoding the pore-containing α subunit. In human and canine ventricles, the isoform KV4.3 predominates and is responsible for a swiftly activating and inactivating form of I_{to}. The isoform KV1.4 then encodes I_{to} with slower dynamics. Differential expression of the isoforms underlies regional variation in the shape of AP between epicardium and endocardium, as well as between left and right ventricle (Niwa and Nerbonne, 2010).

The molecular structure of the rapid delayed rectifier current I_{Kr}, based on the hERG (human Ether-à-go-go[3] gene, was elucidated only recently (Wang and MacKinnon, 2017). Four αsubunits comprise the channel pore, providing potassium selectivity, activation based on voltage, and swift inactivation. Two subtypes of the α subunit (based on hERG 1a and hERG 1b) were shown to be present in the heart, associating *in vivo* together (Jones et al., 2004). Despite historical belief that hERG1a is the crucial subunit component of I_{Kr}, an important role for hERG1b subunit was also demonstrated, suggesting that both subunits are crucial for normal channel functionality (Jones et al., 2014). The slow component of delayed repolarisation current, I_{Ks} is a complex of two subunits: pore-forming α (based on the KCNQ1 gene), and a regulatory β (based on the KCNE1 gene) (Nerbonne and Kass, 2005). Of interest is the importance of the β subunit

[3]This is a human homolog of the drosophila Ether-à-go-go gene: flies with a mutation in this gene shook their legs when exposed to ether in a similar fashion to dancers in the Whisky A Go Go dance club.

in regulation of action potential duration in response to β-AR stimulation, enabling action potential shortening at rapid heart rates (Marx, 2002). The I_{K1} current is mediated via heterotetramers of Kir2.1, Kir2.2, and Kir 2.3 genes. While all the channels based on Kir2 act as rectifiers, Kir2.2 were shown to display considerably increased voltage-dependence of rectification compared to Kir2.1 and Kir2.3 (Zipes and Jalife, 2013).

The sodium-calcium exchanger (I_{NaCa}) is a protein consisting of 10 transmembrane helices with a diamond-shaped site for substrate binding (Liao et al., 2012). Three binding sites correspond to Na^+ and one to Ca^{2+}, consistent with the observed stoichiometry of 3:1 (Shlosman et al., 2017). The sodium-potassium pump (I_{NaK}) is a complex of three protein subunits: the α subunit containing ten transmembrane segments, with additional β and FXYD subunits (Clausen et al., 2017). The pumping works in a way where the pump binds ATP and three Na^+ ions. ATP is then hydrolysed, phosphorylating the pump, releasing ADP, and changing the conformation of the pump to expose the sodium ions to the extracellular space. Given the low affinity for sodium, the ions are released and the pump binds two K^+ ions. This dephosphorylates the pump and makes it return to the original conformation, transporting potassium ions in the cell.

1.1.2.2 Myocyte calcium handling and contraction

While the signal transmission in heart is mediated electrically, the muscle contraction depends primarily on calcium concentration, as overviewed below, based on (Eisner et al., 2017). During an action potential, the L-type calcium current causes an influx of calcium into the cell, which triggers calcium-induced calcium release (CICR) via ryanodine receptors (RyR) from the sarcoplasmic reticulum (SR), an intracellular storage pool that holds calcium. Ryanodine receptors are large homotetrameric channels and are regulated by multiple signalling pathways (e.g., CaMKII or PKA, downstream of β-adrenergic stimulation) and substances (e.g., caffeine or ATP) (Lanner et al., 2010). The flux magnitude mediated by RyR in the heart[4] depends primarily on two criteria: the extra-SR cytoplasmic calcium levels, and the SR calcium loading; both relationships are steep (Shannon et al., 2000). After calcium influx in the cell in the early phase of an action

[4]Interestingly, in skeletal muscle, voltage-gated calcium channels in the membrane directly stimulate release from the SR, rather than via calcium influx (Catterall, 2011).

potential, multiple unitary calcium releases from the SR occur, termed calcium sparks. These sparks elevate calcium levels adjacent to the release sites, provoking further calcium sparks, providing a natural mechanism of synchronisation of intracellular calcium release (Hoang-Trong et al., 2015).

The high calcium concentration induced by CICR then modulates the interaction of actin and myosin, the filaments which mediate the contraction. At low calcium concentration, the I subunit of protein troponin prevents binding of actin and myosin, however, when calcium is present, it binds to the C-subunit of troponin, causing a conformational change, releasing the inhibition of actin-myosin binding. Subsequently, myosin pulls together actin strands, causing a contraction.

The high intracellular calcium levels are eventually brought back to baseline by SR reuptake of calcium via ATP-dependent SERCA pumps and the forward mode of sodium-calcium exchanger; as the concentration decreases, troponin returns to the original inhibitory conformation and allows the cell to relax. SERCA pumps are large proteins relatively similar to the sodium-potassium pump (Sweadner and Donnet, 2001). They pump calcium from cytosol to within the sarcoplasmic reticulum, using ATP for phosphorylation which enables conformational change and release of calcium inside the SR (MacLennan et al., 1997). Key regulator of SERCA pumps is phospholamban, a regulatory protein which binds to SERCA pumps and inhibits them. PKA phosphorylation downstream of β-adrenergic stimulation disables this feature of phospholamban, facilitating faster calcium reuptake into the sarcoplasmic reticulum and enhanced rate of relaxation of the muscle (Sham et al., 1991). Phospholamban inactivation (and relief of SERCA inhibition) is also mediated via CaMKII, providing a distinct mechanism of increasing the reuptake rate.

1.1.2.3 Key species differences in cardiac electrophysiology and calcium handling

Different species possess a different mix of channels of varying properties, or different isoforms of a particular channel (Nerbonne and Kass, 2005). Consequently, different species possess different shape of an action potential, such as the triangular action

potential of a rat, or a shape present in large mammals, where an initial peak is followed by a notch, after which a dome is present, maintaining a plateau potential. These differences are responsible for different relevance of various arrhythmia triggers among species (Edwards and Louch, 2017). Possibly the most obvious difference between species is the action potential duration (ca. 70 ms in rat, 300 in human), related to different heart rates (ca. 400 in rat, 80 in human), which is linked to a different mix of potassium repolarisation currents. For example, rodents such as mice or rats rely predominantly on I_{to} (Gussak et al., 2000), unlike mammals[5], which rely predominantly on a mixture of I_{Kr}, I_{Ks}, and I_{K1}, to achieve repolarisation (Nerbonne and Kass, 2005). The mixture of I_{Kr} and I_{Ks} differs between mammal species: Jost et al (Jost et al., 2013) have shown that canine myocardium manifests 3-4.5-higher density of I_{Ks} compared to human. In general, humans and rabbits rely more on I_{Kr} for repolarisation compared to dogs or guinea pigs, which can compensate for I_{Kr} loss with I_{Ks} and I_{K1}; this is an important property from the point of view of drug therapy, given that I_{Kr} block is a frequent side-effect (Edwards and Louch, 2017).

In contrast to pronounced species differences in repolarisation currents, key depolarisation currents, I_{Na} and I_{CaL} were not clearly shown to differ greatly. Some differences in I_{CaL} inactivation were observed between rabbit, rat, and guinea pig (Linz and Meyer, 2000). In the case of I_{Na}, different transcript pattern of isoforms was observed across species (Blechschmidt et al., 2008), suggesting that at least some I_{Na} properties are likely to be species dependent. However, this was not yet conclusively shown, possibly due to the difficulty of measuring I_{Na} (Edwards and Louch, 2017).

Clear differences in calcium handling are present across species, corresponding to the different requirements for contraction dynamics at different heart rates and heart sizes. At the level of sarcoplasmic reticulum, the rate of calcium transient decay was observed to be fastest in mouse < rabbit < dog < human, signifying different SERCA reuptake rate (Su et al., 2003). At the same time, this study reported similar rate of

[5]While not playing as crucial role as in rodents, I_{to} is also present in mammals (with the exception of the guinea pig where it it is only marginally expressed), underlying the notch in membrane potential following the peak potential (Edwards and Louch, 2017). However, even between mammals, properties of I_{to} differ, such as the slower decay, faster recovery from inactivation, and depolarising shift of steady-state inactivation in human versus dog (Akar et al., 2004).

calcium transient rise among the studied species. In contrast to small rodents which rely primarily on SERCA reuptake for clearance of cytosolic calcium, almost 30% of calcium clearance is mediated via the sodium-calcium exchanger in larger mammals such as human or rabbit (Edwards and Louch, 2017). Diminished function of the sodium-calcium exchanger in rodents is further exacerbated by their higher intracellular sodium levels, limiting the rate of calcium efflux via the exchanger.

1.2 Ventricular fibrillation and sudden cardiac death

Ventricular fibrillation (VF) is a disorganised electrical activation of ventricles where multiple wavelets break and divide, in contrast with normal activation of ventricles, which starts focally and spreads evenly (Weiss et al., 2000). The chaotic electrical activation then translates into lack of synchronised contraction, which stops blood flow, subsequently translating into cardiac arrest and death. VF is typically preceded by ventricular tachycardia (VT), a fast reentrant activation of the ventricle which overdrives the sinus rhythm (Chen et al., 1987; Weiss et al., 2000). Initiation and maintenance of VT/VF is thought to require several abnormalities interacting together, such as structural abnormalities (e.g., post-infarction scarring, hypertrophy), functional abnormalities (e.g., acute ischemia, ionic imbalance, fluctuations of autonomic nervous activity, drug toxicity), or dynamical disturbance (electrical alternans) (Weiss et al., 2000). The common factor in these abnormalities is that they promote electrophysiological heterogeneity.

Arrhythmias are generally classified by their mechanism as focal (spurious waves spreading for one location) or re-entrant (a self-sustaining pattern of activation, e.g., a spiral wave) (Antzelevitch and Burashnikov, 2011). The focal activity may be caused by enhanced automaticity of cells with pacemaking potential, termed accelerated junctional rhythms, e.g., hyperactivity of AV node (De Azevedo et al., 1973) overdriving the SA node pacing rate. Alternatively, premature ventricular activation may be due to out-of-place discharges of Purkinje fibers (Bogun et al., 2008). Finally, focal reactivation of myocardium may arise from cellular depolarisation triggered by preceding action potentials. Such activity is generally divided into early and delayed afterdepolarisations (EADs, DADs respectively).

An EAD is a reactivation of the cell which occurs before the cell repolarises and is usually, but not exclusively associated with prolongation of the action potential (Tse, 2016). Two main mechanisms underlying EADs were proposed: first, in a long action potential, the L-type calcium current may reactivate after recovering from refractoriness, further depolarising the membrane and providing an influx of calcium to also trigger CICR (January and Riddle, 1989). Second, the sodium-calcium exchanger was suggested to depolarise the membrane during a late calcium transient via forward mode of the exchanger (Szabo et al., 1994). Independently of the cause, the increase in membrane potential can reactivate fast sodium current and trigger a new action potential outside normal activation sequence.

DADs are cell reactivations which occur after the cell depolarises and their cause seems to be a spontaneous intracellular calcium release, e.g., in calcium overload (Tse, 2016). A post-repolarisation calcium release may be triggered when the intracellular leak transitions into a full-scale calcium release; the calcium released can then activate calcium-sensitive currents (e.g., sodium-calcium exchanger) to reactivate fast sodium current and trigger a new action potential, similarly to EADs.

A different mechanism from a focal activation is a reentrant activation, where a wave in an excitable medium re-actives its starting point, perpetuating itself. Such a phenomenon was first observed in circular slices of jellyfish, which pulsed rhythmically after a stimulus was administered, triggering a wave propagation around the circle (Mayer, 1906). A crucial feature of such circular re-entry is that the reentrant circuit must be long enough (or the conduction slow enough) so that the starting point of the circuit is not refractory when reached by the wave.

One mechanism of circus reentry is possible when an anatomical obstacle is present, e.g., a nonexcitable scar after myocardial infarction, acting similarly to the hole in the jellyfish circle. In the case of post-infarction myocardial scarring, re-entry is further facilitated by the slow conduction in the infarct border zone (Janse and Wit, 1989), allowing the formation of smaller reentrant circuits than in healthy myocardium.

However, a circular re-entrant activation was observed in rabbit atria even in the absence of any structural obstacle, triggered by premature ventricular stimulation

(Allessie et al., 1973). A premature ventricular activation following a cardiac wave propagation may propagate in one direction only (behind the wave), as the zone of the wave is refractory. In this way, a unidirectional conduction block may be formed even without an anatomical block, potentially translating into the spiral wave reentry (Tse, 2016). Further sources of spatial dispersion of repolarisation which may contribute to a wavebreak and reentry are spatially heterogeneous APD alternans (Gaeta and Christini, 2012) or differences in APD stemming from differential expression of ionic channels.

Importantly, while focal and reentrant arrhythmias are usually classified as distinct entities, it is worth noting that they have much in common. For example, focal activation itself increases the spatial dispersion of repolarisation and may promote reentry. On the other hand, while spatial dispersion of repolarisation may provide a substrate for reentry, the reentry might require a preceding focal activation to translate the dispersion of repolarisation into a conduction block and wavebreak.

Which diseases are associated with an increased risk of VF? The majority of cases of SCD and VF occurs in patients with coronary artery disease, either due to acute ischemia, and/or scarring after previously healed myocardial infarction (Israel, 2014; Deo and Albert, 2012). Less frequent findings in patients with SCD are cardiomyopathies (dilated, hypertrophic, and/or arrhythmogenic right ventricular cardiomyopathy), or genetic diseases, such as long and short QT syndrome, Brugada syndrome, or catecholaminergic polymorphic ventricular tachycardia.

1.3 Myocardial infarction and ventricular fibrillation

Myocardial infarction, also known as heart attack, is the event when coronary artery flow is significantly diminished or stopped, e.g., due to a blockade by a thrombus. The diminished or abolished flow causes ischemia in the region downstream of the blockade, preventing the delivery of oxygen needed for cellular metabolism.

Acute and chronic ischemic damage accounts for the majority of cases of SCD, although the mechanisms of arrhythmogenesis are distinct (Manfredini et al., 1996; Deo and Albert, 2012). The earliest ischemia-associated arrhythmia is VF during acute myocardial infarction (AMI), which is particularly dangerous as it frequently occurs

before a patient becomes monitored (Gheeraert et al., 2006). Mechanistically, AMI results in a sudden decrease in oxygen availability in a part of myocardium, reducing ATP production and forcing the cells into anaerobic metabolism, causing acidosis; also, extracellular potassium levels become elevated. These changes translate into ionic dysbalance, cellular depolarisation, heterogeneous shortening of action potential duration, or calcium mishandling, all of which have pro-arrhythmic effects (Janse and Wit, 1989).

After AMI, the second stage of arrhythmia risk is reperfusion, which occurs when the coronary artery is unblocked by thrombolysis or angioplasty. Even though reperfusion reduces total size of future scar and is associated with smaller contractile dysfunction, the process may trigger additional damage and VF itself (Xing and Martins, 2001). While the mechanisms of reperfusion-induced injury and arrhythmia are still actively researched, it has been established that among the key processes involved are oxidative stress, calcium overload and hypercontracture, or rapid pH restoration inducing cellular death (Hausenloy and Yellon, 2013; Moens et al., 2005).

The subacute phase of myocardial infarction follows in the weeks following the acute infarction and it is characterised by temporary ionic channel and action potential remodelling (Pinto and Boyden, 1999), leading to spatial dispersion of repolarisation in the myocardium. During the healing phase, the myocardium damaged by infarction is healed by myofibroblasts that partially restore the tissue, but at the cost of marked fibrosis and scarring (Turner and Porter, 2013).

In the healed infarction phase, months after the infarction, a stiff akinetic scar is fully developed, predisposing the heart to arrhythmia (Koplan et al., 2009). There are multiple mechanisms of arrhythmia vulnerability in healed infarction stage. First, gap junctions in the infarct border zone are underexpressed and reorganised (Luke and Saffitz, 1991), promoting conduction slowing and heterogeneity. Second, the structure of the scar is heterogeneous: thin, slow-conducting fibres of myocytes were observed to survive in the scar, promoting re-entry when a delayed propagating wave emerges from the infarct (Richardson et al., 2015; De Bakker et al., 1988). A third cause of pro-arrhythmic heterogeneity is ionic and CaMKII remodelling promoting conduction

velocity slowing and altered calcium handling (Hund et al., 2008). In the next section, we describe cardiac alternans, an important contributor to arrhythmogenesis to which are infarcted hearts particularly vulnerable (Koller et al., 2005; Myles et al., 2011).

1.4 Cardiac alternans

Repolarisation alternans, the beat-by-beat alternation of long and short action potential durations present at high heart rates, has been clearly linked to ventricular arrhythmogenesis and subsequent sudden cardiac death (Smith and Wood, 1998; Wilson and Rosenbaum, 2007; Pastore et al., 1999). Episodes of fibrillation were observed to be consistently preceded by alternans formation both in ventricles (Wilson et al., 2009) and atria (Narayan et al., 2011), supporting the view that alternans is among the most important precursors to re-entrant arrhythmias. Post-MI hearts were shown to be vulnerable to repolarisation alternans compared to non-infarcted patients (Koller et al., 2005; Myles et al., 2011), and alternans is an independent predictor of SCD in MI patients (Yu et al., 2012; Ikeda et al., 2006). Moreover, most post-MI arrhythmias originate in the infarct border zone (BZ), the zone of viable myocardium adjacent to the infarct (Stevenson and Soejima, 2007), which has been shown to be more prone to alternans than non-infarcted myocardium (Gardner et al., 2015).

At the tissue level, alternans may be either spatially concordant (the whole tissue oscillating in-phase) or discordant (different regions oscillating in the opposing phase). Spatially discordant alternans is the more pro-arrhythmic variant due to electrical inhomogeneities between zones of shortened and prolonged action potentials which promote conduction block and reentry (Gaeta and Christini, 2012). A specific spatial pattern of alternans is 'spatially heterogeneous alternans', which is discordant or concordant, but crucially is restricted to a sub-region of myocardium (Gardner et al., 2015). This variant is expected to be pro-arrhythmic in a similar fashion to discordant alternans, as it induces repolarisation gradients between alternans-free and alternans-manifesting zones.

At the cellular level, in cells manifesting alternans, calcium transient amplitude oscillates concurrently with the action potential duration (APD) (Figure 1.3a,b). This

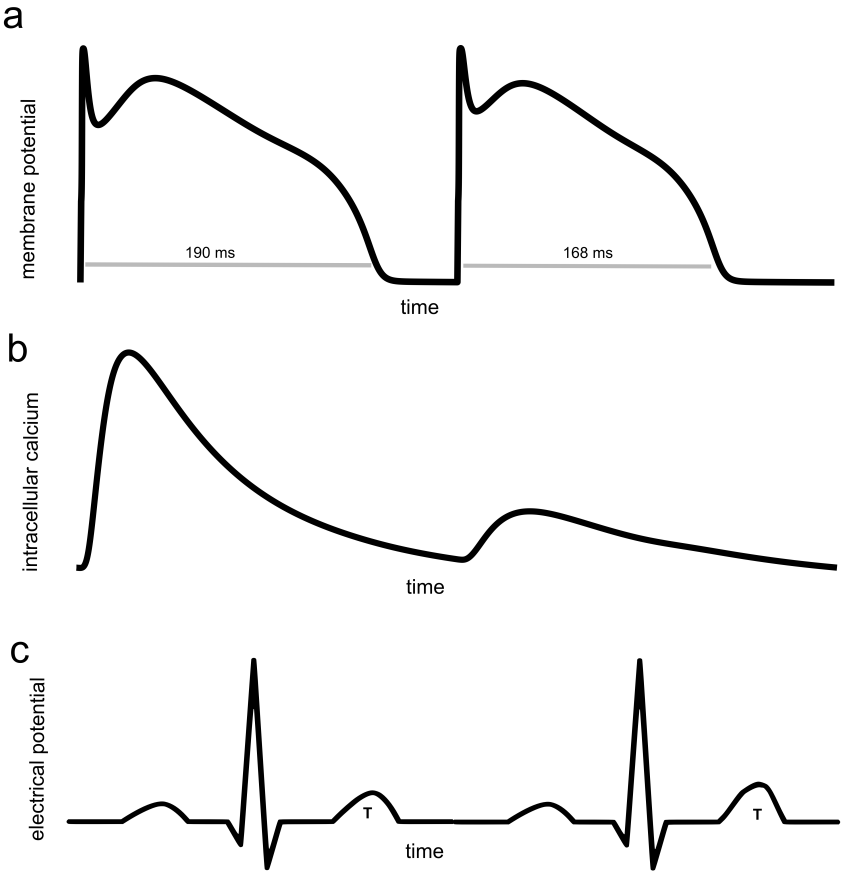


Figure 1.3: Different manifestations of cardiac alternans. a) Repolarisation alternans, showing a prolonged action potential, followed by a shortened one. b) Calcium transient alternans underlying the case (a), showing oscillations in amplitude of intracellular calcium transient. In c) is given an example of T-wave alternans in ECG signal (T symbols mark the T-wave); this plot is not temporally aligned with a,b.

raises the question of which of these two is the primary driver, however, the answer is complicated by the bidirectional coupling between the membrane potential and calcium transients. The evidence supporting either case is discussed below, followed by a description of T-wave alternans, the ECG manifestation of electrical alternans.

1.4.1 Alternans driven by steep restitution of APD

A key feature of cardiomyocytes is that the APD shortens with increased heart rate, allowing electrical propagation of all stimuli from the pacemaker. The "APD restitution" describes the recovery of the APD as a function of the diastolic interval (DI, the interval between repolarisation and the subsequent action potential). While this function is usually flat at slow pacing, it quickly becomes steeper at rapid pacing (i.e., a small

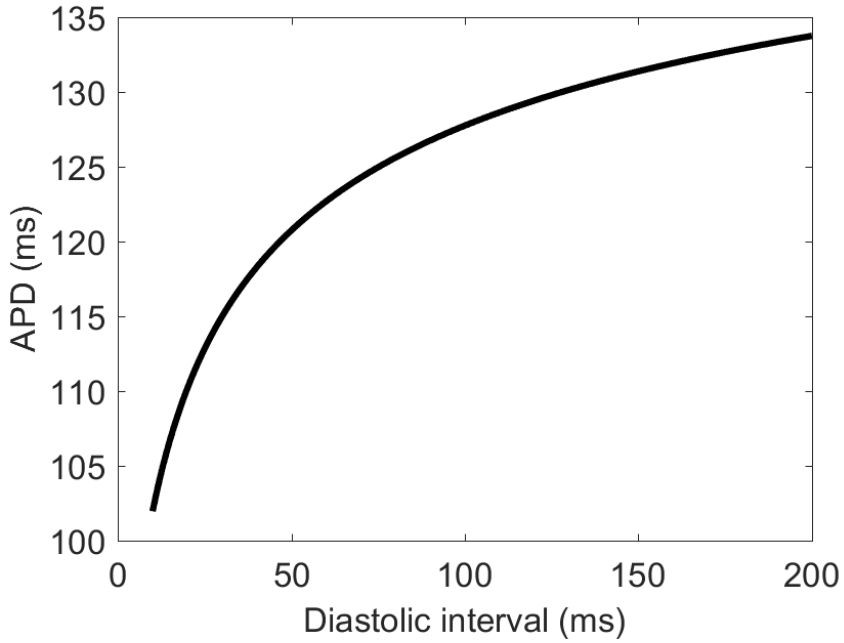


Figure 1.4: An example of a restitution curve, showing APD as a function of diastolic interval.

reduction in DI translates into a relatively large difference in APD); an illustration is provided in Figure 1.4. It was shown that the restitution curve with slope > 1 is associated with electrical instability and fibrillation (Kim et al., 2002; Koller et al., 1998). At the same time, restitution slope of > 1 may drive the APD alternans as shown by Nolasco and Dahlen (1968), which is thought to drive the arrhythmogenesis (Franz, 2003). Briefly, assuming fixed-rate pacing, the slope > 1, and, without loss of generality, a long action potential:

1. The prolonged APD shortens the DI, making subsequent APD much shorter.
2. The short APD translates into long DI, making subsequent APD long again.
3. The cell is essentially in step 1 again, showing how alternans may be perpetuated. The role of slope > 1 is critical in that it makes the difference between long and short APD large enough. With a flat slope of < 1, the oscillations dampen and the alternans would disappear over time.

This electrically driven APD alternans then translates into altered activation of L-type calcium current, which then affects intracellular calcium release and calcium transient

(Shannon et al., 2000), providing a mechanism for voltage-driven alternans in both APD and calcium (Kanaporis and Blatter, 2017).

At the same time, however, the importance of steep restitution has been disputed (Franz, 2003), highlighting the fact that naturally steep restitution curve may be beneficial compared to an overly flat curve. In the context of alternans, the criticism of APD restitution as the sole causative factor is mainly that APD alternans was not observed even when the slope of the restitution curve exceeded 1 (Banville and Gray, 2002) and alternans was observed when the slope was lower than 1 (Saitoh et al., 1988; Cram et al., 2011). Also, the restitution slope is seldom larger than 1 in humans, challenging the relevance of steep restitution in this case (Franz, 2003).

1.4.2 Alternans driven by calcium oscillations

On the other hand, if calcium oscillations were the primary driver, they could modulate membrane potential and APD via the sodium-calcium exchanger and other calcium-sensitive currents (Kanaporis and Blatter, 2015). Shkryl et al. (2012) have shown that calcium alternans occurred even when APD alternans was prevented using a voltage clamp, suggesting the independence of calcium alternans on APD alternans. The study by Pruvot et al. (2004) aimed directly at comparing the causative role of APD oscillations versus calcium oscillation, found calcium oscillations to be the more likely driver of alternans. Two primary mechanistic explanations of calcium alternans exist: the first is alternans due to oscillation of sarcoplasmic reticulum contents, presumably due to mismatch between large release and insufficient reuptake (Szentesi et al., 2004; Weiss et al., 2006). With oscillating contents of SR, the load-release relationship translates the oscillations into oscillations of calcium release and thus calcium transient. An alternative explanation of calcium alternans relies on an intrinsic refractoriness of ryanodine receptors, i.e., the release flux. This stems from the observation by Picht et al. (2006), where a small subset of observed cells manifested calcium alternans without concurrent SR oscillations. In this mechanism, a large calcium release makes the majority of ryanodine receptors refractory for the next action potential, allowing only a small release, however, during the action potential, the originally refractory ryanodine

receptors become available again, allowing the next release to be large again. Further discussion of possible mechanisms of calcium-driven alternans is given in Section 4.4.1, where our interpretation of alternans is discussed in the context of previous knowledge.

1.4.3 T-wave alternans

In a clinical setting, a proxy used for repolarisation alternans is T-wave alternans, the oscillation in location and/or amplitude of the T-wave of the ECG (Figure 1.3c). T-wave alternans was shown to be a powerful predictor of mortality and arrhythmia in multiple diseases (Costantini et al., 2009; Salerno-Uriarte et al., 2007; Nieminen et al., 2007), although this finding is not universal (Gold et al., 2008). At the cellular level, T-wave alternans is thought to arise from spatial repolarisation heterogeneity (Verrier et al., 2011), e.g. due to discordant alternans. An alternative mechanism was proposed by Narayan et al. (2008), where action potential plateau amplitude alternans was strongly associated with T-wave alternans at slower heart rates, rather than APD alternans[6]. It is not clear, however, whether or not the T-wave alternans due to action potential plateau alternans is proarrhythmic in a similar fashion to the T-wave alternans driven by repolarisation alternans.

1.5 The role of cardiac sympathetic nervous system in arrhythmogenesis

Cardiac sympathetic nervous system (CSNS) is the "fight-or-flight" branch of autonomic nervous system, responsible for an increased heart rate and contractility in response to danger or exercise. The pattern of CSNS[7] is given in Figure 1.5, showing how brain-controlled long fibres extend from stellate ganglia, innervating SA node, AV node, atria,

[6] I believe this study is slightly confounded by the methodology used. APD estimation was performed using a threshold at a given level between the plateau and baseline, unlike the conventional level selection between peak and baseline. Consequently, with plateau oscillations, the APD estimation threshold also oscillates; for action potentials with high plateau and prolonged APD, the APD threshold is relatively high, shortening the estimated APD, compared to a low-plateau, shortened APD. This could shroud genuine APD oscillations; however, raw data shown in the article suggest that the APD oscillations are indeed small compared to the pronounced plateau alternans.

[7] The figure also shows the innervation pattern of parasympathetic nervous system, which has generally opposite properties to CSNS, diminishing heart rate and contractility. The sensory nerves then send information about the state of the heart back to brain.

and ventricles. The nerve terminals in contact with cardiomyocytes then act primarily via the release of neurotransmitter norepinephrine, which binds to β-adrenoreceptors on myocytes (predominantly β_1 subtype). This then activates a range of downstream effects, mostly mediated by cAMP-dependent protein kinase A; possible effects are, e.g., potentiation of funny current in pacemaker cells, or enhanced function of L-type calcium current and SERCA pumps, enhancing contractility. Galanin and neuropeptide Y are released in addition to norepinephrine by sympathetic nerves. The precise role of these co-transmitters is still actively researched (Herring et al., 2012; Kalla et al., 2016). A separate source of cardiac sympathetic activation are β-agonists circulating in blood, predominantly epinephrine released by the adrenal medulla under stress, which also activates β-adrenoreceptors (Cryer, 1980).

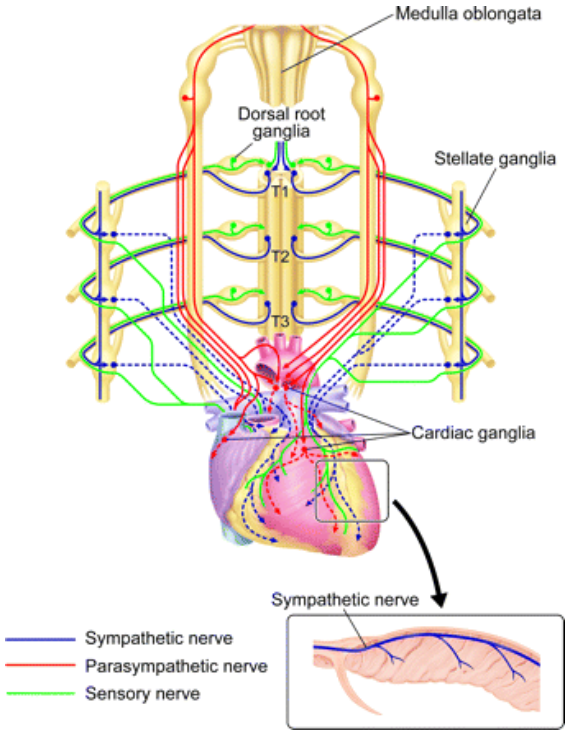


Figure 1.5: Anatomy and distribution of the cardiac nervous system. The cardiac sympathetic nerves (blue) extend from sympathetic neurons in the stellate ganglia, which are located bilateral to the thoracic vertebra. The cardiac parasympathetic nerves (red) extend from parasympathetic neurons in the cardiac ganglia, which are located in the base of both atria. The sensory nerves (green) project to the upper thoracic dorsal horn via dorsal root ganglia. The inset indicates the transverse section of the heart and demonstrates the distribution of sympathetic nerve fibers within the left ventricle. Reproduced with permission from (Kimura et al., 2012)

In addition to the CSNS's physiological role in healthy tissue, excessive activation of CSNS and β-adrenergic stimulation was implicated in promoting arrhythmia formation in most diseases (Shen and Zipes, 2014).

Some studies suggest that CSNS-driven increase in spatial dispersion of repolarisation is a key contributor to arrhythmogenesis (Opthof et al., 1991; Vaseghi et al., 2012); however, it is challenging to design experiments that would unambiguously confirm the relevance of this hypothesis. When relying on direct stimulation of CSNS (Opthof et al., 1991), it is difficult to be certain that all the stellate ganglia were stimulated in a physiologically equivalent way and that some projections were not left unstimulated. Additionally, in *ex vivo* preparations, certain nerve projections may be damaged when the whole heart is excised. Both the inhomogeneous stimulation and neural damage may promote an unphysiological heterogeneity of CSNS activation. Studies relying on perfusion of a β-agonist studying its impact on arrhythmogenesis suffer from possibly different spatial distribution of innervation and β-agonist delivery via blood, as well as from uneven sensitivity to such stimulation. A concrete example is the study by Gardner et al. (Gardner et al., 2015), where denervated zones in the heart were shown to be excessively sensitive to β-agonist perfusion, increasing spatial dispersion of repolarisation under β-adrenergic stimulation. However, it is not clear whether this phenomenon could ever occur in hearts *in vivo*, given that the denervated tissue is by definition not receiving β-AR stimulation (with the exception of low-concentration circulating catecholamines). Thus, further research and careful interpretation of the results are needed in this field.

There is a consensus on the pro-arrhythmicity of CSNS in healthy hearts, and its dangers in certain genetic diseases, such as long QT syndrome (LQTS) or catecholaminergic polymorphic ventricular tachycardia (CPVT), have been established beyond reasonable doubt (Shen and Zipes, 2014). In LQTS1, the most frequent subtype of LQTS which is also most associated with CSNS-driven arrhythmia (Ackerman et al., 2017), a mutation in the gene KCNQ1 (an I_{Ks} subunit) underlies the disease (Wu et al., 2014). Mutations of KCNQ1 which trigger LQTS1 blunt the response of I_{Ks} to β-AR stimulation (Wu et al., 2014). Consequently, β-AR stimulation increases the

heart rate, but does not reduce action potential duration, predisposing the hearts to formation of conduction block (Kass and Moss, 2003)[8]. Another cardiac disease linked to genetics and CSNS is the catecholaminergic polymorphic ventricular tachycardia (CPVT) (Leenhardt et al., 2012), where the polymorphic VT is reliably triggered by β-AR signalling. In CPVT, two causative genes have been identified: RYR2 (encoding RyR, the cardiac SR release channel) and CASQ2 (encoding the JSR buffer calsequestrin). Under these conditions, the β-AR-induced increase in SR release promotes spontaneous calcium release from the SR and subsequent delayed afterdepolarisations (Watanabe and Knollmann, 2011). Disturbed function of RyR, such as increased SR leak, was also observed in arrhythmogenic right ventricular cardiomyopathy (CPVT) (Milting et al., 2006), potentially explaining the arrhythmogenecity of CSNS in this disease (James et al., 2013)[9]. Given the clear involvement of CSNS in these diseases, therapies such as beta-blockers, or cardiac sympathetic denervation are widely used (Collura et al., 2009; Bos et al., 2013; Watanabe and Knollmann, 2011). Cardiac denervation is also successfully used to treat electrical storm, a condition where VT/VF manifests multiple times in short succession, presenting a major risk of death (Vaseghi et al., 2014; Ajijola et al., 2012).

Despite the established pro-arrhythmic role of CSNS in the conditions discussed above, we believe that the role of CSNS on arrhythmogenesis after MI is controversial; at the same time, it is of utmost importance, given the high incidence of SCD and VF in patients with a history of MI.

During an acute MI, the infarct border zone becomes denervated, with subsequent reinnervation labelled “nerve sprouting” following in the months after (Hartikainen et al., 1996; Fallen et al., 1999). Historically, the role of nerve sprouting was considered proarrhythmic in line with observations in healthy hearts; studies supporting this view are overviewed by Shen and Zipes (2014). However, this view is not consistent with recent large-scale human clinical studies which demonstrate that lack of nerve

[8]Interestingly, the root cause of LQTS is crucial with regards to its link to CSNS: in LQTS3, where a gain-of-function mutation promotes late sodium current, a reduction in CSNS activity might be harmful to patients, as the mechanism of arrhythmia is exacerbated at low heart rate (Kass and Moss, 2003).

[9]At the same time, however, reduced adrenergic innervation was associated with future recurrence of VT (Paul et al., 2011). In my opinion, this suggests that increased heart rate might be the cause of arrhythmia rather than a direct effect ventricular innervation.

sprouting after MI is strongly associated with the danger of fibrillation. A summary is given by Malhotra et al. Malhotra et al. (2015), see, e.g., (Fallavollita et al., 2014, 2017). This apparent clash of evidence warrants further research and highlights the necessity of understanding the mechanistic role of CSNS in arrhythmogenesis after MI.

1.6 Model systems in arrhythmia research

Having described the physiological setting of this thesis, we now briefly discuss the background of methods used.

1.6.1 Ex vivo Langendorff heart

The Langendorff perfused heart preparation is a popular experimental technique described originally in 1895 by Oscar Langendorff (Langendorff, 1895), used to study a wide range of phenomena *ex vivo*, such as cardiac haemodynamics, ischemia, arrhythmia, drug effects, or deterioration of pre-transplantation hearts (Skrzypiec-Spring et al., 2007). Despite its limitations which we discuss below, it remains a popular technique and is still used in current research in multiple species, with various modifications enabled by its flexibility (Bell et al., 2011).

In a normal mammalian heart, blood oxygenated in pulmonary circuit enters the left atrium, flows to the left ventricle, and it is subsequently ejected to the systemic circuit. In a Langendorff preparation, the heart is isolated from both systemic and pulmonary blood vessels and is retrogradely perfused via a cannula inserted into aorta, above the aortic valve. Consequently, when an appropriate oxygenated solution flows through the cannula, the pressure seals the aortic valve and makes the solution flow through coronary vessels, bringing oxygen and nutrients to the cardiac muscle, allowing its function in isolation. The solution ultimately flows to the coronary sinus and right atrium, from which it is subsequently ejected. The solution used depends on the particular application: using blood is relatively rare, the Krebs-Henseleit buffer or its modification is possibly the most common perfusate (Bell et al., 2011).

The leading advantages of Langendorff heart are its cheapness and simplicity. Once a Langendorff heart is perfused, a wide range of parameters may be extracted, such

as heart rate and its variability via ECG, left ventricular pressure via intraventricular balloon, or properties of conduction and/or calcium handling imaged using fluorescent dyes. It is also easy to deliver precise doses of substances to the heart, making the model a popular choice for studying dose-response relationships (Skrzypiec-Spring et al., 2007), such as in studies of cardiac drugs.

The main disadvantages of Langendorff heart, beyond the unphysiologicalness of retrograde scheme of perfusion[10], are the lack of osmotic pressure, which may cause edema in long experiments, or continuous deterioration of the prep over time (Bub et al., 2010). Nevertheless, it has been established that Langendorff hearts may be studied for several hours, which is sufficient for most applications (Sutherland and Hearse, 2000). A general hazard associated with *ex vivo* hearts is their relative fragility and low tolerance to prolonged hypoxia, necessitating precise, but fast excision of the heart from the chest and an early intubation with an oxygenated solution.

A concrete implementation of a Langendorff heart used in this thesis is given in Section 2.1.

1.6.2 In vitro cultured cardiomyocytes

Another popular model used to study arrhythmogenesis is the cultured cardiomyocyte monolayer (CCM) (Tung and Zhang, 2006). CCMs may be made by mincing the tissue of interest (usually ventricles) of neonatal hearts, digesting the extracellular matrix using a collagenase, and purifying the remaining mixture of cells. Neonatal or embryonic myocytes, when isolated and cultured, maintain the ability to divide and form gap junctions, allowing the formation of excitable sheets of cardiac-like tissue. Such cultures were used to study arrhythmia-related concepts, such as barrier-induced reentry (Entcheva et al., 2000), spiral wave formation due to poor cell-to-cell coupling (Bub et al., 2002), or instabilities in calcium handling (Bien et al., 2006).

[10]There exists a more physiologically accurate model of *ex vivo* heart, the "working heart" model, where oxygenated solution enters the left atrium and then leaves via aorta, as in a normal mammal heart. However, unless the physiological scheme of perfusion is required, Langendorff hearts are used more frequently, possibly because of the simplicity and quickness of the dissection, minimising the risk of hypoxia and cardiac damage.

Compared to *ex vivo* hearts, CCM offer multiple advantages, relying on superior control over the preparation and simplified structure. First, a relatively arbitrary ratio of myocytes and fibroblasts may be plated, allowing the study of the role of fibroblasts density on conduction, showing, e.g., that fibroblasts are capable of conducting electrical signal over a relatively large distance of 300 micrometers (Gaudesius et al., 2003). Co-cultures with other cell types such as cardiac sympathetic neurons may be also created, studying neural effect on myocyte electrophysiology (Conforti et al., 1991) or conduction properties (Burton et al., 2015a). Second, the cells may be plated in a way that imposes a certain spatial structure, allowing assessment of microstructure on arrhythmogenesis (Bursac et al., 2002); this is particularly relevant for modelling diseases where normal structure of myocardium is disrupted. Third, the cells may be plated on elastic surfaces, enabling the study of stretch-induced changes on cells, such as apoptotic signalling (Persoon-Rothert et al., 2002), or extracellular matrix production (Guo et al., 2013). Fourth, compared to *ex vivo* hearts where the preparation is useful for hours only, cell cultures are viable for days to weeks. This enables studying development of myocyte morphology over time (Kreipke and Birren, 2015), or the impact of long-term treatment on metabolism in myocyte-fibroblast cultures (Schroedl and Hartzell, 1983). Fifth, given that the cultured monolayers are thin and may be plated as to not manifest tissue-scale contraction (with each cell contracting separately), dye-free imaging may be used to assess propagation of electrical waves (Burton et al., 2015b). This avoids the disadvantages associated with voltage and calcium dyes (phototoxicity, photobleaching), allowing continuous observation of the cells for the whole lifespan of the culture.

The undoubted advantages of cultures are bought at the cost of direct physiological relevance. With the wide range of perturbations possible (different cell ratios, different plating conditions, etc.), many unphysiological combinations are inherently created, and many physiological parameters are omitted (such as spatial gradients of expression (Opthof et al., 2017)). Also, the 2D nature, while facilitating observation and understanding, is a considerable simplification compared to full 3D structure of the heart. Ultimately, the neonatal nature of the cultured cells, required for their division and formation of gap junctions, means that the resulting tissue may manifest mechanisms

of arrhythmia that are relevant only to neonatal cells. For example, the neonatal cells abundantly express hyperpolarisation-activated channels underlying pacemaking funny current, which are barely expressed in mature myocytes (Er et al., 2003). These channels are powerfully modulated by β-adrenergic stimulation (DiFrancesco and Tortora, 1991). Consequently, β-adrenergic stimulation of neonatal cultures may increase the beating rate and exacerbate gradients of repolarisation, making the culture prone to arrhythmia, however, the relevance of this particular path to arrhythmia is low in an adult heart. Similarly, given the importance of funny current on upstroke duration and velocity in neonatal cells, modulators of funny current may increase conduction velocity in a way that is not highly relevant for adult tissue.

1.6.3 Computer modelling

The wealth of data recorded from cardiac cells and tissue enabled researchers to reverse engineer mechanisms and assemble computer models of cardiac cells and of the heart. A wide range of spatial scales may be simulated, from whole 3D organs (Lopez-Perez et al., 2015), down to subcellular processes and phenomena (Kekenes-Huskey et al., 2013). Computer models at tissue/organ level were used to understand the organisation of fibrillation (Ten Tusscher et al., 2007), some of its underlying causes (Echebarria and Karma, 2007; Qu et al., 2000), and to study the impact of pharmaceutical intervention (Bernus et al., 2002), drug therapy (Passini et al., 2017), tissue ablation (Ruchat et al., 2007), and defibrillation (Trayanova and Chang, 2015). At the cellular level, simulations were used to improve the insight into calcium handling and CaMKII signalling (Livshitz and Rudy, 2007; Hund and Rudy, 2004), repolarisation abnormalities (Britton et al., 2017; Silva and Rudy, 2005), and beat-to-beat-variability, an important marker of survival prognosis in heart disease (Heijman et al., 2013).

Computer modelling brings the following benefits (Yang and Saucerman, 2011): First, a simplification of a complex system makes it easier to understand key mechanisms driving a certain phenomenon (as opposed to a fully complex biological system where it is not clear what may or may not be involved in the phenomenon in the first place). Second, the simplification enables a search of a wide range of parameters

and/or conditions, which might not be feasible and/or practical using an experimental animal-based approach. Thus, even if a computer simulation may not provide the ultimate answer, it may nevertheless be useful in limiting the breadth of experiments performed, providing life and monetary savings. Third, a computer model offers perfect control and observability, unlike any experimental system, allowing superior insight into its behaviour. That said, independently on the scale, computational models are a simplification of experimentally obtained data, which is a potential intrinsic disadvantage[11].

The most relevant level of granularity for this work is single-cell modelling with the focus at cellular physiology and calcium handling, which may be extended to a fibre or tissue simulation using monodomain or bidomain approach (Potse et al., 2006). With the first model of such a type being the Noble model (Noble, 1960), the Luo-Rudy guinea pig model of 1991 (Luo and Rudy, 1991) seems to be a particularly prominent parent to many of today's models. It has been subsequently modified for modelling of canine myocytes and CaMKII signalling has been included (Hund and Rudy, 2004). The model was updated to improve various current formulations which allowed simulation of different diseases and the development of a human-specific parametrisation (Silva and Rudy, 2005; Faber et al., 2007; Decker et al., 2009; Decker and Rudy, 2010; Heijman et al., 2011; O'Hara et al., 2011). Most currents of these models are formulated using an equation which may depend on ionic concentrations, kinetic changes, or membrane potential. For example, the classical formulation of fast sodium current is:

$$I_{Na} = \overline{G}_{Na} \cdot m^3 \cdot h \cdot j \cdot (V - E_{Na}),$$

[11]Personal comment: This is a frequent criticism of computer models, going along the lines of "it does not include all possible aspects of physiology, thus it is wrong". A common riposte to such a statement is the aphorism "all models are wrong, but some are useful". I believe it is an accurate out-of-the-Box thinking, which can be illustrated with an example of navigation: A tourist map is a gross oversimplification of the real world. For example, it does not contain the information on all the insects present, the rocks on the roads, or eventual black cats at a quayside; the criticism could go on almost infinitely. At the same time, a map is of great help in an unknown area, allowing fast path-finding between two locations precisely because it does not contain the full complexity of the environment. Going back to the serious world of cardiac modelling, one may argue that a computer model is essentially a collection of previous work, similar to a synthesizing review article, with the advantage that it may be validated, it provides quantitative information, and it may be used to test novel hypotheses. Surprisingly, very few people if any protest against synthesising review articles (without the listed advantages) as being wrong oversimplifications.

where $\overline{G}_{Na}$ is the maximum conductance, E_{Na} is the reversal potential of sodium, and m, h, j are gating variables which develop over time based on activation and inactivation properties of the channel (Luo and Rudy, 1991). An alternative option used for several currents in Rudy family of models relies on a Markov model to represent a channel, where different open and closed types of the channel may be represented along with their transitions, providing greater flexibility at an increased computational cost (Oehmen et al., 2002). The concrete cellular models used in this thesis are described in Section 2.2.

1.7 Thesis aims and structure

The main aim of this thesis is to understand the effect of β-AR stimulation on alternans in hearts after myocardial infarction. In greater detail:

1. To assess vulnerability of post-MI hearts to alternans, testing the hypothesis that the infarct border zone is more prone to alternans formation than the noninfarcted myocardium.

2. To characterize the effect of β-AR stimulation on alternans formation in the post-MI hearts.

3. To provide a mechanistic explanation of the observed effects of β-AR stimulation on alternans.

4. To develop software tools for processing the large amount of experimental data obtained in an automated and unbiased way.

After giving an overview of general methodology in Chapter 2, Chapters 3-5 describe how thesis aims are met. Aims 1 and 2 are met in Chapter 3, where we used rat Langendorff hearts with a healed myocardial infarction to show that the infarct border zone is increasedly prone to alternans compared to noninfarcted myocardium and that β-AR stimulation attenuates alternans.

Aim 3 is covered by Chapter 4, where we assembled a model of ventricular myocyte which allows simulating normal and infarct border zone cell, as well as allowing simulated β-AR stimulation. Using this model, we replicated key experimental results from Chapter 3, and analysed the model to show that simulated β-AR stimulation abolishes alternans via acceleration of SR release, which is shown to improve SR reuptake rate. Pro-arrhythmic consequences of alternans were also demonstrated, based on simulations of cellular fibres.

To address the need for automated data processing, specified as Aim 4, we designed and implemented a set of Matlab pipelines which enable the analysis and mapping of alternans and tissue recovery properties (Chapter 2). Additionally, in Chapter 5, we

describe a software tool aimed at processing data from cultured cardiac monolayers, which enables extraction of a rich set of features describing conduction properties (such as velocity, or smoothness).

Underneath the bridge
The tarp has sprung a leak
And the animals I've trapped
Have all become my pets
And I'm living off of grass
And the drippings from the ceiling
But it's okay to eat fish
'Cause they don't have any feelings

Nirvana – Something in the way

2 General methods

In this section, I provide more details of the methodology used. First, the setup of Langendorff heart is described, followed by an overview of infarction procedure and pacing protocols. Second, we describe the computer model of a ventricular myocyte with β-AR stimulation and infarct border zone remodelling, used throughout the thesis.

2.1 Langendorff heart

A diagram of the Langendorff setup used is given in Figure 2.1. The perfusate is stored in two tanks, Figure 2.1A; one tank contains control solution (NaCl 120.3 mM, KCl 4 mM, MgSO4*7H20 1.3 mM, NaH20P4 1.2 mM, CaCl 1.2 mM, NaHCO3 25.2 mM, glucose 11 mM), the other one containing an additive, such as norepinephrine. Both tanks are oxygenated with 95% O_2 and 5% CO_2.The tanks are water-jacketed and heated to warm the perfusate to 37°C at the tip of the cannula perfusing the heart. A system of t-valves is used to choose which tank perfuses the heart (Figure 2.1B). A peristaltic pump (Figure 2.1C, Minipuls 3, Gilson UK) maintains a steady flow of 10 ml/min from the tanks towards the heart. The perfusate is then filtered (Figure 2.1D, cellulose filter and pre-filter, pore size 5 μm).

Before entering the heart, the perfusate flows through a junction block (Figure 2.1E). The block contains a water-jacketed spiralling tube (Figure 2.1E_1) which facilitates

heating the perfusate to the desired temperature. A bubble trap is attached to the tube, preventing bubbles entering the heart, which would block perfusion and cause ischemia (Figure 2.1E_2). Under the junction block is a gel-filled side-tube joining the outflow tube (Figure 2.1E_3). This is used in dye loading, where a syringe needle pierces the gel and an operator ejects the dye without risk of adding oxygen bubbles. Using fluorescent dyes in the heart allows imaging of calcium and membrane potential dynamics. Rhod-2 dye was used for calcium mapping and RH-237 for voltage mapping (injected through the gel; 100 µl over 2 minutes and 20 µl over 1 minute respectively).

The imaging system (Figure 2.1F) is based on the design by Choi and Salama (2000), but here we use two Photometrics Evolve 128 cameras attached to a dual emission image splitter (Cairn Research TwinCam). Light is collected using a 50mm f0.95 lens (Navitar), and is directed to the cameras after passing through a dichroic mirror with a cut-off 630 nm. Fluorescence light below 630 nm passes through a 585 ± 20 nm interference filter and the fluorescence light above 630 nm was passes through a 715 nm high pass filter before being imaged by the cameras. Two green LEDs (530 nm Cairn Research OptoLED) are used to illuminate the heart after being passed through bandpass filters (530 ± 20 nm) to minimize stray excitation light reaching the sensors.

After the perfusate leaves the heart, it is collected at a dish and passed to further tubing (Figure 2.1G). At the start of the experiment, the perfusate is discarded, as the heart needs to be washed internally. After the heart is clean and stabilised, a second peristaltic pump may be used to pass the used perfusate back to the perfusion tanks, where it is reoxygenated. Recycling is particularly convenient when fluorescent dyes and drugs are used, as a much lower amount is required.

2.1.1 Myocardial infarction in Langendorff hearts

Given the focus of this thesis on post-infarction arrhythmogenesis, a particularly important version of Langendorff preparation is the one performed on hearts with a healed[1] myocardial infarction. There are two distinct ways of inducing an infarction experimentally: ligation of left anterior descending coronary artery (LAD) and cryoinfarction.

[1] As opposed to acute infarction which causes arrhythmia by different means.

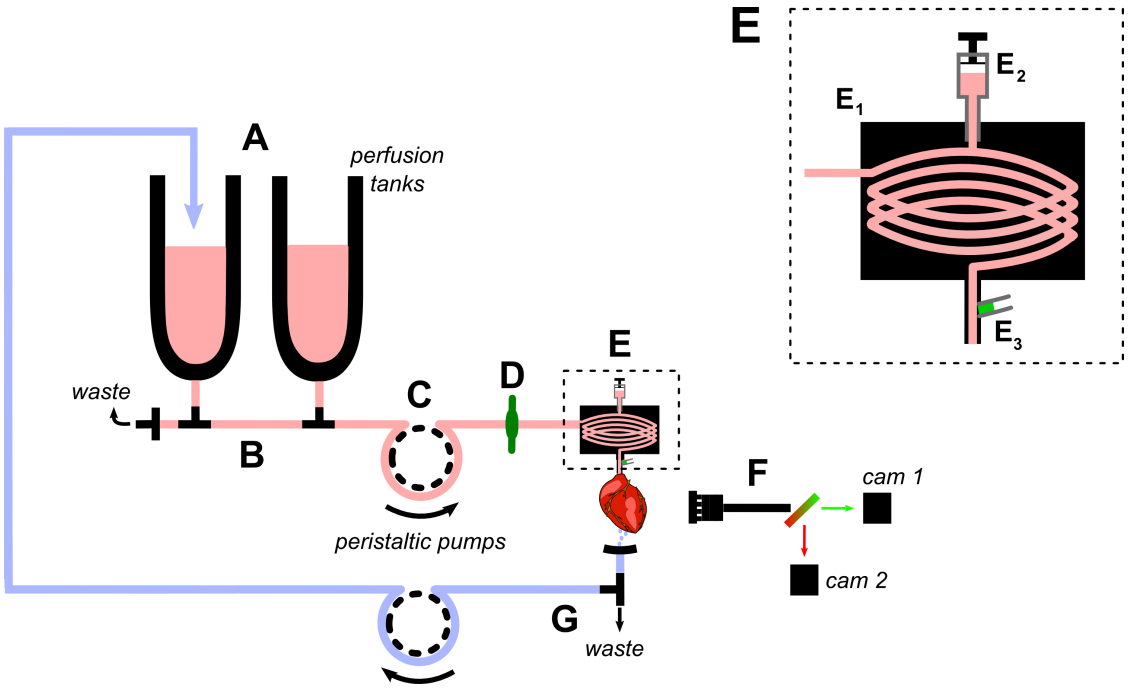


Figure 2.1: A schematic of Langendorff heart setup. A = perfusion tanks; B = T-valves used for selecting perfusion; C = peristaltic pump pushing the solution to the heart; D = a filter; E = junction block (E_1 = waterbath-warmed spiral, E_2 = bubble trap, E_3 = gel-filled tube facilitating dye loading); F = camera lens with adjacent diodes illuminating the heart, followed by a dichroic mirror splitting the fluorescent signal into two photodetectors; G = a t-valve switching between recycling, or discarding the solution passed through the heart.

LAD ligation is historically more common and involves a suture being tied around the left anterior descending coronary artery, blocking blood flow to a myocardial region (Shao et al., 2013). The suture may be either released after a certain period (ischemia-reperfusion) or remain tied (permanent occlusion). This method is still being developed, with new advancements considerably simplifying the procedure, as well as making it shorter and less invasive than traditional, thoracotomy-based approaches (Gao et al., 2010).

An alternative method, used in this work, relies on a cryoinjury causing local ischemia and subsequent myocardial remodelling (e.g., inflammation, reparation, scarring) which is similar to the results of LAD (Ciulla et al., 2004; Lewis, 2017). The cryoinfarction has the following advantages compared to LAD, which is why it was used in our work:

- Finer control over the infarct location and size.

- It enables formation of an anterior infarct, corresponding to clinical practise, unlike LAD, which is prone to formation of apical infarction and ventricular aneurysm (van den Bos et al., 2005).

- Cryoinfarction is less invasive than LAD and is associated with lower perioperative mortality, reducing the number of animals required (van den Bos et al., 2005).

2.1.2 Common pacing protocols in Langendorff hearts

When an electrode is positioned to touch the apex of the Langendorff heart, the natural sinus rhythm may be overdriven by an external pacing, provided the frequency of stimulation is high enough. The first type of pacing protocol commonly used is the "S1 protocol", which is a simple fixed-rate pacing with the stimuli arriving S1 milliseconds apart. The duration of S1 coupling interval is also commonly named "base cycle length". This type of pacing protocol may be used, e.g., to study the development of alternans at rapid pacing (Gardner et al., 2015); common S1 coupling intervals would be 150-250 for canine or human hearts, or 60-120 for small rodents. When using extremely rapid pacing (e.g., 30ms), so called ventricular fibrillation threshold may be tested (Walcott et al., 2011).

The "S1-S2" is the second commonly used pacing protocol, where a sequence of S1 stimuli is applied as in S1 protocol, followed by a single "S2" stimulus emulating an extrasystolic stimulus, with coupling interval of S2 ms after the last S1 stimulus (S1<S2 usually) (Goldhaber et al., 2005; Qu et al., 2010). Typically, a range of S2 coupling intervals is tested and variables of interest, such as APD, are plotted as a function of S2 or diastolic interval, providing information on tissue restitution and refractoriness of membrane potential and/or calcium handling.

2.2 Computational modelling of ventricular myocytes

2.2.1 A model of β-adrenergic stimulation and and post-infarction remodelling in a ventricular myocyte

The simulation work in this thesis is predominantly based on the canine cardiomyocyte model by Heijman et al. (2011), based of the Hund-Rudy family (Hund and Rudy, 2004; Decker et al., 2009). A diagram of the model is given in Figure 2.2, showing the currents and their regulation via CaMKII and β-AR stimulation. The model can reproduce, among other things, action potential adaptation, restitution, and accommodation, as well as β-AR-dependent changes in cyclic AMP levels, site phosphorylation and effects on electrophysiological properties, including APD and CaT amplitude.

The model consists of a state vector (recording ionic concentrations, channel openings, etc.) and differential equations which describe how the elements of the state vector change based on temporal dynamics and other conditions. Below are described the components of the model in greater detail, namely the compartmentalisation, electrophysiological component, calcium handling, β-AR stimulation, and infarct border zone remodelling.

2.2.1.1 Model compartments

The ionic currents and elements of calcium handling are structured in two compartments: main cytosol and "calcium subspace" ("SS" in Figure 2.2). The subspace represents the volume of cell adjacent to T-tubules, where L-type calcium channels and clusters of ryanodine receptors (sarcoplasmic reticulum release units) are located. In this compartment, locally elevated calcium concentrations are formed during calcium-induced calcium release. This local concentration elevation subsequently gradually dissipates, as the calcium diffuses to the main cytosolic pool.

The sarcoplasmic reticulum within a cell is also separated into two compartments: junctional SR (JSR) and network SR (NSR). JSR contains the SR release units, ryanodine receptors, and the calcium is released into junctional SS. NSR contains the SERCA

pumps and reuptakes calcium from the main cytosolic pool. JSR is refilled from NSR along the calcium concentration gradient.

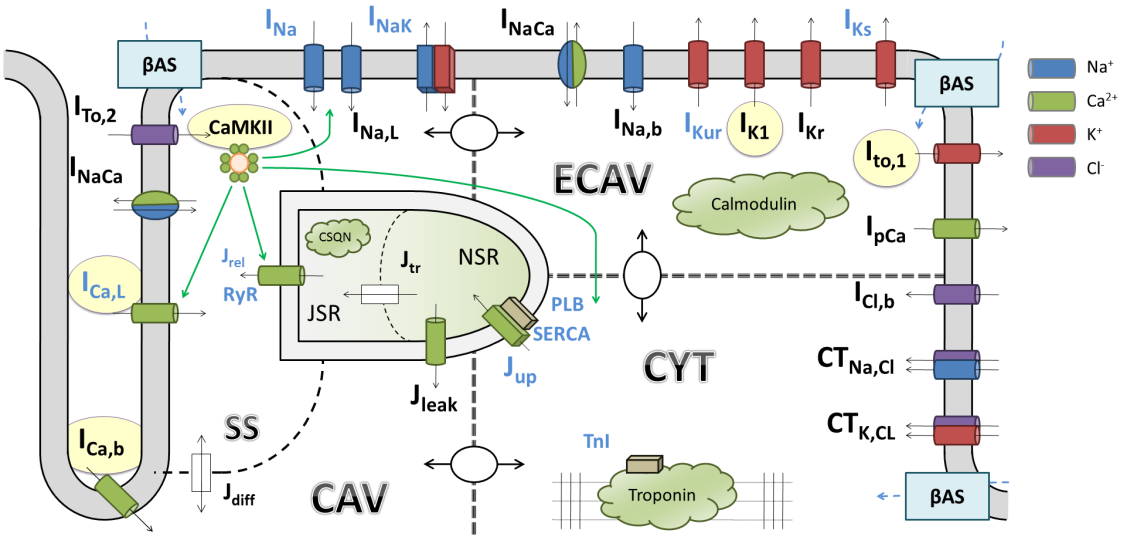


Figure 2.2: A schematic of canine myocyte electrophysiology, calcium handling, and signalling. In blue are written components that are affected by β-adrenergic stimulation. The green arrows indicate activation via CaMKII. SS indicates calcium subspace where calcium influx via I_{CaL} occurs and where calcium is released from the sarcoplasmic reticulum. CAV, ECAV, and CYT are β-AR signalling domains.
Transmembrane currents: $I_{Ca,b}$ (background calcium current), $I_{Ca,L}$ (L-type calcium current), I_{NaCa} (sodium-calcium exchanger; present both in membrane of calcium subspace and in the rest of the cell), $I_{To,2}$ (calcium-dependent transient outward chloride current), I_{Na} (fast sodium current), $I_{Na,L}$ (late sodium current), I_{NaK} (sodium-potassium pump current), $I_{Na,b}$ (background sodium current), I_{Kur} (ultrarapid delayed rectifier potassium current), I_{K1} (inward rectifier current), I_{Kr} (fast component of delayed rectifier current), I_{Ks} (slow component of delayed rectifier current), $I_{To,1}$ (4-aminopyridine-sensitive transient outward current), I_{pCa} (sarcolemmal calcium pump), $I_{Cl,b}$ (background chloride current), $CT_{Na,Cl}$ (sodium-chloride cotransporter), $CT_{K,\,Cl}$ (potassium-chloride cotransporter).
Intracellular space fluxes and signalling: CaMKII (Ca^{2+}/calmodulin-dependent protein kinase II), JSR (junctional sarcoplasmic reticulum), NSR (network sarcoplasmic reticulum), J_{rel} (JSR release flux via RyR, ryanodine receptors), J_{diff} (diffusion between SS and the rest of the cell), J_{leak} (leak from NSR), J_{tr} (diffusion from NSR to JSR), J_{up} (reuptake via SERCA pumps; modulated by PLB, phospholamban), TnI (troponin-I). The figure is based on a diagram used in (Tomek et al., 2017). See (Heijman et al., 2011) for details of signalling domains.

2.2.1.2 Electrophysiology and calcium handling in the Heijman-Rudy model

The model contains the major transmembrane ionic currents present in canine myocardium, such as:

- fast sodium current, I_{Na}, responsible for action potential upstroke),
- L-type calcium current, I_{CaL}, responsible for calcium influx and triggering CICR,
- transient outward potassium current, I_{to}, forming the characteristic spike-and-dome shape of an action potential,
- fast and slow component of delayed rectifier potassium current, I_{Kr}, $_{IKs}$, which are the leading currents underlying recovery of membrane potential to baseline in canine myocytes,
- time-dependent potassium current, I_{K1}, determining the slope of the final phase of repolarisation,
- sodium-potassium pump, I_{NaK}, a pump restoring the ionic balance,
- sodium-calcium exchanger, I_{NaCa}, bringing additional calcium into the cell after the influx via I_{Na} and then ejecting calcium released from the SR.

All other currents are listed in Figure 2.2 with details and full equations in (Heijman et al., 2011).

The calcium handling cycle during an action potential is triggered by a calcium influx via I_{CaL}. In response to this, calcium is released from the JSR via RyR. Subsequently, the released calcium diffuses to the main cytosolic pool and it is reuptaken to the NSR by SERCA pumps. A part of the released calcium is extruded via sodium-calcium exchanger. Within the SR, JSR is refilled from NSR given the concentration gradient (partly maintained due to calcium buffering in the JSR via calsequestrin).

Electrophysiology and calcium handling within the simulated cell are powerfully modulated by CaMKII. CaMKII is activated by increased calcium levels in junctional SS; activated CaMKII then phosphorylates ionic channels and proteins of the SR. CaMKII phosphorylation enhances I_{Na}, I_{Na}, I_{CaL}, RyR (and thus potentiates J_{rel}), and SERCA pumps reuptake rate (and thus J_{up}). This enhancement is critical in rate-dependent behaviour of the cell, such as increased calcium transient amplitude.

2.2.1.3 β-AR signalling in the HeRd model

The β-AR signalling pathway in the model is complex and the full description may be found in (Heijman et al., 2011). The signalling component of the model ultimately translates simulated isoproterenol concentration into phosphorylation of target sites, potentiating the respective currents or fluxes. Elements affected are: on L-type calcium current (I_{CaL}), SERCA pumps, slowly activating delayed-rectifier potassium current (I_{Ks}), RyR, troponin-I (TnI), fast sodium current (I_{Na}), sodium-potassium pump (I_{NaK}), and ultra-rapid plateau potassium current (I_{Kur}), as described in the original article. The model is implemented in a way that allows turning off the signalling pathway and setting of site phosphorylation levels manually, which may be used to save computational performance.

2.2.1.4 Simplified activation of RyR via β-AR stimulation

In order to facilitate analysis of the model's behaviour, we simplified the activation of RyR by β-AR stimulation in the model, while maintaining all relevant properties of the original model behaviour. The number of parameter differences between phosphorylated and non-phosphorylated formulations has been reduced from 4 to 3 (activation constant, increased SR calcium leak, and maximum release current multiplier). In greater detail: β-ARS has been observed to affect the dynamics of calcium release from the SR through cardiac ryanodine receptor (RyR), independent of other β-ARS induced downstream effects, such as increased SR loading and L-type calcium current (Ginsburg and Bers, 2004). While the total amount of calcium released from the SR for a given SR calcium load and trigger amplitude appears to be similar in the absence or presence of β-ARS (Ginsburg and Bers, 2004), RyR under β-ARS do a) open earlier during an action potential, causing increased CaT upstroke velocity, and b) open more synchronously, increasing peak SR calcium release and also shortening the total release duration (Song et al., 2001). These macroscopic features are replicated by the phenomenological model of SR calcium release by Heijman et al. (2011). The alteration of RyR dynamics in the source model is implemented via a) explicitly increased SR calcium leak, b) reduced time constant of RyR channel activation and inactivation, c) ignoring the effect of CaMKII

phosphorylation in RyR modulated by β-AR stimulation, and d) increasing the flux through RyR to compensate for the other changes. The additional effect of CaMKII in the phosphorylated group was removed to implicitly reflect the possibility that the β-ARS-dependent changes in SR calcium release were in fact already CaMKII mediated. In this case, further active modulation by CaMKII would not be possible. However, although there is extensive crosstalk between the signalling pathways and the debate of relevance of various phosphorylation sites is still ongoing, it is generally accepted that RyR has separate phosphorylation sites for β-ARS-activated protein kinase A (PKA, Ser2809 and/or Ser2030) and CaMKII (Ser2815) (Heijman et al., 2011).

In order to simplify the model and generalize its structure to allow independent regulation by both PKA and CaMKII, we developed an alternative model for SR calcium release with three β-ARS-dependent parameters and similar CaMKII effects on both phosphorylated and non-phosphorylated RyR. We found that a near-identical phenotype to the original model can be obtained by maintaining the explicitly increased SR leak, setting the multiplier of SR release (RyR_{Amp}) to 0.65 (original value 1.9925) and reducing the multiplier of time constant of RyR opening and closing to 40% of its original value 0.5357. The largest difference beyond altered parameter values is that the effect of CaMKII phosphorylation on RyR is maintained. Demonstration of the similarity of the original and modified model may be found in Appendix B, figures B.1 (NZ cell) and B.2 (BZ cell).

2.2.2 Infarct border zone remodelling

A border zone cell was modelled using the Heijman model by applying border zone electrophysiological remodelling described in (Hund et al., 2008), changing CaMKII autophosphorylation rate (+425%), I_{CaL} (-36%), I_{Na} (-61%), transient outward potassium current (I_{To} ; full block), background calcium current ($I_{Ca,b}$; +33%) and time-independent inward-rectifier potassium current (I_{K1}; -40%). The remodelled components are placed on yellow background in Figure 2.2. The validation of these remodelling changes is given in the original study by Hund et al. (2008); we ascertained that the remodelling

changed the behaviour of our baseline model in a similar way as described there. BZ cells maintain the original model of β-AR stimulation.

2.2.3 Numerical solutions of systems of differential equations

A single simulated myocyte's behaviour is determined by:

- state vector: membrane potential, ionic concentrations, gating variables of currents, levels of phosphorylation of various sites, etc.
- ordinary differential equations describing how the variables of the state vector develop over time; a variable may depend on its previous value, as well as on values of other variables.

Given the complexity of the models, the sets of differential equations produced are solved numerically. This involves gradually increasing the time point in a simulation and computing an update that evolves the state vector towards the next time point.

The simplest update rule is the so called "Forward Euler" method. Let us assume we are in the n-th step of the simulation and the current state vector is denoted y_n. We assume for simplicity's sake that the method uses fixed time step, i.e., subsequent steps of simulation are h arbitrary time units apart. Then, the update rule to obtain the state vector in the next time step is:

$$y_{n+1} = y_n + hf'(y_n, t_n)$$

where h is the time step and f' is the set of differential equations describing the development of y over time.

The geometrical intuition of the Forward Euler method is that at a given point in the space of state vectors, a tangent is drawn in the nth step and followed for h units to obtain the state vector in the step $n + 1$. More formally, the method may be derived from the Taylor's theorem. The Taylor theorem can be phrased as follows: Let k be a positive integer and the real function f be k times differentiable at the point a. Then there exists a function h_k such that:

- $f(x) = f(a) + f'(a)(x-a) + \frac{f^{(2)}(a)}{2!}(x-a)^2 + ... + \frac{f^{(k)}(a)}{k!}(x-a)^k + h_k(x)(x-a)^k$

- $\lim_{x \to a} h_k(x) = 0$

The notation $f^{(i)}$ represents the i-th derivative of f and ! represents a factorial. The theorem thus states that a k-differentiable function may be approximated with a k-degree polynomial plus a remainder term ($h_k(x)(x-a)^k$) which however approaches zero as the point x approaches point a. If we truncate the polynomial by discarding all the elements with a derivative of order 2 and higher, we get:

$$f(x) = f(a) + f'(a)(x-a) + R_1(x)$$

where R_1 is the remainder term encompassing the remainder term from the Taylor polynomial, as well as all the higher order elements. Let us also rewrite x as $a + h$:

$$f(a+h) = f(a) + hf'(a) + R_1(x)$$

Discarding the remainder $R_1(x)$ term (it can be shown that the error thus produced it is proportional to h^2) and interpreting $f(a)$ as y_n and $f(a+h)$ as y_{n+1}, we obtain the update rule of

$$y_{n+1} = y_n + hf'(y_n, t_n)$$

The major advantage of the Forward Euler method is its simplicity and computational cheapness that may frequently enable such a small time step that the error made is sufficiently small. The accuracy may be further enhanced when fewer elements of the polynomial are discarded, keeping also higher derivatives (these are referred to as higher-order methods, such as Runge-Kutta family). However, in cardiac simulations, the differential equations may be very stiff (changing rapidly over a short time), making fixed-step methods inefficient, given that only a very short time during an action potential (opening of fast sodium channels) requires a tiny time step, while later stages of the action potential may be relatively accurately simulated with coarser sampling. Consequently, adaptive-step methods are used, adjusting the time step to the gradient steepness at the given time point. For example, the Forward Euler method may be modified to use adaptive step size in the following way: first, an estimate of the state vector after a time step h is computed directly using the Forward Euler rule. Second, an

alternative solution after h time units is obtained by updating the original state vector with a step size $h/2$ and using this new estimate for another update with step size $h/2$, providing a more accurate estimate of the state vector after h time units. Using the two approximations, it is possible to estimate the error made by coarser sampling compared to finer one. If the error is sufficiently high, the simulator adopts the finer time step (trying to refine it further until the error becomes small enough). For our single-cell simulations, we used Matlab's adaptive-step ode15s method, which furthermore adjusts the degree of Taylor polynomial in each step; the mathematics behind the method are complex and full details may be found in Shampine and Reichelt (1997). In simulations of fibres or coupled tissue, using adaptive-step methods is comparably tricky, given that different parts of the simulated tissue require different time step at different times. Consequently, many simulators instead use the basic Forward Euler method, as is the case with Myokit, the tool we used for fibre simulations in this thesis (Clerx et al., 2016).

Close the door, put out the light.
You know they won't be home tonight.
.

Led Zeppelin – No Quarter

3

β-adrenergic stimulation and alternans in post-infarction hearts

3.1 Introduction

The leading aim of this thesis is to understand how alternans in infarcted hearts is modulated by the cardiac sympathetic nervous system's activity via β-AR signalling. To directly address this aim, we used dual voltage and calcium mapping of rat Langendorff hearts with a healed chronic myocardial infarction, using the sympathetic neurotransmitter and β-agonist norepinephrine to stimulate β-adrenoreceptors in the hearts.

We observed that the infarcted hearts were generally vulnerable to alternans at physiologically relevant heart rates and that the infarct border zone tissue was selectively more prone to alternans than noninfarcted myocardium, providing a substrate for spatially heterogeneous alternans. The perfusion of the infarcted hearts with a sympathetic neurotransmitter norepinephrine led to a considerable attenuation of alternans, providing a concrete mechanism of the anti-arrhythmic effect of β-adrenergic stimulation. Norepinephrine perfusion also exerted a positive effect on upstroke velocity recovery and calcium recovery using the S1-S2 pacing protocol.

3.2 Methods

Male Sprague-Dawley rats weighting 350-500 g were used. Myocardial infarction was induced via cryoinfarction, followed by a 2 month healing period. Subsequently, MRI scanning was performed, followed by Langendorff heart preparation and dual voltage and calcium mapping. Details of each of these steps are given in sections. The investigation conformed to the Guide for the Care and Use of Laboratory Animals published by the National Institutes of Health (Publication No. 85-23, revised 1996) and the Animals Scientific Procedures Act 1986 (United Kingdom). Procedures were performed under British Home Office license requirements.

3.2.1 Cryoinfarction procedure and magnetic resonance imaging

Anaesthesia was induced in male Sprague-Dawley rats weighing 350-500 g using 4% isoflurane in medical oxygen and maintained at 2% isoflurane. The trachea was intubated to ventilate the lungs and a left thoracotomy performed. The heart was exteriorised and a 9mm aluminium cryoprobe cooled to the temperature of liquid nitrogen applied to the antero-apical myocardium for approximately 15 seconds to achieve a medium-size infarct of ca. 5% of total heart surface.. The chest was closed in layers and analgesia provided with meloxicam and buprenorphine. The cryoinjury damage was applied as adapted from the method of Ciulla et al. (2004). The Carr group has previously compared hearts with damage induced by cryoinjury with those from ischemia/reperfusion and found a similar pattern of fibrosis and macrophage infiltration, with a more reproducible infarct size (Lewis, 2017).

Cardiac structure and function was assessed in vivo using cine magnetic resonance imaging (MRI) on a 7 T MR scanner (Varian Medical Systems, Yarnton, UK) using a quadrature high pass birdcage volume transmit RF coil with a 72 mm internal diameter (RAPID Biomedical GmbH, Germany) and a phase array 4-channel RF surface receive coil (RAPID Biomedical GmbH, Germany). Anaesthesia was induced at 2.5–3% isoflurane in oxygen and nitrous oxide (4:1, total of 2 L/min) and maintained at 2 isoflurane. Animals were placed in a home-built animal handling system (Cassidy et al., 2005).

Body temperature was maintained using air heating, and a two-lead electrocardiogram (ECG) for cardiac gating was obtained using leads placed subcutaneously into the upper forelimbs. A series of sagittal and axial scout electrocardiogram (ECG)-gated fast low-angle shot (FLASH) cardiac-localised images were acquired and used to define the axes of the heart following global shimming. Between 10 and 11 contiguous cine-MR images (28-35 frames per cardiac cycle) were acquired of the heart in the short-axis orientation covering the entire heart. Imaging parameters were as given; field of view: 51.2 x 51.2 mm, matrix size: 192 x 192, slice thickness: 1.6 mm, TE/TR: 1.43/4.6 ms, Gaussian RF excitation pulse: approximately 25 degrees and 4 averages. Heart rate remained stable throughout the procedure. End-diastolic (ED) and end-systolic (ES) frames were selected as those with the largest and smallest cavity volumes and were recorded as the end diastolic and end systolic lumen respectively. Epicardial and endocardial borders were outlined using the freehand drawing function of ImageJ (National Institutes of Health, USA). Measurements from all slices were summed to calculate ED volume (EDV), ES volume (ESV), stroke volume (SV = EDV - ESV), ejection fraction (EF = SV/EDV). LV mass was calculated as myocardial area x slice thickness x myocardial specific gravity (1.05). Average mass was then computed as the average of LV mass at systole and at diastole. In each MRI slice, the length of hypocontractile epicardium and the total length of epicardial surface in a slice were recorded as $hypo_i$ and $total_i$ for the i-th slice. Then, relative infarct size was defined as $\sum_i \frac{hypo_i}{total_i}$.

3.2.2 Langendorff heart preparation and imaging

The Langendorff heart setup is described in section 2.1. The animals were anaesthetized using isoflurane and sacrificed with pentobarbitol. Subsequently, the chest was opened and the heart rapidly excised and connected to the Langendorff rig. The hearts were perfused with oxygenated Tyrode solution (flow rate 10ml/min; NaCl 120.3 mM, KCl 4 mM, MgSO4*7H20 1.3 mM, NaH20P4 1.2 mM, CaCl 1.2 mM, NaHCO3 25.2 mM, glucose 11 mM). Blebbistatin (10 μM) added to a perfusate tank was used to stabilise the heart and prevent motion artifacts during imaging; light in the room was turned off before blebbistatin addition and was kept off for the whole imaging to avoid damage of

photosensitive substances used. Pluronic (100 µl per 200 ml of Tyrode solution) added to a perfusate tank was used to aid dye loading. After the heart stopped moving, a thin plastic tube was inserted to the left ventricle via left atrial appendage to prevent perfusate pressure buildup. A pacing electrode was positioned to touch the heart's apex. Custom written software by Prof. Bub was used to capture images from both cameras and control the pacing stimulator (Model DS2A, Digitimer Ltd). The software interfaced with a micro-controller (Arduino Uno) to synchronize excitation lights, both cameras and the stimulator to minimize phototoxicity (excitation lights were switched on for 1 second at the end of a stimulation protocol to capture the results of stimulation protocols).

After hanging the hearts in a way where the field of view (FOV) contained both the infarct border zone and the adjacent normal myocardium (Figure 3.1a,b), a forceps tip easily visible on the microscope was positioned in front of the heart close to its surface and moved within the FOV, observing the myocardium under the forceps, making sure that the FOV contains both areas of tissue. A second validation of the FOV positioning was differential loading of dyes in the BZ versus NZ. The position of the normal-border zone boundary was recorded for future image analysis, when determining which pixels belong to which zone. After dye loading, the Langendorff rig was set to recycle perfused Tyrode solution.

3.2.3 Pacing protocols

The pacing electrode was placed at the apex of the heart in a direction that prevented fluid accumulation between the electrode tips. The calcium and voltage imaging were performed using two stimulation protocols programmed using GView software written by Prof. Gil Bub: "alternans mapping" and "recovery curve measurement". In a single episode of alternans mapping, the heart was consecutively paced using S1 protocol at basic cycle lengths (bcl) of 140, 130, 120, 110, 100, 95, 90, 85, 80 ms, pacing for 10 seconds at each bcl, recording the last second of the condition. For reference, the exercise heart rate in rat corresponds to a 100ms bcl (Corre et al., 1976). In recovery curve measurement, the S1-S2 protocol was used, with S1=150 ms applied for 50 beats, followed by a S2 stimulus at coupling interval 140, 130, 120, 110, 100, 90, 80, 70, 60, 50 ms.

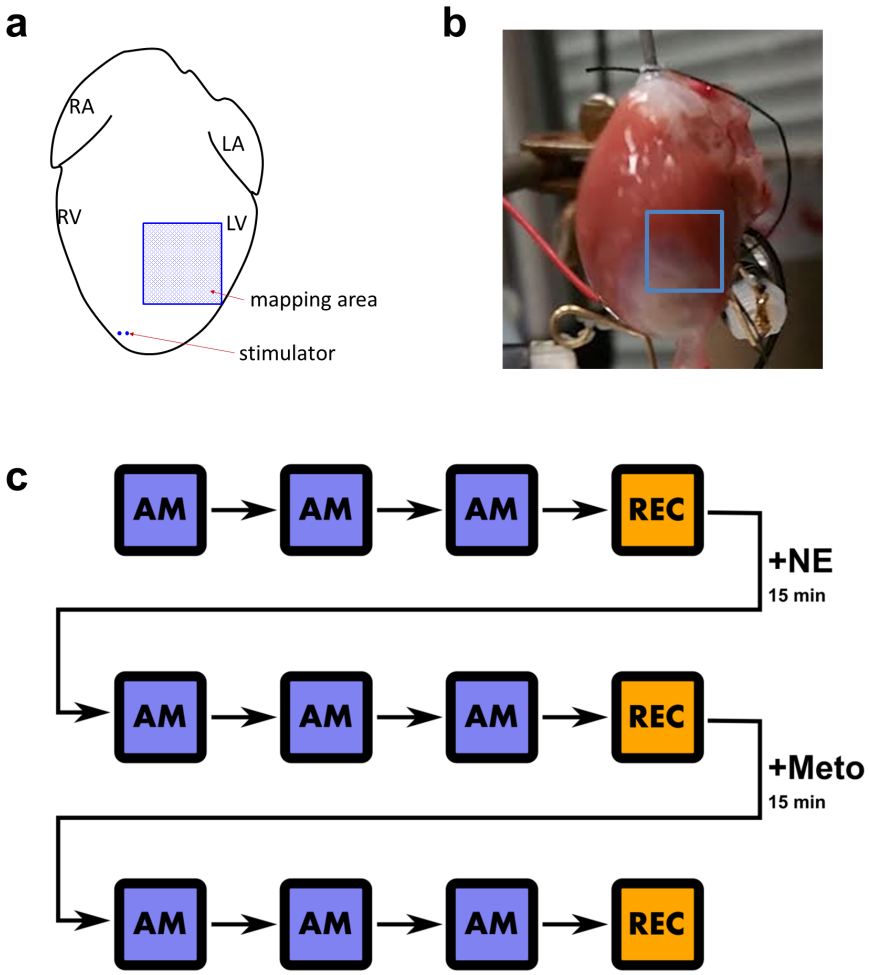


Figure 3.1: Langendorff heart overview. a) Schematic depiction of the positioning of stimulator and the mapped area. b) A concrete example of the mapped field of view in an infarcted heart. c) A schematic illustration of the pacing and stimulation protocol. AM = Alternans mapping, REC = recovery curve measurement, +NE = norepinephrine perfusion for 15 minutes, +Meto = metoprolol perfusion for 15 minutes. After each AM instance, the heart was not stimulated for 2-3 minutes for the heart rate to stabilise before the following measurement took place.

Raw spatial resolution of the 7-by-7 mm FOV was 128-by-128 pixels, reduced to 32-by-32 via on-chip binning to improve signal-to-noise ratio and allow the 1KHz sampling.

As overviewed in Figure 3.1c, three episodes of alternans mapping were recorded at control conditions[1], followed by a single recovery curve measurement. Then, nore-

[1]We decided to measure several repeats to increase the likelihood of capturing the true alternans vulnerability, rather a potential random deviation. Given available data on deterioration of Langendorff hearts over time and practical experience of Dr. Hao and Prof. Herrring, we selected three repeats to be the maximum number in which the deterioration should be low.

pinephrine was added to the Tyrode solution (1 µM, recycled to maintain the concentration), perfused for 15 minutes, and alternans mapping was repeated three times again, followed by recovery curve measurement. Afterwards, metoprolol (10µM, recycled) was perfused for 15 minutes and the same set of measurements was taken as described above. We used calcium transient duration shortening to ascertain the correct functioning of norepinephrine and metoprolol; the rationale for using transient duration over transient amplitude is that the amplitude is unaffected by dye reloading and/or photobleaching.

3.2.4 Image processing methods

In this section, variable names are given in $italic$ and the syntax $a : b : c$ represents a vector ranging between a and c with step size b.

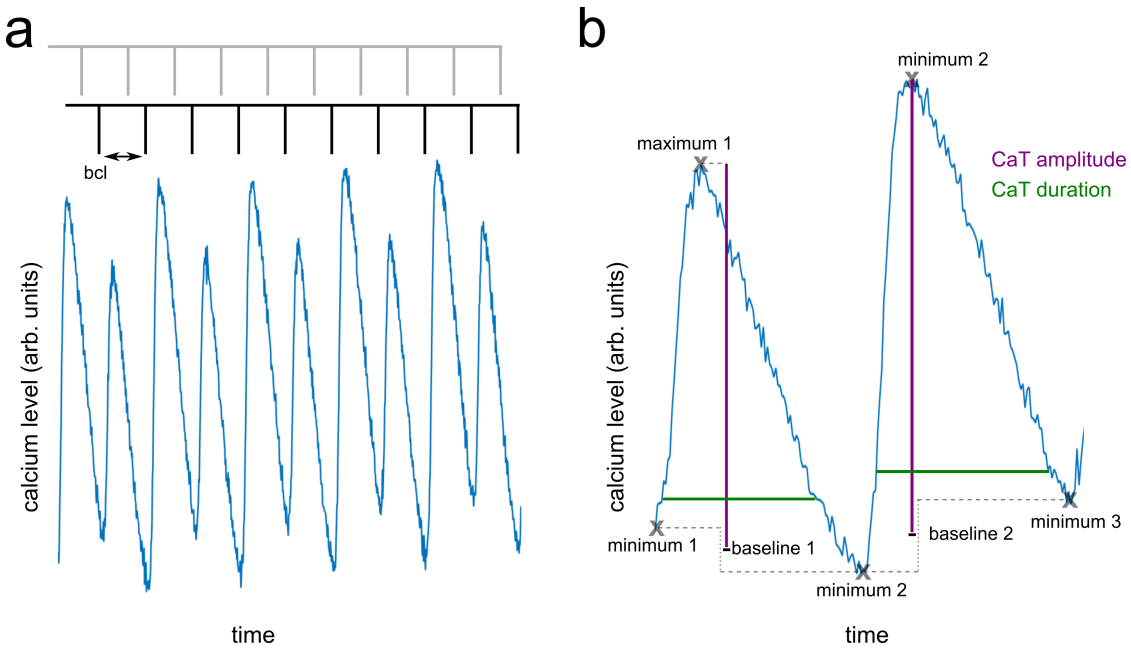


Figure 3.2: Illustration of calcium trace processing. a) Comb approach to detection of maxima or minima in a signal from fixed-rate paced hearts. Above the calcium dye fluorescence signal in blue are shown two examples of a "comb" – a vector of positions bcl ms apart (bcl is known from the experimental protocol). In black is shown a comb with the lowest possible average value under the pins, indicating that the pins correspond to locations of minima. In grey is shown a comb with comparably high underpinning value. b) An illustration of how calcium transient amplitude (purple) and duration (green) are extracted given known positions of minima around action potentials, as well as the maxima between the respective minima. The calcium transient durations in green are shown at the level of their respective thresholds as described in the main text.

3.2.4.1 Calcium alternans mapping

For each recording:

- The raw 32-by-32 pixel wide images are binned to 16-by-16 initially to improve signal stability and reliability. The $trace$ is the time series representing fluorescence intensity over time for a given pixel. For each $trace$:
  - $trace$ is linearly detrended and smoothed with Gaussian filter of width 20 (representing 20 ms).
  - The vector of local minima of trace is obtained using an approach we term "comb algorithm", illustrated in Figure 3.2a. The algorithm utilises the fact that given a fixed-rate pacing with known bcl, the minima are spaced approximately bcl frames apart. For a fixed position $start$, a "comb" of equidistant positions in the 1000ms long signal may be constructed as $start : bcl : X$, where X is the largest integer of the form $X = start + n * bcl$ & $X \leq 1000$, with n being an integer. In finding the vector of minima for a given signal, we constructs a comb for every possible location of $start$ = 1,2,...$bcl - 1$, computing the mean signal intensity at the positions given by the comb. The comb with the lowest average intensity at its respective positions provides a good estimate of locations of minima and the respective vector of candidate minima is then used as seeds for the next step. There, each seed's temporal neighbourhood with radius of 15 frames is searched to find an absolute minimum in the interval, which is stored for later use. The first and last minima are discarded as the calcium transients before the first one and after the last one may be incomplete.
  - For each pair of consecutive minima (with a calcium transient between these) and $subTrace$, the segment of trace between the minima:
    - $baseline$ is estimated as the average of the trace's values in those minima (these values may be different when alternans is present); $maximum$ is the maximum of the trace between the consecutive minima.

* Calcium transient amplitude is estimated as $CaTA = maximum - baseline$ and calcium transient duration at 90% level is estimated as the length of $subTrace$ segment above the threshold of $baseline + 0.1 \cdot (maximum - baseline)$. An illustration of both CaTA and CaT duration extraction is given in Figure 3.2b.

– Let $evenCaTAs$ and $oddCaTAs$ be the CaTAs of even and odd APs respectively. Then, normalised calcium alternans magnitude of trace and the respective pixel is defined as

$$\frac{|mean(evenCaTAs) - mean(oddCaTAs)|}{mean(evenCaTAs) + mean(oddCaTAs}.$$

– Calcium transient duration associated with $trace$ and the respective pixel is taken as an average of all durations of calcium transients in $trace$.

- The resulting maps of normalized alternans magnitude and calcium transient duration can be then spatially average to produce an average of the given recording, and/or split into normal zone values and border zone values using the manually obtained map of the infarct border zone.

During the imaging, three measurements were taken for a given condition (control/norepinephrine/norepinephrine + metoprolol) and bcl. When reporting total alternans magnitude, the three respective alternans maps were first spatially averaged to produce three numbers, which were then averaged to produce a single value per condition and base cycle length.

3.2.4.2 Repolarisation alternans mapping

The generation of action potential duration (APD) maps from voltage mapping is broadly similar to the extraction of calcium transient amplitude alternans; however, the task is more challenging given the unstable baseline of the voltage traces and the relative difficulty of extracting the duration of an AP, compared to the amplitude. Voltage signals are more susceptible to residual tissue motion as RH237 fluorescence displays a small fractional change with each action potential compared to Rhod-2 fluorescence. Below are the steps of processing for a single $trace$:

- The trace is flipped up-down so that high membrane potentials are oriented upwards. Linear detrending and smoothing is performed as in calcium mapping, however, the smoothing filter width was reduced to 10 ms to preserve the morphology of the membrane potential upstroke.

- The vector of local minima is obtained as in calcium mapping, as well as the vector of local maxima (the algorithm is identical, except that it works on $-trace$ rather than the original one).

- For each local minimum, the value of the local estimate of the signal baseline is defined as the 10-percentile value within a 15-frame radius of the given minimum (10-percentile was chosen over total minimum to reduce the effect of noise). Total $baseline$ of $trace$ is defined as the average of those values. The estimate of maximum AP fluorescence, $peak$, is defined as the average over trace's values in local maxima, which represent the highest points of each AP.

- The baseline estimates of the local minima are split into sets of even (b_e) and odd ones (b_o). As a quality control, traces with $\frac{std(b_e)}{peak-baseline} > 0.075$ or $\frac{std(b_o)}{peak-baseline} > 0.075$ are discarded (the respective mapping values set to NaN), as we observed traces with such an unstable baseline to provide poor APD estimates. The split into even and odd baseline estimates is performed to represent the fact that at the fastest pacing rates, even the membrane potential baseline may oscillate under alternans and the increased standard deviation could thus be both due to instability or alternans, which is undesirable.

- For each segment of signal between two consecutive minima, representing an action potential, APD at any $level$ scaled between 0 and 1 may be estimated as the longest segment above $threshold = baseline + (1 - level) \cdot (peak - baseline)$.

The APD maps are then generated in a similar fashion as maps in the calcium mapping. The only difference is that the reference border zone/normal zone maps are flipped left to right to reflect that the voltage mapping FOV is a mirror image of the FOV of calcium mapping in our imaging setup.

3.2.4.3 Membrane potential upstroke recovery

The input to the following image analysis is two traces, one from a region in the normal zone, one from a region in the border zone. The regions are circles with diameter 7 pixels (taken from unbinned images of 32-by-32), selected to lie completely in their respective zones. Each trace contains three S1 action potentials, 150ms apart, followed by a single action potential at a given S2 interval. The trace is flipped upside-down, smoothed (filter size 10) and linearly detrended, as in APD alternans mapping, and discrete derivative $diffTrace$ (differences between consecutive elements) of the trace is computed. Then, $diffTrace$ is thresholded with threshold of 30%-quantile of $diffTrace$ and the first four segments above the threshold, representing three S1 and one S2 action potential, are recorded. Within each of those four segments, the maximum is found, providing values $uvS1_1$, $uvS1_2$, $uvS1_3$, and $uvS2_1$, representing peak upstroke velocities of the respective action potentials. Then, normalized upstroke velocity of the trace is defined as:

$$\frac{uvS2_1}{\frac{uvS1_1+uvS1_2+uvS1_3}{3}}.$$

Using this approach, the resulting value does not depend on the absolute fluorescence levels nor the signal amplitude. All the values and locations of maxima of upstroke velocity were manually verified and the level of quantile of thresholding used to obtain times of S1 and S2 action potentials was adjusted in cases where the default value failed to locate the correct locations, e.g., due to noise.

3.2.4.4 Calcium upstroke recovery

The processing of calcium traces obtained in S1-S2 protocols from normal and border zone works largely similarly as in membrane potential upstroke recovery; chief differences stem from the fact that instead of the upstroke velocity, we monitor the upstroke amplitude. The first difference is that the traces are not flipped upside-down. The second difference is that the whole upstroke duration is obtained using thresholding ($diffTrace > 0$ in calcium signal used as a binary indicator vector; holes of length 1 were filled to remove artifacts). For each upstroke (a connected component in the binary

vector $diffTrace > 0$), let us define $upstroke_{first}$ and $upstroke_{last}$ as the indices of frames at which the upstroke starts and ends respectively. Then, upstroke amplitude of the i-th action potential in a given trace $trace$ is $uaS_i = trace[upstroke_{last}] - trace[upstroke_{first}]$. Then, normalized calcium upstroke amplitude of trace is

$$\frac{uaS2_1}{\frac{uaS1_1+uaS1_2+uaS1_3}{3}}.$$

3.3 Results

3.3.1 Development of healed myocardial infarction

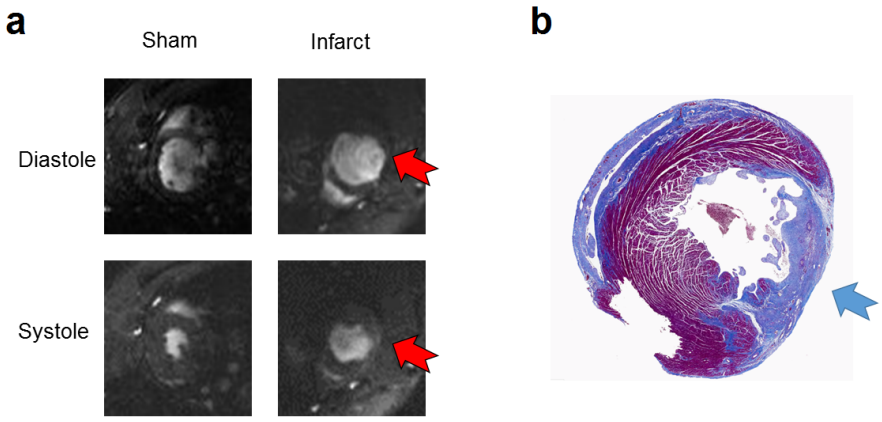


Figure 3.3: Examples of infarct imaging. a) examples of the MRI data (systole and diastole in a sham and an infarcted heart, with red arrows indicating the position of hypocontractile infarct). b) an example of Massons trichrome staining of apical tissue section showing fibrotic scar formation (blue arrow), adopted from a different study with identical infarction protocol; provided by A/Prof. Carolyn Carr.

Myocardial infarction in the left ventricle developed in hearts that underwent cryoinfarction. Examples of MRI imaging and Massons trichrome staining showing the fibrotic scarring are given in Figure 3.3a,b. The infarcted hearts manifested light, but significant systolic dysfunction as seen in the left ventricular ejection fraction (LVEF) and end systolic lumen that indicates diminished contractility (Table 3.1). There was a trend towards increased average mass of the infarcted hearts compared to shams, hinting at possible cardiac hypertrophy. Given the late stage of infarct healing (2 months after infarction), the developed scars were clearly visible when the hearts were

excised, facilitating subsequent detection of the border zone when selecting the region of interest to be imaged; a sample photograph of an infarction is given in Figure 3.1b.

Feature	Infarcted (n=8)	Sham (n=3)	p-value
Relative infarct size (%)	6.5 (3.5-9.5)	0 (0-0)	**0.012**
LVEF	61 (57.5-66)	74 (68.75-78.5)	**0.036**
Heart rate	210 (200-230)	240 (210-255)	0.47
Average mass (mg)	993.5 (959-1047)	897 (825-935)	0.085
End systolic lumen (µl)	266 (216.5-316.5)	163 (148-171.25)	**0.012**
End diastolic lumen (µl)	668 (589-828)	635 (558-690.5)	0.63
Body weight (g)	493 (487.5-513)	524 (455-524)	**0.012**

Table 3.1: Baseline cardiac properties in infarcted and sham hearts. Shown is the median (interquartile range), with the statistical difference between groups assessed using Wilcoxon rank-sum test. All features but heart rate were determined using MRI as described in the methods, with heart rate measured after the heart has been hung on the Langendorff rig and has stabilised. LVEF = left ventricular ejection fraction. Body weight was measured at the time of MRI, which is why the weights are higher than initial range of 300-500 g.

3.3.2 Rapid pacing induces calcium alternans in hearts

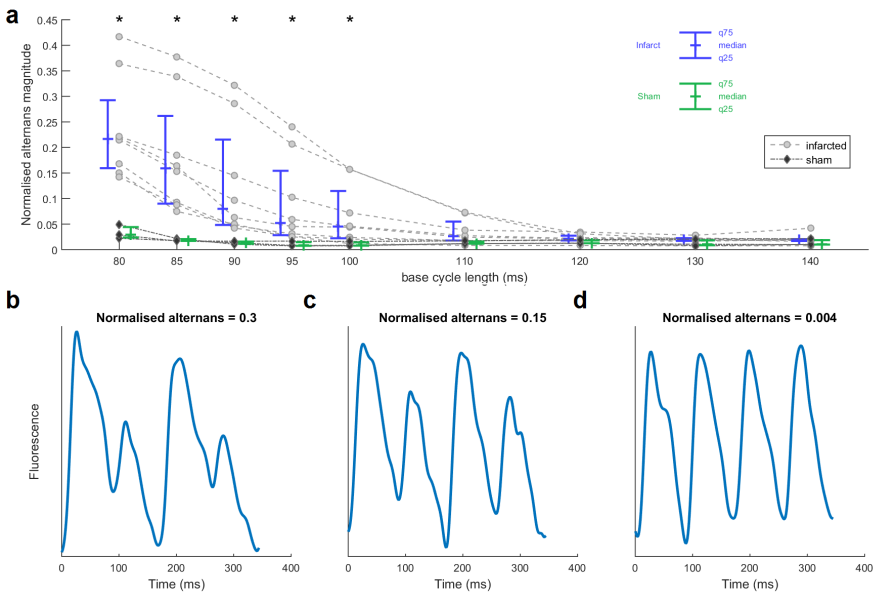


Figure 3.4: Rapid pacing induces calcium alternans in sham and infarcted hearts. a) Mean normalised calcium alternans magnitude of recordings in control condition against base cycle length for infarcted and sham hearts. Asterisks represent statistical significance of the difference between sham and infarcted hearts at the level of 0.05 (*). b,c,d): Sample smoothed calcium traces illustrating the values of normalised alternans magnitude.

In all tested hearts, increasing the pacing frequency resulted in increased occurrences of calcium alternans (Figure 3.4). Infarcted hearts generally manifested visible alternans at base cycle length (bcl) up to 100 ms, significantly more so than sham hearts ($p < 0.05$; Wilcoxon signed rank test), which manifested visible alternans only at the very highest pacing frequencies.

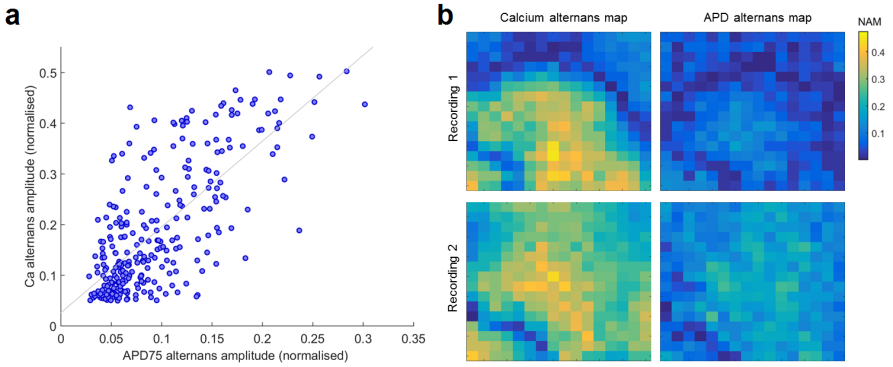


Figure 3.5: Calcium and APD75 alternans comparison. a) The correlation of normalised calcium and APD75 alternans amplitude for combinations of condition (control/norepinephrine/norepinephrine + metoprolol) and base cycle length where Ca alternans amplitude > 0.05. b) Sample comparison of calcium and APD75 alternans maps from two recordings. The colour heat codes for normalised alternans amplitude (NAM), showing a good agreement of spatial distribution of alternans including the nodal lines.

Normalised calcium alternans amplitude was clearly correlated with normalised APD75 alternans amplitude in the presented data (Figure 3.5a, $p < 10\text{-}47$ using slope test for correlation significance), typically including the spatial distribution of alternans within a single recording (Figure 3.5b). Given the good correlation of the two types of alternans and the lower stability of APD alternans estimation, we use only the calcium alternans mapping in the rest of the article. The lower accuracy of APD alternans estimation is chiefly due to a frequently unstable baseline in the voltage traces and lower fractional change of the voltage signal compared to the calcium signal during an action potential. This results in the increased difficulty of estimating duration of an action potential compared to amplitude of calcium transient, which is a relatively simple task.

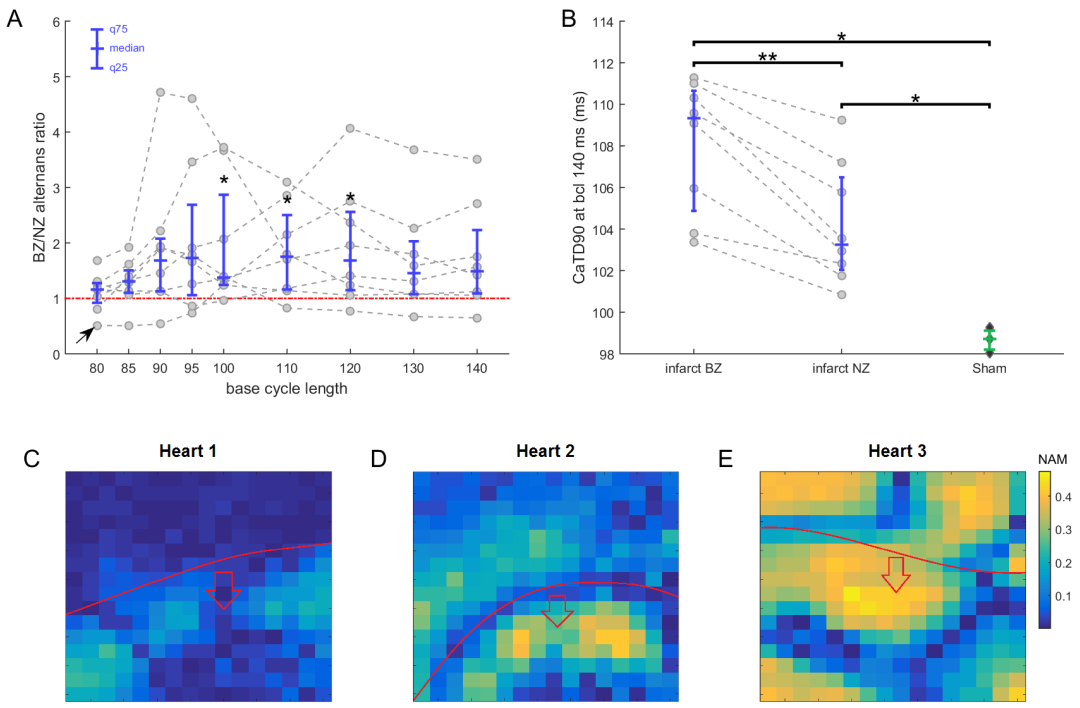


Figure 3.6: Border zone vulnerability to alternans. a) The ratio of alternans magnitude in border zone and normal zone of each recording, plotted against bcl. Points above the red line manifest more alternans in border zone than in normal zone. Asterisks represent statistical significance of the difference in alternans in normal zone versus border zone at the level of or 0.05 (*). The black arrow in bottom left corner indicates a special trace discussed further in the text. B: Duration of calcium transient at 90% calcium recovery at bcl 140 in infarcted hearts (NZ=normal zone, BZ = border zone) and in sham hearts. Asterisks represent statistical significance of difference between sham and infarcted hearts at the level of 0.01 (**) or 0.05(*); the Wilcoxon signed rank test has been used for comparing BZ and NZ, given the paired nature of data, while for the other two comparisons, Mann-Whitney U test was used. c) An example of spatially heterogeneous alternans restricted to BZ. The colour in each pixel denotes normalised alternans magnitude (NAM). d) An example of nodal line passing along the edge of BZ. e) An example of nodal line pattern with no obvious relationship to BZ edge. In C,D,E, the red line marks the edge of the BZ, with the red arrow showing which side of the red line contains BZ. Subfigures C,D,E come from different hearts.

3.3.3 The infarct border zone is more prone to alternans than noninfarcted myocardium

The infarct border zone was more prone to alternans, as demonstrated by the ratio of alternans magnitude in border zone versus normal zone (Figure 3.6a, example in 3.6c), with the difference statistically significant for bcls of 100–120 ($p < 0.05$; Wilcoxon signed rank test) and near-significant at 95, 130, and 140 ms (p=0.0781, 0.0547, 0.0781

respectively; Wilcoxon signed rank test), possibly due to insufficient statistical power. Medium pacing intervals (bcl 100–120) led to the largest increase of alternans in border zone compared to normal zone. During slower pacing (bcl 130–140), the increase was smaller (Figure 3.6a) which can be explained by low levels of alternans throughout the tissue (Figure 3.5a). During rapid pacing (bcl 80–90), even the normal zone manifested alternans, making the BZ/NZ ratio approach 1. An exaggerated case of this is the single trace with BZ/NZ ratio of approximately 0.5 for high pacing frequencies (Figure 3.6a, arrow at bottom left). While at slower pacing, the border zone tissue manifested clearly higher alternans than normal zone issue 3.7b, this did not hold for fast pacing 3.7a. There, the presence of nodal lines in BZ made the total border zone alternans low compared to the normal zone. Given the presence of nodal lines in the border zone and homogeneous alternans in the normal zone, however, this phenomenon does not necessarily imply lower arrhythmogenicity of the border zone.

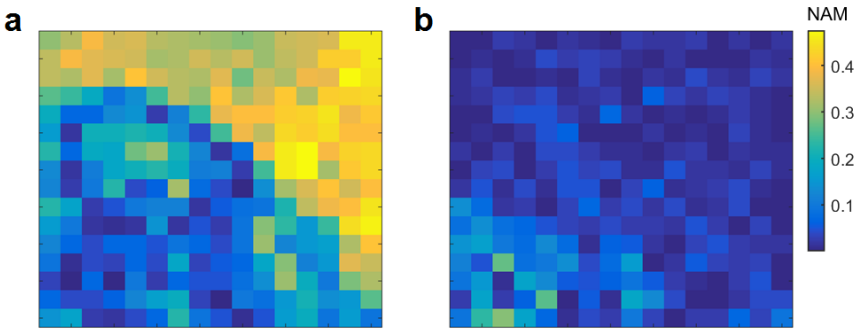


Figure 3.7: Singular case of low alternans in the border zone at rapid pacing. Shown are alternans maps of a single heart with the infarct border zone under the main diagonal of the map, at fast pacing (a; bcl = 85 ms) and at slower pacing (b; bcl = 120 ms). NAM = normalised alternans magnitude.

The mechanism of calcium-driven alternans is usually considered to stem from insufficient calcium reuptake (Pruvot et al., 2004), which would manifest as a prolonged calcium transient. We therefore measured the average calcium transient duration at 90% calcium recovery (CaTD90, an analogue of APD90; at pacing of 140 bcl during which no alternans occurred) in all hearts. CaTD90 was significantly prolonged in border zone compared to normal zone tissue (p=0.0078, paired Wilcoxon signed rank test; Figure 3.5b), suggesting a dysfunction of calcium cycling in the border zone, thus making it

more prone to alternans. Sham hearts manifested significantly shorter CaTD90 than both the normal and border zones of infarcted hearts (p=0.012, unpaired Mann-Whitney U test; Figure 3.5b), suggesting that more efficient calcium cycling contributes to the resistance of sham hearts to alternans.

In some cases, predominantly at rapid pacing frequencies, discordant alternans developed. In some cases, there was an obvious spatial correspondence between the edge of the border zone and nodal lines (Figure 3.5d), consistent with the hypothesis on structure-based location of nodal lines (Garfinkel, 2007). However, in other cases, no such relationship was apparent (Figure 3.5e), suggesting a different cause of formation of nodal lines, such as via calcium diffusion and fluctuation (Sato et al., 2013), or dynamic origin of nodal lines perpendicular to the direction of propagation (Garfinkel, 2007). Given that in several recordings we observed a rather complex structure of nodal lines without any obvious perpendicularity to the direction of propagation (Figure 3.5e), the calcium diffusion and fluctuation hypothesis seems to be a more likely explanation.

3.3.4 Norepinephrine perfusion attenuates alternans

In order to observe the effect of β-adrenergic stimulation on alternans, we perfused the hearts with norepinephrine, the main sympathetic neurotransmitter. The specificity of its effect was confirmed by subsequent application of beta-blocker metoprolol. Norepinephrine potently attenuated alternans in the hearts at rapid pacing intervals (80–90 bcl, p = 0.0078, median 60% reduction in alternans; confidence interval of 52-65%) and this effect was blocked using metoprolol (Figure 3.8a,b); full frequency-dependent plots are given in Appendix A.

We observed shortening of the CaTD90 at pacing of 140 bcl in all infarcted hearts after NE perfusion (p=0.0156 for control versus NE; Figure 3.8c), which is consistent with the known effects of β-adrenergic stimulation on calcium transient duration (Chakir et al., 2009). This shortening was reverted with metoprolol (p=0.58 for CaTD90 control versus NE+Meto; Figure 3.8c). The reduction of calcium transient duration with norepinephrine was due to a reduction of time to peak of calcium transient (median

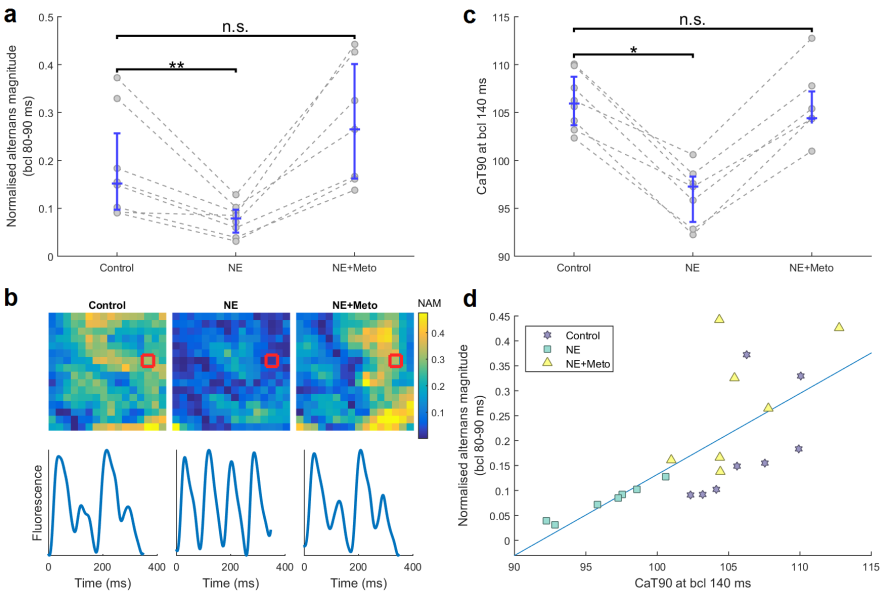


Figure 3.8: Effects of norepinephrine and subsequent beta-blockade. a) The effect of norepinephrine perfusion and subsequent beta-blockade on mean normalised alternans magnitude at high pacing frequencies (each circle is an average of normalised alternans magnitudes of the given heart over bcls of 80, 85, and 90). Asterisks represent statistical significance at the level of 0.01. b) Sample alternans maps from a single recording under the three conditions (control, norepinephrine, and norepinephrine+metoprolol), with sample smoothed traces of the red-marked-pixels shown below. NAM = normalised alternans magnitude. c) The effect of norepinephrine and subsequent beta-blockade on CaTD90 (calcium transient duration, at 90% calcium recovery level) at pacing of 140 bcl. d) Correlation between CaTD90 from a) and normalised alternans magnitude at fast pacing frequencies from c), matched by heart and condition.

reduction 0.75 ms, IQR 0.02-2.74) as well as the time from peak to 90% recovery (median reduction 8.58 ms, IQR 6.15-9.64).

Interestingly, CaTD90 at non-alternans pacing of 140ms bcl strongly correlated with normalised alternans formation at 80–90 ms bcl (Figure 3.8d, R^2 = 0.52, p = 1.66e-4, using the Regression slope test), providing further evidence that impaired calcium handling might be the primary driver of alternans in our experiments.

3.3.5 S1-S2 protocol and β-adrenergic stimulation

Heterogeneity of conduction is thought to be another important cause of arrhythmias post MI (Luke and Saffitz, 1991). We therefore measured the heterogeneity between the border zone and normal zone as the normalised peak upstroke velocity (NPUV) recovery during the S1-S2 pacing protocol (see Methods; sample traces in Figure 3.9).

In the S1-S2 protocol, a train of stimuli with bcl S1 is delivered, followed by a single stimulus S2 ms after the last S1 stimulus. Then, recovery is the function of a given variable against various values of S2.

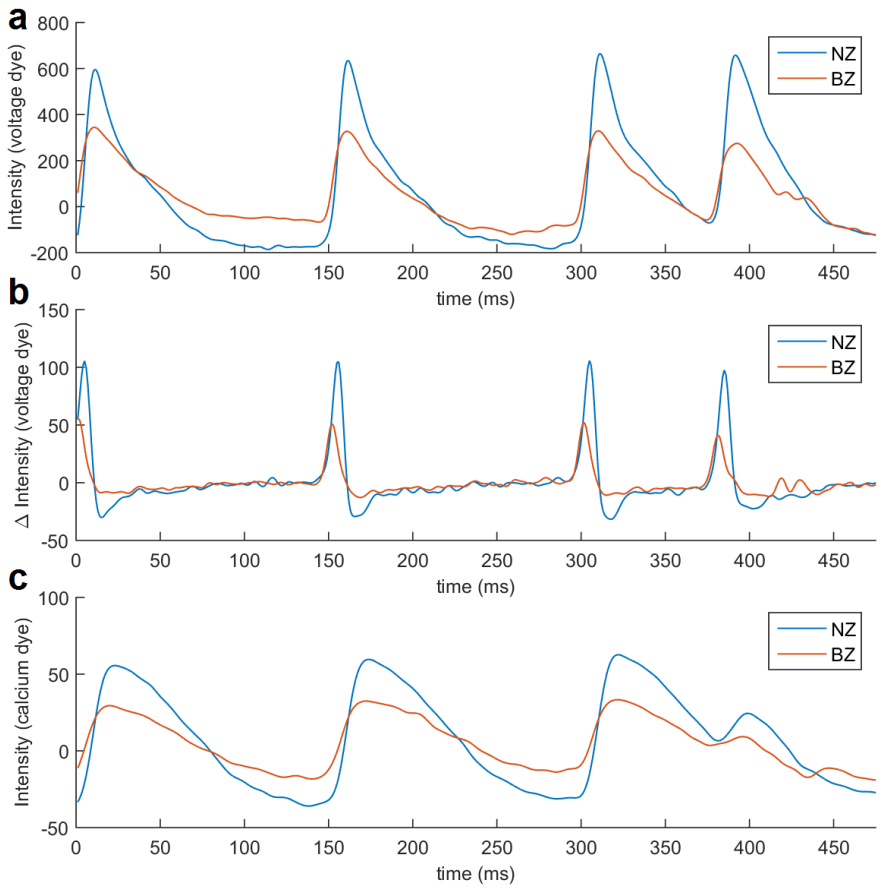


Figure 3.9: Comparison of AP upstroke and calcium transient amplitude recovery between NZ and BZ regions. a) Intensity trace of a NZ and BZ region using a voltage dye for S1=150 ms and S2 = 80 ms (the traces were flipped upside down, smoothed, and zero-centered). b) ΔIntensity of voltage dye; the difference between consecutive values of panel a). The peaks represent maximum upstroke velocity. In NZ, the peaks are 105.5, 104.6, 105.9, 97.54, yielding the normalised peak upstroke velocity (NPUV) of 0.926. In BZ, the peaks are 54.95, 51.12, 52.11, and 40.62, with NPUV = 0.77, therefore, BZ manifests poorer recovery of upstroke. c) Intensity trace of a NZ and BZ region using a calcium dye. In NZ, the upstroke amplitudes are 91.8, 95.6, 93.35, 17.92, giving calcium upstroke recovery of 0.1912. In BZ, the upstroke amplitudes are 50.15, 50.74, 47.14, and 5.7, yielding calcium upstroke recovery 0.116, which is again lower than in NZ, illustrating the calcium handling deficiency of BZ.

Under control conditions, using voltage mapping we observed a clear NZ-BZ difference in NPUV, with BZ manifesting a decreased recovery, indicating a potential for spatial heterogeneity of conduction velocity (Figure 3.10a). The NZ-BZ heterogeneity has been considerably attenuated with norepinephrine, but the median BZ upstroke

velocity remained below the median NZ upstroke velocity (Figure 3.10b). We note that given that the traces for NZ and BZ are a spatial average of multiple cells (and would have been even if a single pixel has been selected), the upstroke velocity is not a pure representation of single-cell upstroke velocity, but also may be diminished by slow conduction velocity (CV). Thus, given that the presented voltage recovery curves are most likely a mixture of CV recovery and cell-level upstroke velocity reduction, which in itself implies reduced CV, a reduction in the measured upstroke velocity implies reduction of CV, providing evidence of potential conduction heterogeneity between NZ and BZ.

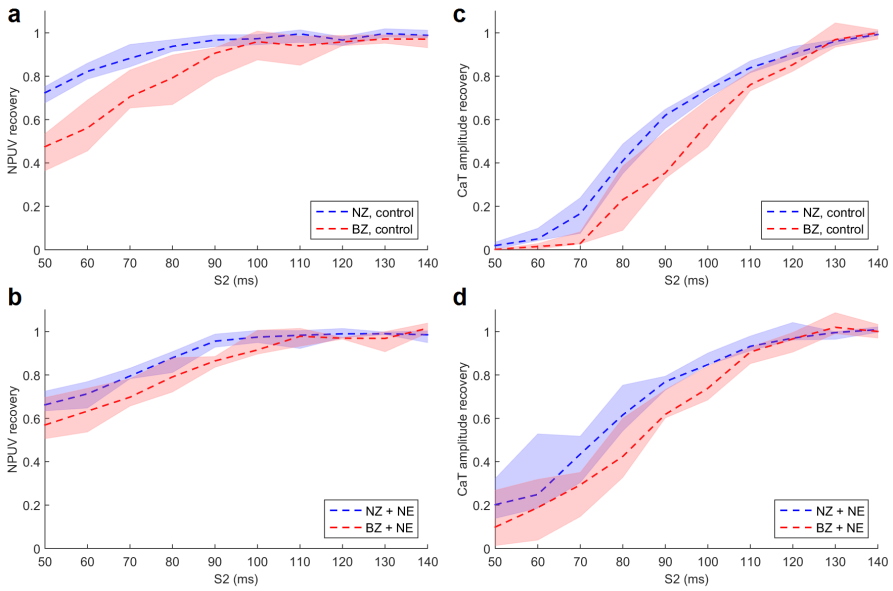


Figure 3.10: Voltage and calcium recovery in the S1-S2 protocol. First column: NPUV (normalised peak upstroke velocity) in control condition (a) and after norepinephrine perfusion (b). Second column: CaT amplitude of S2 calcium transient normalised to average S1 CaT amplitude in control condition (c) and after norepinephrine perfusion (d). In all panels, dashed lines indicate median, with the shaded area representing the interval between 25 and 75 percentiles.

Using the calcium imaging data, we measured the recovery of normalised calcium transient amplitude (S2 CaT amplitude over the average of preceding S1 CaT amplitudes), a surrogate of recovery of the calcium subsystem. In both control and norepinephrine conditions, the BZ manifested a slightly diminished calcium recovery, with norepinephrine improving the recovery in both NZ and BZ, but not apparently changing the balance between NZ and BZ (Figure 3.10c,d).

3.3.6 Other arrhythmia markers

Apart from mapping alternans and recovery curves, occasional episodes of arrhythmia and/or its precursors were observed several times as summarised in Table 3.2. An example of nonsustained tachycardia or fibrillation is shown in Figure 3.11).

Type	control	NE	NE+Meto
S1-S2 nonsustained tachycardia	3	1	3
S1-S2 fibrillation	3	0	2
Rapid pacing fibrillation	0	0	2
Sum	6	1	7

Table 3.2: Arrhythmia and its precursors in S1-S2 protocol and during rapid pacing for three tested conditions. Shown are numbers of hearts manifesting at least one episode of the tachycardia or fibrillation during various protocols in the infarcted hearts (n=8). All cases of fibrillation were reverted to sinus rhythm with further electrical stimulation. NE = norepinephrine, NE+Meto = norepinephrine + metoprolol.

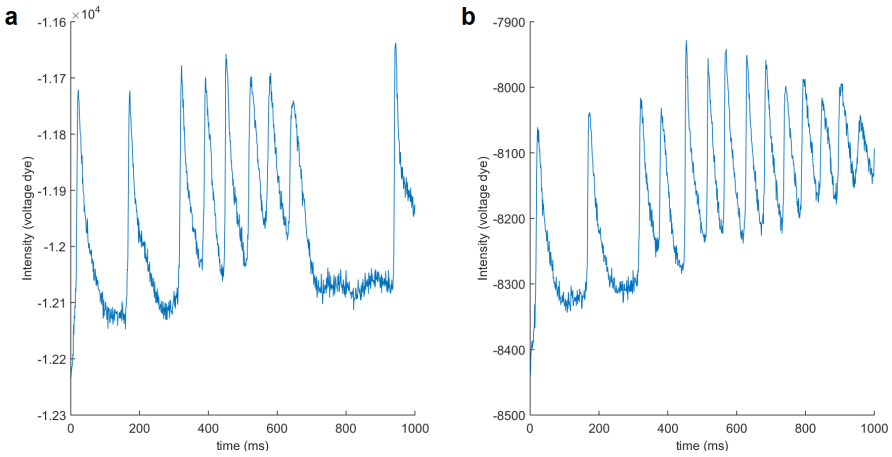


Figure 3.11: An example of nonsustained tachycardia (a) and degeneration to ventricular fibrillation (b). Intensity traces were flipped upside down to better correspond with membrane potential.

The event numbers are too low to reach statistical significance between conditions. After pooling different types of arrhythmia (i.e., using "Sum") it is possible to compare event frequencies. In control conditions, there were 6 events in total out of 24 (8 hearts, 3 types of arrhythmia $\Rightarrow$ 24 possible events), with 1 in 24 after norepinephrine (NE) perfusion and 7 in 24 after metoprolol addition (NE+Meto). Using Fisher's exact test, p-value for control versus NE is 0.09 and 1 for control versus NE+Meto. When numbers

of events and possible events are added for control and NE+ME (as these represent the condition without sympathetic stimulation), comparing 6/24 with 13/48, the p-value of difference is 0.026, which is statistically significant for common significance level of 0.05. However, given the relative artificiality of such pooling, the importance of such significance is not to be interpreted with caution.

3.4 Discussion

The main findings presented in this chapter are:

1. Infarct border zone tissue is more prone to alternans than normal zone tissue, predisposing hearts to spatially heterogeneous alternans.

2. β-adrenergic stimulation attenuates alternans in infarcted hearts.

3. β-adrenergic stimulation has the potential to reduce inhomogeneities between normal and border zone tissue and to reduce arrhythmia incidence at fixed-rate pacing.

3.4.1 Infarct border zone is vulnerable to alternans formation

Consistent with previous work in humans (Koller et al., 2005), we demonstrated that hearts with a healed MI are prone to the formation of alternans (both in calcium transient amplitude and APD). In particular, the border zone tissue manifested stronger alternans than the normal zone tissue, predisposing the hearts to spatially heterogeneous alternans. Spatially heterogeneous alternans promotes conduction and repolarisation inhomogeneities in a similar fashion as spatially discordant alternans, which is clearly linked to an increased risk of VF (Wilson and Rosenbaum, 2007; Gaeta and Christini, 2012). In the infarcted hearts, we observed visible alternans in the BZ at frequencies within the physiological range of the rat heart rate during exercise (Corre et al., 1976; Bolter and Atkinson, 1988). This observation supports the importance of alternans in post-MI arrhythmogenesis, as alternans is reliably present at a given pacing frequency, unlike other drivers of VF, such as spontaneous depolarisations, which are comparably sparse events. Interestingly, vulnerability to alternans at faster pacing

(80-90ms bcl) could be predicted from calcium transient duration at slower pacing (140ms bcl), suggesting calcium oscillations as the alternans driver.

3.4.2 β-adrenergic stimulation attenuates formation of alternans in post-infarction hearts

In order to investigate the role of β-adrenergic stimulation on alternans after myocardial infarction, we applied the sympathetic neurotransmitter norepinephrine to the hearts, which considerably attenuated alternans magnitude (approximately 55% at fast pacing rates). This effect was reverted with the beta-blocker metoprolol confirming β-adrenergic stimulation as the causative factor.

3.4.3 β-adrenergic stimulation normalises upstroke velocity and reduces arrhythmia incidence during S1-S2 protocol

The S1-S2 protocol revealed a marked reduction of the recovery of membrane potential upstroke in the BZ, and differences between the BZ and NZ were partly attenuated with norepinephrine, possibly by reducing the electrophysiological heterogeneity of the cardiac substrate. The total number of VT/VF events during alternans-inducing rapid pacing and S1-S2 protocol was lower (however, not significantly unless control and beta-blocker conditions were pooled, possibly due to scarcity of the events) with norepinephrine than at control condition or using metoprolol, suggesting that the benefit of sympathetic stimulation might not be limited to alternans attenuation.

The observation on reduced arrhythmia incidence does not, on its own, mean a generally anti-arrhythmic effect of β-adrenergic stimulation in the context of premature stimuli. While our results suggest that provided an extrasystolic stimulus, the β-stimulated heart may be more resistant to it than an unstimulated one, it has been reported that β-adrenergic stimulation increases the likelihood of such stimuli in the first place (Xie et al., 2013), making the net effect unclear.

3.4.4 Sympathetic nervous system and arrhythmia after myocardial infarction

As discussed in thesis introduction, there is an interesting controversy in the role of reinnervation (also called "nerve sprouting"), following initial denervation after myocardial infarction. Our results support the results of the recent human clinical studies (Malhotra et al., 2015), suggesting that the long-standing opinion of the proarrhythmicity of such innervation is not necessarily correct. Also, the study in isolated mouse hearts performed by Gardner et al. (2015) supports these studies synergistically with our work, suggesting an anti-arrhythmic role of border zone reinnervation. Unlike our study, the work by Gardner et al. focussed at chronic, pre-excision effect of reinnervation, given that the sympathetic nerves were not activated after the heart isolation. Some the beneficial results of reinnervation of the study by Gardner et al. could be alternatively explained by the potential pro-angiogenic action of tyrosine phosphatase σ inhibition (Ostman et al., 2006) aiding the revascularisation of the border zone and improving metabolism. On the other hand, a second stream of research, based mainly on animal studies, summarised by Shen and Zipes (2014) claims that post-infarction nerve sprouting is proarrhythmic. These observations may be somewhat reconciled if excessive hyperinnervation provides similar amount of repolarisation heterogeneity as denervation, also acting pro-arrhythmically. Intriguingly, the human clinical studies that demonstrate pro-arrhythmicity as a consequence of denervation do not seem to report cases of hyperinnervation, while conversely, the studies showing pro-arrhythmicity of nerve sprouting report hyperinnervation and no cases of border zone denervation.

Our results are consistent with studies that report pro-arrhythmic effects of denervation, providing a novel mechanistic insight into post-infarction arrhythmogenesis. In the case of non-reinnervated border zone, two pro-arrhythmic factors seem to combine. The first aspect is the established observation that neural heterogeneity itself promotes electrophysiological conduction heterogeneity, which is proarrhythmic (Yoshioka et al., 2000), exacerbating the heterogeneity between normal zone and border zone. The second aspect, highlighted by our study, is the vulnerability of the border zone to

electrical alternans, allowing the genesis of spatially heterogeneous alternans, which is proarrhythmic in a similar way to discordant alternans. Indeed, the combination of APD shortening in the innervated normal zone with APD prolongation in alternating APs might generate vast repolarisation gradients. Reinnervation of the infarct border zone and the subsequent β-adrenergic stimulation of the innervated tissue then has potential to both eliminate the first pro-arrhythmic aspect of border zone denervation, but also to attenuate alternans, preventing arrhythmia via two distinct mechanisms.

3.5 Limitations

Some limitation of the Langendorff heart include the lack of osmotic pressure, which may cause edema in long experiments, or continuous deterioration of the prep over time (Bub et al., 2010). That said, it is established that a Langendorff heart may be studied for several hours (Sutherland and Hearse, 2000), with our experiments typically lasting under 2 hours. We also believe that our protocol of control, norepinephrine, and norepinephrine + metoprolol shows that the anti-arrhythmic effects of norepinephrine are not due to deterioration of the heart, as in that case, this would not be reverted by beta-blockade. Another potential limitation of the Langendorff heart perfused with drugs which increase the heart rate, such as norepinephrine, is that with a constant perfusion rate, the heart may lack sufficient energy to compensate for the increased heart rate (unlike in the physiological case where the increased heart rate would also translate into increased coronary blood flow). Given that our measurements were taken at fixed-rate pacing, we believe this issue to be relatively minor.

Using rat as a model system is also a limitation when considering scaling to humans. While the rat Langendorff heart is possibly the most common and well-characterised variant (Sutherland and Hearse, 2000), the rat action potential shape differs from the human one, lacking the plateau phase, although no rodent model accurately replicates human cardiac electrophysiology. The difference is largely due to a different balance of repolarisation currents (Varró et al., 1993). Thus, we believe this limitation is more important for studying repolarisation rather than calcium handling, as is the case of this work.

As opposed to studying the effect of naturally present sympathetic nerves, we used a perfusion of norepinephrine to achieve consistent β-adrenergic stimulation (infarct border zone was shown to be well perfused (Scherrer-Crosbie et al., 2000)). This is motivated by the fact that the literature is not in agreement on whether hyperinnervation or hypoinnervation is more common and clinically relevant condition after myocardial infarction, and the same holds for the function of beta-receptors. It would be therefore difficult to interpret the relevance of a rat model with its potentially species-dependent post-infarction neural and beta-receptor remodelling. As opposed to this, using perfusion of norepinephrine provides information on the general effect of β-adrenergic stimulation, which is independent on altered neural structure. Perfusion may be still affected by different expression of beta-receptors in the normal and border zone, but we believe that the vast majority of our results does not depend on the difference between properties of normal and border zone; the only exception is Section 3.3.5.

3.6 Conclusions

We have demonstrated why infarct border zone innervation may reduce the risk of arrhythmia, as observed in human clinical data, explaining why patients with a denervated border zone are at high risk of further arrhythmia (Malhotra et al., 2015). The attenuation of calcium and repolarisation alternans with β-AR stimulation is expected to considerably reduce the spatial gradients of repolarisation adjacent to the myocardial infarction, reducing the risk of wave break and reentry. The importance of this phenomenon is highlighted by the general vulnerability of infarcted hearts to alternans formation, particularly in the infarct border zone.

Ooh ooh ooh someone's really smart
Ooh ooh ooh complete control, that's a laugh

The Clash – Complete Control

4

Computer simulations of infarct border zone remodelling and β-adrenergic stimulation

4.1 Introduction

In this chapter we use computational modelling of ventricular cardiomyocytes to understand formation and modulation of calcium-driven alternans. Following on the previous chapter, we aim to understand alternans-vulnerability of the infarct border zone and how alternans may be attenuated by β-adrenergic stimulation. Detailed experimental characterization of the role of hyperinnervation in border zone arrhythmias is challenging due to the numerous distinct localised effects of post-MI remodelling and the diversity of species-specific (sub)cellular mechanisms controlling calcium handling, repolarisation alternans, and other pro-arrhythmic factors, all of which are modulated by β-AR stimulation. Computational models have been developed that can reproduce experimental electrophysiological characteristics, including repolarisation and CaT alternans, observed experimentally (Fox et al., 2002; Livshitz and Rudy, 2007; Zhou et al., 2016). Furthermore, these models allow perfect control over all parameters, ease of isolation of factors contributing to the behaviour of the system, complete observability and have been employed to characterize subcellular mechanisms of

alternans in more detail (Fox et al., 2002; Livshitz and Rudy, 2007; Zhou et al., 2016; Qu et al., 2016). However, very few of these studies addressed border zone cardiomyocyte electrophysiology and none incorporated regulation by β-AR stimulation previously.

We characterised the interplay of BZ electrophysiological remodelling and β-AR stimulation on the likelihood of alternans by fusing an existing state-of-the-art computational model of β-AR stimulation in the canine ventricular cardiomyocyte (Heijman et al., 2011) with a model of post-infarction electrophysiological remodelling in the BZ (Hund et al., 2008). Our results indicate that β-AR stimulation can indeed suppress alternans. Moreover, we identified a critical role for the regulation of SR calcium release, both through activation of RyR channels and indirectly through regulation of SR calcium load, in the suppression of alternans. Subsequently, we have extended the single-cell model to a multicellular fibre, using it to study the proarrhythmic potential of spatially heterogeneous alternans, akin to alternans manifesting selectively in the border zone.

4.2 Methods

The main simulations were performed using the Heijman model of canine ventricular myocyte and its variant including electrophysiological remodelling of the infarct border zone, as described in Methods, section 2.2. Below are described pacing protocols, modifications to the baseline model, modification of the O'Hara-Rudy model used to show generality of the key result achieved, and the extension of the single-cell modified Heijman model to a 1D fibre.

4.2.1 Single-cell pacing protocols for alternans simulations

A simulated S1 protocol was used to study the formation of repolarisation alternans and underlying CaT alternans at a given basic pacing cycle length (bcl). The pacing stimulus was a 1 ms long pulse at -53 pA/pF, because in the less excitable BZ cells, the duration of 0.5 ms common in in silico studies failed to trigger an action potential (AP) at rapid pacing rates. Amplitude of repolarisation alternans was defined based on AP duration (APD) as max(APD)-min(APD) of the last ten APDs of each simulation. The alternans ratio of APD or CaT amplitude was defined as 1 – MIN / MAX, reflecting

the minimum and maximum values of two successive beats, respectively, in line with previous experimental studies (Florea and Blatter, 2012; Hammer et al., 2015). A simulation was labelled as manifesting alternans when the amplitude of its APD alternans exceeded 3 ms or when alternans ratio was larger than 0.02. To determine the impact of downstream effects of β-AR stimulation separately (used in sections 4.3.3 and 4.3.4), the signalling cascade of the model was turned off and the phosphorylation levels of various sites were manually clamped to either 0 (non-phosphorylated) or to 1 (fully phosphorylated). The model was modified to similarly allow isolating the distinct effects of RyR activation via β-AR stimulation in section 4.3.4.

Measurements were taken in a quasi-stable state. In an oscillatory system possibly manifesting alternans, the notion of stability needed to be redefined compared to the common definition. We consider the cellular model to be in quasi-stable state when the maximum and minimum value of a variable var during two consecutive beats each change less than 0.2% per 100 beats for var = membrane potential, intracellular calcium, intracellular potassium, and intracellular sodium. Maxima and minima of beat pairs are used to allow cells manifesting alternans to be considered stabilised. For all tested pacing frequencies, 2500 beats were sufficient to reach the quasi-stable-state.

4.2.2 Modulation of RyR under β-AR stimulation in the O'Hara-Rudy human model

To demonstrate the generality of the results from the canine model, we also repeated the key experiments in the O'Hara-Rudy human ventricular cardiomyocyte model (O'Hara et al., 2011), by implementing the accelerated and shortened SR calcium release due to β-AR stimulation-dependent RyR regulation. The endocardial parametrisation of the model has been used, as it was the only one that manifested alternans at rapid pacing rates, unlike epicardial or midmyocardial variants. In order to achieve the faster activation and shorter duration of SR calcium release during β-AR stimulation dependent RyR activation similar to the single-cell HeRd model (section 2.2), we reduced the activation constant β_τ to 1.583 ms (1/3 of the original value of 4.75 ms) to represent

faster RyR opening and closing and we increased α_{rel} 6 times to match the total amount of calcium released from SR to a cell with unchanged RyR dynamics.

4.2.3 Multicellular simulations

The cellular fibres in this article are based on the single cell model described in General methods, section 2.2. Four minor modifications were applied to the baseline single-cell model. First, a 25% increase in fast sodium current (I_{Na}) was included to compensate for electrical coupling of the cells in the fibre, allowing alternans formation (an identical modification has been used in (Tomek et al., 2017)). Second, a 35% reduction in expression of SERCA pumps in the BZ cells has been included, consistent with literature (Shi et al., 2015). Third, only in fibre simulations, the downregulation of I_{Na} in BZ cells in the original model was excluded in order to be able to allow us to attribute decreased excitability and subsequent arrhythmogenicity to alternans as opposed to a mixture of alternans and I_{Na} downregulation. Fourth, the modulation of inactivation and activation dynamics of I_{Na} under β-AR stimulations, as formulated in the original model (Heijman et al., 2011), was omitted (leaving an increased current amplitude by 25%); these changes caused a considerable post-repolarisation refractoriness in the original model, not consistent with literature showing that sympathetic stimulations shortens effective refractory period (Martins and Zipes, 1980).

Propagation of electrical excitation was simulated through one dimensional cardiac fibres consisting of 256 cells, being either all-NZ cells (control fibre), or with cells 96-160 being the BZ cells, used to study spatially heterogeneous alternans. All fibres were pre-paced for 500 or 501 beats (to have one state starting with a short action potential and one state starting with a long action potential), by stimulating an initial segment of the fibre with 1ms stimulus of -53 mV. A version of S1-S2 protocol (regular pre-pacing at S1 = 300 or 400 ms bcl, followed with a single stimulus, presented after S2 < S1 ms) was used to test the vulnerability to conduction block. This involves stimulating an initial segment of the fibre with a train of S1 stimuli, followed by a S2 stimulus at the same location. The window of vulnerability to conduction block is the range of S1-S2 coupling intervals (CI), where conduction stops in the infarct border zone. Similarly, a version of

S1-S2 protocol was used to test vulnerability to premature ventricular complex (PVC) propagation; however, in this case, the central segment of the fibre was stimulated with the S2 stimulus, mimicking a PVC. The S1-S2 coupling intervals reported in PVC testing are the interval between S1-driven activation at the central fibre segment and the activation induced via S2 stimulus. For each S1-S2 protocol, a range of possible CIs was explored: we re-loaded the pre-paced fibre after S1 stimulation for each tested S2 value.

4.2.4 Implementation notes

Single-cell simulations were performed using the previously published MATLAB (The Mathworks, Natick, MA) code of the Heijman model (Heijman et al., 2011), employing the ode15s solver. Fibre simulations were performed using the Myokit software package (Clerx et al., 2016). The OpenCL-based support for parallel computation available in Myokit was used for multi-cellular simulations with a fixed time step of 0.002 ms. We thank NVidia

4.3 Results

4.3.1 Alternans formation in the HeRd model

Before using computer models to understand alternans and its modulation via β-adrenergic stimulation, we first characterise how alternans is generated in the model. We describe how the refractoriness of the SR calcium cycling drives alternans in the HeRd model. The validation of the fact that alternans in Hund-Rudy family of models is driven by oscillations of calcium subsystem in the first place has been performed by Livshitz and Rudy (2007), also suggesting that alternans in the model is driven by refractoriness of SR release. We provide a more extensive insight to the mechanism below, extending their work.

Let us first briefly review key components in calcium handling, with a diagram (Figure 4.1). During an action potential, L-type calcium current (I_{CaL}) induces an influx of calcium which is sensed by ryanodine receptors (RyR), and which induces a large-magnitude release of calcium via RyR (this process is named CICR: calcium-induced calcium release). The amount of calcium released via RyR depends mainly on the

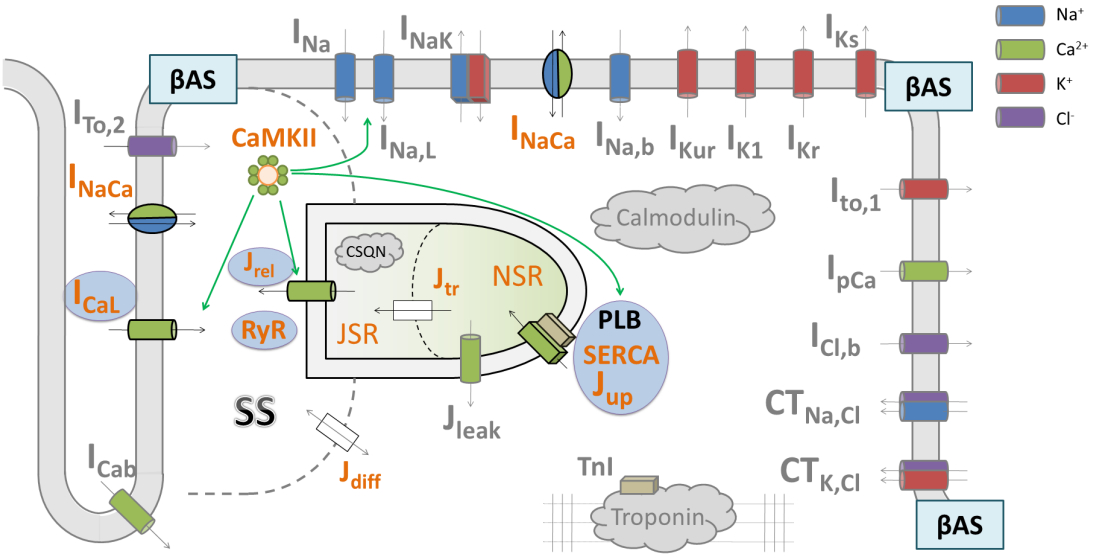


Figure 4.1: A simplified diagram of HeRd model with focus at calcium handling. Key factors to calcium handling are written in orange. I_{CaL} = L-type calcium current; SS = junctional sarcoplasmic subspace; JSR = junctional sarcoplasmic reticulum; NSR = network sarcoplasmic reticulum; RyR = ryanodine receptors; J_{rel} = SR release flux; J_{tr} = calcium flow from NSR to JSR; J_{up} = reuptake to NSR via SERCA pumps, J_{diff} = diffusion from SS to the main intracellular pool, I_{NaCa} = the current of sodium-calcium exchanger, CaMKII = Ca^{2+}/calmodulin-dependent protein kinase II. Components regulated by β-AR stimulation are placed on blue ellipses.

calcium stimulus via I_{CaL} and the load-release relationship of junctional sarcoplasmic reticulum containing RyR (JSR): the fuller the JSR is, the more calcium it releases (Shannon et al., 2000). This relationship is steep, as shown in a previous study of the Hund-Rudy model (Livshitz and Rudy, 2007) and experiment (Shannon et al., 2000), i.e., a relatively small increase in JSR contents may increase fractional release considerably. The released calcium then diffuses to the intracellular space and eventually to SERCA pumps, which reuptake the calcium back to network sarcoplasmic reticulum containing SERCA pumps (NSR). Ultimately, within sarcoplasmic reticulum, calcium diffuses from NSR to JSR along the concentration gradient (J_{tr}), where it is partially buffered by calsequestrin (Faggioni and Knollmann, 2012); consequently, only a fraction of total JSR calcium is effectively free for release.

The HeRd model includes the calcium handling processes described above and given that it is capable of manifesting alternans (Livshitz and Rudy, 2007), it may be used for the investigation of its causes. We first propose how alternans sustains itself in the

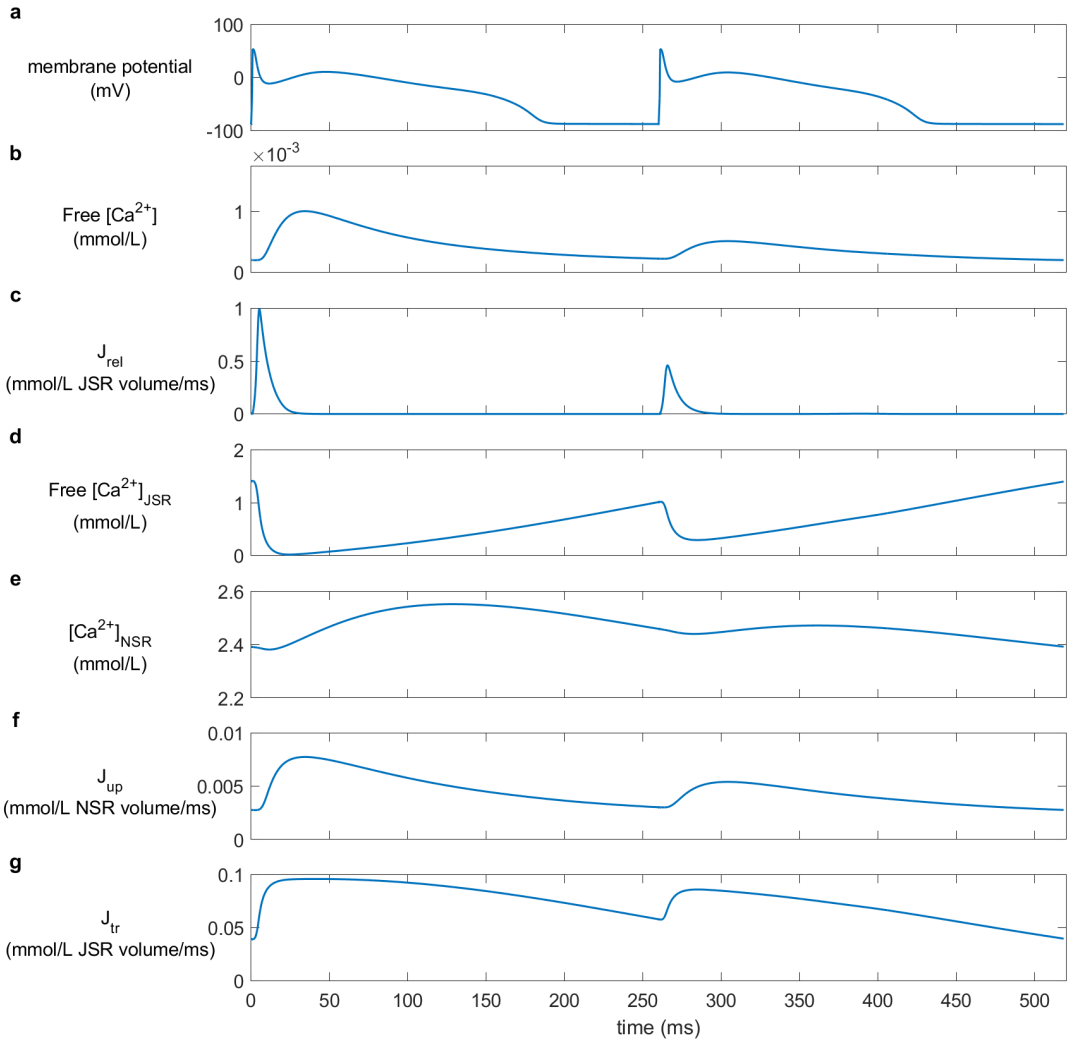


Figure 4.2: An overview of key variables during alternans. Two action potentials after reaching the stable state are shown, starting with a prolonged action potential (a) with underlying large calcium transient (b). Further variables shown are J_{rel}, the release current via RyR (c), free JSR calcium (d), NSR calcium (e), J_{up}, the reuptake via SERCA pumps (f), and J_{tr}, the diffusion from NSR to JSR.

stable state of the simulation, using this afterwards to show how alternans originates in the first place. Visualising two beats manifesting alternans, after 2500 beats of pre-pacing at base cycle length (bcl) 260 ms, the first action potential is prolonged and manifests an increased calcium transient amplitude (Figure 4.2a-b). The first release is increased (Figure 4.2c), directly translating into increased depletion of JSR (Figure 4.2d). At the same time as JSR is emptied, it starts being refilled from NSR via J_{tr}, eventually increasing free JSR calcium again (Figure 4.2g,d). The reuptake during the first AP is stronger than during the second one, given that there is a larger amount of calcium available for reuptake after the larger first release and the NSR is emptier (Figure 4.2f). As a consequence of the increased reuptake, NSR loading also increases (Figure 4.2e). The fact that alternans is sustained at this stage is due to two characteristics of the model: the steepness of the load-release relationship and the limited rate of the NSR→JSR diffusion. First, the steep load-release relationship of JSR release translates the high initial loading of JSR into a large release in the first AP, which is too large to be refilled by J_{tr} in time; consequently, the JSR calcium is lower at the start of the second AP (Figure 4.2d). Given the lower loading of JSR, a smaller release occurs, leaving a relatively large amount of calcium in the JSR (Figure 4.2c,d). Given that the gradient between NSR and JSR is still relatively large (see values of [Ca]NSR and [Ca]JSR in Figure 2d,e), J_{tr} adds a large enough amount of calcium to JSR to load it more than at the start of the second AP, causing the next calcium release to be large again, forming alternans.

Having described how alternans is maintained, the next question is how alternans starts in the first place. Given the pacing of 260 bcl, alternans starts developing at beat 875, both in APD and calcium transient (Figure 4.3a,b). A key driver of alternans development is the rising CaMKII activity (Figure 4.3c), responsible for rate-dependent adaptation of calcium handling, e.g. via phosphorylation of I_{CaL}, RyR, and SERCA pumps; when CaMKII activity was clamped to a pre-alternans value, alternans did not develop at all (not shown). The combination of slightly increasing JSR loading at the start of an AP (Figure 3d) downstream of growing NSR loading (Figure 4.3g), combined with decreasing minimum JSR calcium concentration per action potential (Figure 4.3e) represents increasing fractional emptying and explains increasing total calcium release

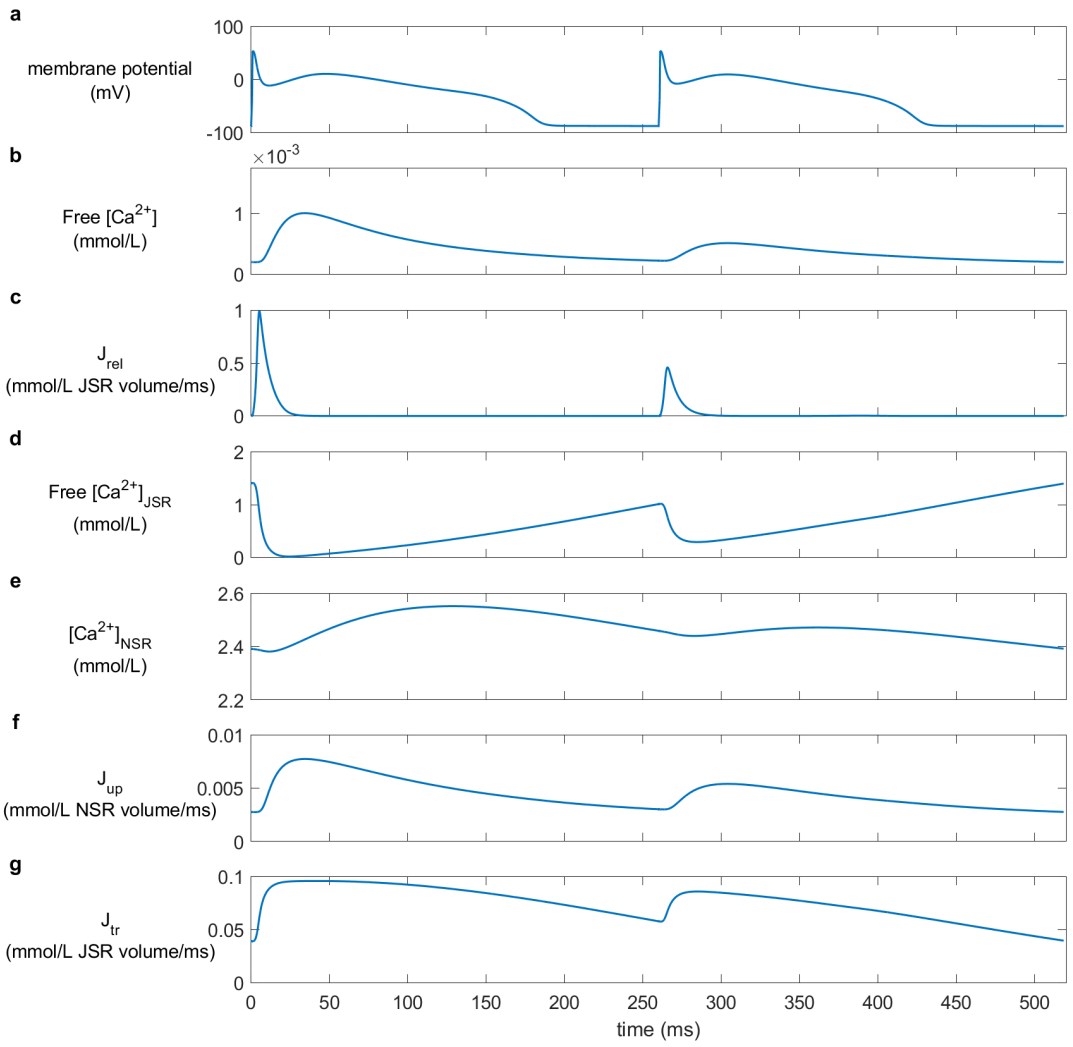


Figure 4.3: Alternans development during rapid pacing. Shown are the following variables for action potentials 700-1050: a) action potential duration, measured as the time from peak dV/dt to 95% repolarisation, b) calcium transient alternans magnitude, defined as maximum intracellular calcium per action potential minus the minimum, c) CaMKII activity at the start of the given AP, d) free JSR calcium at the start of an action potential, e) minimum (post-release) free JSR calcium per action potential, f) the integral of SR release flux, total calcium released, g) NSR calcium at the start of an action potential.

(Figure 4.3f). This increasing release becomes so large at a certain stage (AP_x), that JSR cannot be refilled to the original state in time, making the next release (AP_{x+1}) smaller, however, as described above, JSR at the start of the following AP (AP_{x+2}) may be filled even more than in AP_x, given lower JSR emptying in AP_{x+1}, which then promotes into even larger release. This exacerbates the impossibility of adequate JSR refilling, making AP_{x+3} manifest an even lower release, which is how alternans develops.

4.3.2 β-adrenergic stimulation abolishes APD and CaT alternans

To study the effect of β-adrenergic stimulation on alternans in NZ and BZ cells, we simulated the APD rate dependence and measured alternans occurrence at various bcls in NZ and BZ with and without maximal β-AR stimulation (1.0 μmol/L ISO; Figure 4.4). BZ cells manifested repolarisation alternans at slower pacing frequencies than NZ cells (alternans onset at bcl of 340 versus 280 ms; Figure 4.4c), which was also evident from the rate dependence of alternans ratio (Figure 4.4e-f). β-AR stimulation abolished both APD and CaT alternans in NZ and BZ models at all bcls. These results are qualitatively matching our experimental results presented previously in chapter 3, although β-AR stimulation merely attenuated alternans, unlike in the computational model where it was abolished entirely.

4.3.3 Electrophysiological mechanisms underlying alternans inhibition via β-AR stimulation

In order to discern which of the eight downstream targets of β-AR signalling incorporated in the model are responsible for the abolishment of CaT alternans, we analysed CaT alternans formation at bcl of 260 ms for all the 256 combinations of either dephosphorylated or fully phosphorylated targets. The strongest alternans-abolishing effect was achieved with the simulated phosphorylation of RyR, preventing CaT alternans in all the 128 combinations involving this downstream effect (not shown), this phenomenon will be further investigated in the following section.

There are 128 (2^7) possible combinations of β-AR signalling phosphorylation targets in the absence of RyR phosphorylation, 88 of which show alternans at bcl of 260 ms (e.g.,

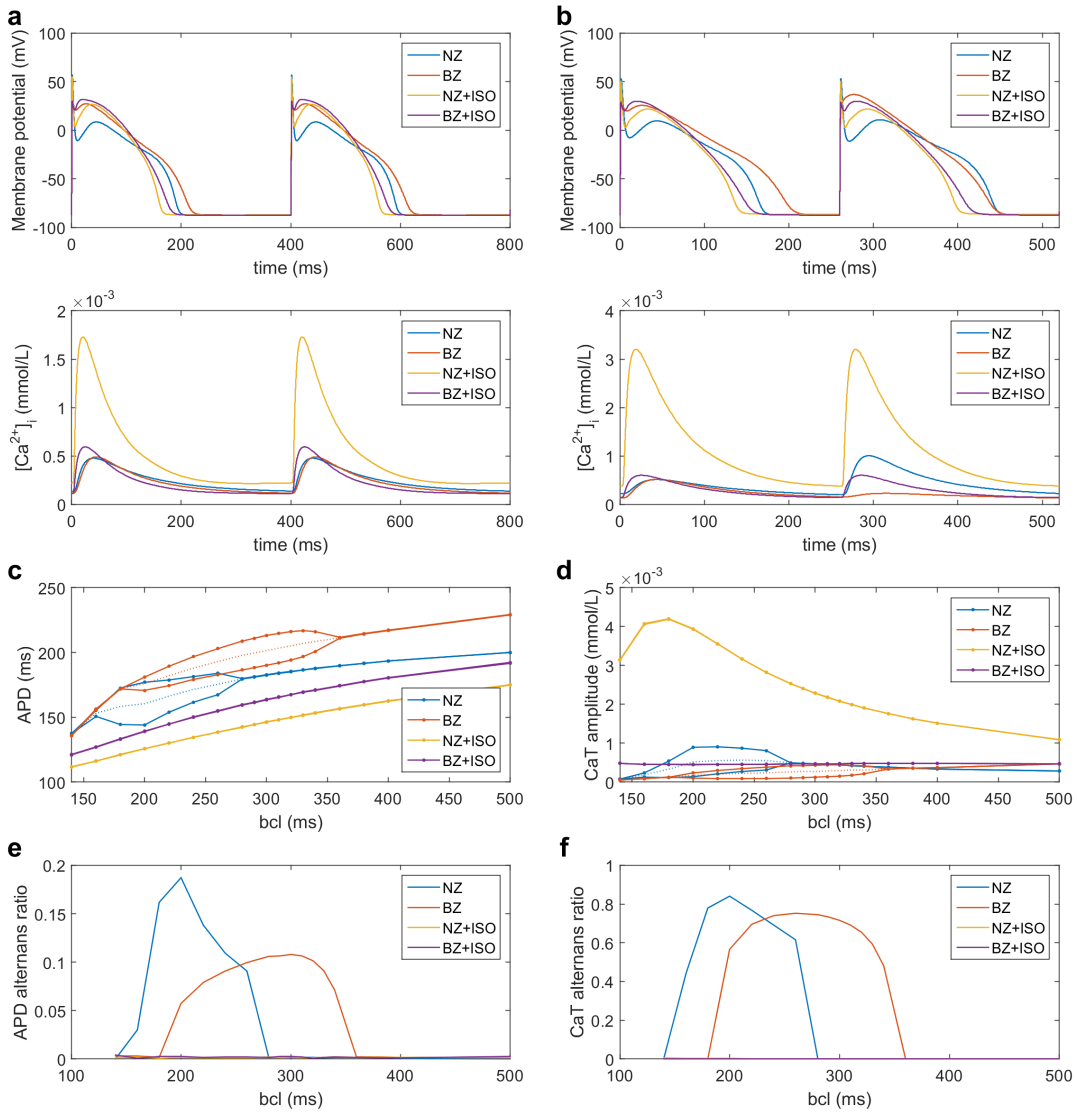


Figure 4.4: Effect of β-AR stimulation on rate dependence of alternans. a) Membrane potential and calcium transients of four model configurations at bcl of 400 ms: normal zone cell (NZ), border zone cell (BZ), β-AR-stimulated (1.0 µmol/L ISO) NZ cell (NZ + ISO), β-AR-stimulated BZ cell (BZ + ISO). b) Analogous plot at bcl of 260 ms, showing APD and CaT alternans in NZ and BZ cases in the absence of β-AR stimulation. c, d) APD and CaT rate dependence curves for the four simulated configurations. Bifurcation in NZ and BZ curves indicates the occurrence of alternans. The dotted lines represent the mean of minimum and maximum APD during alternans. e,f) Alternans ratio for APD and CaT alternans in the four groups.

phosphorylated I_{CaL}+I_{Kur}) and 40 of which do not (e.g., phosphorylated I_{Ks}+I_{NaK}; Figure 4.5a-c). Figure 4.5d-e shows the amount of APD and CaT alternans as a function of the total amount of calcium released from the SR during two bcls (two bcls were used instead of a single beat in order to enable comparisons between cells in alternans, and without) for each of these 128 combinations. Combinations without RyR phosphorylation that did not manifest APD and CaT alternans could be divided into two major groups. The first group involved those combinations of downstream effects that diminish SR calcium release (e.g., phosphorylation of I_{NaK}, which increases its activity and lowers sodium and calcium levels). As discussed previously in section 4.3.1,

The second major group of β-AR stimulation-dependent effects preventing the formation of alternans in our model was the group with the largest SR calcium release and a fast calcium reuptake. This group involves increases in I_{CaL} and SERCA activity (via reduced PLB-mediated inhibition upon phosphorylation), optionally with other β-AR-mediated effects that do not decrease SR calcium release. In this case, SR loading is increased so much that JSR empties entirely or almost entirely in every beat. In a normal, non-emptying cell, increasing J_{tr} between consecutive action potentials may increase the release considerably due to steep relationship between Ca_{JSR} and release, which may trigger alternans as in section 4.3.1. However, when JSR becomes emptied in every action potential, the only possible increase of release between consecutive action potentials is exactly by the additional amount J_{tr} brings (there is no further "reserve" of calcium which could be released), making the load-release relationship linear (all in, all out). At the same time, J_{tr} is not a limiting factor that could trigger alternans, given that it is strong enough to fill JSR so much that it empties itself entirely. This high J_{tr} requires high NSR loading, which may stem either from increased SERCA function (e.g., due to phosphorylation) or from increased amount of calcium to be reuptaken (e.g. due to phosphorylated I_{CaL}). However, we do not believe the phenomenon of complete functional JSR depletion is present in real organisms, given the existing literature on this topic, reporting at most 60-80% depletion of releasable calcium (Shannon et al., 2000; Bassani et al., 1995), showing release reserve even during alternans (Shkryl et al., 2012).

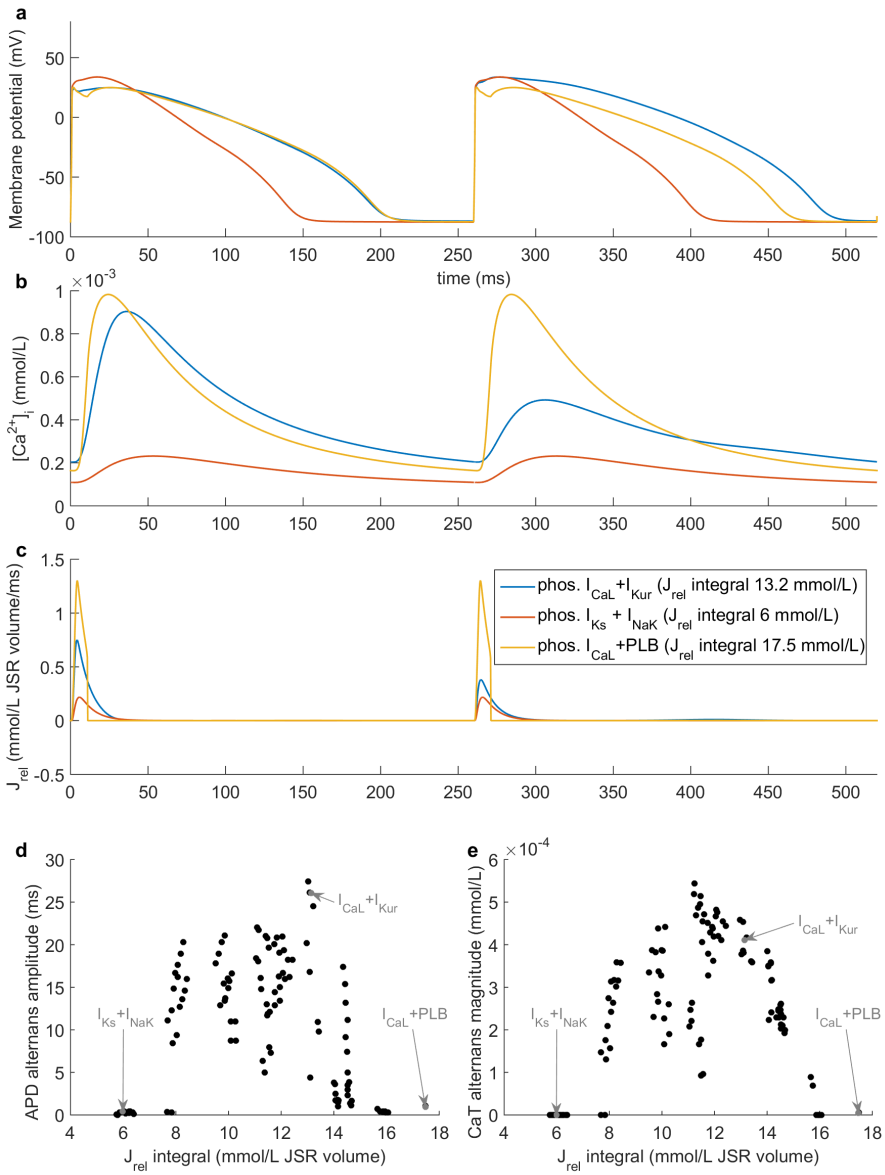


Figure 4.5: Role of SR calcium release magnitude in alternans. Membrane potential (a), cytosolic calcium concentration (b), and SR calcium release flux (J_{rel} (c) for three combinations of downstream β-AR stimulation effects at bcl = 260 ms. Lower panels show magnitude of APD (d) and CaT (e) alternans for all 2^7 = 128 different combinations of downstream effects of β-AR without RyR activation versus the integral of J_{rel} over two consecutive APs. The two conditions shown in panels a-c are indicated with arrows.

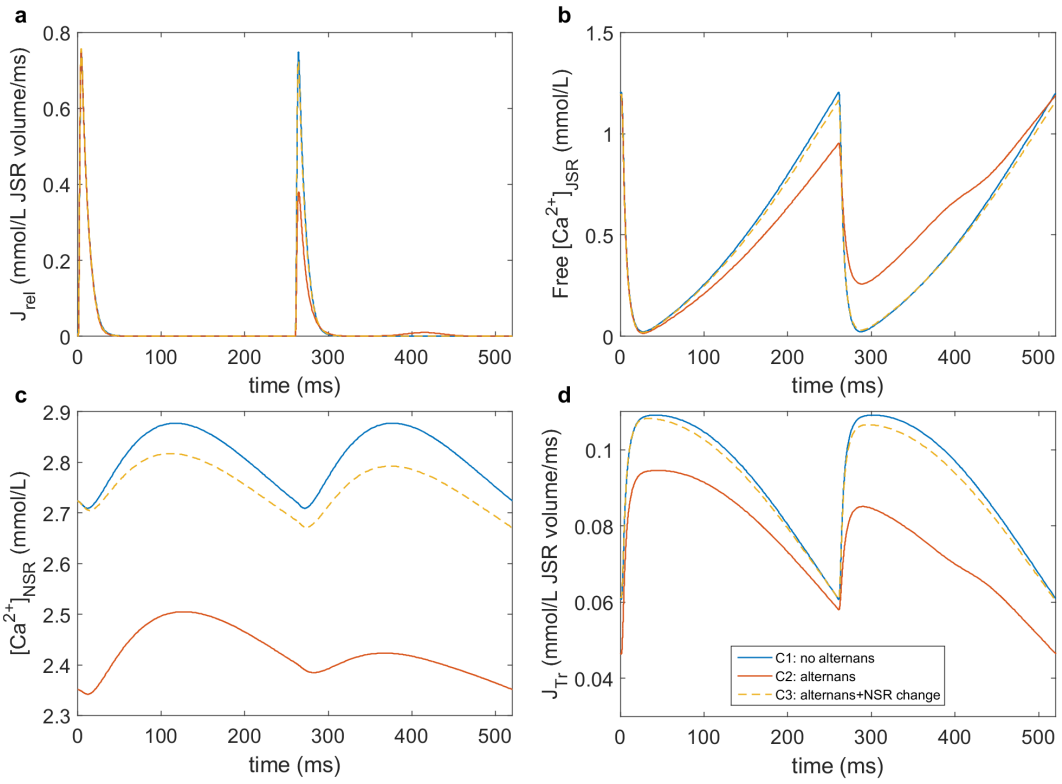


Figure 4.6: Effect of SR calcium load on alternans. SR calcium release flux (a), JSR (b) and NSR (c) calcium concentrations, and calcium transport between NSR and JSR (d) are shown for three simulations: C1 (a combination of β-ARS downstream effects with high release and no alternans), C2 (a combination of β-ARS downstream effects with relatively high release, manifesting alternans), and C3 (C2 with NSR calcium content changed to that of C1 at the beginning of the plotted period).

To illustrate the importance of large J_{tr} in models that do not manifest alternans due to very high calcium release, we considered two combinations of downstream effects: C1, free of alternans due to large calcium release (simulated phosphorylation of I_{CaL}+PLB+TnI+I_{Na}), and C2, manifesting alternans (phosphorylation of I_{CaL}+I_{Kur}), with the large calcium release in C2 closely matching the calcium releases of C1. Calcium-handling properties of these variants during two APs at a bcl of 260 ms are illustrated in Figure 4.6. In C1 and C2 the first calcium release was nearly identical despite the different NSR contents, which affected the speed of JSR transport (J_{tr}) and thus JSR refilling. Because in the C2 model the JSR was not refilled sufficiently after the first release, and given that the SR calcium load-release relationship is steep, the next calcium release was comparatively small and a relatively large amount of calcium remained in

the JSR. More calcium was then added to the JSR during and after the second release, but the process is limited by the high level of calcium in the JSR, reducing the concentration gradient between NSR and JSR 4.6. As a third case (C3), we considered a model with the same parameters as C2, but which has its NSR contents artificially changed to the value of C1 at the start of the larger J_{rel} at the beginning of the shown interval. In this case, the second release is almost identical to the first release, supporting the importance of NSR loading (promoted by a high calcium reuptake rate) in alternans prevention.

Considering the relative importance of RyR phosphorylation versus total release modulation in alternans attenuation, we find the RyR phosphorylation to be the more important factor, given that with all downstream effects of β-AR stimulation, total release over 2 action potentials is 13.6 mmol/JSR volume, which in itself would be associated with pronounced alternans based on the amount released (Figure 4.5 and this thus would not explain the lack of alternans.

4.3.4 Biophysical RyR properties regulating CaT alternans

With simulated downstream effects of β-AR stimulation on RyR, alternans was never present, independent of the integrated J_{rel} over two APs (ranging from 5.2 to 16.4 mmol/L). Thus, the total amount of calcium released is not the key mechanism behind the abolishment of alternans under these conditions. In order to discern the mechanism behind the anti-alternans effect of RyR activation, we isolated and separately simulated the three downstream effects of β-AR stimulation on RyR biophysical properties. The three effects are a) the time-constant of RyR activation and deactivation is reduced to 21% of the original value, b) the SR calcium release multiplier is reduced to 65%, c) the JSR calcium leak is explicitly increased. All effects of β-AR stimulation other than RyR activation were disabled in these simulations unless stated otherwise, in order to isolate the effects of altered RyR dynamics from other downstream effects.

We simulated all eight possible combinations of the three β-ARS-induced changes to release dynamics being turned on or off (Table 4.1). Most combinations of RyR activation changes abolished CaT alternans, but the mechanisms involved turned out to be distinct. Additionally, in order to better understand the impact of the RyR activation

RyR_{Tau}	RyR_{Amp}	RyR leak	APD alt. amp. (ms)	$\int J_{rel}$
No β-ARS			20.13	8.62
ON	ON	ON	0.32	7.69
ON	ON	OFF	0.35	8
ON	OFF	ON	0.19	8.02
ON	OFF	OFF	0.39	8.32
OFF	ON	ON	0.49	8.18
OFF	ON	OFF	0.37	8.54
OFF	OFF	ON	14.05	8.43

Table 4.1: BZ model with individual effects of RyR activation via β-ARS (with all other β-ARS downstream effects disabled). APD alt. amp. is the amplitude of APD alternans in ms. The SR calcium-release integral is a sum of the calcium-induced calcium-release flux and the JSR leak over two beats. ON/OFF indicates whether or not the modification of the given feature was used or not during the simulated RyR modulation.

changes on alternans formation, we stimulated a BZ cell without β-AR stimulation at bcl 260 and acutely introduced each of the three single RyR activation changes individually, allowing us to observe the immediate effect of these changes, without potentially confounding effects on intracellular ionic concentration or SR calcium load (Figure 4.7).

A faster time constant (RyR_{Tau}) produced an immediate decrease in the duration of SR calcium release (measured as the duration of $J_{rel} > 0.025$; Figure 4.7a), accompanied by a small decrease in the integrated SR calcium release (Figure 4.7c), which could also be observed as slightly reduced fractional emptying of the JSR (Figure 4.7f). With reduced RyR_{Tau}, J_{up} exceeds J_{rel} (Figure 4.7d), resulting in steeply increasing NSR loading (Figure 4.7e). There are two important features associated with shortened SR release with similar total release implying that the release amplitude is higher. First, faster SR calcium release leads to comparatively higher calcium gradients between cytosol and NSR, increasing the efficiency of reuptake via SERCA. Second, the faster upstroke and earlier peak of calcium release means that the main calcium load is released earlier than with baseline calcium-release dynamics, giving more time for calcium reuptake. Both these factors thus improve reuptake, allowing higher NSR loading, which then translates into improved JSR refilling. The importance of these two consequences of SR release altered by β-AR stimulation are further investigated in section 4.3.4.1, using clamping to allow more precise control over calcium handling. The most notable effect

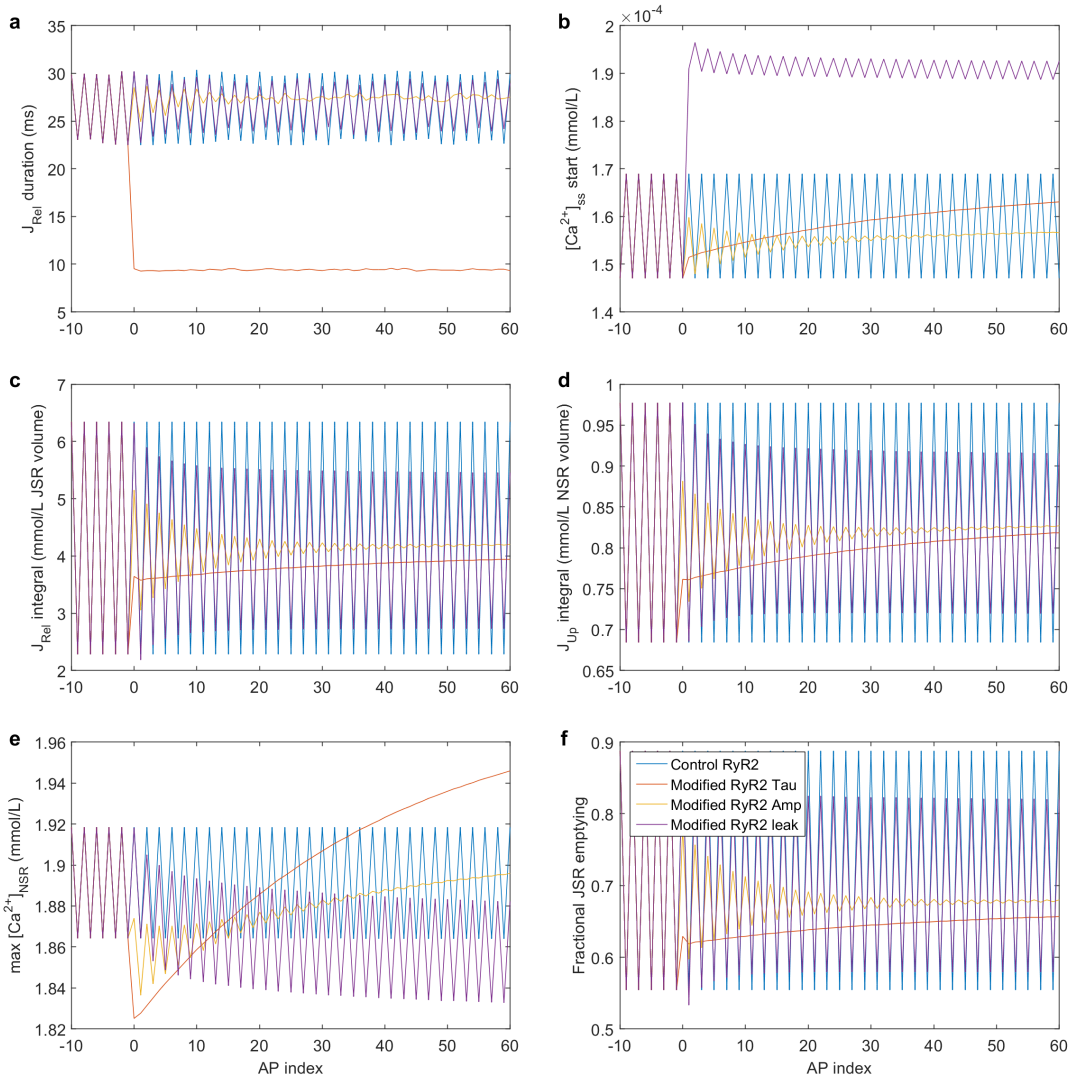


Figure 4.7: The effect of acute introduction of single RyR activation changes on alternans. Release duration (a), diastolic $[Ca^{2+}]$ in the subspace (b), SR calcium release integral (c), SR calcium uptake integral (d), maximal NSR calcium content (e), and fractional JSR emptying (f) are shown as a function of AP index after stabilization (APs 2437-2480 are shown from an AP sequence of 2500 APs, the point of acute introduction of RyR activation is x=0; absolute AP index of 2440. The model was paced at a bcl of 260 ms under control conditions or with selective changes to RyR time constants (Tau), RyR amplitude of SR calcium release (Amp), or JSR calcium leak.

of increased JSR calcium leak was an increased calcium concentration in the subspace between RyR and L-type calcium channels (Figure 4.7b), contributing to higher I_{CaL} inactivation. Consequently, the increased leak then acted as a dampener, limiting the systolic SR calcium release (Figure 4.7c), preventing overt emptying of the JSR, and providing more calcium for the next release (Figure 4.7g), thus gradually reducing

alternans, not abolishing it entirely. Finally, the anti-alternans effect of decreasing RyR_{Amp} was chiefly due to limiting the amount of calcium released, which acted first during the large SR calcium release, thereby providing more calcium for the next release, similar to an increase in SR calcium leak.

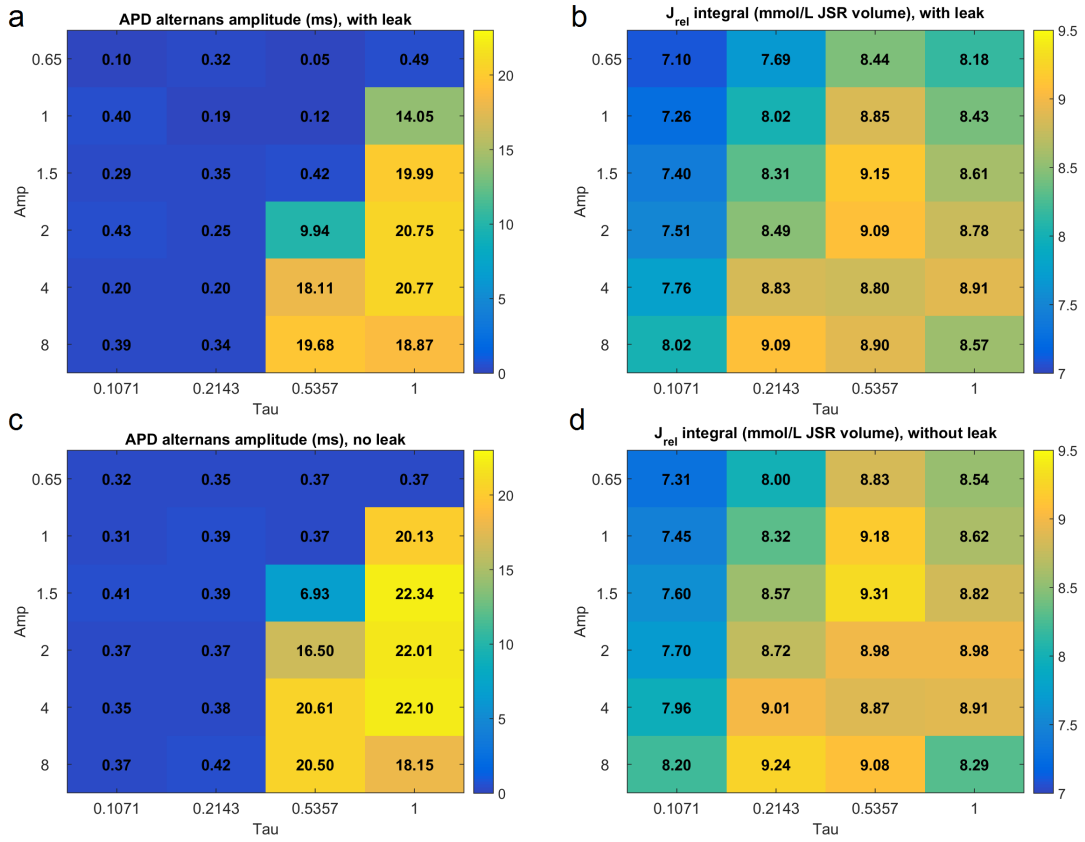


Figure 4.8: Sensitivity analysis of the effects of altered RyR gating on alternans. Alternans amplitude is shown for different combinations of Tau and Amp properties of the RyR, either with increased JSR leak (a), or without (c). Similarly, subfigures (b) and (d) depict the integral of SR calcium release over two consecutive APs with or without the presence of increased JSR leak, respectively.

In order to investigate the robustness of these results, we evaluated a range of RyR_{Amp} and RyR_{Tau} values, measuring the APD alternans amplitude and the integral of SR calcium released over two consecutive APs (Figure 4.8). A wide range of parameter combinations could prevent alternans, particularly those where RyR_{Tau} was reduced. As shown in the last columns of plots in Figure 4.8, a decrease in RyR_{Amp} could prevent alternans only by directly decreasing the amount of calcium released, i.e., producing a leftward shift to the non-alternans region in Figure 4.5. A decrease in RyR_{Tau}, on

the other hand, prevented alternans even in cases when the amount of SR calcium released was higher than the 8.62 mmol/L from the control case (RyR_{Amp}=RyR_{Tau}=1 and no additional leak), suggesting that the accelerated SR calcium-release dynamics are the most important factor limiting alternans.

4.3.4.1 SR release clamping to study impact of release dynamics on alternans vulnerability

In order to investigate the importance of SR dynamics in greater depth and in a more controlled environment, we have designed the following synthetic experiment, allowing a more precise control over the release dynamics.

In order to control release pattern, we modified the model to allow a clamp of SR release J_{rel} in the form of a triangle starting at 1ms after the stimulus administration (similarly to normal SR release), with controllable base width (duration of release), peak position (absolute time after stimulus administration), and area (total released calcium); an approximation of the native release using a triangle is shown in Figure 4.9a. Calcium leak from JSR ($I_{leak,JSR}$) was set to 0 when the triangular clamp was used.

While a cell with clamped J_{rel} does not manifest alternans as such, we may use the release clamping to define an index of alternans vulnerability. Using the HeRd model without β-adrenergic stimulation as previously, we pre-paced a cell at bcl 400 ms for 2500 beats and stored the final state to be loaded in further simulations. Then, using this pre-paced model, we applied a single AP with a clamped J_{rel} of given parameters, observing the ability of the cell to refill JSR to the state at the beginning of the AP. Given that alternans in HeRd model starts with incapability of the cell to refill JSR to pre-release state, let us call a cell with clamped J_{rel} that fails to refill JSR to the pre-release state "alternans-prone". Then, for a tuple of (base width, peak position), let us define the alternans threshold t as the lowest total release t per AP, such that the J_{rel} with given properties, releasing t calcium in a single AP is alternans-prone. Consequently, cells with parameters of SR release that have a high alternans threshold may be considered more resistant to alternans formation, given that they are able to sustain larger SR release without failing to refill JSR.

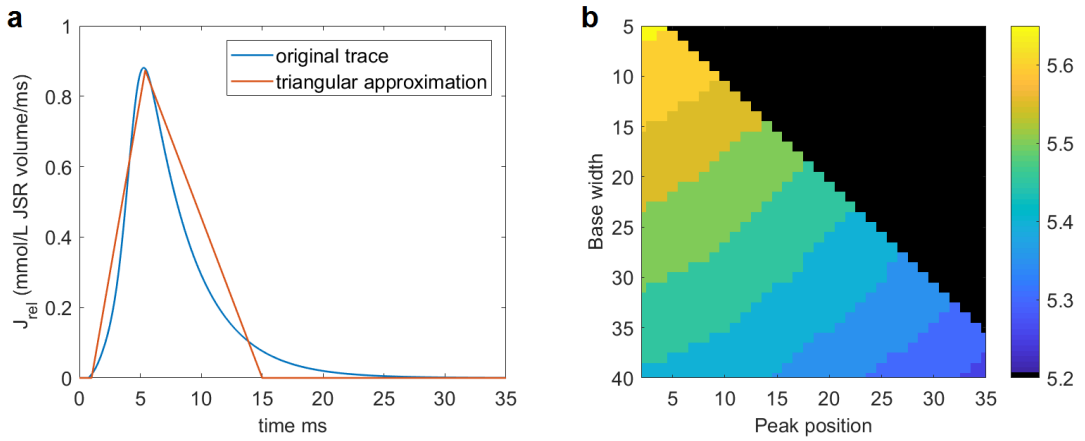


Figure 4.9: Triangular clamping of J_{rel}. a) An illustration of the approximation of native HeRd J_{rel} using a triangle, b) alternans threshold coded by colour for various combinations of base width and peak position.

Mapping the alternans threshold over a range of tuples (base width, peak position), it is apparent that both shortened J_{rel}, as well as the presence of an earlier peak improve JSR refilling and are therefore expected to attenuate alternans (Figure 4.9b).

4.3.5 Difference in alternans vulnerability between NZ and BZ

In the simulations, BZ was more vulnerable to alternans formation, both by manifesting it at slower pacing frequencies (Figure 4.4) and by requiring a higher dose of ISO to abolish alternans at bcl 260 ms (Figure 4.10a,b).

The previous section has shown that faster time constants (i.e., a lower RyR_Tau parameter) inhibit alternans formation, but the baseline BZ model has a markedly longer duration of SR calcium release than the NZ model (4.10c), making the BZ cells more vulnerable to alternans via the same effect, but of opposite orientation. β-AR stimulation reduces the SR calcium release duration (Figure 4.10e), but more β-AR stimulation is needed to overcome the baseline characteristics of the BZ model that promote alternans. The key contributor to prolonged SR release in the BZ cell is the phosphorylation of RyR via CaMKII, in agreement with experimental results, where CaMKII overexpression prolonged calcium sparks (Maier et al., 2003), which would also prolong J_{rel}.

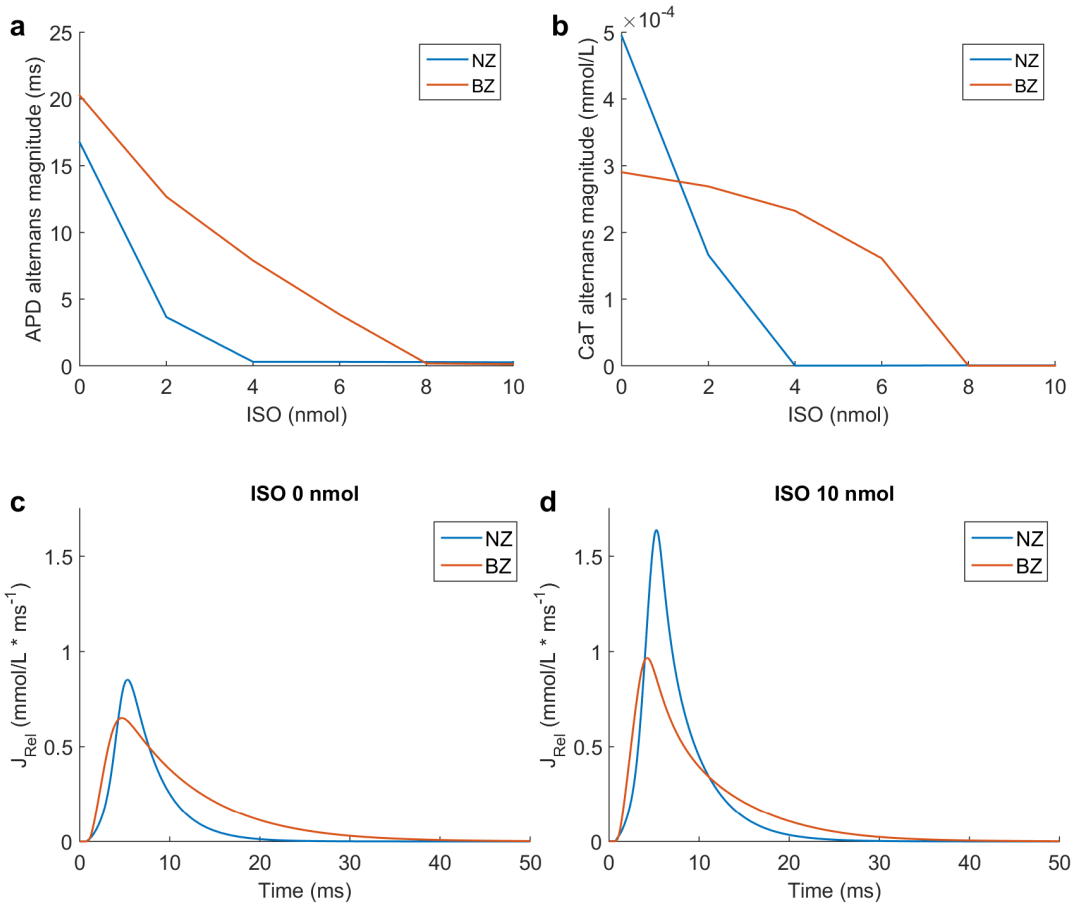


Figure 4.10: Differences in β-adrenergic sensitivity between NZ and BZ. The APD (a) and CaT (b) alternans magnitude and fraction of phosphorylated RyR (c) versus ISO concentration are shown at bcl of 260 ms for a normal zone (NZ) cell and a border zone (BZ) cell. Panels (d) and (e) compare SR calcium release flux at bcl of 500 ms between NZ and BZ in the absence (d) or presence (e) of β-AR stimulation (10 nmol/L ISO)

4.3.6 Alternans and RyR activation in O'Hara-Rudy model

We confirmed the generality of this result by testing the effect of decreasing the SR calcium-release time constant on alternans formation in another computational model; the state-of-the-art human ventricular cardiomyocyte model by O'Hara et al. (2011). The endocardial parametrisation of the model was used, as it is the only one that manifested alternans at rapid pacing rates, unlike epicardial or midmyocardial variants. In order to achieve the faster activation and shorter duration of SR calcium release during β-ARS-dependent RyR activation, we reduced the activation constant to 1.583 ms (1/3 of the original value of 4.75 ms) to represent faster RyR opening and closing

and we increased αrel 6 times to match the total amount of calcium released from SR to a cell with unchanged RyR dynamics. As can be seen in Figure 4.11a,b, the revised model indeed manifests a shorter calcium release of increased amplitude, consistent with the experimentally observed effects of β-ARS-dependent RyR regulation in the literature (Ginsburg and Bers, 2004).

With these modifications, the integral of release per 2 action potentials at bcl 260 in a normal cell was 16.69 in the baseline versus 17.16 in the revised model incorporating β-ARS-dependent RyR regulation. At bcl 400, the integral over 2 action potentials was 15.89 in a normal cell and 15.3 in a RyR-activated cell, respectively, showing that at pacing frequencies relevant for alternans formation, the altered SR calcium release dynamics did not considerably change the total amount of calcium released.

As shown in Figure 4.11c, the original human ventricular cardiomyocyte model manifested alternans at bcl smaller than 280 ms, while the model with altered RyR dynamics never exceeded alternans amplitudes of 1 ms, in agreement with our findings in the canine model.

4.3.7 Arrhythmia precursors in a simulated myocardial fibre

Using Langendorff perfusion, we have shown that hearts after myocardial infarction are prone to formation of spatially heterogeneous alternans. Here we conduct computer simulations to confirm the experimental results in a large mammal ventricular model, and to investigate mechanisms that translate alternans into arrhythmia and their potential attenuation via β-AR stimulation. The chief motivation for using computer simulations for this purpose is to overcome limitations of experiments as induction of arrhythmia experimentally would render hearts useless for repeated measurements, making an ex vivo approach impractical.

After 500 beats of pre-pacing of a cardiac fibre including a central BZ surrounded by normal cells, spatially heterogeneous APD alternans was present, restricted to the border zone virtual cardiomyocytes (Figure 4.12a).

Simulation of addition of beta-agonist abolished alternans in the border zone segment (Figure 4.12b, "β-ARS pre-paced fibre"), which is consistent with our previous

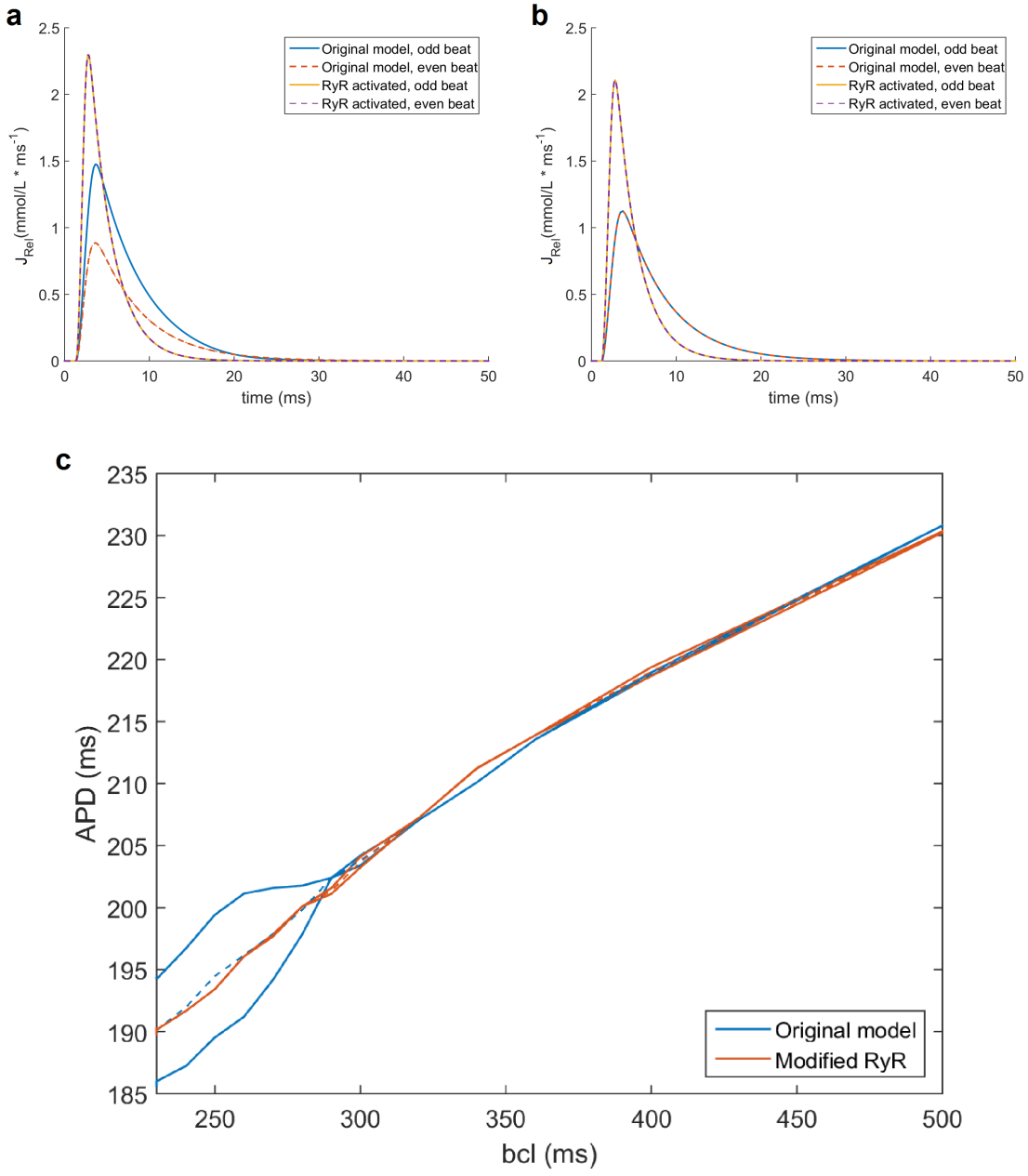


Figure 4.11: SR calcium release in original vs. RyR-modified model. Shown is J_{rel} at bcl 260 ms (a) and 400 ms (b). In both cases, even and odd beats are shown to facilitate the evaluation of presence of alternans. In c) is the minimum and maximum APD of both cell types at each tested bcl (with average shown using dashed line). Alternans with amplitude larger than 1 ms was present between bcl 230 and 280 ms in the original model only. In both models, a 2:1 block occurred at pacing rates faster than a bcl of 230 ms.

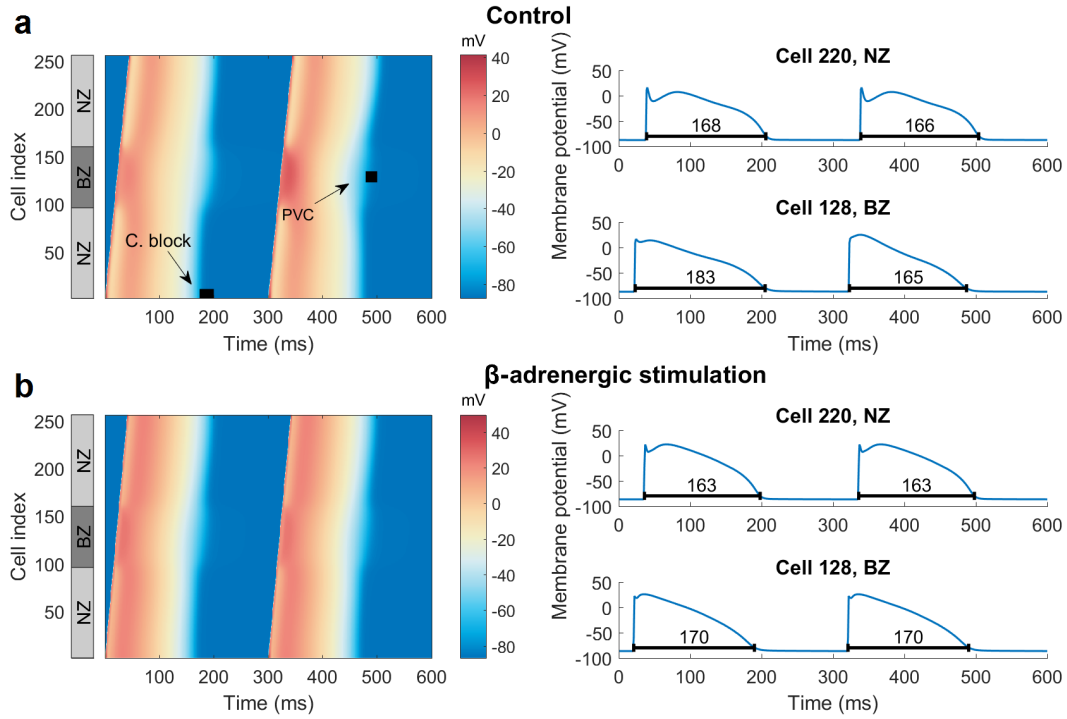


Figure 4.12: Pre-paced fibre states at control condition and with simulated β-adrenergic stimulation. a) In the left half is a heatmap of membrane potential of cells in the fibre over time, visualising two action potentials manifesting alternans in the border zone (the gray NZ/BZ/NZ box indicates the location of normal (NZ) and border (BZ) zones). The black rectangle labelled "C. block" indicates the segment of the fibre and the time of stimulation used in searching for the vulnerable window of conduction block. The black square labelled "PVC" shows the segment and time used in testing vulnerability to PVCs. To the right are examples of action potentials from NZ and BZ, corresponding to single rows of the heatmap. In b) is an analogy of a) with β-adrenergic stimulation.

single cell simulations and confirms our experimental results. In both normal zone and border zone segments, β-adrenergic stimulation also shortened the APD, which is in agreement with literature (Taggart et al., 2003).

In the next two sections, we use the myocardial fibre model to further explore how alternans increases vulnerability to arrhythmia and how this vulnerability is affected by β-adrenergic stimulation.

4.3.7.1 Discordant alternans promotes conduction block

In order to investigate the pro-arrhythmic consequences of alternans in the BZ, we first tested the hypothesis that the prolonged APD during alternans would promote conduction block. Thus, we quantified the vulnerable window for conduction block

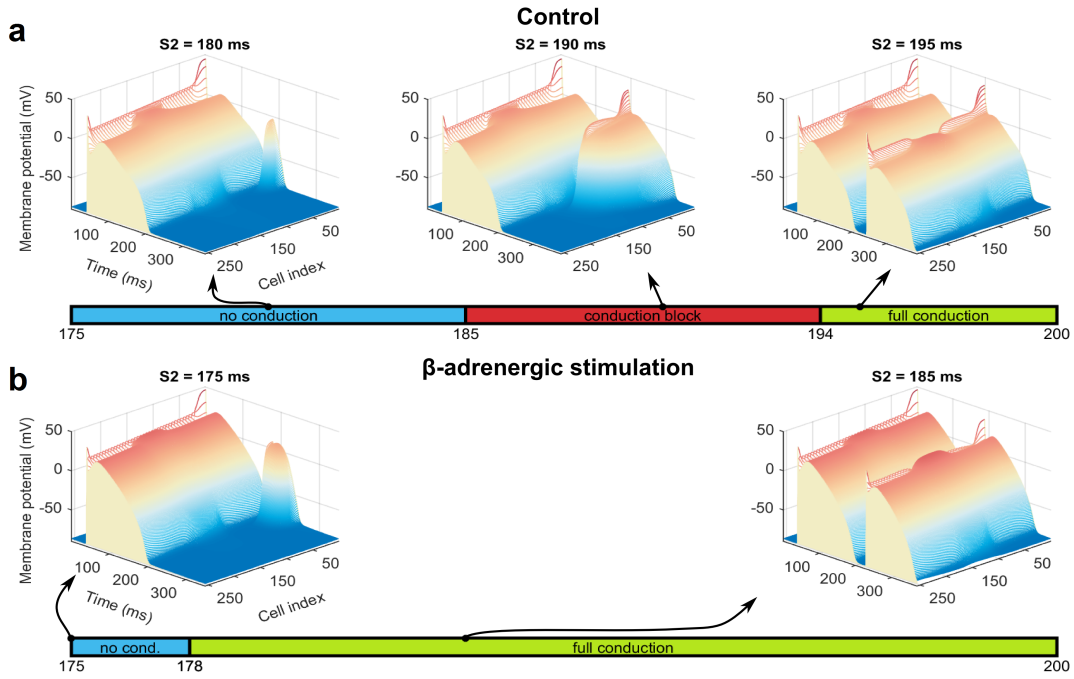


Figure 4.13: Alternans and conduction block. a) Examples of three scenarios observed for S2 interval between 175 and 200 ms, with heat and elevation coding the membrane potential: no conduction for early S2 stimulus (left image), a conduction block in the BZ (central image), and full conduction through the fibre (right image). The bar under these three cases shows the S2 intervals in which these three conditions occurred. b) Results of an identical protocol as in (a), but using a fibre pre-paced in the presence of β-adrenergic stimulation and manifesting no alternans. No conduction block has been observed and thus is not shown.

as explained in Methods, with S2 extra-stimulus applied at varying CI following the action potential with long APD during alternans in the border zone ("C block" label in Figure 4.12a) in both the control (ISO-free) and the ISO-perfused pre-paced MI fibres. In the control MI fibre, a conduction block occurred in the border zone for S2 applied at CI = 185-194 ms (Figure 4.13a middle). For S2 applied at CI <185ms, no electrical propagation ensued as tissue was still refractory (Figure 4.13a left), while stimuli applied at CI >194 ms propagated through the whole fibre normally as all tissue was fully recovered (Figure 4.13a right).

β-AR stimulation application resulted in no vulnerability to conduction block following S2, as CI < 178 ms resulted in no propagation, and CI $\geq$ 178 ms resulted in full propagation through the fibre (Figure 4.13b). The increased window of excitability (S2 $\geq$ 178 ms compared to S2 $\geq$ 185 ms) under β-AR stimulation was due to the shortened

APD and faster recovery of excitability (Figure 4.12b).

4.3.7.2 Alternans increases vulnerability to premature ventricular complex propagation

In contrast to the risk of conduction block associated with APD prolongation in the previous section, we then hypothesised that the APD shortening in the opposite alternans phase might increase vulnerability to spontaneous depolarisations in cardiac tissue, via shortening the refractory period. This could enable an earlier re-activation following a premature ventricular complex (PVC) (Bogun et al., 2008).

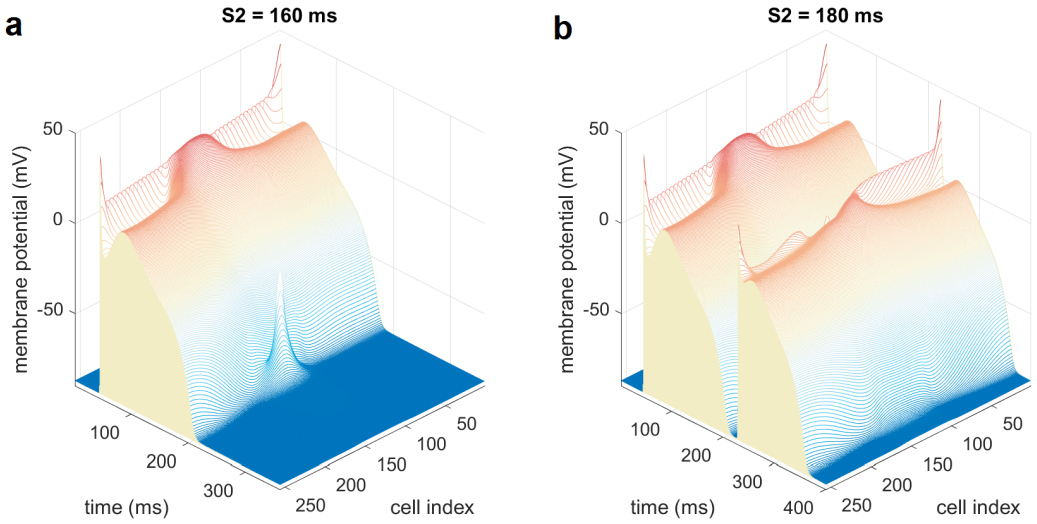


Figure 4.14: Propagation of simulated (PVCs) in the border zone. a) An example of the lack of propagation of a stimulus to the BZ manifesting shorter of the two APDs in alternans, 160 ms after the previous activation of the stimulated segment. b) An example of a propagating stimulus, 180 ms after the previous activation of the stimulated segment; again, the stimulus was applied to the centre of the BZ, following a shortened APD.

To mimic a PVC, we applied a S2 stimulus at varying CIs in the border zone following the action potential manifesting APD shortening in the border zone ("PVC block" label in Figure 4.12a). Five different pre-paced fibres were compared (Table 4.2). In all cases, short enough S2 CIs resulted in no propagation (Figure 4.14a), whereas longer S2 CIs led to propagation in both directions (Figure 4.14b), with the difference between the fibres being in the minimum value of S2 allowing propagation (Table 4.2).

First, we compared a fibre used in the previous section, manifesting alternans in the BZ ("fibre A") with a fibre consisting of NZ cells only ("fibre B"), manifesting no

Fibre ID	Bcl (ms)	NZ/BZ composition	β-ARS (nM)	S.p. S2 (ms)
A	300	NZ-BZ-NZ	0	176
B	300	NZ only	0	181
C	400	NZ-BZ-NZ	0	190
D	400	NZ only	0	184
E	300	NZ-BZ-NZ	100	180

Table 4.2: Propagation of simulated premature ventricular complexes (PVCs) in several myocardial fibres. Bcl gives the pacing frequency used during pre-pacing, NZ/BZ composition determines whether the fibre contains a BZ zone or is entirely composed of NZ cells, β-ARS gives the concentration of ISO used, and S.p. is the shortest propagating S2 interval (the interval before the previous activation of the centre of the fibre and the activation triggered by the S2 stimulus), representing the cell's length of refractory period.

alternans. Fibre A after the alternans-shortened AP was more vulnerable to premature activation than fibre B (minimum propagating S2 CI of 176 vs 181 ms, Table 4.2 rows A–B), supporting the view that alternans might increase vulnerability to PVCs. In order to ascertain that this observation was due to alternans and not, for example due to a higher baseline vulnerability of the BZ, we repeated the measurements in fibres C and D, similar to A and B respectively, but pre-paced at 400 ms bcl, manifesting no alternans (Table 4.2 rows C–D). We observed a lower vulnerability of fibre C to premature activation, compared to fibre D (minimum propagating S2 CI of 190 vs 184 ms respectively), showing that the effective refractory period of BZ cells is longer than in NZ cells, consistent with the literature (Wit et al., 1982). This is consistent with the hypothesis that the difference between fibres A and B is due to alternans, rather than baseline cellular properties.

Ultimately, we measured the vulnerability to PVCs in fibre E; similar to fibre A, but with β-adrenergic stimulation suppressing alternans, as in the previous section (Figure 4.12b). Fibre E was less vulnerable to PVCs than fibre A (minimum propagating S2 of 180 ms in E, versus 176 ms in A; Table 4.2 row E), showing a potential antiarrhythmic benefit of reducing alternans beyond a simple decrease in the risk of conduction block. That said, β-adrenergic stimulation in general shortens APD, which in itself makes the vulnerable window for PVCs wider; the beneficial effect of vulnerable window narrowing may occur only when alternans is present and can be attenuated by β-adrenergic stimulation.

4.4 Discussion

The main findings of this section are:

1. Alternans in the HeRd model is driven by a combination of steep load-release relationship and insufficient replenishment of releasable calcium.

2. β-adrenergic stimulation abolishes alternans.

3. This abolishment is mediated by accelerated release dynamics of ryanodine receptors and. Conversely, slowed release dynamics may promote alternans in infarct border zone or heart failure.

4. Spatially heterogeneous repolarisation alternans increases vulnerability to conduction block and increases the vulnerable window to extrasystolic stimuli.

4.4.1 Alternans in HeRd model is driven by SR cycling refractoriness

Numerous previous studies have investigated the subcellular determinants of CaT and repolarisation alternans (Fox et al., 2002; Livshitz and Rudy, 2007; Zhou et al., 2016; Qu et al., 2016; Weiss et al., 2006; Picht et al., 2006). In general, these studies have identified a critical role for SR calcium-cycling properties in CaT alternans development, focusing either on refractoriness of release via slow reactivation of RyR (Picht et al., 2006), or slow calcium reuptake resulting in a release-reuptake mismatch (Weiss et al., 2006). Our work highlights a third explanation, named "SR cycling refractoriness".

The explanation of alternans presented in this thesis relies primarily on steepness of load-release relationship combined with limited rate of diffusion between NSR and JSR preventing timely refilling of releasable calcium (the importance of NSR→JSR diffusion in alternans was first proposed by Kihara and Morgan (1991)). It is consistent with research suggesting SR reuptake to be a key driver of SR release recovery (Ramay et al., 2011; Szentesi et al., 2004), as improved reuptake translates into higher NSR loading and thus higher concentration gradient between NSR and JSR. This then allows faster JSR refilling and recovery of releasable pool of calcium. Alternans due to SR cycling

refractoriness bears similarities with the two major explanations (release-reuptake mismatch and RyR refractoriness), but is distinct at the same time, as discussed below.

Similarly to the hypothesis of release-reuptake mismatch, SR calcium oscillations play an important role in alternans generation. Furthermore, improved reuptake attenuates alternans in both models. On the other hand, the release-reuptake hypothesis does not include any form of SR release refractoriness (Szentesi et al., 2004), shown to be crucial in alternans generation (Shkryl et al., 2012). These hypotheses offer a slightly different point of view on the experimental observation that the upregulation of SERCA pumps and thus improved reuptake ameliorates alternans (Cutler et al., 2012; Stary et al., 2016). Based on our explanation, it can be seen that even if all released calcium is reuptaken, it might not diffuse from the reuptake to the release site in time, failing to prevent alternans. At the same time, in the models without NSR→JSR diffusion, such a phenomenon would be sufficient to abolish alternans. Instead, in the more advanced model including intra-SR diffusion, increased expression of SERCA pumps may be seen as a way of increasing NSR loading. This subsequently translates into larger gradient between NSR and JSR and thus faster NSR→JSR diffusion and consequently improved JSR refilling (reducing release refractoriness), which is what actually prevents alternans in the HeRd model.

The alternans driven by SR cycling refractoriness presented here is similar to the hypothesis on RyR refractoriness driving alternans (Picht et al., 2006) in that both models rely on a form of SR refractoriness; however, the mechanism of refractoriness is different. Picht et al. observed alternans to not manifest oscillations of diastolic SR calcium in 20% of cells studied, which is hard to explain using the SR cycling refractoriness based on refilling of JSR calcium. Indeed, Ramay et al. (2011) observed that the frequency of calcium sparks may be increased (via caffeine) or decreased (tetracaine), suggesting an intrinsic form RyR refractoriness. At the same time, RyR reopening soon after the first opening was associated with considerably diminished spark amplitude and RyR sensitisation via caffeine did not affect its recovery (time constant 94 ms for both caffeine and control conditions). This suggests that local JSR refilling also plays an important role in refractoriness of total SR release. Thus, it

appears that refractoriness of SR release may be decreased both by a) reducing RyR reopening refractoriness, increasing spark frequency, b) by increasing JSR refilling and consequent increased recovery of spark amplitude. Based on available evidence, we believe that both types of refractoriness are plausible and physiologically relevant.

4.4.2 β-adrenergic stimulation attenuates alternans via accelerated SR release dynamics.

We used simulated β-adrenergic stimulation to study its impact on alternans formation, based on the β-adrenergic component of the HeRd model. Beyond the electrophysiological component which we used to study alternans origins, the model incorporates the entire β-AR signalling cascade from receptor to target phosphorylation and it can reproduce the major effects of β-AR stimulation including changes in AP morphology and duration, increased CaT amplitude and faster CaT decay (Heijman et al., 2011). The anti-alternans effect of β-AR stimulation observed here in the present study is in agreement with our results from the previous chapter and other experimental studies in both atrial and ventricular noninfarcted cardiomyocytes of a variety of species (Florea and Blatter, 2012; Hammer et al., 2015). However, given the complex downstream effects of β-AR stimulation, affecting numerous ion channels, calcium-handling proteins and signalling cascades, it is experimentally challenging to identify the exact molecular mechanisms involved. As such, we employed the perfect observability and control provided by computational modelling to provide insight into which combinations of downstream effects may abolish CaT alternans. We identified modulation of SR calcium-release properties, either directly or indirectly, as central element of the anti-alternans effects of β-AR stimulation, as discussed below.

We show the key role of the modulation of SR calcium-release properties in the inhibitory effects of β-AR stimulation on CaT alternans. In particular, we demonstrate how modulation of SR release dynamics and/or amount released may attenuate alternans.

The modulation of the amount of calcium released via RyR inhibited CaT alternans by either lowering the release, which reduces JSR emptying and prevents the formation of large-enough SR release so that JSR may not be refilled, or by significantly increasing

SR calcium release. In eight specific combinations of phosphorylation effects, the SR calcium release was strong enough to release the entire contents of the JSR, leading to an abrupt drop in SR release to zero. This type of release acts against alternans by flattening the steep load-release relationship (to linear all-in all-out) and by the large-magnitude release translating into potent reuptake. Given the high reuptake and subsequent high NSR loading, the JSR refilling is rapid, but with the total release limited by JSR contents, the high refilling and loading does not translate into further increases in release that could drive alternans, as there is no more calcium to be released. This phenomenon of complete JSR emptying and consequently abruptly terminated SR release has recently been observed in a study using in vivo human data and computational modelling to investigate the formation of so-called eye-type alternans (alternans that opens as the pacing frequency increases, then disappearing with further increase in frequency) (Zhou et al., 2016). There, this calcium-release phenotype was detected in a subpopulation of virtual cardiomyocytes with upregulated I_{CaL}, where it occurred in the closed phase of eye-type alternans at high frequencies. Thus, this mechanism could be relevant for explaining why alternans may disappear as the pacing frequency is increased, although more research is needed in showing that complete functional JSR depletion may occur. The current evidence suggests that the depletion is only 60-80% at most (Shannon et al., 2000; Bassani et al., 1995), even during alternans (Shkryl et al., 2012), however, it is possible that the cells studied in these works were of the type that would not manifest the eye-type alternans in the first place. Alternatively, it is possible that caffeine used to measure fractional emptying experimentally allows larger JSR release than would be possible with a physiological stimulus, leaving the option of "practically empty" JSR, even though further emptying is achievable with caffeine intervention.

The exact pathways and phosphorylation sites mediating β-AR stimulation-dependent modulation of RyR dynamics remain controversial (Dobrev and Wehrens, 2014). However, despite the lack of understanding of the exact mechanism, β-AR stimulation appears to sensitize RyR gating, producing faster and shorter calcium-induced calcium release transients during systole (Song et al., 2001; Zhou et al., 2009; Ginsburg and Bers, 2004). Our model of RyR activation by β-AR stimulation replicates these key

macroscopic features of SR calcium release under β-AR stimulation. We were able to link the accelerated RyR opening to alternans attenuation via improved SR reuptake and thus higher NSR loading and faster JSR refilling. Of note, this mechanism can be independent from changes in RyR refractoriness previously reported to modulate CaT alternans (Picht et al., 2006). However, the earlier-peak and earlier-terminated SR release associated with β-AR stimulation would presumably also provide more time for RyR channels to recover from refractoriness, making changed SR calcium release kinetics also relevant for RyR refractoriness-driven alternans. Independently on the exact mechanism of alternans, improved reuptake was observed to attenuate alternans (Cutler et al., 2012; Stary et al., 2016). Given that we've shown that accelerated calcium release dynamics under β-ARS selectively improve reuptake, we believe our results are generally applicable and are not tied to a single alternans mechanism.

To ensure that the observed effects did not solely apply to the particular formulation of SR calcium handling in the canine ventricular cardiomyocyte model, we incorporated the effects of β-AR stimulation on SR calcium release in the O'Hara-Rudy model of the human ventricular cardiomyocyte (O'Hara et al., 2011), similarly observing the attenuation of alternans. Furthermore, these effects are consistent with experimental data showing that caffeine-induced sensitization of RyR reduces CaT alternans in rabbit hearts (Wang et al., 2014), although this may be simply a consequence of SR depletion due to large leak.

Given that with all effects of β-AR stimulation in place, the amount of calcium released (indirect alternans modulation) would predict large amplitude alternans, while there was no alternans present, we find the altered dynamics to be the key anti-alternans factor involved in β-AR stimulation, rather than modulation of total SR release.

4.4.3 Slow SR release dynamics increase vulnerability to alternans

In the previous section, we discussed how accelerated SR release dynamics attenuate alternans. At the same time, however, the presented analysis suggests that prolongation of J_{rel} is likely to promote alternans, which is the case with the BZ cell model in

this article. This observation provides interesting links to cardiac diseases associated with alternans vulnerability, such as heart failure (Kodama et al., 2004), hypertrophic cardiomyopathy (Cannon et al., 1986), or myocardial infarction (Gardner et al., 2015). To discuss J_{rel} dynamics changes in these diseases, we rely on the experimentally observable calcium sparks, microscopic releases from JSR, the sum of which constitutes J_{rel} (Collier et al., 2000). In heart failure, longer time-to-peak and slower decay of calcium sparks, together with reduced amplitude (Lindner et al., 2002) corresponds precisely to the phenotype of longer release with reduced amplitude, which is expected to be vulnerable to alternans according to our model. In the other diseases, an indirect link may be established via the activity of CaMKII, which increases the duration of calcium sparks, prolonging the release (Maier et al., 2003; Guo et al., 2006). At the same time, activity of CaMKII is increased in hypertrophy and heart failure (Anderson et al., 2011), as well as post-infarction border zone (Hund et al., 2008), which is a region vulnerable to alternans (Gardner et al., 2015). Therefore, we can conclude that the prolongation of SR release might be contributing to alternans vulnerability in a wide range of cardiac diseases.

4.4.4 Alternans and arrhythmia in a fibre model

Ultimately, using a computational model of a fibre comprising canine ventricular myocytes with a BZ segment, we show that both APD prolongation and shortening during calcium-driven repolarisation alternans may be proarrhythmic, although for different reasons. First, we validated the standing hypothesis that spatially heterogeneous alternans promotes conduction block after prolonged APD, which can then induce reentry (Wilson and Rosenbaum, 2007). Similarly to our experimental results, simulated β-adrenergic stimulation abolished alternans in the fibre, removing the increased risk of conduction block. Second, we propose a novel contribution of alternans to arrhythmogenesis via an increase in the risk of propagation of pathological spontaneous ventricular depolarisations, such as PVCs triggered by discharges of Purkinje fibres (Bogun et al., 2008; Szumowski et al., 2004). Using the fibre model, we demonstrate how alternans extends the window of vulnerability to PVCs. An interesting feature of this proarrhythmic aspect of alternans is that it would be present during spatially

concordant alternans, which has been considered largely benign compared to spatially discordant alternans (Wilson and Rosenbaum, 2007).

4.5 Limitations

We employed detailed pool models of the canine and human ventricular cardiomyocyte to study the effects of β-AR stimulation on alternans. However, subcellular cardiomyocyte calcium handling is spatially heterogeneous and subject to strong local positive feed-back systems. Previous work has shown that stochastic channel gating and local calcium handling produce complex temporal repolarisation variability (Heijman et al., 2013; Pueyo et al., 2011, 2016) and these factors may similarly modulate the susceptibility to CaT alternans (Qu et al., 2016; Weiss et al., 2006). Of note, BZ cardiomyocytes undergo pronounced structural remodelling, which may further modulate subcellular calcium handling and alternans formation. Indeed, simulated t-tubule disruption was shown to alter the SR load-release relationship and synchronization of sparks, thereby promoting alternans (Nivala et al., 2015). Here, we investigated the effects of β-AR stimulation at steady-state. Hammer et al. (2015) identified a transient period during β-AR stimulation in which alternans was spatially discordant. Modelling studies have shown that differences in the phosphorylation rate of individual β-AR targets may indeed result in transient periods of repolarisation alternans (Xie et al., 2014), although calcium handling was not investigated. Finally, recent tissue-level models investigated spatial aspects of repolarisation alternans in heart failure and atrial fibrillation (Bayer et al., 2016; Chang et al., 2014). Integration of the detailed β-AR signalling pathway employed here in single-cell and strand simulations into these tissue models and simulation over the time-frames required for β-AR stimulation currently requires a prohibitive amount of computational resources, but, in the future, may enable a more detailed analysis of the effects of spatially heterogeneous sympathetic innervation on arrhythmogenesis.

4.6 Conclusions

We created a model of canine ventricular myocyte, which allows simulation of the infarct border zone phenotype and β-AR stimulation at the same time. We observed that the infarct border zone cells are more susceptible to the development of repolarisation alternans than the normal zone cells, in agreement with our experimental data from chapter 3. Simulated β-AR stimulation abolishes alternans in the model, similarly to our experiments[1]; this effect was mediated predominantly through direct modulation of RyR properties. Generalising the modulation of RyR gating, we showed that high-amplitude SR calcium release of short duration attenuates alternans, while conversely, low-amplitude SR calcium release of long duration promotes it, potentially explaining alternans vulnerability of failing hearts or hearts after myocardial infarction, which manifest a prolonged calcium release. Together, the modelling results support the view that border zone reinnervation may prevent the development of proarrhythmic repolarisation alternans.

[1]Interestingly, we did not "tweak" the assembled model in any way in order to replicate the experimental data, which is commonly done in modelling studies. By assembling two existing models (of β-AR and infarct border zone remodelling), we produced a model that behave consistently with the data "out-of-the-box", showing how predictive and general the computer models are becoming.

Into this house we're born
Into this world we're thrown
Like a dog without a bone
An actor out on loan
Riders on the storm

The Doors – Riders on the storm

5

Ccoffinn: a toolkit for processing high-resolution optical mapping data in cardiac cell cultures

5.1 Introduction

As discussed in the thesis introduction, section 1.6.2, CCMs are a popular model of arrhythmogenesis due to the excellent control over the preparation and simple observability. In this chapter, we describe a software tool we have developed, focussed at processing optical mapping data obtained using high-resolution imaging of CCMs. Given that infarcted *ex vivo* hearts became available throughout the doctorate, requiring a specific set of processing techniques, the software tool was ultimately not used for the bulk of the work in this thesis, although we used it in various collaborations with other researchers.

Optical mapping techniques are used to observe wave propagation in CCMs. Two types of optical mapping are used: dye-based (similar to *ex vivo* hearts) and dye-free. Typically, cell activity is recorded using fluorescence imaging, either using voltage-sensitive or calcium-sensitive dyes (Herron et al., 2012). Although these techniques directly measure key biophysical properties, they tend to suffer from two major drawbacks: phototoxicity and photobleaching, rendering longer recording of tissue nearly

impossible. An alternative approach is based on dye-free visualisation of contraction of cardiac cells, using either phase imaging (Hwang et al., 2004) or off-axis illumination (Burton et al., 2015b). While dye-free techniques do not capture membrane voltage or calcium concentration, they allow direct visualisation of wave patterns without the drawbacks associated with fluorescent imaging approaches.

All the optical mapping techniques are capable of producing a large quantity of image data, but the analysis of such data is still frequently done manually (Linnenbank et al., 2014), or largely manually (Doshi et al., 2015), which is subjective and time-consuming. An automated analysis of wave propagation in optically mapped tissue would be less prone to operator bias and has the potential to increase throughput. However, most of the existing automated methods for analysing optical mapping data focus on the properties of single cells or patches of tissue, rather than macroscopic behaviour of the tissue; examples of tasks previously researched in automated processing of optical mapping are: image segmentation, brightness drift compensation, or temporal processing of brightness traces (Laughner et al., 2012).

There are existing automated approaches to the analysis of higher-level activity (e.g., waves), but their focus seems to be mainly on the analysis of data from electrode arrays (Bayly et al., 1998; Weber et al., 2010); an example task being solved is keeping track of the number of waves in a recording, recording the events of splitting and fusion (Kay and Rogers, 2006; Rogers et al., 1997). Such electrophysiological recordings are characterised by an excellent temporal resolution of above 1 kHz, low amount of noise and relatively poor spatial resolution (e.g., 22x23 and 24x21 arrays used in (Bayly et al., 1998)). These techniques have been successfully applied to voltage sensitive dye recordings collected by specialized low resolution, high speed detectors (Laughner et al., 2012).

Recently, relatively inexpensive high resolution, low noise sCMOS sensors with moderate frame rates have been made widely available for biomedical research (Beier and Ibey, 2014). These detectors yield data sets with relatively poor temporal resolution of up to 100 Hz and signals typically have a lower signal to noise ratio, but their high spatial resolution offers several advantages. Such an increase in spatial resolution may be used to measure detailed properties of wave propagation, such as the distribution of

wavefront speeds for different parts of a wave, or to track small and short-lived wavelets (Entcheva and Bien, 2006), which cannot be measured with lower resolution devices. The golden standard for measuring conduction properties is the method by Bayly et al. (1998), developed for conduction velocity estimation in electrophysiological recordings, also used in the toolkit Rhythm (Laughner et al., 2012). However, in our experience, the method is not ideally suited for processing high-resolution, heterogeneously conducting tissue; a discussion of its shortcomings and a comparison with the methods developed by us can be found in the Supplementary materials, section S7.

Because of the lack of suitable software for analysis of the behaviour of waves in high spatial resolution data sets, particularly for recordings where the activation is not a continuous pattern (such as obtained using conventional calcium imaging), but a discrete one, we designed the toolkit Ccoffinn (Cardiomyocyte Cultures Optically-mapped: Fast Feature extractIoN and trackiNg) presented in this text; the code (with user guide and sample data) is available from https://ccoffinn.dpag.ox.ac.uk/. The approach is based on the segmentation of single cells or groups of neighbouring cells, using the information of their activity to construct a representation of waves and track their movement. After these steps, features are extracted, describing the quantitative properties of the observed waves, such as wavefront speed, wavefront smoothness (or lack of), or several measures of order in the recorded activity. The presented methods are validated using synthetic data and used as a proof-of-concept to demonstrate the difference in conduction properties of myocyte cultures and a co-cultures of myocytes and cardiac neurons. The whole process of segmentation, tracking, and feature extraction, is implemented mainly in Matlab and it is relatively high-throughput, allowing for processing of hundreds of datasets per day on a PC. While the software was designed for data sets obtained using a dye-free imaging approach, we demonstrate that it can be also directly applied to data sets collected using fluorescence techniques with continuous pattern of activation.

5.2 Materials and Methods

This section briefly sketches the functionality of Ccoffinn, describing the process of wave segmentation, tracking, and subsequent feature extraction, as well as characterisation

of the datasets used. An overview of parameters of the algorithms is given in section C.1.

5.2.1 Wave segmentation and tracking

The main aim of the wave segmentation is to estimate which parts of tissue are firing in a synchronised manner in each frame of a source video. In addition to simple wave segmentation, we also propose a method for detection of a wavefront (the part of a wave that advances forward). Using the methods for segmenting waves, we can then track movement of wavefronts and extract features describing the waves. An example output of Ccoffinn for both dye-free and calcium imaging is shown in Figure 5.1. Below is a more detailed description of the algorithms used to get from a source video to extracted features: segmenting spatial blobs manifesting activity (section 5.2.1.1), finding times of activity of these blobs (section 5.2.1.2), segmenting waves in the data (section 5.2.1.3), and tracking wavefronts (section 5.2.1.4) .

5.2.1.1 Blob segmentation

The aim of this step is to estimate locations of pixel clusters that are activated at the same time (given available temporal resolution). This can be single cells, or clusters of cells, depending on the spatial resolution used. Using the off-axis illumination dye-free imaging, active cells or groups of cells manifest as bright blobs; thus, the segmentation of the cell culture is reduced to blob detection. The segmentation is greatly simplified as the blobs in monolayers do not change their location throughout the recording. Therefore, we can average all the frames of the video, obtaining an image with an excellent signal-to-noise ratio, containing all the blobs that were active. The averaged image is then segmented using the 4-connected version of SeNeCA algorithm (Tomek et al., 2013) chosen for its computational simplicity and its ability to cope with data with uneven background brightness, which is a common feature in our datasets. The algorithm uses three parameters, *hlt*, *llt*, and *cws* standing for higher light threshold, lower light threshold, and contrast window size respectively. It first identifies points that are at least *hlt* times brighter than the mean of their surroundings (a *cws*-by-*cws* pixels square centered at the given point). It then runs a wave (in a fashion similar to

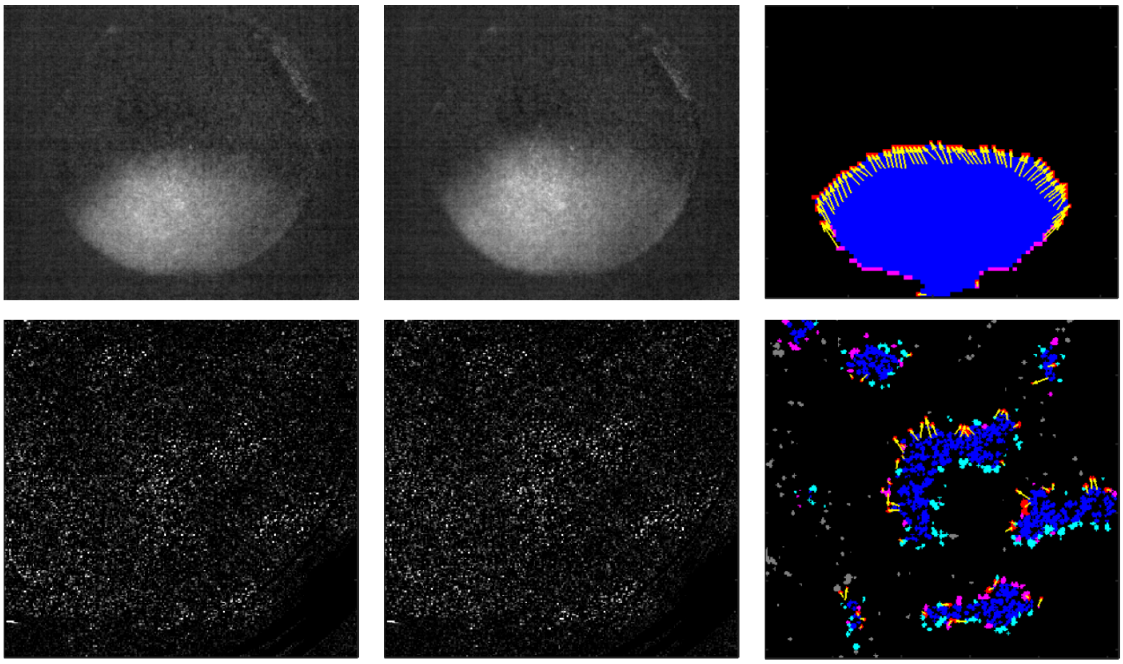


Figure 5.1: A sample output of wave segmentation and tracking. Each row contains two consecutive frames of a recording and then segmentation and annotation by Ccoffinn in the third column. In the first row is a straight wave imaged using a calcium dye at 200 fps. The second row is a case of dye-free imaged wavelets at 50 fps with spurious activity (which is the most difficult type of activity to process). The colours in the images encode the role of blobs within the waves. Blue represents area inside waves. In cyan are borders of waves which are not in the upstroke phase. In magenta are wavefront blobs: borders blobs in the upstroke phase. In red are wavefront blobs that were not wavefront in the previous frame ("became-wavefront"). In yellow are tracking arrows, linking border blobs from the first shown frame to became-wavefront in the second shown frame.

watershed techniques) that stops spreading at points that are less bright than *llt* times than their surroundings. When a wave from a single seed stops running, the resulting shape covered by the wave represents a single blob of increased brightness.

For cases of data when the imaged tissue does not manifest clear blobs (e.g., macroscopic calcium imaging), an alternative segmentation method based on filtered binning is included in Ccoffinn. Using this approach, a frame of the video is binned into squares with a chosen side length (parameter $binningSize$, see Section S3). Using the whole source video, the signal-to-noise ratio (SNR) is measured for each of brightness traces of the squares using Matlab `snr` function. Optionally, the squares with SNR smaller than a given threshold (parameter $minSNR$) are discarded. The remaining squares are then considered to be segmented blobs in a similar manner as if segmented

using the default approach.

5.2.1.2 Determining times of blob activity

Once the blobs have been segmented, the next task is to determine which blobs are active at which frame of the recording. Simple thresholding of intensities performed poorly on our data, given the wide range of brightness and/or signal-to-noise ratio of blob traces. We did not want to use shape-specific methods (such as template matching) as our aim was to keep the method flexible with respect to different imaging modalities and species-specific action potential morphologies. Methods based on the derivative of the measured intensity, which are often used as surrogates for the rate of change of membrane voltage (Laughner et al., 2012), cannot be used solely, as it only provides the time of the upstroke and not information, such as action potential duration. We designed a simple spike-mining algorithm that uses derivative of intensity to detect spikes as events, then using temporal surroundings of the detected event to extract the start and end of the particular spike. The pseudocode summarising the spike-mining process is given in Pseudocode 1 with further details below.

First, $diffThreshold$ is computed as $activityThreshold/frameRate$, which scales the $activityThreshold$ by an element proportional to the duration between consecutive frames, dt. When we later compare discrete derivative of intensity (dV) to a threshold, this scaling makes sure we are comparing dV/dt to an element proportional to a fixed-value $activityThreshold$, which makes the threshold invariant to sampling frequency used.

Then, a list of pixels belonging to each blob is extracted from the segmentation mask in `getCP`. In the second step (`getBI`), the average brightness of a blob's pixels is measured for all the blobs in all frames and stored in the matrix *bI*, so that:

$$bI(i,j) = \frac{\sum_{\forall k} b(B_k^i(j))}{||B^i||} \tag{5.1}$$

where B^i is the list of pixels belonging to the i-th segmented blob and $b(B_k^i(j))$ is the brightness of the k-th pixel belonging to the i-th blob in frame j. $||B^i||$ is the number of pixels belonging to the i-th blob.

Pseudocode 1 The algorithm for determining which blobs are active in which frames.

```
function blobActivity = getActivity(
          frames, {Sequence of recorded frames}
          mask {Result of blob segmentation}
          smoothingParameter {Kernel width for averaging filter}
          frameRate {Frame rate of the frame sequence}
          activityThreshold {Threshold for finding spike times}
          apdN {Level of APD-N%, on scale 0-1}
          minSpike, maxSpike {Limits of spike duration}
          isDoubleHump {1 if additional filtering is to be applied}
            )
begin

diffThreshold = activityThreshold / frameRate;
{Get pixels occupied by each blob.}
blobPositions = getCP(mask);
{Getting and filtering intensity traces}
bI = getBI(frames, blobPositions); {Blob intensities}
bIfilt = filterBI(bI, frameRate, isDoubleHump);
[upstrokeTimes, zeroTimes] = processDVDT(bIfilt, frameRate,
                                         diffThreshold);
blobActivity = findSpikes(bIfilt, upstrokeTimes, zeroTimes,
                          minSpike, maxSpike, frameRate);
end;
```

In `filterBI`, the intensity of each blob is first scaled to the 0–1 range and its baseline is subtracted (the baseline is estimated as the intensity after median filtering with the filter size representing 2s duration, thus with the filter size depending on the frame rate, with symmetric treatment at the edges of the trace). Then, the intensity is smoothed using a median filter with filter size of *smoothingParameter*, yielding *bIfilt*. Median filtering has the advantage that it does not change the time of the action potential upstroke, unlike filters based on averaging. If *isDoubleHump* is true, zero-phase averaging of the same filter width is further applied to connect the two humps representing an action potential. Traces with two humps per action potential are commonly seen in temporally filtered traces from dye-free imaging experiments, since both excitation and contraction generate an increase in intensity. The added averaging step helps to connect the two humps so that they are segmented as a single spike for the purposes of activation detection.

In `processDVDT`, times of maximum *dV*/*dt* are determined first (*dV* stands for intensity in general, which traditionally represents voltage). For each blob, *dIS* is defined so that *dIS*[1] = 0 and *dIS*[i] = *bIfilt*[i] - *bIfilt*[i-1]. The variable *dIS* is then thresholded using *diffThreshold* and within each block above threshold, the maximum value of *dIS* is found and saved in *upstrokeTimes*. Furthermore, all times when *dIS* is zero or crosses zero are saved in *zeroTimes*.

Ultimately, the times of activity of each blob are determined in `findSpikes`. For each blob and time of its upstroke t_u, let us consider the following variables:

- $tBaseline_{prev}$: The last element of $zeroTimes$ smaller than t_u. This gives a time when the blob is likely to be repolarised before the currently processed action potential.
- $tBaseline_{peak}$. The first element of $zeroTimes$ that is larger than t_u. This is the time of maximum intensity of the given action potential.
- $tBaseline_{2after}$. The second element of $zeroTimes$ that is larger than t_u. This gives the time when the blob is likely to be repolarised after the current action potential.
- $intensity_{prev}$ = $bIfilt[intensity_{prev}]$
- $intensity_{peak}$ = $bIfilt[intensity_{peak}]$
- $intensity_{after2}$ = $bIfilt[intensity_{after2}]$
- $baseline = \frac{intensity_{after}+intensity_{before}}{2}$

Then, we define a threshold for the given spike as follows:

$$spikeThreshold = baseline + (1 - apdN)(intensity_{peak} - baseline)$$

The particular blob is then considered active in the interval of frames represented by the segment of $bIfilt > spikeThreshold$ which contains frame t_u (note that this happens for each upstroke detected in the particular blob and the times of activity are

combined, rather than overwriting one another). Also, if the duration of the interval in ms (obtained using the number of frames taken and *frameRate*) does not fit within *minAPD* and *maxAPD*, the interval is discarded as an artifact.

5.2.1.3 Wave segmentation

Here, we aim to detect waves in each frame. Informally, a wave is defined as a "sufficiently large group of active blobs which are sufficiently dense". Our approach works frame-by-frame and in each frame, it takes all the blobs active in the particular frame, considers those in areas of dense-enough activation, and divides them into groups using the following recursive criterion: Blobs a and b belong to the same wave $\Leftrightarrow$ a and b are close enough or if there exist blobs c and d so that a is close enough to c, b is close enough to d and c and d belong to the same wave (The case when $a = c$ or $b = d$ is allowed.). The blobs are then further segmented according to their "role": blobs within a wave, blobs at the border of the wave, and the blobs that are at the border and are furthermore wavefront blobs (i.e., the wave is propagating across them, as opposed to, e.g., the border blobs that are at the tail of the wave and are ceasing to be active, rather than becoming active).

In greater detail, the first step of wave segmentation is to split blobs active in a particular frame to separate waves. Then, each wave is divided into border blobs ($\mathcal{B}$ blobs) and inside blobs ($\mathcal{I}$ blobs). The $\mathcal{B}$ blobs are labelled as wavefront blobs ($\mathcal{W}$ blobs) if they are in the phase of an action potential when voltage rises, and the subset of these that were not wavefront blobs in the previous frame are labelled new-wavefront blobs ($\mathcal{NW}$ blobs). The whole process is sketched in Pseudocode 2; described below in depth for a single frame:

Using the output of `getActiveBlobs`, we first extract the locations of blobs that are active in the given frame. The function `filterActiveBlobs` filters the active blobs according to their centroids to retain as active only the ones that have at least *minDensity* neighbours within *distanceThreshold* pixels, while the rest are rejected (This helps to remove spurious action potentials and helps the later tracking steps focus on the propagation of organised activity.).

Pseudocode 2 The algorithm for segmenting blobs active in a given frame into waves. The blobs are also labelled according to their position in their respective wave.

```
procedure waveSegmentation(
          frames, {Sequence of recorded frames}
          frameRate, {Rate of acquiring frames}
          mask, {a matrix with the same size as a frame,
                  with 1 where blobs are, 0 elsewhere}
          blobActivities, {output of getActivity}
          bISmoothed, {as computed within getActivity}
          minDensity, {Minimum density of blobs}
          distanceThreshold) {Minimum allowed distance of waves}
begin
[centroids, dist] = getInfo(mask) {Get centroids and distances

for frame in frames do
begin
  {Part a) Segmenting blobs into waves}
  activeBlobs = getActiveBlobs(frame, blobActivities);
  activeBlobsFiltered = filterActiveBlobs(centroids[activeBlobs],
                                distanceThreshold, minDensity);
  V = centroids[activeBlobs];
  E = getEdges(activeBlobsFiltered, distanceThreshold);
  waves = getConnectedComponents(V,E, dist);

  {Part b) Determining which active blobs are are border blobs
   and which are inside blobs}
  waveMask = cleanMask(mask, waves);
  wH = getWrapperHull(waves, waveMask, distanceThreshold);
  [insideBlobs, borderBlobs] = splitIB(activeBlobs, wH);

  {Part c) Further segmenting border blobs}
  [wfBlobs, nonwfBlobs] = splitWavefront(borderBlobs, frameRate,
                                blobBrightnessBS);
end;
end;
```

Then, a graph *G=(V,E)* is created. The vertices *V* are the centroids of active blobs in this frame. In `getEdges`, near blobs are linked with an edge: $\forall v_i, v_j \in V : (v_i, v_j) \in E \Leftrightarrow d(v_i, v_j) <= \textit{distanceThreshold}$, where *d* is Euclidean distance and *distanceThreshold* a parameter. The graph *G* is then decomposed into connected components which represent separate waves.

The next step is to determine which blobs are at the border of the waves. To do this, a *wave mask* is created (in `cleanMask`):

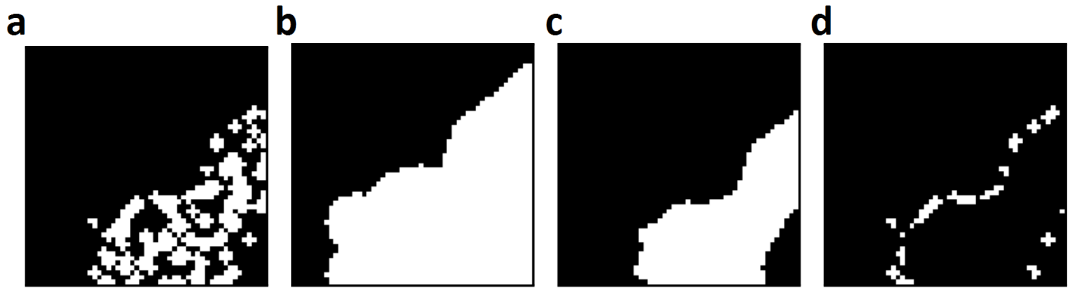


Figure 5.2: Four stages of determining the border blobs. In (a), a part of the binary mask of blobs active in a given wave is shown (white codes for active blobs), with the result of its morphological dilation in (b). The wrapper hull, morphological erosion of (b) is shown in (c). Ultimately, (d) shows the pixels that were 1 in (a), but not in (c): these represent the blobs at the border of the given wave.

$$wave\ mask(i,j) = \begin{cases} 1, & \text{If } \exists k \text{ such that } (i,j) \in P_k \\ 0, & \text{otherwise} \end{cases} \tag{5.2}$$

where P_k is the k-th blob active in the current frame.

Then, we compute a *wrapper hull* as a binary mask obtained using the following steps, illustrated in Figure 5.2. The name 'wrapper hull' is used due to similarities with a a convex hull, However, since the waves are not always convex objects, a convex hull would not work sufficiently well in this application.

1. Morphologically dilate the wave mask with a circular structural element of radius $\lfloor \frac{distanceThreshold-1}{2} \rfloor$. Note that due to the waves being at least $distanceThreshold$ apart by their definition, this operation cannot merge separate waves into a single object.

2. Morphologically erode the wave mask with a circular structural element of radius $\lfloor \frac{distanceThreshold-1}{2} \rfloor$+2.

To obtain $\mathcal{B}$ blobs (in `splitIB`), the wave mask is taken and all 1s in it that are also 1s in the wrapper hull are set to 0. Only the blobs that were not fully removed from the wave mask are then labelled as $\mathcal{B}$ blobs: their existence is a consequence of the morphological erosion being performed with a slightly larger structural element than the dilation.

Ultimately (`splitWavefront`), the $\mathcal{B}$ blobs are further separated according to the slope of *cISmoothed* at the given frame; the slope is estimated as the difference between consecutive elements. The border blobs with positive slope at the given frame (i.e., becoming activated) are labelled as $\mathcal{W}$ blobs; the rest of the blobs stays labelled as $\mathcal{B}$ blobs.

5.2.1.4 Wavefront tracking

After the blobs are segmented into various types according to their position in waves, the next step is to track the movement of the wavefronts throughout the recording. The tracking information may be then used to estimate wavefront-related features of interest. Unlike in traditional tracking of blobs, the blobs are stationary in our data and only the pattern of their activation is tracked. This means that the number of tracked objects (wavefront blobs) is highly variable throughout the recording and waves tend to disappear completely, unless they are reentrant.

For wavefront tracking, Ccoffinn uses a novel algorithm based on solving a minimum-cost bipartite matching problem to link wavefront blobs of a wave with the border blobs of the same wave in the previous frame. This approach is optimal in the total distance between the linked cells and is sufficiently fast for recordings with less than ten thousand segmented blobs. The detailed explanation of the algorithm is given in the section S1.3.

Alternatively, we have implemented the method of Bayly et al. (1998), which may be used for smoothly conducting recordings.

The wavefront tracking is performed in a hierarchical way. First, separate waves (connected components of active blobs) in frame *f* are linked to separate waves in frame *f-1*. For each wave w_i in frame *f*, a wave w_j in frame *f-1* is chosen so that the number of active blobs that are present both in w_i and w_j is the maximum possible. If the size of the largest found intersection is 0, no link is formed. These steps ensure that only blobs belonging to the same wave are tracked.

When the high-level links (w_i, w_j) are formed between waves, $\mathcal{W}$ blobs in w_i and $\mathcal{B}$ blobs in w_j are then tracked as described below. An illustration of the tracking output of our software is given in Figure 5.3a.

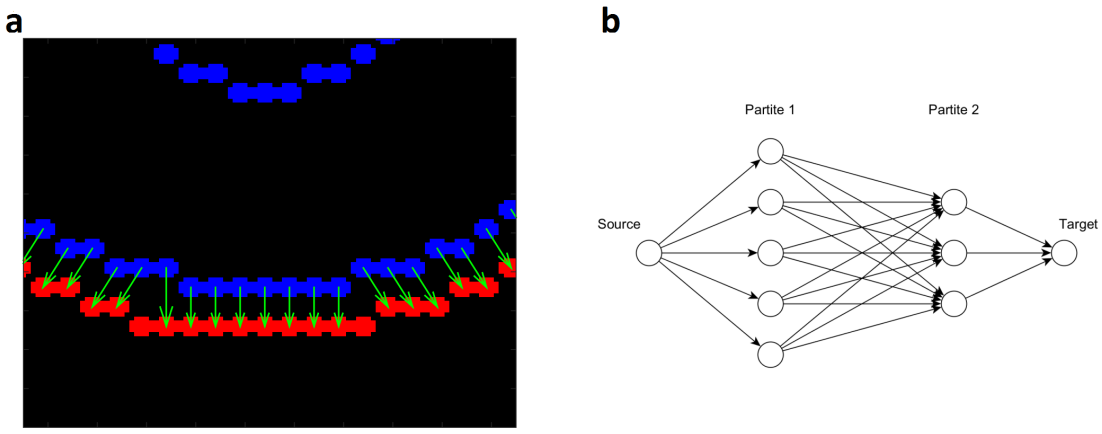


Figure 5.3: Illustration of the tracking algorithm. In a) is an example of tracking problem in a section of a spiral or target wave. In blue are the $\mathcal{B}$ blobs in the previous frame, in red are the $\mathcal{NW}$ blobs in the current frame. The resulting tracking arrows are shown in green. Due to the fact that there are more $\mathcal{NW}$ blobs than $\mathcal{B}$ blobs, two $\mathcal{NW}$ are not linked to anything via an arrow. In b) is an illustration of a graph used in computation of minimum-cost maximum-flow.

.

Two groups of tracking arrows are defined:

- The trivial group is "zero" arrows: if a $\mathcal{W}$ blob in frame f is also a $\mathcal{B}$ blob in frame $f-1$, it means that the wave is static there, not propagating further.

- The second group of tracking arrows contains the arrows representing an actual movement of a wavefront. However, rather than linking full wavefronts at frames f and *f-1*, we link all the border blobs in frame *f-1* to the $\mathcal{NW}$ blobs ($\mathcal{W}$ blobs in frame f that were not $\mathcal{W}$ in frame *f-1*) to obtain a smaller integer programming problem later. Also for increased computational performance, we disregard the $\mathcal{B}$ blobs in frame *f-1* with no $\mathcal{NW}$ blob in frame f within *maxSpeed*; these removed border blobs are too far from the wavefront to be linkable to the new wavefront. Finally, tracking arrows longer than *maxSpeed* are removed.

To obtain the nontrivial tracking arrows, we form a complete oriented bipartite graph with $G = (V_1 \cup V_2, E)$ where vertices in V_1, the first partite, represent centroids of eligible $\mathcal{B}$ blobs in frame $f-1$ and vertices in V_2 represent $\mathcal{NW}$ blobs in frame f, with $(u, v) \in E \Leftrightarrow u \in V_1, v \in V_2$. Furthermore, we set $\forall (u, v) \in E : c(u, v) = 1, a(u, v) = d(u, v)$, where c is capacity, a is cost and d is Euclidean distance of the vertices. We can

then formulate the problem of finding the best tracking arrows as finding the maximum-size matching of the two partites in G with minimum total cost. Such a matching may be found, for example, by maximising network flow. Using this approach, the source and sink vertices are added to the graph (also with unitary capacities, but zero costs) and linked to their respective partites as shown in Figure 5.3b. Then, we aim to find the cheapest flow f of size $\phi = min(|V_1|, |V_2|)$. In order to make sure that an edge is either fully used in the flow or not at all (i.e., a tracking arrow is present there or not), we formulate the task as an integer programming problem with variables $x_{(u,v)} = f(u, v)$:

$$\text{minimize:} \quad \sum_{u \in V_1, v \in V_2} x_{(u,v)} a(u, v) \tag{5.3.1}$$

$$\text{subject to:} \quad x_{(u,v)} \leq 1 \qquad \forall (u, v) \in E \tag{5.3.2}$$

$$x_{(u,v)} \geq 0 \qquad \forall (u, v) \in E \tag{5.3.3}$$

$$\sum_{(u,v) \in E} x_{(u,v)} - \sum_{(v,w) \in E} x_{(v,w)} = 0 \qquad \forall v \in V_1 \cup V_2 \tag{5.3.4}$$

$$\sum_{(source,v) \in E} x_{(source,v)} = \phi \qquad \forall v \in V_1 \tag{5.3.5}$$

$$\sum_{(v,sink) \in E} x_{(v,sink)} = \phi \qquad \forall v \in V_2 \tag{5.3.6}$$

$$x_{(u,v)} \in \mathbb{Z} \qquad \forall (u, v) \in E \tag{5.3.7}$$

After the optimum of this system is found via the Branch and Bound method, the arrows are filtered. The arrows longer than *maxSpeed* are discarded, as well as arrows that are estimated to pass outside wrapper hull in the frame containing the blobs at the end of the arrows; this heuristic aims to discard artifactory arrows between unrelated wavefronts which typically pass through zones outside waves. The exact criterion for discarding arrows is as follows: First, for the i-th arrow considered, L_i is the set of pixels under the i-th tracking arrow, determined using Bresenham's line-drawing algorithm between the arrow's start and end points. Then, let $\|wh(L_i)\|$ be the number of pixels of L_i belonging to wrapper hull and $\|L_i\|$ is the total number of pixels belonging to L_i. The i-th arrow is then discarded if $2\|wh(L_i) > L_i\|$ and $\|wh(L_i) > 2\|$. The first condition serves to discard arrows predominantly traversing outside the wrapper hull,

the second condition then protects very short arrows in slow conducting zones: due to the nature of wrapper hull and the fact that erosion is larger than dilation by two pixels, each arrow traversing less than four pixels would be discarded automatically.

The arrows passing the filtering that are not longer than *maxSpeed* are drawn in places of oriented edges $(u, v) : u \in V_1, v \in V_2$ where $x_{(u,v)} = 1$ and the coordinates of their start and end points are saved for future use in feature extraction, along with the "trivial" zero-length arrows representing static wavefronts.

Note that the integer programming formulation above is fairly restrictive, allowing only a single arrow leaving a blob and a single arrow pointing to a blob. This prevents the artifactory behaviour of nearest-neighbour tracking which tends to label several blobs with many outcoming or incoming arrows, however, the tradeoff is that the algorithm may under-track the propagation. An example of a potential problem is a target wave spreading faster in one direction than in others. In such a case, conduction velocity and potentially direction of conduction would be under-tracked; a concrete example of this problem is given in section 5.3.8.

The integer programming may be modified to accommodate for more arrows entering or leaving a blob. The parameter *maxArrows* determines the maximum allowed number of arrows leaving/entering a blob. It can be set to 'auto', which then uses the smallest integer value that is sufficient to cover all the blobs from the larger partite of the tracking graph; e.g., if movement from 4 to 10 blobs is tracked, *maxArrows*='auto' is considered 3. The exact value is computed separately for each instance of the tracking problem. The integer programming may be then modified as follows:

- The upper bound on flow in the inequality 4.2 is increased to *maxArrows* for all edges from the source to the first partite and from the second partite to the sink. Then, e.g., when flow 3 enters a vertex in the first partite, this then forces the tracking to send three distinct arrows from the given vertex (the maximum capacities of edges between the partites are still capped at 1, preventing duplicate arrows).

- ϕ is redefined from $\phi = min(|V_1|, |V_2|)$ to $\phi = min(max(|V_1|, |V_2|), maxArrows \cdot min(|V_1|, |V_2|))$, where V_1, V_2 are the first and second partite respectively. The first component of the minimum makes sure that more tracking arrows are never required than is the size of the larger partite. The second component then makes sure that more arrows than available are never requested of the tracking algorithm. It can be clearly seen that for *maxArrows* = 1, the original algorithm is obtained, while for *maxArrows* = 'auto', the number of tracking arrows is precisely the size of larger partite.

For convenience, Ccoffinn contains an implementation of the frequently used method by Bayly et al. (1998), although in general case, the above-described minimum-cost-maximum-flow approach might be preferable, as discussed in section 5.3.3. For cases when high number of blobs is present and the default approach would be too computationally demanding, Ccoffinn also contains a common and computationally cheap algorithm that can be used in place of the default one: the nearest-neighbour tracking (Konstantinova et al., 2003). There a wavefront blob in frame *f* is linked to the nearest border blob in frame time *f-1*. According to our experience, however, the method performs poorly in the case of waves that are not very simple (e.g., in case of spiral or wavelet waves).

5.2.2 Feature extraction

Rather than to observe wave segmentation and tracking in a video visually, it may be more convenient to extract several features that describe the dataset using an automated method. Furthermore, an automated approach avoids operator bias, which can occur if researchers are free to select regions manually, possibly causing false positive results (Ioannidis, 2005). Ultimately, an automated analysis is more easily scaled to high throughput applications (e.g. drug screening). For the purpose of the automated description of the recorded behaviour, we have designed several features that either simply describe the data, or may serve as a way of showing a difference between two groups of data. Most features are actually multisets, which can be further summarised, e.g. averaged over time (producing a spatial map), over space (producing

a development over time), or both (producing a single number). The features extracted are given below, followed by their precise definitions.

- conduction-oriented: wavefront speed (conduction velocity), wavefront roughness
- organisation-oriented: entropy, perimeter-to-area ratio
- spike properties: action potential duration (APD), interspike duration, firing frequency
- structural: number of blobs, sparseness of blobs (spatial)

5.2.2.1 Number of blobs

A scalar value giving the total number of blobs segmented in the dataset.

5.2.2.2 Sparseness of blobs

A multiset containing the distances from each blob to their nearest non-self neighbour, providing information on how evenly are blobs spread in the culture.

5.2.2.3 Wavefront speed

A multiset of lengths of tracking arrows found throughout the recording, including or excluding the zero-length arrows, based on the value of *useZeroArrows*. The mean value may be used as an indicator of overall conduction velocity, however, note that unlike manual operators who generally focus on the propagation of the fastest wavefronts, mean *wavefront speed* takes into account the speed of wave propagation in all directions where wavefronts are propagating. According to our observations, the 90th or 95th percentile can be used in our datasets to obtain the conduction velocity in the fastest-propagating wavefronts. Using only the longest arrow per dataset is problematic as in complex wave patterns, such as wavelets, long artefactual arrows may appear, linking two parts of the observed wave, that should not be considered representative.

The choice of *useZeroArrows* depends largely on the data available. The motivation for using zero arrows is that in slow-conducting tissue (or very quickly sampled one), a motion may not be captured between consecutive frames, even though it is present. E.g.,

a straight wave moving one layer of blobs per two frames has a speed 0.5 layer per frame, but the nonzero arrows will be only of length one; these would be captured every other frame, while in the complementary frames, only zero-length arrows are recorded. Thus, averaging all the arrow lengths, one gets the correct answer of 0.5 when considering zero-length arrows. On the other hand, the zero-length arrows may introduce artefactual drop in wavefront speed estimation in, e.g., a well conducting tissue where a dish edge is present – when the wave reaches the dish edge, it will contain zero-length arrows there for several consecutive frames, contributing low CV information to the overall pool of tracking arrows. Thus, the switch *useZeroArrows* should be set to 1 in tissues with low propagation velocity in pixels/frame, while being set to 0 in other cases.

5.2.2.4 Interspike duration

For each blob, let us consider its vector of activity (i-th row of *blobActivities*, as obtained in the Section 5.2.1.2). Then, for i-th blob, let IS_i be the multiset of lengths of 2-connected sequences of **0**s that are not leading, nor trailing, that cannot be further extended (i.e., bordering with **1**s on both sides of the interval of **0**s). The leading and trailing intervals of **0**s are excluded as they may not represent a full period between two action potentials. Then,

$$interspike\ duration = \biguplus_{i=1,\ldots,n} IS_i \tag{5.4}$$

where n is the number of blobs and $\uplus$ stands for multiset union (i.e., union with allowed repeats of elements). Ultimately, all the values are scaled by $1000/frameRate$ to convert the interspike duration in frames to milliseconds.

5.2.2.5 APD

This feature is an analogy of interspike duration, except that lengths of non-trailing and non-leading intervals of **1**s are computed. Note, that while feature is a correlate of physiological APD, it may not represent it exactly and the level of APD-N it represents may depend on the nature of the data. This is chiefly due the fact that the APD-N is estimated using the median-filtered signal and sharp peaks in the signal (as seen in

the synthetic data) are removed. Thus, estimating, for example, APD70 of the filtered signal may not be equivalent to APD70 in the original signal as the thresholds used for measuring action potential shape depend on the signals peak value.

5.2.2.6 Wavefront roughness

Wavefront roughness serves to describe the lack of smoothness in signal propagation. A tracking arrow from location u to location v in frame f is called *suitable* if there is another tracking arrow in the frame f with the origin closer than *usm* (a parameter) micrometers from u. Informally, suitable arrows are these with an arrow nearby in the same frame. For the i-th suitable arrow α, we define β_i as the set of tracking arrows in the same frame with their origin closer than *usm* to the origin of α (including α). Then, we can define:

$$wavefront\,roughness = \biguplus_{i=1,\ldots,m} \overline{S}(\varphi(\beta_i)) \tag{5.5}$$

where $\varphi(\beta_i)$ is the set of angular components of polar coordinates (in degrees) of all the arrows in β_i, $\overline{S}$ is the circular standard deviation and m is the number of suitable tracking arrows.

It is expected that when a wavefront is propagating smoothly, such as in straight waves, most of its tracking arrows will point in the same direction, contributing low values to *wavefront roughness*, while chaotic activity with many wavebreaks will display lack of local smoothness (i.e., high $\varphi(\beta)$), contributing high values of *wavefront roughness*.

5.2.2.7 Beat frequency

Beat frequency of a recording can be used to estimate the beating rate of blobs in the recording. For a single blob and its brightness trace, we define its beat frequency as the number of spikes per second. The *beat frequency* of the whole recording is then simply a multiset union of the beat frequencies of single blobs.

5.2.2.8 Entropy

This feature is a variant of the spatiotemporal entropy described previously (Jung et al., 2000), using the representation of a wave as a set of blobs, rather than a set of pixels (which seems to be the approach used by Jung). Let us construct a 3D

space S where $(x, y, f) \in S \Leftrightarrow \exists$ blob c so that (x, y) is the centroid of blob c and $blobActivitiesFiltered(c, f) = 1$ (*blobActivitiesFiltered* is obtained in Section S5.2.1.3 via `filterActiveBlobs`). Informally, a point is present in the space if it represents a centroid of an active blob in a certain frame.

We then define a distance d_S in the space S:

$$d_S((x_1, x_2, x_3), (y_1, y_2, y_3)) = \sqrt{(x_1 - y_1)^2 + (x_2 - y_2)^2 + \zeta(x_3 - y_3)^2} \tag{5.6}$$

where ζ is the mean of *Sparseness of blobs* feature. This distance function is essentially an euclidean distance with weighted distance in the z-axis (this is equivalent to an ordinary euclidean distance in a space where frames are spaced ζ pixels apart).

Let us define a graph $G'(V', E')$, where V' contains vertices representing all points in space S and $(u, v) \in E' \Leftrightarrow d_S(u, v) < distanceThreshold$. A *spatiotemporal wave* is then defined as a connected component of G' with the number of the points in the connected component giving its size.

Using notation from the work by Jung (Jung et al., 2000), spatiotemporal volume of class of size s is defined as $V_s = s \cdot n_s$, where s is the size of connected component and n_s is the number of such connected components in the data. Then, relative coverage of a size class s is $v_s = \frac{V_s}{\sum_s V_s}$. Spatiotemporal entropy is then defined as follows:

$$S = -\sum_s v_s \ln v_s \tag{5.7}$$

Even though entropy is a popular measure of order, providing a single number for the whole dataset, it has its limitations. We can observe, for example that a completely random activity of isolated blobs, yielding many connected components of size 1, has the same (zero) entropy as when there is a single large wave present in the recording. Also, a very heterogeneous wave, such as a group of wavelets, may still be a single connected object in the 3D space, depending on the exact shape of the waves and quantity of noise; this feature then becomes fairly unstable, with small changes to the recording causing large difference in entropy.

Efficient computation of entropy in our context, namely the decomposition of G' into connected components is not entirely trivial. The only difficulty in computing

the entropy is the decomposition of the graph G' into connected components due to large size of the graph itself. With hundreds of active blobs per frame and a video that is thousand frames long (which are both possible in our data), the number of edges present in the graph can be too large to fit into memory of a desktop computer (especially using memory-inefficient representations, such as adjacency matrix).

The first observation that helps is that the whole graph does not have to be represented explicitly at any time for us to obtain the decomposition into connected components. The standard DFS-based algorithm for finding connected components can be adapted to not require the whole graph. Let us recall that an edge is present between vertices in G' if the two vertices are closer than *distanceThreshold*. Thus, the step when the search expands into a vertex's neighbours (usually determined directly from the graph representation) can be modified to instead query all the other unlabelled vertices (candidate neighbours), expanding into these that are near enough to the vertex expanded. While this greatly reduces the memory complexity from $O(|V|)^2$ to $O(|V|)$, it also increases the time complexity from $O(|V|)$ to $O(|V|)^2$, making the computation impractically long.

A second improvement to the basic algorithm is restricting the search of candidate neighbours so that not all vertices are searched. We can divide the 3D spatiotemporal space occupied by the vertices of G' into cubes with side length of *distanceThreshold* and for each cube, we record the list of vertices present in it. Then, when looking for neighbours of a vertex to be expanded v, instead of testing the distance to all the vertices in the space, we test only the distance to the same cube and the 26 neighbouring ones. In a standard case of our data, 256x256 pixels and *distanceThreshold* of ca. 16, we search only at most 27 cubes instead of 4096 there are, which is a considerable time-saver. This function has been implemented in C to further improve performance and connected to the main code via MEX interface.

5.2.2.9 Perimeter-to-area ratio

In order to counteract the deficiencies of *entropy*, we have designed a different measure of the degree of order of the recorded activity. For each frame, we obtain the mask

of active blobs in the frame (after filtering out blobs in sparse regions, i.e., using *blobActivityFiltered*). Morphological closing with circular structural element and radius *distanceThreshold*/2 is performed to fill holes between blobs belonging to a same wave (but not mixing separate waves together). Then, we define the *perimeter-to-area ratio* in the i-th frame as:

$$perimeter - to - area(i) = \frac{\#sidePixels(m_i)}{\#pixels(m_i)} \tag{5.8}$$

where m_i is the processed mask of the i-th frame, $\#sidePixels(m_i)$ is the number of one-containing pixels in m_i that border with a zero ("perimeter"), and $\#pixels(m_i)$ is the total number of ones in m_i ("area").

The whole feature *perimeter-to-area ratio* is then defined as a multiset union of all the $perimeter - to - area(i)$ such that $\#pixels(m_i) > 0$.

We can clearly see that a wavelet activity will have overall high *perimeter-to-area ratio* due to large perimeter and low area, unlike, e.g., round target waves, which have large areas and small perimeters.

A slightly different approach would be to compute the surface and volume of a 3D voxel, instead of computing perimeter-to-area ratio for each frame separately. However, such approach would be then very sensitive to wave speed: an organised wave that moves very fast would have larger surface than a wave of the same type that travels more slowly due to larger number of facets between two frames. We consider this effect undesirable, as a measure of wavefront structure should not depend on propagation speed, which is why we have adopted the frame-by-frame approach instead.

A limitation of this approach is that waves entering the field of view (FOV) may have a fairly high *perimeter-to-area ratio* at the given frame, as most of the true area of the wave is not seen. However, such cases are highly unlikely to affect the feature value in a major way, as waves tend to be present in FOV for multiple frames. If this limitation affects the results severely for some unexpected reasons, the code for this feature's extraction could be modified to ignore several leading and trailing of activity in each wave when *perimeter-to-area ratio* is determined, thus discarding the frames when a wave enters or leaves the FOV altogether.

5.2.3 Data description

5.2.3.1 Cell culture data

Two types of slow-conducting cell cultures imaged using a dye-free approach were used to evaluate the effectiveness of the toolkit: a culture of ventricular myocytes from SD rat pups (n=19) and a co-culture of ventricular myocytes grown along stellate cardiac neurons of litter mates of the rats (n=16). The protocol of culturing is given in (Burton et al., 2015b). A temporal filter has been applied to the raw data, replacing f_i with $abs(f_i - f_{i-5})$, where f_i is the i-th frame. The filtered data can be interpreted as the amount of motion (contraction or relaxation) in a given pixel. A sample script is provided with Ccoffinn, showing how to apply such filtering to a dye-free dataset obtained using phase imaging.

Additionally, several datasets of calcium-imaged cell cultures (with high CV compared to the dye-free imaged cultures) were used to demonstrate the usefulness of Ccoffinn for such an imaging modality. The protocol used is described in (Ambrosi and Entcheva, 2014).

5.2.3.2 Synthetic data

While it is important to demonstrate usefulness of methodology using real data, such an evaluation is limited as the underlying signal is intrinsically unknown and the irregularity of the activity in real systems makes it complex to analyse. Therefore, in addition to evaluating our software on real data, we also performed an evaluation using synthetic datasets, where we can determine the correctness of the evaluated methodology. The main aim is to investigate the robustness of the method to sampling frequency and noise quantity in the data.

The cardiac activity was modelled using a cellular automaton (Bub et al., 2003), which allowed us to create various types of waves and to measure them at different sampling frequencies. Below are described three experiments: Syn1, Syn2, and Syn3, which aim to test different properties of the process of feature extraction. All created videos have the resolution of 255x255 pixels and include 2601 blobs (a grid of 51-by-51). Examples of frames of the synthetic data can be found in Figure 5.4 and Figure 5.6.

5.2.4 Implementation notes

The methods for segmentation and tracking of waves, as well as the feature extraction, were written in Matlab, using C code and MEX interface in performance-critical areas. Pure-Matlab alternatives to the C functions are also provided for convenience and greater platform independence. The GLPK library was used as a fast integer programming solver, connected to Matlab via GLPKMEX interface. The cellular automata used to generate the synthetic datasets is written in Java. The runtime of the segmentation and tracking depends greatly on the quantity and the pattern of activity of the blobs in the data. On the real data analysed in this report, the average number of objects segmented in a video was ≈ 4300 and the average runtime of segmentation and tracking was 0.11 seconds per frame (with the visualisation and console verbosity turned off). The computer used for the computation was a PC with a six-core processor Intel Xeon E5-1650 v3, 16GB of operating memory and a magnetic hard drive.

5.3 Results

5.3.1 Analysing behaviour of cell cultures

We have made two comparisons using the available dye-free data (more details on the data are provided in the supplementary section S4.2). First, we manually divided the recordings into organised waves (target, spiral, or straight) and disorganised (wavelet, or chaotic activity). We then compared the features extracted from organised versus disorganised waves. Second, we have compared the properties of organised waves in myocyte cultures versus organised waves in co-cultures of myocytes and neurons. In both comparisons, we used rank sum test to compare features of the groups of recordings. Furthermore, the evaluation of Ccoffinn using synthetic data is given in the section S6.

The results of comparing the recordings of organised and disorganised activity are given in Table 5.1, top. The disorganised cultures had a significantly higher *perimeter-to-area ratio* and *wavefront roughness*. This is an expected result, as these two features are mainly aimed at orderliness of propagation in tissue. The third feature aimed at this, *entropy*, has failed to discern the two classes of data, supporting the opinion

Feature	Org Median (IQ range)	Dis Median (IQ range)	p value
Number of cells	4678 (4138–5087)	4890 (4318–5573)	0.1909
Wavefront speed (mm/s)	11.3 (7.6–20.8)	5.9 (5.2–7.4)	0.0024
Interspike period (ms)	443.2 (331.8–564.3)	372.1 (341.9–466.1)	0.2673
APD (ms)	138.5 (112.1–180.4)	138.2 (103.6–150.3)	0.3286
Cell sparseness (µm)	170.2 (152.8–204.6)	192.4 (168.5–210.7)	0.3453
Wavefront roughness (°)	27.1 (23.3–30.9)	37.7 (32.7–38.9)	0.0010
Beat frequency (Hz)	0.838 (0.606–1.403)	1.173 (0.894–1.437)	0.1694
Entropy	0.322 (0.034–2.130)	0.127 (0.060–0.509)	0.7281
Perimeter-to-area	0.139 (0.093–0.162)	0.188 (0.161–0.229)	0.0022

Feature	Myo Median (IQ range)	Co Median (IQ range)	p value
Number of cells	4956 (4751–5313)	4411 (4127–4835)	0.1471
Wavefront speed (mm/s)	6.5 (5.3–9.5)	17.8 (11.1–21.5)	0.0110
Interspike period (ms)	564.3 (432.9–643.1)	366.3 (307.7–464.6)	0.0420
APD (ms)	180.4 (134.4–204.5)	133.5 (107.3–151.3)	0.0559
Cell sparseness (µm)	184.3 (159.5–204.8)	169.3 (146.1–204.4)	0.7925
Wavefront roughness (°)	29.6 (24.1–38.6)	26.6 (23.1–29.3)	0.2635
Beat frequency (Hz)	0.599 (0.516–0.929)	0.947 (0.815–1.891)	0.0559
Entropy	0.667 (0.306–2.081)	0.168 (0.003–2.179)	0.3676
Perimeter-to-area	0.152 (0.135–0.192)	0.117 (0.084–0.162)	0.2198

Table 5.1: Comparison of features between groups. Top table: **Org**=organised recordings (target, spiral, or straight wave) versus **Dis**=disorganised (wavelets) activity. Bottom table: **Co**=organised co-cultures of myocytes and neurons versus **Myo**=organised cultures of myocytes. For each feature (or mean of feature), median and interquartile range are given. The features differing significantly ($p < \alpha = 0.05$) between the respective groups, are marked by red background.

from the evaluation of synthetic data that it is not a useful feature. Wavefront speed was significantly increased in the group containing organised activity, which is an expected result as well.

The results of comparing recordings of organised activity in myocyte cultures and co-cultures of myocytes and neurons are given in Table 5.1. The most striking result is the large increase of *wavefront speed* in co-cultures, compared to myocyte cultures. At the same, the *perimeter-to-area ratio* is not significantly different between the two groups of data; thus, the difference in *wavefront speed* and *wavefront roughness* is unlikely to be caused by different morphology of waves. Also, we can observe a borderline-significantly faster beat rate in co-cultures (this trend is further bolstered by shorter

APD and interspike period, consistent with more frequent spiking).

In order to link the results using real data to the analysis of synthetic data (in the section S6), we have estimated the noise standard deviation in the real data using the method by Immerkær (Immerkær, 1996) The mean over recordings of standard deviation of the noise was 0.1063 with a standard deviation of 0.0583, suggesting that the results presented in this section should not be affected by the presence of noise too severely.

5.3.2 Evaluation of Ccoffinn using synthetic data

sectionResults: Validation using synthetic data We designed three evaluation experiments based on synthetically generated data (Syn1, Syn2, Syn3), to test various properties of Ccoffinn's functionality. In experiment Syn1, three 400 frame videos sampled at 50 fps are compared, containing a spiral wave, a planar wave, and a target wave respectively. These three types of waves are the major types of waves observed in cardiac monolayers and our aim was to confirm that they are segmented correctly.

In experiment Syn2, three different types of a wave (planar, spiral, and wavelet) are visualised at three different sampling frequencies (25, 50, and 100 fps; 200, 400, and 800 frames respectively) and we observe the effect on the values of the features extracted. The recording is generated at 100fps and then subsampled to the respective lower sampling frequencies.

In experiment Syn3, the same three types of wave are observed for 400 frames at 50 fps with three levels of Gaussian additive noise with zero mean and variances 0.02, 0.04, 0.06,..., 1 (on a scale of 0-1) and the focus is on the effect of the noise on the features extracted.

5.3.2.1 Syn1: Results

Figure 5.4 shows an output of the segmentation and tracking algorithms on three model waves. The output of the segmentation and tracking algorithms was visually assessed and found to be correct.

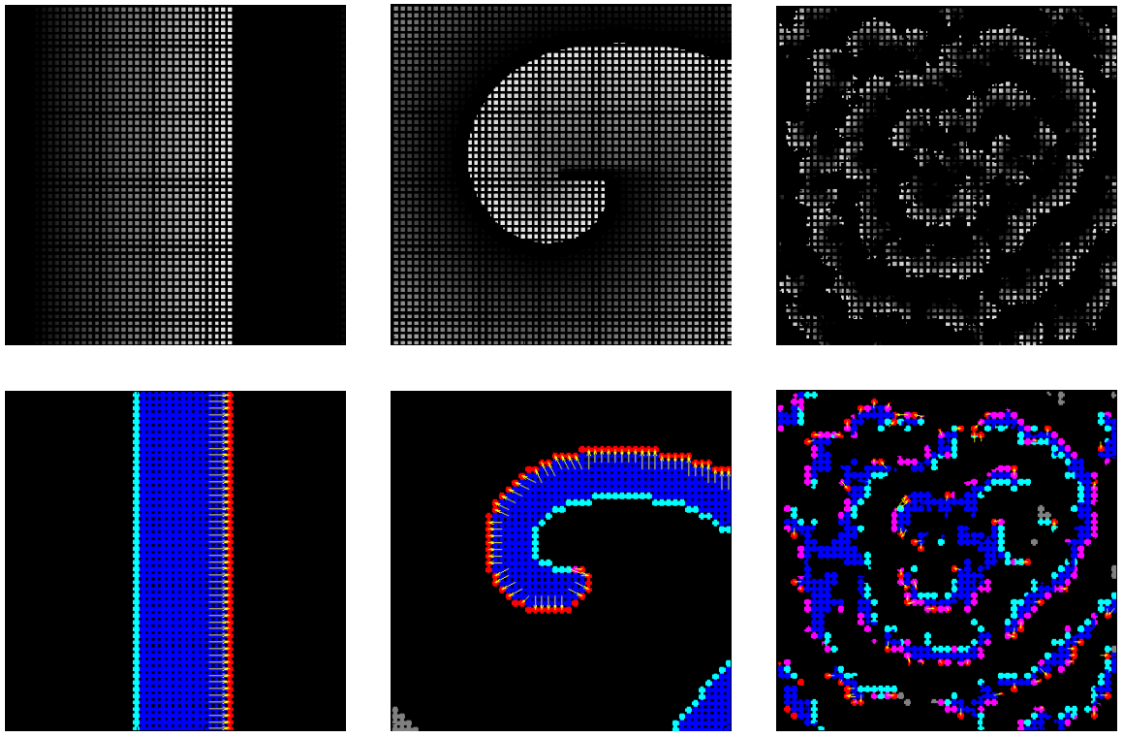


Figure 5.4: An illustration of synthetic data. Three types of synthetic waves, before (top) and after (bottom) segmentation and tracking (we note that the tracking depends on the previous frame). To the left is a straight wave, in the middle is a spiral wave, and to the right is a wavelet wave. The interpretation of colours is identical to Figure 1 in the main text.

5.3.2.2 Syn2: Results

The features extracted from the three datasets (varying by their sampling frequency) show that the sampling frequency of the video generally does not seem to drastically affect the features extracted (note that the change in *number of blobs* is minuscule, as can be judged from y-axis). However, we note that while *entropy* does not seem to be overly affected by the sampling frequency, it does not capture the complexity of waves very well. Intuitively, we would expect straight waves to be the most orderly with wavelets most disorganised. However, it is clearly not so and the straight waves have by far the largest entropy. The reason for this is that in the 3D spatiotemporal space, different iterations of a straight wave are completely separate objects of possibly slightly different size. Unlike that, spiral waves (and many wavelet activities) are merely a single connected spatiotemporal object. Thus, even though *entropy* is an elegant and theoretically well-justified method, this flaw is too serious for the feature to be practically useful and

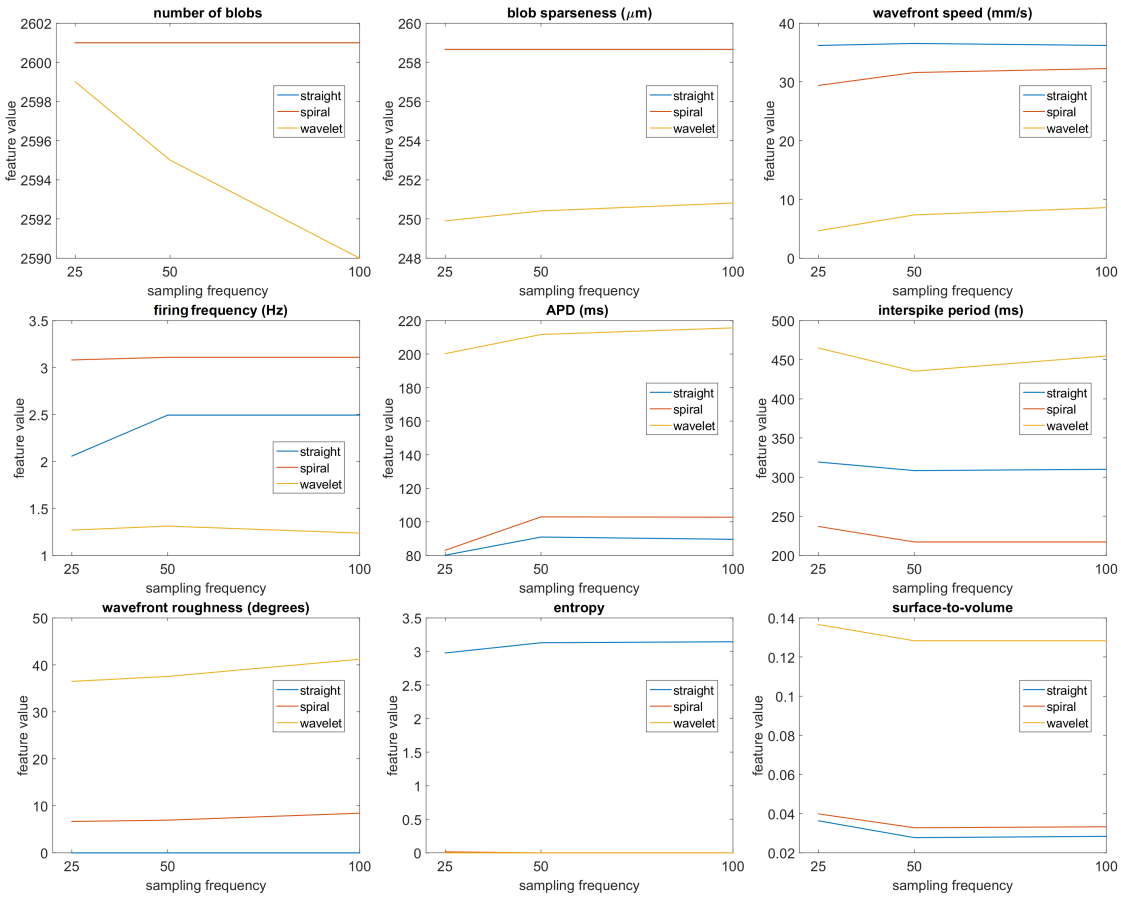


Figure 5.5: The effect of sampling frequency on values of features (or means of features in case of non-scalar features). In *number of blobs* and *blob sparseness*, spiral and straight wave have the same values for all sampling frequencies; the same holds for wavelet and spiral wave values in *entropy*. In all the waves, ground truth for *number of blobs* is 2601. For straight waves, ground truth values of *wavefront speed*, *firing frequency*, and *wavefront roughness* can be estimated; the values are 36.8 mm/s, 2.5 Hz, and 0°, respectively.

alternative methods of order estimation provided in the toolkit are recommended.

5.3.2.3 Syn3: Results

An example of data with four selected levels of additive noise are given in Figure 5.6. Figure 5.7 shows how features are affected by increasing noise. In features based on segmentation, namely *number of blobs* and *blob sparseness* (min distance to nearest neighbour), the only case with a trend effect of noise is the case of straight waves, where at high noise levels, locations of blobs are sometimes estimated incorrectly with the centroid being slightly shifted. We wondered why there is a difference between straight and spiral waves, which are both organised. Examining the data, we found

that the straight-waves pass through any given point less frequently than in the case of spiral waves (this is also manifested in the *firing frequency*) and that the process of segmenting the averaged frames of the recording thus has an input with poorer signal-to-noise ratio in the case of straight waves (relatively more frames of noise for a given pixel than in the case of spiral wave), which is why straight waves are more damaged by the noise. This reveals an important observation that if Ccoffinn was to be used for recordings with very high levels of noise and very sparse waves, the recording should be summarised in a different way than the average of input frames, as this approach is sensitive to noise (e.g., an approach based on high quantiles and/or maximum might be better in such a context, as pixels containing pure noise are unlikely to manifest as high values as pixels that contain genuine activation).

The feature *wavefront speed* tends to decrease with increasing noise level. The reason behind is the fact that overly long arrows are deleted. Considering a single arrow in a noise-free environment, when noise is added, the arrow can stay the same, shorten, or prolong; however, the prolongations are limited as too long arrows are removed. For this reason, the net effect of noise perturbation is mean arrow shortening.

In *firing frequency*, we see a decrease as the noise is added, accompanied by prolongation of both *APD* and *interspike period*. This is again due to the asymmetric filtering process: an action potential is much more likely to be shortened below the *minAPD* (or even to be completely removed by noise) than prolonged above *maxAPD*.

The *wavefront roughness* grows with noise in the organised waves, as their usually smooth wavefronts become jagged and heterogeneous, increasing the roughness of propagation. We note, however, that at all levels of noise, the three types of waves are ordered in their most natural order of smoothness of propagation. *Entropy* again fails to discern the degree of order associated with the types of waves, similarly to the result from experiment Syn2. *perimeter-to-area ratio* changes little with increasing noise and maintains the ordering of organised versus disorganised waves at all noise levels. The separation of spiral and straight waves is relatively small, but stable.

Overall, we believe that while the whole process of data analysis and feature extraction is not immune to the quantity of noise present in the data, it is at least

fairly resistant, giving good results even at high noise levels in most features (the only exception is *wavefront roughness*). Especially in the case of noise with standard deviation smaller than 0.2, most features are highly stable.

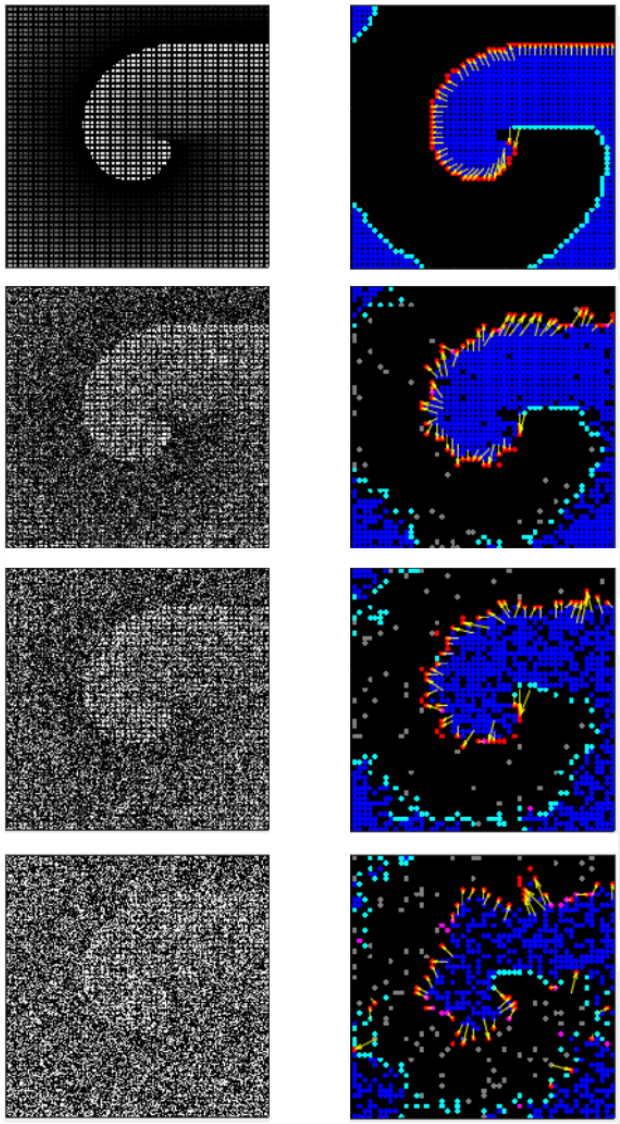


Figure 5.6: An illustration of noise in synthetic data. Shown is a spiral wave generated using a cellular automaton with four levels of additive noise (given as the standard deviation of the noise on scale 0-1): 0, 0.2, 0.4, and 1. The interpretation of colours is identical to Figure 1 in the main article.

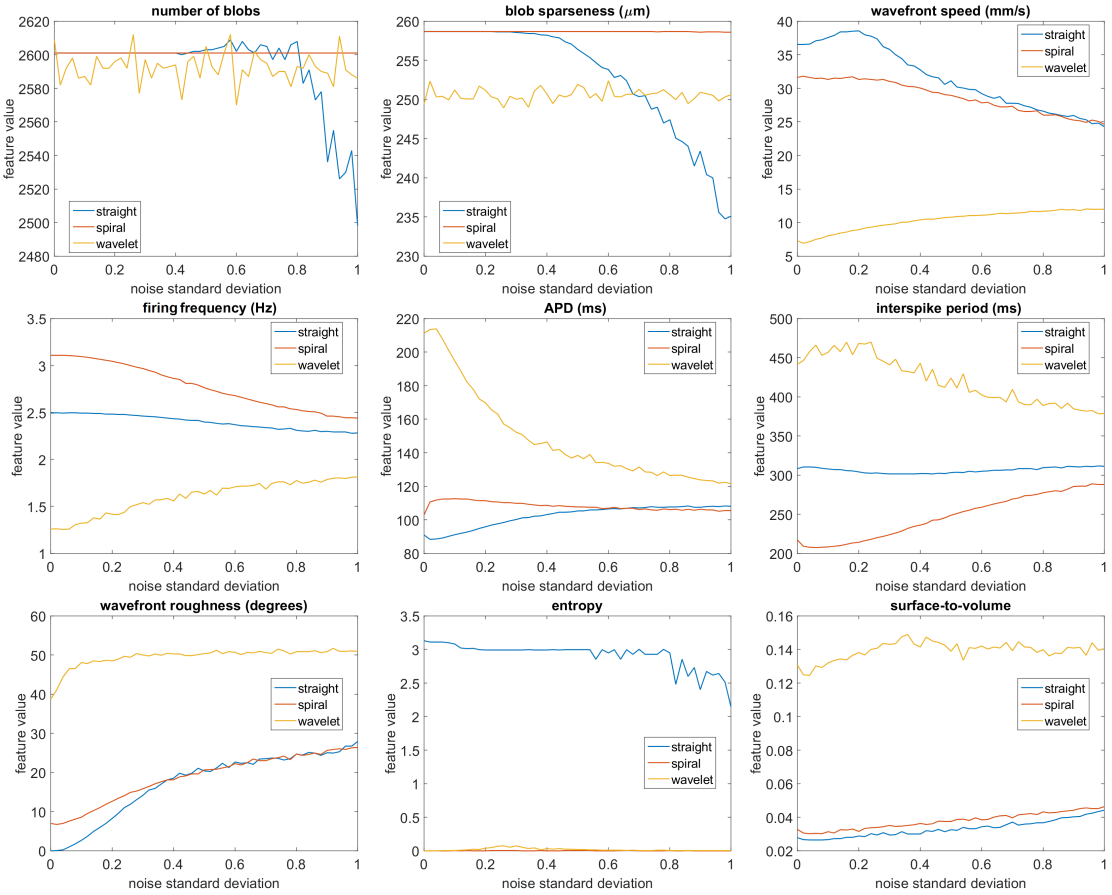


Figure 5.7: The effect of increasing noise standard deviation on values of features (or means of features in case of nonscalar features). In all the waves, ground truth for *number of blobs* is 2601. For straight waves, ground truth values of *wavefront speed*, *firing frequency*, and *wavefront roughness* can be estimated; the values are 36.8 mm/s, 2.5 Hz, and 0°, respectively.

5.3.3 Comparison of MCMF and Bayly algorithms

In this section are discussed the problems associated with the algorithm for wave tracking and conduction velocity (CV) estimation by Bayly et al. (1998) in high-resolution, heterogeneously conductive tissue, as well as discussing potential shortcomings of the MCMF algorithm which is the default approach of Ccoffinn.

Bayly's method considers each "active point" in a wave (e.g., a pixel), finds points in 3D spatiotemporal space that are closer than given thresholds in the x,y,t dimensions, and fits a quadratic surface through these using least squares criterion. Partial derivatives are then used along x,y axes to find a velocity vector for the given active point. A small problem intrinsic to this approach is the fact that the problem of surface fitting may be poorly conditioned, making an estimation of CV impossible in a given

point. This problem happened several times in most datasets available to us, however, this error did not occur frequently enough to significantly impact CV mapping or make the results uninformative.

In the relatively high-resolution data available to us, where a wave is represented by up to thousands of active objects and for a reasonably sized spatiotemporal neighbourhood, the basic algorithm is fairly slow, taking almost a minute per frame of data, making high-throughput analysis impossible. However, using Ccoffinn's framework for wave segmentation, an adjustment to the basic algorithm can be made, where for an active point (x, y, f) (in frame f), "near active points" are taken only from wavefront blobs in frames $f-1$, f, and $f+1$, closer than *maxSpeed* in the plane given by first two dimensions of the space. Using only two adjacent frames along the one in which the point (x, y, f) is used, as a quadratic surface does not have enough degrees of freedom to correctly fit all the points in a larger temporal neighbourhood.

Considering only wavefront blobs, rather than all the active blobs, the algorithm becomes much faster, even though it is still an order of magnitude slower than the minimum-cost-maximum-flow (MCMF) approach described previously. We note that this holds for the data available to us at the moment; it would most likely not scale for extremely large wavefronts of hundreds of thousands blobs, where the potential exponentiality of the integer programming used to solve the MCMF problem would overcome the high-multiplicative-constant polynomial complexity of the Bayly's algorithm. However, both algorithms would be extremely slow in such a case and an entirely new approach to tracking would have to be adopted.

The main issue associated with Bayly's algorithm is that in heterogeneously conductive tissue (such as poorly coupled cell cultures, cultures rich in fibroblasts, or intact myocardial tissue with myocardial infarction), where the heterogeneity captured by sufficiently high resolution imaging method is genuine, the surface fitting approach can consistently yield counterintuitive and incorrect results due to its dependence on smoothing. Below are several examples of wavefront topologies constructed to illustrate certain scenarios, where Bayly's algorithm fails to provide correct answer. We note that the errors demonstrated below are not not a principal flaw of Bayly's algorithm, as it

was designed for low-resolution electrophysiological data where the problems tend not to occur, but rather an illustration of the algorithm's struggles with heterogeneously conducting tissue. According to our experience, even in high-resolution data, Bayly's method performs well as long as the tissue is isotropic/homogeneously conducting. Furthermore, in section S7.5 are also discussed potential issues associated with the non-generalised and generalised MCMF algorithm used in Ccoffinn, showing how both MCMF and Bayly's method may struggle in certain context.

We visualise the tracking information using 2D plots containing points in the plane, representing the wavefront, where the colour further codes for the time slice in which the points are considered active; the warmer the colour, the later in the "recording". Estimated vectors are shown using arrows of the given direction and length. When an arrow is missing, it was either a case of a poorly conditioned problem, or the arrow was rejected as too long (longer than neighbourhood radius, which is essentially a representation of maximum conduction velocity). When a particular point is discussed, it is encircled in red and the spatial neighbourhood is shown using a dashed magenta circle (however, only points that are at most 1 frame away from the encircled point may be considered, even if they were close enough in the spatial plane). Furthermore, in selected cases, we show the points in neighbourhood in 3D with the quadratic surface fitted to them.

5.3.4 Slow band in a straight wave

Figures 5.8 and 5.9 show a case of a straight wave travelling from bottom to top (with central point of the wavefront slowing down over time, limping behind the rest of the wavefront), with three different radii of neighbourhood shown.

In the panel 5.8a are shown velocity vectors for the case when neighbourhood radius is 30. The main systematic error is present at the centre of the wave, where tracking arrows tend to aim towards the centre, rather than purely to the top of the frame. The reason is that in frames 6 and 7, only two points are present within the magenta circle, while in frame 8, three points are present; two a part of "normal" wavefront, one a part of the slowed band. The fitted surface (shown in 5.8b) passes

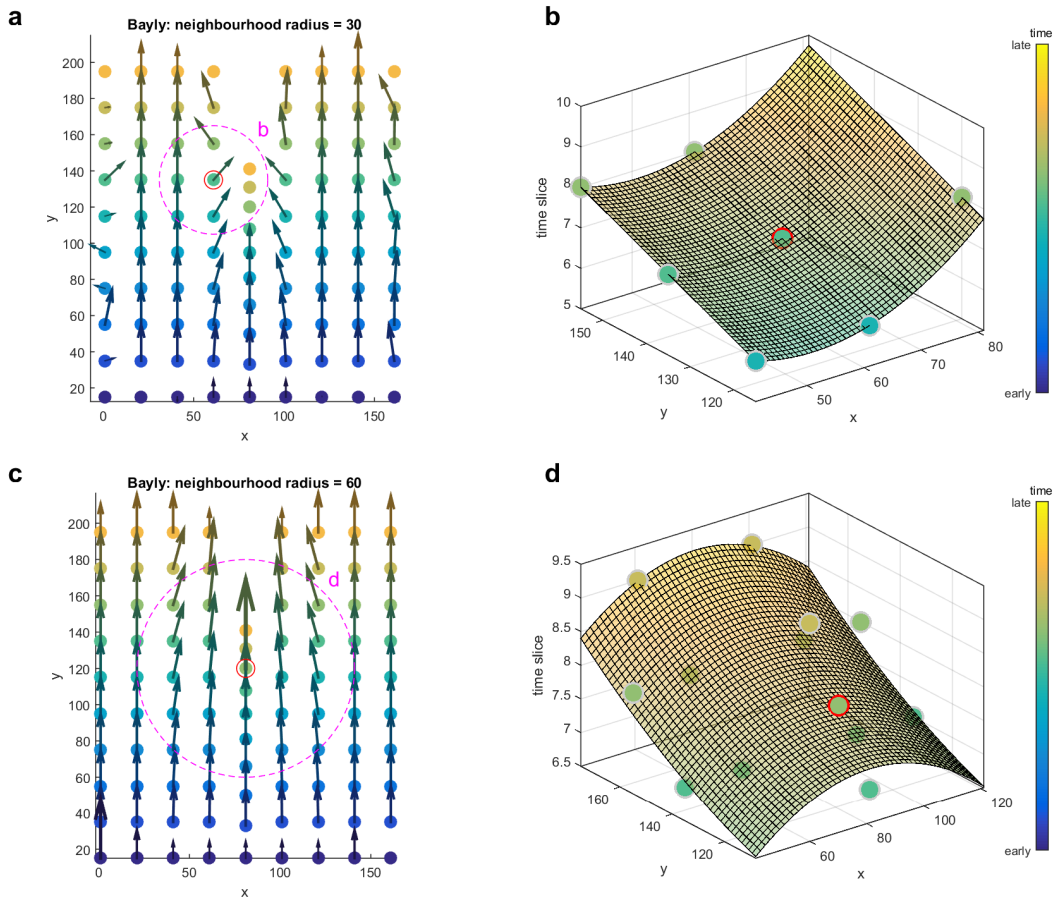


Figure 5.8: An illustration of Bayly's algorithm. In the left column are diagrams of wavefront of a straight wave travelling from bottom to top with a slowing-down segment. The colours code for time. Velocity vectors obtained using Bayly's algorithm are superimposed on the locations of "wavefront blobs". In a) is the tracking information for neighbourhood radius 30, in b) for neighbourhood radius 60. In the right column are shown quadratic surfaces fitted through the respective points and their surroundings shown in the left column.

exactly through the seven points in the neighbourhood, but is practically wrong, both in the direction, and the conduction velocity estimate. A secondary type of error is present at the edges of the frame, where the optimal fit is not unique and the fitting procedure in Matlab returns unstable results. In practical settings, these cases would be best detected automatically and discarded.

At the bottom of panel 5.8c is an identical scenario, but with neighbourhood radius of 60. The problem with unstable borders is solved at the sides (where for each point at the side, 9 points are in its neighbourhood rather than 6 in the previous case, making the optimal solution unique). However, the problem with incorrect estimation of direction in

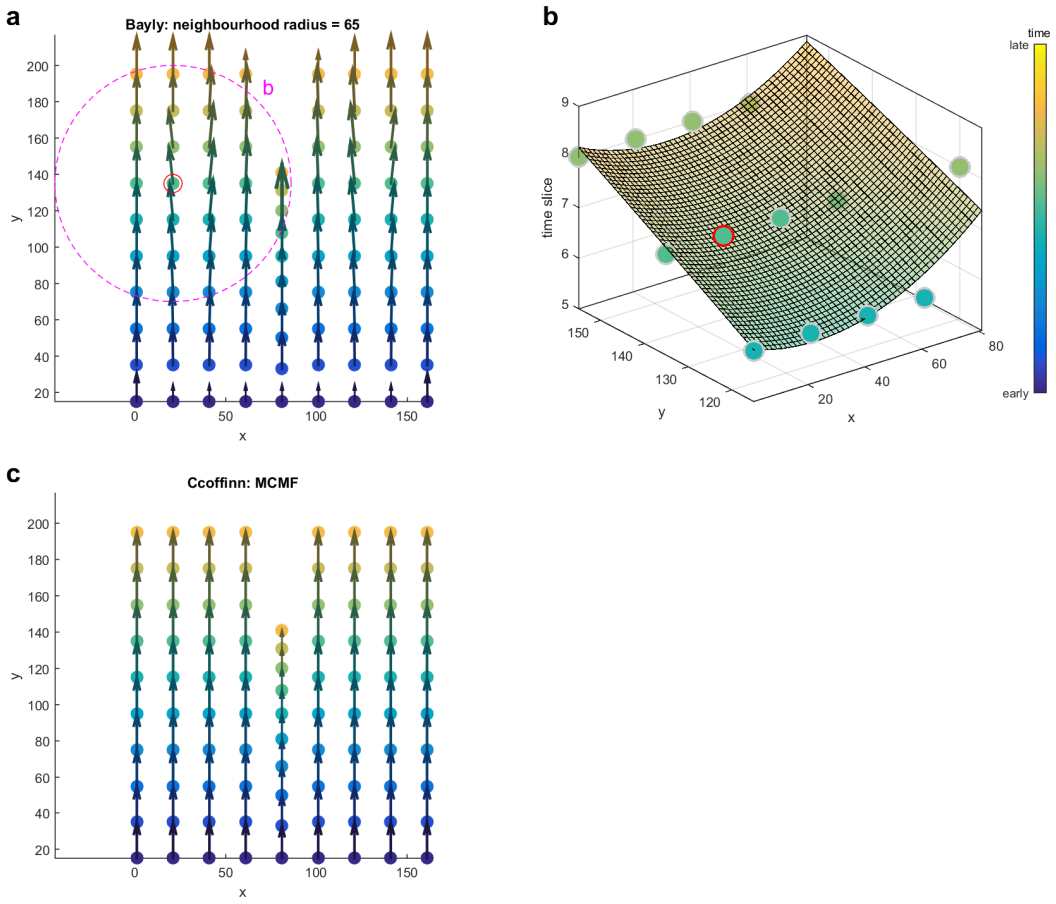


Figure 5.9: An illustration of Bayly's algorithm; larger neighbourhood. a) and b) are an analogy of the previous figure, with neighbourhood radius 65. In c) is given the tracking information obtained using Ccoffinn's MCMF tracking algorithm.

the vicinity of the slowing down band is aggravated overall. Furthermore, CV becomes overestimated severely in the slowing down band, as demonstrated by the case of the encircled point (producing the longest arrow shown in the plot) and the respective fitted surface. This is due to the fact that when a surface is fitted around the encircled point, the algorithm also considers the points of the fast part of wavefront that are some distance away, which results in an incorrect high CV estimate. Indeed, this error increases as the distance between the fast and slow wavefront increases making the estimated CV excessively large.

Increasing the neighbourhood size to 65 yields the plot in 5.9a, revealing yet another type of error, e.g., in the point circled in red, where the velocity vector points away from the slowing down band. When fitting the respective surface (shown in 5.9b),

the surface has to be lifted at its right part to pass near the point belonging to the slow part of the wavefront; however, as the fitted model is a quadratic surface, this forces the left part of the surface to be lifted up, making the partial derivative such that the velocity vector then aims away from the centre of both the fitted surface, and the centre of the velocity plot.

The panel 5.9c contains the wave tracking information by Ccoffinn's MCMF method, providing correct estimation of both CV and conduction direction.

The three examples of various mistakes made by Bayly's algorithm on the particular data also highlight the sensitivity of the method to the neighbourhood radius, as the tracking outputs in the vicinity of the slowing down segment differ between the three examples rather considerably. At the same time, there is no "correct" neighbourhood size in general. In a heterogeneously conducting excitable medium, the example given above may be only a small part of the overall activation pattern; "good" values of neighbourhood size may then differ substantially between distinct areas of the tissue. As the algorithm allows only a single parametrisation of neighbourhood size, it then follows that at least some areas will contain tracking artifacts. This issue could be probably ameliorated by extending the Bayly's algorithm to somehow dynamically determine an appropriate neighbourhood size.

5.3.5 Near wavefronts in a single wave

A second type of problem associated with the surface-fitting approach of Bayly is that different wavefronts of a single wave can affect one another; one example is shown in the panel 5.10a. The panel shows a wave spreading towards the top and bottom of the plot; it also steers towards left in its top-travelling segment. The steering then affects the direction and length of several arrows associated with the bottom-travelling segment of the wave, which is incorrect. The tracking by MCMF shown in the panel 5.10b is correct.

5.3.6 Wave shape affects CV and direction estimation

The panel 5.11a shows two waves of identical CV (10 arbitrary units), travelling from bottom to top; a straight wave to the left and a pointed "arrow" wave to the right. While

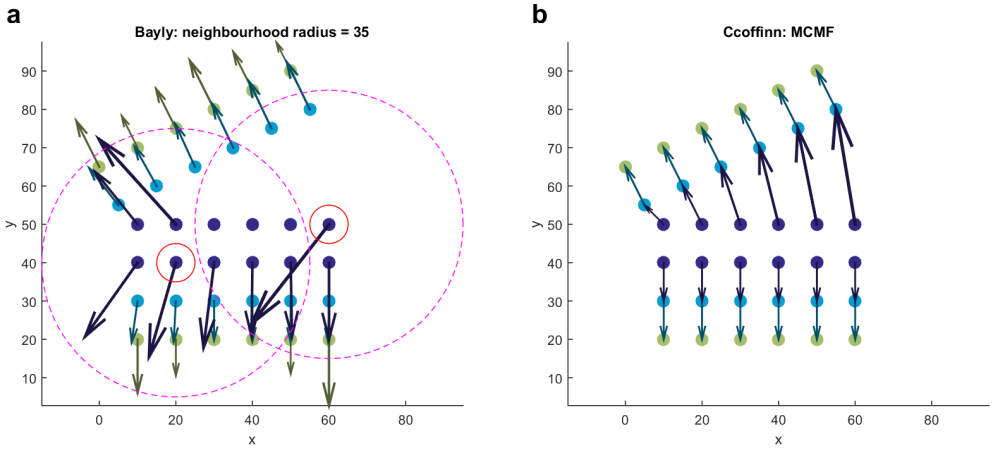


Figure 5.10: An illustration of the problem with multiple near wavefronts in Bayly's algorithm. In a) is shown the activation diagram of a simulated wave spreading simultaneously towards the top and the bottom of the plot; the interpretation of colours and arrows obtained using Bayly's algorithm is identical to the previous figure. In b) is given the tracking information obtained using Ccoffinn's MCMF algorithm.

the CV estimation is correct in the straight wave, when the first and last temporal slices are ignored, both local CVs and propagation directions are almost all incorrect in the arrow-shaped wave, suggesting at a major sensitivity of the Bayly's algorithm to the wave shape, rather than purely to the actual conduction velocity. The panel 5.11b gives the surface fitted to the left encircled point's surroundings, showing why CV is mildly overestimated at the point. The panel 5.11c then shows the surface fitted to the right encircled point, showing why the direction of propagation is incorrectly estimated. The panel 5.11d contains the correct tracking outcome obtained using MCMF algorithm.

5.3.7 Wavefront jaggedness yields overestimation of CV

In Figure 5.12 is shown the tracking output of Bayly's algorithm on a straight wave with jagged wavefront that propagates from bottom to top. Even though the true CV is 10 units per time step, the estimated CV is clearly and systematically estimated to be higher. In certain cases (e.g., the encircled one), the direction is also estimated poorly, due to the asymmetrical positioning of neighbouring active points in the neighbourhood.

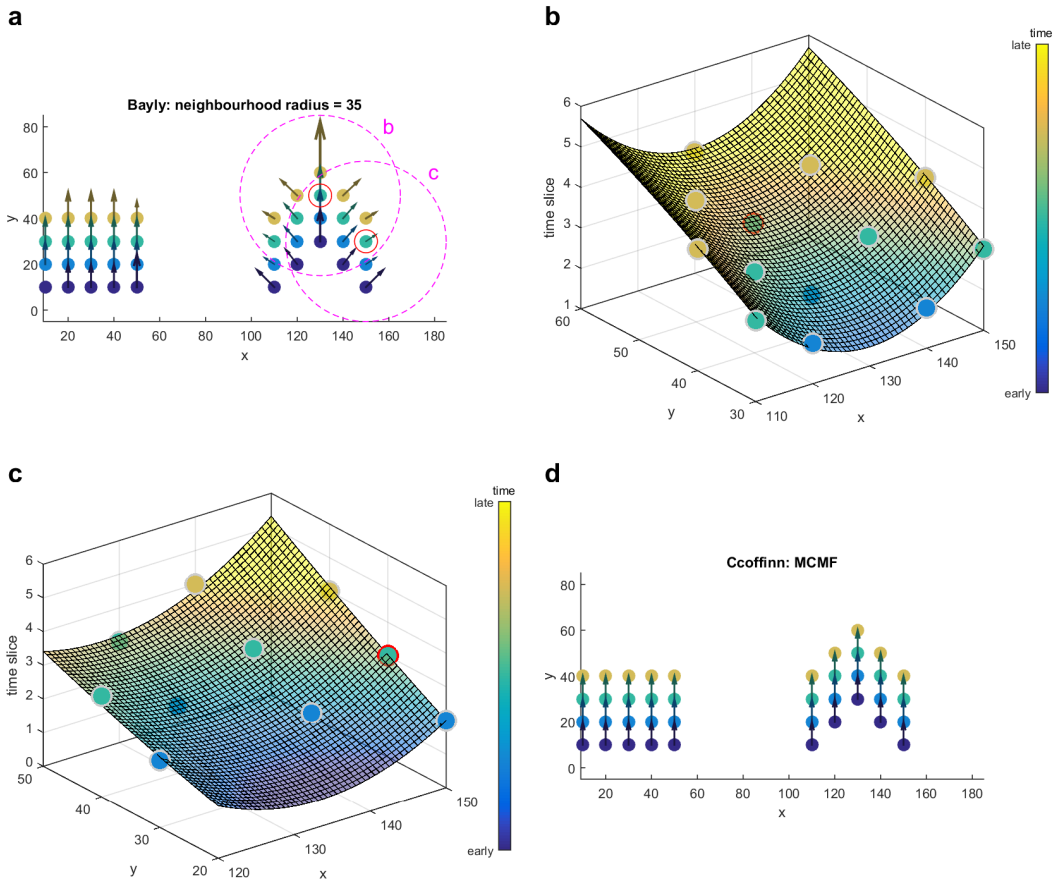


Figure 5.11: An illustration of the importance of wave shape in Bayly's algorithm. In a) is shown the activation diagram of two simulated waves of identical conduction velocity: a straight wave to the left, and a arrow-shaped wave to the right; the interpretation of colours and arrows obtained using Bayly's algorithm is identical to the previous figure. In b) and c) are the surfaces fitted to the respective points in a) and their surroundings. In d) is given the tracking information obtained using Ccoffinn's MCMF algorithm.

5.3.8 Heterogeneously spreading target waves and changing wavefront size

A case where the basic version of MCMF algorithm (allowing at most one arrow entering and leaving a blob) may struggle primarily is the case when wavefront size changes considerably (such as in origination of a target wave), possibly under-tracking the propagation. An example of such under-tracking is shown in Figure 5.13a. The issue is the most problematic between frames 1 and 2, where the basic MCMF algorithm generates one arrow where there should be four. The CV is estimated correctly in the frame, but the information on direction of propagation is insufficient. In the last two

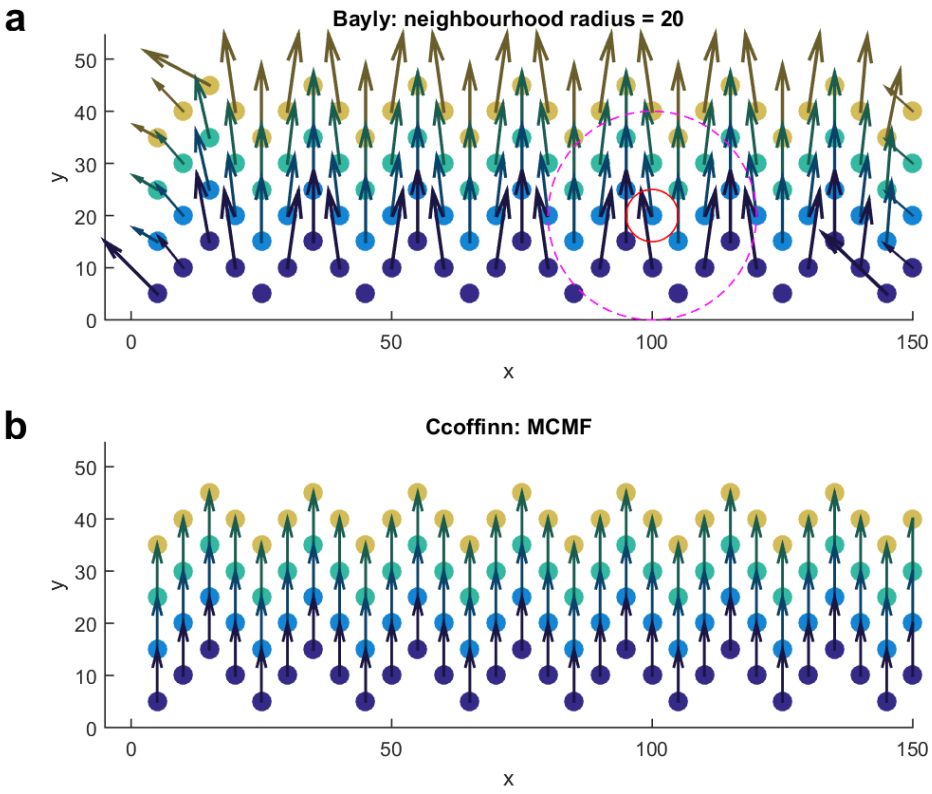


Figure 5.12: An illustration of Bayly's algorithm overestimating CV of a jagged wavefront. In a) is shown the activation diagram of a simulated straight wave with jagged wavefront travelling from bottom to top; the interpretation of colours and arrows obtained using Bayly's algorithm is identical to the previous figure. In b) is given the tracking information obtained using Ccoffinn's MCMF algorithm.

frames it can be clearly seen how the algorithm chooses the shortest arrows possible, underrepresenting the faster-propagating parts of the wave, thus underestimating CV.

In Figure 5.13b is shown the performance of the generalised MCMF algorithm with *maxArrows* = 'auto', showing improved tracking of the previously underrepresented parts of the wave. The perpendicular arrow pairs in certain regions is an artifact caused by the use of synthetic data in this example which rarely observed in real data; weighted spatial averaging of the arrows might be performed to obtain more smooth velocity field. Figure 5.13c,d shows the output of Bayly's method on the same data (differing in neighbourhood size of 35 and 60 respectively). It is noteworthy that Bayly's algorithm also does not work perfectly in this case as arrows leaving blobs in frames 1 and 2 are either not present due to poor conditioning or they are too long

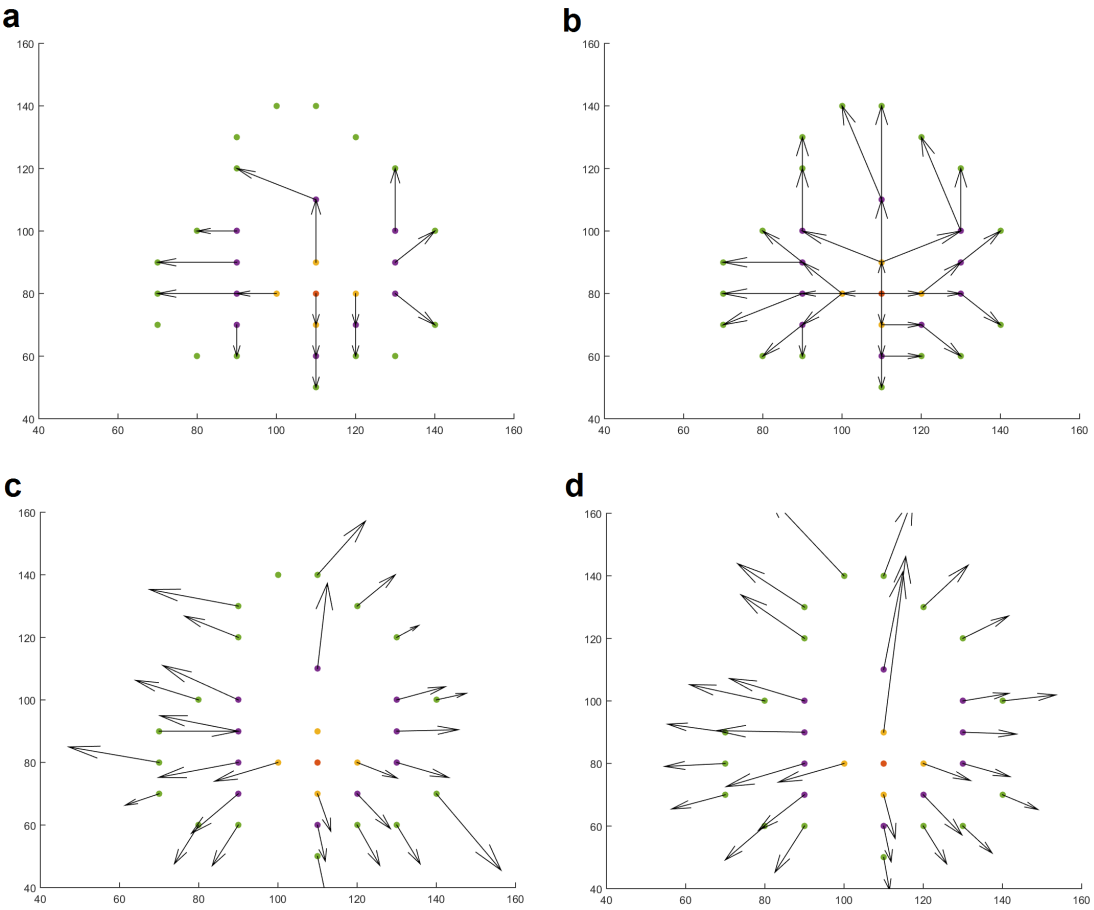


Figure 5.13: Target wave and undertracking with MCMF algorithm. In a) is shown the tracking of an uneven target wave using the basic MCMF approach. In b) is the same scenario using generalised MCMF tracking with the parameter *maxArrows* set to 'auto'. In c) and d) are shown the outputs of Bayly's algorithm for neighbourhood size 35 and 60 respectively.

and the CV is overestimated in some other regions as well (e.g., the arrow from the blob at the location of x=90, y = 100).

Unfortunately, the generalisation of MCMF with *maxArrows*> 1 does not always perform better than the basic version of the algorithm. The first example is a wave leaving field of view in a corner, as shown in Figure 5.14, where the generalised algorithm considers the wave leaving the field of view to be genuinely narrowing, while the basic algorithm and Bayly's method maintain its relative straightness. At the same time, it is important realise that the same wave morphology might happen within field of view due to conduction heterogeneity making a wave narrow down; in such a case, the generalised MCMF with *maxArrows*> 1 would provide the best tracking information.

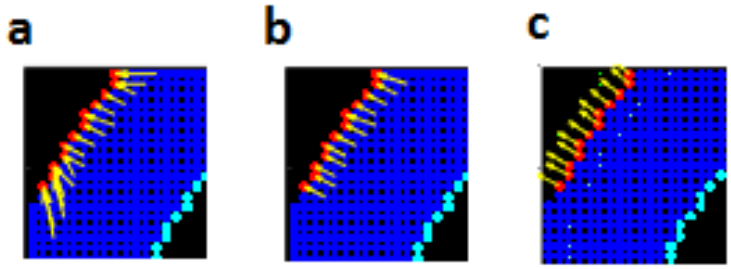


Figure 5.14: Comparing MCMF and Bayly's algorithm at the image edges. A segment of a spiral wave leaving the field of view, as tracked by MCMF with *maxArrows* = 'auto' (a), *maxArrows*$= 1$ (b), and Bayly's method (c).

There are two cases where MCMF with *maxArrows*> 1 may generate incorrect tracking information. First, in the case of steep increase in wavefront size, the method becomes more vulnerable to noise causing a non-spiking blob to be randomly detected as spiking in the vicinity of the main wave; in such a case, the larger value *maxArrows* is allowed, the more artefactual arrows will enter or leave these "fake-spiking" blobs, polluting the tracking information. A second problematic case happens when a slow wave is imaged at high sampling frequency: even if the wavefront maintains constant size, only a fairly small proportion of the wavefront will be tracked due to the fact that only the became-wavefront blobs are candidates for incoming arrows. At the same time, the set of blobs allowing outcoming arrows (previous-border blobs) will be comparatively large. As a consequence, multiple arrows will be pointing to most became-wavefront blobs, most of these being necessarily wrong, overestimating conduction velocity and roughness of propagation.

We note that in real use, an obvious underrepresentation of propagation with MCMF and *maxArrows*$= 1$ happened only fairly rarely in the data available to us and the cases with the largest potential for steep difference (such as the first two frames capturing the origin of a target wave) are implicitly treated by the fact that Ccoffinn requires waves to have a sufficient size/density to be tracked in the first place. In Figure 5.15 is shown a sequence of four frames showing origin of a target wave (sample dataset **dataCa2_target**), as tracked using MCMF with *maxArrows*$= 1$, showing no major systematic flaw of tracking. The problem of under-tracking is somewhat present in the

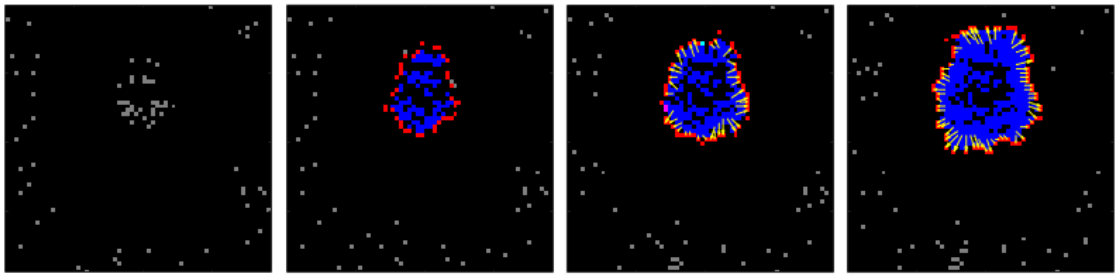


Figure 5.15: Tracking wave origins with MCMF. Four frames of an originating target wave tracked by MCMF with *maxArrows*= 1.

top left part of the wave between frames 3,4, but the bulk of the wavefront is tracked correctly, even the bottom part which is also heterogeneously quickly conducting.

For the reasons stated above, we believe that too high values of *maxArrows* are expected to bring more problems than benefit and values of 1 or 2 are likely to work best, unless a particular dataset requires otherwise.

5.4 Discussion

In this chapter, we described the toolkit Ccoffinn, a novel approach to segmentation and wave tracking in optically mapped tissue, with subsequent feature extraction, focussed on the analysis of high-resolution recordings with heterogeneously conducting tissue. The method was validated using synthetic data and applied to a large cardiac culture data set, where it successfully detected significant differences in properties of two types of cell cultures. Ccoffinn has the ability to extract many different features from data sets, describing various properties of the imaged tissue, which, to our knowledge, were not analysed automatically before (e.g., wavefront roughness).

Concerning the physiological relevance of the features extracted, *Wavefront speed*, *APD*, and *firing frequency* are widely reported measures of cardiac wave dynamics that yield information on connectivity, upstroke velocity, automaticity, and ion channel kinetics, e.g. calcium dynamics (Bayly et al., 1998; Miragoli et al., 2006; Campbell et al., 2012). The features *wavefront roughness*, *entropy*, and *perimeter to area ratio* attempt to quantify the relative complexity of propagating waves in tissue. Since complex dynamics can be caused by a wide variety of different causes, it is often

impossible to assign a one to one electrophysiological or structural correlation to these measures. However, these measures are directly relevant to the understanding wavefront interactions and arrhythmogenesis in our preparations. *Wavefront roughness* is an indirect measure of the connectivity of the tissue as well as the number and size of local structural heterogeneities. Well connected tissue will generate smooth wavefronts whereas locally disconnected tissue, or tissue in the presence of spatially distributed heterogeneities, tend to generate wavefronts that appear fractured (Bub et al., 2002; Steinberg et al., 2006; Rohr, 2004; Fast et al., 1996; Spach and Kootsey, 1983). *Entropy* is a measure of spatiotemporal complexity (Schlemmer et al., 2015b,a; Jung et al., 2000), and can be used to quantify variability in wavefront structure. Tissue experiencing changes in electrophysiology, or connectivity (Bub et al., 2005) may be expected to display higher entropy values. However, *entropy* may be difficult to interpret as it does not necessarily map onto an intuitive understanding of complex cardiac dynamics: for example, many multiple interacting wavelets (e.g. during fibrillation) may have low entropy if the wavefronts have similar sizes and/or if the wavelets are spatially connected. Entropy calculation is also sensitive to noise and the threshold for activation. In contrast, the feature *perimeter to area ratio* we defined in our work directly maps to an intuitive measure of spatial complexity in our data sets. Wave *perimeter to area ratio* gives information on the shape of a wave (larger values map to smaller waves and waves with non-circular shapes). As with *wavefront roughness*, *perimeter to area ratio* is a function of local heterogeneity, but also a measure of dynamic instability in homogeneous tissue. For example multiple wavelets caused by steep restitution can have a low roughness value and a high perimeter to area value, whereas multiple wavelets caused by local heterogeneity are expected to have high values for both descriptors. Taken together, these measures can be used to differentiate different experimental preparations (e.g. Table 1).

We believe that the main future use of the toolkit will be for discovering and quantifying the effects of pharmacological agents on cardiac propagation, or for determining functional differences between tissue types, similar to the proof-of-concept application presented in this text. The versatility of Ccoffinn is supported by its spreading use

during this DPhil project. First, a beta-version of Ccoffinn was initially used to study wave pattern in cell cultures (Burton et al., 2015a). Second, the final version of the toolkit is currently used in the group of Prof. Casadei in Oxford to study distinct properties of different parts of atria. Third, a slightly modified version of Ccoffinn is used to study slow calcium waves in the development of drosophila wings at University of Southern California.

5.5 Limitations

The main limitation of Ccoffinn is the offline nature of the software; this is very convenient for blob segmentation tasks, but having a real-time implementation might be also very useful. Implementing a real-time version of the toolkit is feasible, provided that no complex visualisation of the segmentation is needed. The main change needed would be an alternative algorithm for determining which cells are active and which are not. A frame-by-frame use of SeNeCA algorithm might be an option as this has been validated in (Tomek et al., 2013).

A second limitation of the toolkit is poor performance of the feature describing spatiotemporal entropy; however, this is intrinsic to how entropy is defined. Since entropy is the slowest feature to compute and the feature describing surface-to-volume ratio of waves serves a very similar purposes and performs far better, we do not consider this to be a critical flaw.

5.6 Conclusions

We developed a high-throughput software tool which characterises high-resolution imaging data of cardiac cell cultures using a set of physiologically relevant features, such as conduction homogeneity, conduction velocity, or spatial complexity of the activation pattern. We hope that the approaches described may be readily adopted to aid basic research in cardiology, or to improve data analysis in drug safety testing applications, where *in vitro* approaches increase in prominence.

There goes the breakfast bell
Back from heaven, back to hell
Naked howling freedom - Hell's Ditch

The Pogues – Hell's Ditch

6 Concluding discussion

6.1 Key findings and contributions

Here we overview how the thesis aims listed in section 1.7 were addressed.

The first key finding of our work is that the infarct border zone in hearts with a healed myocardial infarction is prone to formation of cardiac alternans compared to noninfarcted myocardium. This was shown using rat Langendorff hearts 2 months after myocardial infarction, using dual calcium and voltage mapping. Incidence of alternans during rapid pacing was strongly associated with the duration of calcium transients at slower pacing, suggesting impaired calcium handling as a potential cause.

The second key finding is that β-adrenergic stimulation via norepinephrine, the main sympathetic neurotransmitter, potently attenuates alternans; this effect was abolished with a beta-blocker metoprolol. Together with the finding on alternans vulnerability of the infarct border zone, the effect of norepinephrine offers an explanation of the observations in human clinical studies which show that patients with denervated infarct border zone are at a high risk of arrhythmia compared to patients with reinnervated border zone (Malhotra et al., 2015). Given that the post-MI hearts are particularly vulnerable to alternans in the border zone, and, at the same time, denervation of the border zone strips it of the protection against alternans via norepinephrine, the phenotype of the denervated border zone is expected to be associated with formation

of strongly heterogeneous alternans localised almost exclusively to the border zone, forming large repolarisation gradients, predisposing the heart to conduction block, wave breakup, and reentry.

The third key contribution is the development of a computer model of a ventricular cardiomyocyte enabling infarct border zone remodelling and β-adrenergic stimulation. The model replicated the experimental results, showing increased vulnerability of border zone myocytes to alternans, as well as attenuation of alternans via simulated β-adrenergic stimulation. Analysis of the model's behaviour revealed that accelerated calcium release dynamics underlie alternans attenuation via β-AR stimulation. Conversely, slowed down release dynamics (such as found in the infarct border zone) cause increased vulnerability to alternans, potentially explaining alternans vulnerability in multiple cardiac diseases. Furthermore, we have demonstrated how alternans restricted to the infarct border zone promotes arrhythmia via increasing the vulnerability of the border zone to conduction block and propagation of premature ventricular complexes. Beside the condition-specific results, our analysis provides novel thorough explanation of alternans formation in the studied family of models.

The fourth contribution is the development of software tools for a) processing microscopic imaging data from cultured cardiomyocyte monolayers, capable of processing dye-based and dye-free imaging datasets, providing a rich set of features describing activation patterns, b) processing macroscopic calcium and voltage imaging data from *ex vivo* hearts. The software tools created have already been adopted by several laboratories in the UK and USA, confirming our hope they will be of use to the scientific community.

6.2 Clinical perspective

Taken together, our results challenge the historical view that infarct border zone innervation is pathological and pro-arrhythmic (Shen and Zipes, 2014). Instead, they support the view, which is also supported by clinical data published during this DPhil, positing that border zone denervation, rather than innervation, is pathological (Malhotra et al., 2015; Fallavollita et al., 2017)[1].

[1] A more in-depth discussion of the evidence is given in section 3.4.

The potential protective role of infarct border zone reinnervation provides an interesting perspective on the arrhythmogenicity of the cardiac sympathetic nervous system, suggesting a dual role: while ventricular innervation may be anti-arrhythmic via alternans attenuation, at the same time, particularly in denervated hearts without any defence against alternans in the border zone, sympathetic-driven increase in heart rate via SA node innervation may be pro-arrhythmic by increasing the heart rate, driving the heart into an alternans-vulnerable pacing window. This duality hints at potential future therapeutic applications via selective inhibition of heart rate increase due to sympathetic stimulation, while maintaining or boosting the potential benefit of homogeneous innervation in the ventricles and periinfarction β-adrenergic activity. The former goal might be achieved, e.g., via SA node sympathetic denervation or by administration of ivabradine (a blocker of funny current, reducing heart rate), while the latter could be possibly pursued via transvenous electrical stimulation as proposed by Meyer et al. (2010).

Our results may be relevant for understanding the benefits of beta-blockade. Beta-blockers, the blockers of β-AR stimulation, are the mainstay of therapy after myocardial infarction, with demonstrated improvement in mortality (Taqueti and O 'Gara, 2015), however, the precise mechanism of the improvement may not be clear. Possibly the most popular explanation of reduction in arrhythmogenesis is that beta-blockers offer protection from post-infarction nerve sprouting (Chen et al., 2001), which was at the time considered purely pathological. We believe that the results of this thesis offer several alternative points of view. First, beta-blockers reduce heart rate by blocking the increase in heart rate due to sympathetic stimulation of the SA node. Given that alternans, which appears to be a key driver of arrhythmia (Pastore et al., 1999; Wilson et al., 2009), appears at high heart rates, it is possible that at least a part of the anti-arrhythmic effect of beta-blockers could be mediated simply by prevention of an overt increase in heart rate. Second, since beta-blockers cause hyperinnervation on their own (Clarke et al., 2010), it is possible that they help reinnervate the infarct border zone and prevent the hazardous phenotype of a denervated periinfarct zone; this is in fact a hypothesis that can be relatively easily tested in a laboratory. Third, in hearts

failing due to myocardial dilation, which is a frequent complication of patients with a history of myocardial infarction, beta-blockers were shown to restore sensitivity to sympathetic nervous stimulation (Heilbrunn et al., 1989). This highlights the fact that the net effect of beta-blocker therapy on ventricular sympathetic activation is not necessarily only inhibitory.

Given that innervation heterogeneity appears to be far more pro-arrhythmic than β-AR stimulation alone, we might speculate about the utility of the following treatment of patients with denervated infarct border zone after MI: a beta-blockade combined with a low effective dose of a β-agonist. Systemic perfusion of a β-agonist should provide a fairly homogeneous delivery to the tissue, which we observed to not increase the arrhythmia incidence in our experiments (we observed a trend towards its reduction). At the same time, beta-blockers would be expected to prevent overt sympathoexcitation, which is deleterious. Thus, the combined β-agonist&antagonist therapy could replace the heterogeneous adrenergic substrate of a denervated-border-zone heart with a relatively homogeneous one. Beyond reducing β-AR heterogeneity, the elevated β-AR activity of the infarct border zone could provide protection from alternans, as shown in this thesis. At the same time, the presence of a β-agonist in the border zone might attenuate the formation of localised β-adrenergic supersensitivity (Gardner et al., 2015). Ultimately, the combined treatment might help the heart maintain cardiac output, while avoiding the excessive and damaging β-agonist hyperactivity, as would be the case without beta-blockers.

Finally, we believe that our observation that calcium alternans vulnerability may be predicted using calcium transient duration at slow pacing when no alternans is present might be used for risk stratification of patients after MI. These patients are at an increased risk of VF and thus SCD via multiple possible mechanisms and the optimal treatment might vary considerably between groups. It would be beneficial to have a reliable predictor of alternans which does not endanger the patient via direct testing of alternans formation by increasing the heart rate. The main obstacle to implementing this method of risk stratification is the lack of calcium dyes certified for diagnostic use.

6.3 Future work

The thesis aims were fulfilled throughout the project, however the following projects provide a natural follow-up:

- This thesis focussed on the role of β-AR signalling via norepinephrine. However, cardiac sympathetic activation also involves co-transmitters such as NPY (Herring et al., 2012), and other catecholamines, such as epinephrine, making total effect slightly different to pure norepinephrine. Also, while perfusing norepinephrine provides good control over the strength of the stimulation and it is expected to be relatively homogeneous, native sympathetic activity may be heterogeneous. To counteract both of these simplifications, a direct neural stimulation of the sympathetic stellate ganglia could be used (Kalla et al., 2016). We have considered this option and tried it in several preliminary experiments, however, with the protocol used, we did not achieve full ventricular stimulation, most likely by not stimulating all the stellate ganglia projecting to the heart. We hope to develop the protocol to achieve full sympathetic stimulation (possibly by optogenetic stimulation of stellate ganglia, without their excision) in future.

- The *ex vivo* nature of the preparation means that the vascular effects of β-agonists, mediated also via α-receptors, are ignored. At the same time, changes in blood pressure and coronary perfusion powerfully modulate cardiac workload and myocardial metabolism. Consequently, to increase the physiological relevance of our results, *in vivo* experiments could be carried out with an implantable pacemaker to induce alternans, and direct neural stimulation to study the effect of sympathetic activity on alternans and arrhythmia.

- The computer simulations involved single cells and 1D fibres. Extending the models to 2D sheets of tissue or full 3D structure would enable the study of infarct border zone structure and/or location within the heart. Both tissue and neural heterogeneity could be modelled, allowing us to understand the criteria for the relationship of cardiac sympathetic system and arrhythmia in a more realistic

setting. Also, modelling structural obstacles could make the model manifest discordant alternans, which was absent in our simulations. However, 2D or 3D simulations will require a considerable simplification of the myocyte model and β-AR signalling, as simulations of the current model would be too computationally expensive.

- The Ccoffinn toolkit (or its simplified version) could be modified to run in real time. With such modification, it could be used together with cardiac optogenetic activation of the imaged tissue (Entcheva, 2013), allowing automated control of illumination for feedback applications that depend on wavefront location or velocity. Ccoffinn could greatly improve the reaction time to experimental events and could allow the application of patterns of stimulation that are well beyond the capabilities of human operators. This could be particularly useful in the context of optogenetic defibrillation (Bruegmann et al., 2016), which is currently based on using very simple and pre-determined optical stimuli. With a live feedback system, it would be possible to instead "read" the activation pattern of the tissue and use lower-energy, spatiotemporally targeted optical stimulation to e.g., break up spiral waves (Casa et al., 2009).

Death or glory, just another story...
The Clash – Death or glory

Bibliography

Ackerman M. J., Priori S. G., Dubin A. M., Kowey P., Linker N. J., Slotwiner D., Triedman J., Van Hare G. F., and Gold M. R. Beta-blocker therapy for long QT syndrome and catecholaminergic polymorphic ventricular tachycardia: Are all beta-blockers equivalent? *Heart Rhythm*, 14(1):e41–e44, 2017. ISSN 15563871. doi: 10.1016/j.hrthm.2016.09.012.

Ajijola O. A., Lellouche N., Bourke T., Tung R., Ahn S., Mahajan A., and Shivkumar K. Bilateral cardiac sympathetic denervation for the management of electrical storm, 2012. ISSN 07351097.

Akar F. G., Wu R. C., Deschenes I., Armoundas A. a., Piacentino V., Houser S. R., and Tomaselli G. F. Phenotypic differences in transient outward K+ current of human and canine ventricular myocytes: insights into molecular composition of ventricular Ito. *American journal of physiology. Heart and circulatory physiology*, 286(2):H602–H609, 2004. ISSN 0363-6135. doi: 10.1152/ajpheart.00673.2003.

Allessie M. A., Bonke F. I., and Schopman F. J. G. Circus movement in rabbit atrial muscle as a mechanism of trachycardia. *Circulation research*, 33(1):54–62, 1973. ISSN 0009-7330. doi: 10.1161/01.RES.33.1.54.

Ambrosi C. and Entcheva E. Optogenetic control of cardiomyocytes via viral delivery. *Methods Mol Biol*, 1181:215–228, 2014.

Anderson M. E., Brown J. H., and Bers D. M. CaMKII in myocardial hypertrophy and heart failure, 2011. ISSN 00222828.

Antzelevitch C. and Burashnikov A. Overview of basic mechanism of cardiac arrhythmia. *Card Electrophysiol Clin.*, 3(1):23–45, 2011. ISSN 18779182. doi: 10.1016/j.ccep.2010.10.012.Overview.

Area K. Incidence of ventricular fibrillation in patients with out-of-hospital cardiac arrest in Japan: survey of survivors after out-of-hospital cardiac arrest in Kanto area (SOS-KANTO). *Circulation journal : official journal of the Japanese Circulation Society*, 69(10):1157–1162, 2005. ISSN 1346-9843. doi: 10.1253/circj.69.1157.

Banville I. and Gray R. A. Effect of action potential duration and conduction velocity restitution and their spatial dispersion on alternans and the stability of arrhythmias. *Journal of cardiovascular electrophysiology*, 13(11):1141–1149, 2002. ISSN 1045-3873. doi: 10.1046/j.1540-8167.2002.01141.x.

Bassani J. W., Yuan W., and Bers D. M. Fractional SR Ca release is regulated by trigger Ca and SR Ca content in cardiac myocytes. *The American journal of physiology*, 268(5 Pt 1):C1313–C1319, 1995. ISSN 0002-9513.

Bayer J., Lalani G., Vigmond E., Narayan S., and Trayanova N. Mechanisms Linking Electrical Alternans and Clinical Ventricular Arrhythmia in Human Heart Failure. *Heart Rhythm*, 2016. ISSN 15475271. doi: 10.1016/j.hrthm.2016.05.017.

Bayly P. V., KenKnight B. H., Rogers J. M., Hillsley R. E., Ideker R. E., and Smith W. M. Estimation of conduction velocity vector fields from epicardial mapping data. *IEEE Transactions on Biomedical Engineering*, 45(5):563–571, 1998.

Beier H. T. and Ibey B. L. Experimental comparison of the high-speed imaging performance of an EM-CCD and sCMOS camera in a dynamic live-cell imaging test case. *PLoS ONE*, 9(1), 2014.

Bell R. M., Mocanu M. M., and Yellon D. M. Retrograde heart perfusion: The Langendorff technique of isolated heart perfusion, 2011. ISSN 00222828.

Bernus O., Van Eyck B., Verschelde H., and Panfilov A. V. Transition from ventricular fibrillation to ventricular tachycardia: a simulation study on the role of Ca(2+)-channel blockers in human ventricular tissue. *Physics in medicine and biology*, 47(23):4167–79, 2002. ISSN 0031-9155. doi: 10.1088/0031-9155/47/23/304.

Bien H., Yin L., and Entcheva E. Calcium instabilities in mammalian cardiomyocyte networks. *Biophysical journal*, 90(7):2628–40, 2006. ISSN 0006-3495. doi: 10.1529/biophysj.105.063321.

Blechschmidt S., Haufe V., Benndorf K., and Zimmer T. Voltage-gated Na+ channel transcript patterns in the mammalian heart are species-dependent. *Progress in Biophysics and Molecular Biology*, 98(2-3):309–318, 2008. ISSN 00796107. doi: 10.1016/j.pbiomolbio.2009.01.009.

Bodi I., Mikala G., Koch S. E., Akhter S. A., and Schwartz A. The L-type calcium channel in the heart: the beat goes on. *The Journal of clinical investigation*, 115(12):3306–17, 2005. ISSN 0021-9738. doi: 10.1172/JCI27167.

Bogun F., Crawford T., Chalfoun N., Kuhne M., Sarrazin J. F., Wells D., Good E., Jongnarangsin K., Oral H., Chugh A., Pelosi F., and Morady F. Relationship of frequent postinfarction premature ventricular complexes to the reentry circuit of scar-related ventricular tachycardia. *Heart Rhythm*, 5(3):367–374, 2008. ISSN 15475271. doi: 10.1016/j.hrthm.2007.11.026.

Bolter C. P. and Atkinson K. J. Maximum heart rate responses to exercise and isoproterenol in the trained rat. *The American journal of physiology*, 254(5 Pt 2): R834–9, 1988. ISSN 0002-9513.

Bos J. M., Bos K. M., Johnson J. N., Moir C., and Ackerman M. J. Left cardiac sympathetic denervation in long QT syndrome: Analysis of therapeutic nonresponders. *Circulation: Arrhythmia and Electrophysiology*, 6(4):705–711, 2013. ISSN 1941-3149. doi: http://dx.doi.org/10.1161/CIRCEP.113.000102.

Britton O. J., Bueno-Orovio A., Virág L., Varró A., and Rodriguez B. The electrogenic Na+/K+ pump is a key determinant of repolarization abnormality susceptibility in human ventricular cardiomyocytes: A population-based simulation study. *Frontiers in Physiology*, 8(MAY), 2017. ISSN 1664042X. doi: 10.3389/fphys.2017.00278.

Bruegmann T., Boyle P. M., Vogt C. C., Karathanos T. V., Arevalo H. J., Fleischmann B. K., Trayanova N. A., and Sasse P. Optogenetic defibrillation terminates ventricular arrhythmia in mouse hearts and human simulations. *Journal of Clinical Investigation*, 126(10):3894–3904, 2016. ISSN 15588238. doi: 10.1172/JCI88950.

Bub G., Camelliti P., Bollensdorff C., Stuckey D. J., Picton G., Burton R. A., Clarke K., and Kohl P. Measurement and analysis of sarcomere length in rat cardiomyocytes in situ and in vitro. *American journal of physiology. Heart and circulatory physiology*, 298(5): 25, 2010. ISSN 0363-6135. doi: 10.1152/ajpheart.00481.2009.

Bub G., Shrier A., and Glass L. Spiral wave generation in heterogeneous excitable media. *Physical review letters*, 88(5):058101, 2002. ISSN 0031-9007. doi: 10.1103/PhysRevLett.88.058101.

Bub G., Tateno K., Shrier A., and Glass L. Spontaneous initiation and termination of complex rhythms in cardiac cell culture. *Journal of cardiovascular electrophysiology*, 14(10 Suppl):S229–S236, 2003. ISSN 1045-3873.

Bub G., Shrier A., and Glass L. Global organization of dynamics in oscillatory heterogeneous excitable media. *Physical Review Letters*, 94(2), 2005. ISSN 00319007. doi: 10.1103/PhysRevLett.94.028105.

Bursac N., Parker K. K., Iravanian S., and Tung L. Cardiomyocyte cultures with controlled macroscopic anisotropy: a model for functional electrophysiological studies of cardiac muscle. *Circ Res*, 91(12):e45–54, 2002. ISSN 0009-7330. doi: 10.1161/01.RES.0000047530.88338.EB.

Burton R., Tomek J., Aslam S., Bilton S., Larsen H., Sharkey A., Stephens G., Mann E., Paterson D., and Bub G. Sympathetic stellate neurons increases cardiac conduction velocity and alters wave patterns in a myocyte-neuron co-culture model system. *Autonomic Neuroscience*, 192:72–73, nov 2015a. ISSN 15660702. doi: 10.1016/j.autneu.2015.07.062.

Burton R. A. B., Klimas A., Ambrosi C. M., Tomek J., Corbett A., Entcheva E., and Bub G. Optical control of excitation waves in cardiac tissue. *Nature Photonics*, 9(12):813–816, 2015b. ISSN 1749-4885. doi: 10.1038/nphoton.2015.196.

Campbell K., Calvo C. J., Mironov S., Herron T., Berenfeld O., and Jalife J. Spatial gradients in action potential duration created by regional magnetofection of hERG are a substrate for wavebreak and turbulent propagation in cardiomyocyte monolayers. *The Journal of physiology*, 590(Pt 24):6363–79, 2012. ISSN 1469-7793. doi: 10.1113/jphysiol.2012.238758.

Cannon R., Schenke W., Bonow R., Leon M., and Rosing D. Left ventricular pulsus alternans in patients with hypertrophic cardiomyopathy and severe obstruction to left ventricular outflow. *Circulation*, 73, 1986.

Casa M. A. D., Rubia F. J. D., Ivanov P. C., de la Casa M. A., and de La Rubia F. J. Spiral wave annihilation by low-frequency planar fronts in a model of excitable media. *EPL (Europhysics Letters)*, 86(1):18005, 2009. ISSN 0295-5075. doi: 10.1209/0295-5075/86/18005.

Cassidy P. J., Schneider J. E., Grieve S. M., Lygate C. A., Tyler D. J., Neubauer S., and Clarke K. An animal handling system for small animals in vivo MR. In *ISMRM (Abstract)*, page 488, 2005.

Catterall W. A. Voltage-gated calcium channels. *Cold Spring Harbor Perspectives in Biology*, 3(8):1–23, 2011. ISSN 19430264. doi: 10.1101/cshperspect.a003947.

Catterall W. A. Structure and function of voltage-gated sodium channels at atomic resolution. *Experimental Physiology*, 99(1):35–51, 2014. ISSN 09580670. doi: 10.1113/expphysiol.2013.071969.

Chakir K., Daya S. K., Aiba T., Tunin R. S., Dimaano V. L., Abraham T. P., Jaques-Robinson K. M., Jacques K., Lai E. W., Pacak K., Zhu W.-Z., Xiao R.-P., Tomaselli G. F., and Kass D. A. Mechanisms of enhanced beta-adrenergic reserve from cardiac

resynchronization therapy. *Circulation*, 119(9):1231–40, 2009. ISSN 1524-4539. doi: 10.1161/CIRCULATIONAHA.108.774752.

Chang K. C., Bayer J. D., and Trayanova N. A. Disrupted Calcium Release as a Mechanism for Atrial Alternans Associated with Human Atrial Fibrillation. *PLoS Computational Biology*, 10(12), 2014. ISSN 15537358. doi: 10.1371/journal.pcbi.1004011.

Chen P. S., Chen L. S., Cao J. M., Sharifi B., Karagueuzian H. S., and Fishbein M. C. Sympathetic nerve sprouting, electrical remodeling and the mechanisms of sudden cardiac death. *Cardiovascular Research*, 50(2):409–416, 2001. ISSN 00086363. doi: 10.1016/S0008-6363(00)00308-4.

Chen V., Chen Y. H., and Downing S. E. An improved isolated working rabbit heart preparation using red cell enhanced perfusate. *Yale Journal of Biology and Medicine*, 60(3):209–219, 1987. ISSN 00440086.

Choi B. and Salama G. Simultaneous maps of optical action potentials and calcium transients in guinea-pig hearts: mechanisms underlying concordant alternans. *J.Physiol*, 15(529):171–88, 2000.

Ciulla M. M., Paliotti R., Ferrero S., Braidotti P., Esposito A., Gianelli U., Busca G., Cioffi U., Bulfamante G., and Magrini F. Left ventricular remodeling after experimental myocardial cryoinjury in rats. *Journal of Surgical Research*, 116(1):91–97, 2004. ISSN 00224804. doi: 10.1016/j.jss.2003.08.238.

Clarke G. L., Bhattacherjee A., Tague S. E., Hasan W., and Smith P. G. ß-Adrenoceptor Blockers Increase Cardiac Sympathetic Innervation By Inhibiting Autoreceptor Suppression of Axon Growth. *The Journal of neuroscience : the official journal of the Society for Neuroscience*, 30(37):12446–12454, 2010. ISSN 0270-6474. doi: 10.1523/JNEUROSCI.1667-10.2010.

Clausen M., Hilbers F., and Poulsen H. The Structure and Function of the Na,K-ATPase Isoforms in Health and Disease. *Frontiers in Physiology*, 8(371), 2017.

Clerx M., Collins P., de Lange E., and Volders P. G. A. Myokit: A simple interface to cardiac cellular electrophysiology. *Progress in Biophysics and Molecular Biology*, 120 (1-3):100–114, 2016. ISSN 00796107. doi: 10.1016/j.pbiomolbio.2015.12.008.

Cobb L. A. Changing Incidence of Out-of-Hospital Ventricular Fibrillation, 1980-2000. *JAMA*, 288(23):3008, 2002. ISSN 0098-7484. doi: 10.1001/jama.288.23.3008.

Collier M. L., Ji G., Wang Y.-X., and Kotlikoff M. I. Calcium-induced Calcium Release in Smooth Muscle - Loose Coupling between the Action Potential and Calcium Release. *J. Gen. Physiol*, 115:653–662, 2000. ISSN 00221295. doi: 10.1085/jgp.115.5.653.

Collura C. A., Johnson J. N., Moir C., and Ackerman M. J. Left cardiac sympathetic denervation for the treatment of long QT syndrome and catecholaminergic polymorphic ventricular tachycardia using video-assisted thoracic surgery. *Heart Rhythm*, 6(6): 752–759, 2009. ISSN 15475271. doi: 10.1016/j.hrthm.2009.03.024.

Conforti L., Tohse N., and Sperelakis N. Influence of sympathetic innervation on the membrane electrical properties of neonatal rat cardiomyocytes in culture. *Journal of developmental physiology*, 15(4):237–246, 1991. ISSN 0141-9846 (Print).

Corre K., Cho H., and Barnard R. Maximum exercise heart rate reduction with maturation in the rat. *Journal of applied physiology*, 40(5):741–4, 1976.

Costantini O., Hohnloser S. H., Kirk M. M., Lerman B. B., Baker J. H., Sethuraman B., Dettmer M. M., and Rosenbaum D. S. The ABCD (Alternans Before Cardioverter Defibrillator) Trial. Strategies Using T-Wave Alternans to Improve Efficiency of Sudden Cardiac Death Prevention. *Journal of the American College of Cardiology*, 53(6):471–479, 2009. ISSN 07351097. doi: 10.1016/j.jacc.2008.08.077.

Cram A. R., Rao H. M., and Tolkacheva E. G. Toward prediction of the local onset of alternans in the heart. *Biophysical Journal*, 100(4):868–874, 2011. ISSN 00063495. doi: 10.1016/j.bpj.2011.01.009.

Cryer P. E. Physiology and pathophysiology of the human sympathoadrenal neuroendocrine system, 1980. ISSN 00284793.

Cutler M. J., Wan X., Plummer B. N., Liu H., Deschenes I., Laurita K. R., Hajjar R. J., and Rosenbaum D. S. Targeted sarcoplasmic reticulum Ca2+ ATPase 2a gene delivery to restore electrical stability in the failing heart. *Circulation*, 126(17):2095–104, 2012. ISSN 00097322. doi: 10.1161/CIRCULATIONAHA.111.071480.

De Azevedo I. M., Watanabe Y., and Dreifus L. S. Atrioventricular junctional rhythm: classification and clinical significance, 1973. ISSN 00123692.

De Bakker J. M., van Capelle F. J., Janse M. J., Wilde A. A., Coronel R., Becker A. E., Dingemans K. P., van Hemel N. M., and Hauer R. N. Reentry as a cause of ventricular tachycardia in patients with chronic ischemic heart disease: electrophysiologic and anatomic correlation. *Circulation*, 77(3):589–606, 1988. ISSN 0009-7322. doi: 10.1161/01.CIR.77.3.589.

Decker K. F. and Rudy Y. Ionic mechanisms of electrophysiological heterogeneity and conduction block in the infarct border zone. *American journal of physiology. Heart and circulatory physiology*, 299(5):H1588–H1597, 2010. ISSN 0363-6135. doi: 10.1152/ajpheart.00362.2010.

Decker K. F., Heijman J., Silva J. R., Hund T. J., and Rudy Y. Properties and ionic mechanisms of action potential adaptation, restitution, and accommodation in canine epicardium. *American journal of physiology. Heart and circulatory physiology*, 296(4):H1017–H1026, 2009. ISSN 0363-6135. doi: 10.1152/ajpheart.01216.2008.

Deo R. and Albert C. M. Epidemiology and genetics of sudden cardiac death. *Circulation*, 125(4):620–637, 2012. ISSN 00097322. doi: 10.1161/CIRCULATIONAHA.111.023838.

DiFrancesco D. and Tortora P. Direct activation of cardiac pacemaker channels by intracellular cyclic AMP. *Nature*, 351(6322):145–147, 1991. ISSN 0028-0836. doi: 10.1038/351145a0.

Dobrev D. and Wehrens X. H. T. Role of RyR2 phosphorylation in heart failure and arrhythmias: Controversies around ryanodine receptor phosphorylation in cardiac

disease. *Circulation Research*, 114(8):1311–1319, 2014. ISSN 15244571. doi: 10.1161/CIRCRESAHA.114.300568.

Doshi A. N., Walton R. D., Krul S. P., de Groot J. R., Bernus O., Efimov I. R., Boukens B. J., and Coronel R. Feasibility of a semi-automated method for cardiac conduction velocity analysis of high-resolution activation maps. *Computers in Biology and Medicine*, 65: 177–183, 2015. ISSN 18790534. doi: 10.1016/j.compbiomed.2015.05.008.

Echebarria B. and Karma A. Mechanisms for initiation of cardiac discordant alternans. *European Physical Journal: Special Topics*, 146(1):217–231, 2007. ISSN 19516355. doi: 10.1140/epjst/e2007-00182-y.

Edwards A. G. and Louch W. E. Species-dependent mechanisms of cardiac arrhythmia: A cellular focus, 2017. ISSN 11795468.

Eisner D. A., Caldwell J. L., Kistamás K., and Trafford A. W. Calcium and Excitation-Contraction Coupling in the Heart, 2017. ISSN 15244571.

Entcheva E., Lu S. N., Troppman R. H., Sharma V., and Tung L. Contact fluorescence imaging of reentry in monolayers of cultured neonatal rat ventricular myocytes. *Journal of cardiovascular electrophysiology*, 11(6):665–76, 2000. ISSN 1045-3873. doi: 10.1111/j.1540-8167.2000.tb00029.x.

Entcheva E. Cardiac optogenetics. *American journal of physiology. Heart and circulatory physiology*, 304(9):H1179–91, 2013. ISSN 1522-1539. doi: 10.1152/ajpheart.00432.2012.

Entcheva E. and Bien H. Macroscopic optical mapping of excitation in cardiac cell networks with ultra-high spatiotemporal resolution, 2006.

Er F., Larbig R., Ludwig A., Biel M., Hofmann F., Beuckelmann D. J., and Hoppe U. C. Dominant-negative suppression of HCN channels markedly reduces the native pacemaker current If and undermines spontaneous beating of neonatal cardiomyocytes. *Circulation*, 107(3):485–489, 2003. ISSN 00097322. doi: 10.1161/01.CIR.0000045672.32920.CB.

Faber G. M., Silva J., Livshitz L., and Rudy Y. Kinetic Properties of the Cardiac L-Type Ca2+ Channel and Its Role in Myocyte Electrophysiology: A Theoretical Investigation. *Biophysical Journal*, 92(5):1522–1543, 2007. ISSN 00063495. doi: 10.1529/biophysj.106.088807.

Faggioni M. and Knollmann B. C. Calsequestrin 2 and arrhythmias. *AJP: Heart and Circulatory Physiology*, 302(6):H1250–H1260, 2012. ISSN 0363-6135. doi: 10.1152/ajpheart.00779.2011.

Fallavollita J., Dare J., Carter R., Baldwa S., and Canty J. M. J. Denervated Myocardium Is Preferentially Associated With Sudden Cardiac Arrest in Ischemic Cardiomyopathy: A Pilot Competing Risks Analysis of Cause-Specific Mortality. *Circ Cardiovasc Imaging*, 10, 2017. doi: 10.1161/CIRCIMAGING.117.006446.

Fallavollita J. A., Heavey B. M., Luisi A. J., Michalek S. M., Baldwa S., Mashtare T. L., Hutson A. D., Dekemp R. A., Haka M. S., Sajjad M., Cimato T. R., Curtis A. B., Cain M. E., and Canty J. M. Regional myocardial sympathetic denervation predicts the risk of sudden cardiac arrest in ischemic cardiomyopathy. *Journal of the American College of Cardiology*, 63(2):141–149, 2014. ISSN 07351097. doi: 10.1016/j.jacc.2013.07.096.

Fallen E. L., Coates G., Nahmias C., Chirakal R., Beanlands R., Wahl L., Woodcock G., Thomson M., Kamath M., E.L. F., G. C., C. N., R. C., R. B., L. W., G. W., M. T., and M. K. Recovery rates of regional sympathetic reinnervation and myocardial blood flow after acute myocardial infarction. *American Heart Journal*, 137(5):863–869, 1999. ISSN 0002-8703.

Fast V. G., Darrow B. J., Saffitz J. E., and Kléber A. G. Anisotropic activation spread in heart cell monolayers assessed by high-resolution optical mapping. Role of tissue discontinuities. *Circulation research*, 79(1):115–127, 1996. ISSN 0009-7330. doi: 10.1161/01.RES.79.1.115.

Florea S. M. and Blatter L. A. Regulation of cardiac alternans by β-adrenergic signaling pathways. *AJP: Heart and Circulatory Physiology*, 303(8):H1047–H1056, 2012. ISSN 0363-6135. doi: 10.1152/ajpheart.00384.2012.

Fox J. J., McHarg J. L., and Gilmour R. F. Ionic mechanism of electrical alternans. *American journal of physiology. Heart and circulatory physiology*, 282(2):H516–H530, 2002. ISSN 0363-6135. doi: 10.1152/ajpheart.00612.2001.

Franz M. The Electrical Restitution Curve Revisited:. Steep or Flat Slope-Which is Better? *Journal of Cardiovascular Electrophysiology*, 14(s10):S140–S147, 2003. ISSN 1045-3873. doi: 10.1046/j.1540.8167.90303.x.

Gaeta S. and Christini D. Non-Linear Dynamics of Cardiac Alternans: Subcellular to Tissue-Level Mechanisms of Arrhythmia. *Frontiers in Physiology*, 3(157), 2012.

Gao E., Lei Y. H., Shang X., Huang Z. M., Zuo L., Boucher M., Fan Q., Chuprun J. K., Ma X. L., and Koch W. J. A novel and efficient model of coronary artery ligation and myocardial infarction in the mouse. *Circulation Research*, 107(12):1445–1453, 2010. ISSN 00097330. doi: 10.1161/CIRCRESAHA.110.223925.

Gardner R., Wang L., Lang B., Cregg J., Dunbar C., Woodward W., Silver J., Ripplinger C., and Habecker B. Targeting protein tyrosine phosphatase sigma after myocardial infarction restores cardiac sympathetic innervation and prevents arrhythmias. *Nature Communications*, 6, 2015.

Garfinkel A. Eight (or more) kinds of alternans. *Journal of Electrocardiology*, 40(6 SUPPL. 1), 2007. ISSN 00220736. doi: 10.1016/j.jelectrocard.2007.06.011.

Gaudesius G., Miragoli M., Thomas S. P., and Rohr S. Coupling of cardiac electrical activity over extended distances by fibroblasts of cardiac origin. *Circulation Research*, 93(5):421–428, 2003. ISSN 00097330. doi: 10.1161/01.RES.0000089258.40661.0C.

Gheeraert P. J., De Buyzere M. L., Taeymans Y. M., Gillebert T. C., Henriques J. P. S., De Backer G., and De Bacquer D. Risk factors for primary ventricular fibrillation during acute myocardial infarction: A systematic review and meta-analysis, 2006. ISSN 0195668X.

Ginsburg K. S. and Bers D. M. Modulation of excitation-contraction coupling by isoproterenol in cardiomyocytes with controlled SR Ca2+ load and Ca2+ current trigger. *The Journal of physiology*, 556(Pt 2):463–80, 2004. ISSN 0022-3751. doi: 10.1113/jphysiol.2003.055384.

Gold M., Ip J., Constantini O., Poole J., McNulty S., Mark D., Lee K., and Bardy G. Role of Microvolt T-Wave Alternans in Assessment of Arrhythmia Vulnerability Among Patients With Heart Failure and Systolic Dysfunction. *Circulation*, 118:2022–2028, 2008.

Goldhaber J. I., Xie L.-H., Duong T., Motter C., Khuu K., and Weiss J. N. Action potential duration restitution and alternans in rabbit ventricular myocytes: the key role of intracellular calcium cycling. *Circulation research*, 96(4):459–466, 2005. ISSN 1524-4571. doi: 10.1161/01.RES.0000156891.66893.83.

Guo T., Zhang T., Mestril R., and Bers D. M. Ca2+/calmodulin-dependent protein kinase II phosphorylation of ryanodine receptor does affect calcium sparks in mouse ventricular myocytes. *Circulation Research*, 99(4):398–406, 2006. ISSN 00097330. doi: 10.1161/01.RES.0000236756.06252.13.

Guo Y., Zeng Q. C., Zhang C. Q., Zhang X. Z., Li R. X., Wu J. M., Guan J., Liu L., Zhang X. C., Li J. Y., and Wan Z. M. Extracellular matrix of mechanically stretched cardiac fibroblasts improves viability and metabolic activity of ventricular cells. *International Journal of Medical Sciences*, 10(13):1837–1845, 2013. ISSN 14491907. doi: 10.7150/ijms.6786.

Gussak I., Chaitman B. R., Kopecky S. L., and Nerbonne J. M. Rapid ventricular repolarization in rodents: electrocardiographic manifestations, molecular mechanisms, and clinical insights. *Journal of electrocardiology*, 33(2):159–170, 2000. ISSN 00220736. doi: 10.1016/S0022-0736(00)80072-2.

Hall J. E. and Guyton A. C. *Textbook of Medical Physiology*. Elsevier, 2006. ISBN 978-1-4160-4574-8. doi: 10.1136/pgmj.51.599.683-c.

Hammer K. P., Ljubojevic S., Ripplinger C. M., Pieske B. M., and Bers D. M. Cardiac myocyte alternans in intact heart: Influence of cell-cell coupling and beta-adrenergic stimulation. *Journal of Molecular and Cellular Cardiology*, 84:1–9, 2015. ISSN 10958584. doi: 10.1016/j.yjmcc.2015.03.012.

Hartikainen J., Kuikka J., Mäntysaari M., Länsimies E., and Pyörälä K. Sympathetic reinnervation after acute myocardial infarction. *American Journal of Cardiology*, 77 (1):5–9, 1996. ISSN 00029149. doi: 10.1016/S0002-9149(97)89125-4.

Hausenloy D. and Yellon D. Myocardial ischemia-reperfusion injury: a neglected therapeutic target. *J Clin Invest*, 123(1):92–100, 2013. ISSN 1558-8238. doi: 10.1172/JCI62874.92.

Heijman J., Volders P. G. a., Westra R. L., and Rudy Y. Local control of β-adrenergic stimulation: Effects on ventricular myocyte electrophysiology and Ca(2+)-transient. *Journal of molecular and cellular cardiology*, 50(5):863–71, 2011. ISSN 1095-8584. doi: 10.1016/j.yjmcc.2011.02.007.

Heijman J., Zaza A., Johnson D. M., Rudy Y., Peeters R. L. M., Volders P. G. A., and Westra R. L. Determinants of Beat-to-Beat Variability of Repolarization Duration in the Canine Ventricular Myocyte: A Computational Analysis. *PLoS Computational Biology*, 9(8), 2013. ISSN 1553734X. doi: 10.1371/journal.pcbi.1003202.

Heilbrunn S. M., Shah P., Bristow M. R., Valantine H. A., Ginsburg R., and Fowler M. B. Increased beta-receptor density and improved hemodynamic response to catecholamine stimulation during long-term metoprolol therapy in heart failure from dilated cardiomyopathy. *Circulation*, 79(3):483–490, 1989. ISSN 0009-7322. doi: 10.1161/01.CIR.79.3.483.

Herring N., Cranley J., Lokale M. N., Li D., Shanks J., Alston E. N., Girard B. M., Carter E., Parsons R. L., Habecker B. A., and Paterson D. J. The cardiac sympathetic co-transmitter galanin reduces acetylcholine release and vagal bradycardia: Implications for neural control of cardiac excitability. *Journal of Molecular and Cellular Cardiology*, 52(3):667–676, 2012. ISSN 00222828. doi: 10.1016/j.yjmcc.2011.11.016.

Herron T. J., Lee P., and Jalife J. Optical imaging of voltage and calcium in cardiac cells & tissues, 2012.

Hoang-Trong T. M., Ullah A., and Jafri M. S. Calcium Sparks in the Heart: Dynamics and Regulation. *Research and reports in biology*, 6:203–214, 2015. ISSN 1179-7274. doi: 10.2147/RRB.S61495.

Hund T. J. and Rudy Y. Rate dependence and regulation of action potential and calcium transient in a canine cardiac ventricular cell model. *Circulation*, 110(20):3168–3174, 2004. ISSN 00097322. doi: 10.1161/01.CIR.0000147231.69595.D3.

Hund T. J., Decker K. F., Kanter E., Mohler P. J., Boyden P. A., Schuessler R. B., Yamada K. A., and Rudy Y. Role of activated CaMKII in abnormal calcium homeostasis and INa remodeling after myocardial infarction: Insights from mathematical modeling. *Journal of Molecular and Cellular Cardiology*, 45(3):420–428, 2008. ISSN 00222828. doi: 10.1016/j.yjmcc.2008.06.007.

Hwang S. M., Yea K. H., and Lee K. J. Regular and alternant spiral waves of contractile motion on rat ventricle cell cultures. *Physical Review Letters*, 92(19):198103–1, 2004.

Ikeda T., Yoshino H., Sugi K., Tanno K., Shimizu H., Watanabe J., Kasamaki Y., Yoshida A., and Kato T. Predictive Value of Microvolt T-Wave Alternans for Sudden Cardiac Death in Patients With Preserved Cardiac Function After Acute Myocardial Infarction. Results of a Collaborative Cohort Study. *Journal of the American College of Cardiology*, 48(11):2268–2274, 2006. ISSN 07351097. doi: 10.1016/j.jacc.2006.06.075.

Immerkær J. Fast Noise Variance Estimation. *Computer Vision and Image Understanding*, 64:300–302, 1996. ISSN 10773142. doi: 10.1006/cviu.1996.0060.

Ioannidis J. P. A. Why most published research findings are false. *PLoS Medicine*, 2(8): e124, 2005. ISSN 1549-1277. doi: 10.1371/journal.pmed.0020124.

Israel C. W. Mechanisms of sudden cardiac death, 2014.

James C. A., Bhonsale A., Tichnell C., Murray B., Russell S. D., Tandri H., Tedford R. J., Judge D. P., and Calkins H. Exercise increases age-related penetrance and arrhythmic risk in arrhythmogenic right ventricular dysplasia/cardiomyopathy-associated desmosomal mutation carriers. *Journal of the American College of Cardiology*, 62(14): 1290–1297, 2013. ISSN 07351097. doi: 10.1016/j.jacc.2013.06.033.

Janse M. J. and Wit A. L. Electrophysiological mechanisms of ventricular arrhythmias resulting from myocardial ischemia and infarction. *Physiological reviews*, 69:1049–1169, 1989. ISSN 0031-9333. doi: 10.1.1.959.7455.

January C. T. and Riddle J. M. Early afterdepolarizations: Mechanism of induction and block. A role for L-type Ca2+current. *Circulation Research*, 64(5):977–990, 1989. ISSN 00097330. doi: 10.1161/01.RES.64.5.977.

Jones D. K., Liu F., Vaidyanathan R., Eckhardt L. L., Trudeau M. C., and Robertson G. A. hERG 1b is critical for human cardiac repolarization. *Proceedings of the National Academy of Sciences*, 111(50):18073–18077, 2014. ISSN 0027-8424. doi: 10.1073/pnas.1414945111.

Jones E. M., Roti Roti E. C., Wang J., Delfosse S. A., and Robertson G. A. Cardiac IKrchannels minimally comprise hERG 1a and 1b subunits. *Journal of Biological Chemistry*, 279(43):44690–44694, 2004. ISSN 00219258. doi: 10.1074/jbc.M408344200.

Jost N., Virág L., Comtois P., Ördög B., Szuts V., Seprényi G., Bitay M., Kohajda Z., Koncz I., Nagy N., Szél T., Magyar J., Kovács M., Puskás L. G., Lengyel C., Wettwer E., Ravens U., Nánási P. P., Papp J. G., Varró A., and Nattel S. Ionic mechanisms limiting cardiac repolarization reserve in humans compared to dogs. *Journal of Physiology*, 591(17):4189–4206, 2013. ISSN 00223751. doi: 10.1113/jphysiol.2013.261198.

Jung P., Wang J., Wackerbauer R., and Showalter K. Coherent structure analysis of spatiotemporal chaos. *Physical review. E, Statistical physics, plasmas, fluids, and related interdisciplinary topics*, 61(2):2095–8, 2000. ISSN 1063-651X.

Kalla M., Chotalia M., Coughlan C., Hao G., Crabtree M. J., Tomek J., Bub G., Paterson D. J., and Herring N. Protection against ventricular fibrillation via cholinergic receptor stimulation and the generation of nitric oxide. *The Journal of Physiology*, 594 (14):3981–3992, 2016. ISSN 00223751. doi: 10.1113/JP271588.

Kanaporis G. and Blatter L. A. The mechanisms of calcium cycling and action potential dynamics in cardiac alternans. *Circulation Research*, 116(5):846–856, 2015. ISSN 15244571. doi: 10.1161/CIRCRESAHA.116.305404.

Kanaporis G. and Blatter L. A. Membrane potential determines calcium alternans through modulation of SR Ca2+ load and L-type Ca2+ current. *Journal of Molecular and Cellular Cardiology*, 105:49–58, 2017. ISSN 10958584. doi: 10.1016/j.yjmcc.2017.02.004.

Kass R. S. and Moss A. J. Long QT syndrome: novel insights into the mechanisms of cardiac arrhythmias. *The Journal of Clinical Investigation*, 112(6):810–815, 2003. ISSN 0021-9738. doi: 10.1172/JCI200319844.Historical.

Katritsis D. G., Gersh B. J., and Camm A. J. A Clinical Perspective on Sudden Cardiac Death. *Arrhythmia & Electrophysiology Review*, 5(3):177, 2016. ISSN 2050-3369. doi: 10.15420/aer.2016:11:2.

Kay M. W. and Rogers J. M. Epicardial rotors in panoramic optical maps of fibrillating swine ventricles. In *Annual International Conference of the IEEE Engineering in Medicine and Biology - Proceedings*, pages 2268–2271, 2006. ISBN 1424400325. doi: 10.1109/IEMBS.2006.260635.

Kekenes-Huskey P. M., Liao T., Gillette A. K., Hake J. E., Zhang Y., Michailova A. P., McCulloch A. D., and McCammon J. A. Molecular and subcellular-scale modeling of nucleotide diffusion in the cardiac myofilament lattice. *Biophysical Journal*, 105(9): 2130–2140, 2013. ISSN 00063495. doi: 10.1016/j.bpj.2013.09.020.

Keller S. P. and Halperin H. R. Cardiac Arrest: the Changing Incidence of Ventricular Fibrillation, 2015. ISSN 15343189.

Kihara Y. and Morgan J. P. Abnormal Cai2+ handling is the primary cause of mechanical alternans: study in ferret ventricular muscles. *The American journal of physiology*, 261(6 Pt 2):H1746–H1755, 1991. ISSN 0002-9513.

Kim B.-S., Kim Y.-H., Hwang G.-S., Pak H.-N., Lee S. C., Shim W. J., Oh D. J., and Ro Y. M. Action potential duration restitution kinetics in human atrial fibrillation. *Journal of the American College of Cardiology*, 39(8):1329–36, 2002. ISSN 0735-1097. doi: 10.1016/S0735-1097(02)01760-6.

Kimura K., Ieda M., and Fukuda K. Development, maturation, and transdifferentiation of cardiac sympathetic nerves, 2012. ISSN 00097330.

Kodama M., Kato K., Hirono S., Okura Y., Hanawa H., Yoshida T., Hayashi M., Tachikawa H., Kashimura T., Watanabe K., and Aizawa Y. Linkage between mechanical and electrical alternans in patients with chronic heart failure. *Journal of Cardiovascular Electrophysiology*, 15(3):295–299, 2004.

Koller M. L., Riccio M. L., and Gilmour R. F. Dynamic restitution of action potential duration during electrical alternans and ventricular fibrillation. *The American journal of physiology*, 275(5 Pt 2):H1635–H1642, 1998. ISSN 0002-9513.

Koller M. L., Maier S. K. G., Gelzer A. R., Bauer W. R., Meesmann M., and Gilmour R. F. Altered dynamics of action potential restitution and alternans in humans with structural heart disease. *Circulation*, 112(11):1542–1548, 2005. ISSN 00097322. doi: 10.1161/CIRCULATIONAHA.104.502831.

Konstantinova P., Udvarev A., and Semerdjiev T. A study of a target tracking algorithm using global nearest neighbor approach. *Proceedings of the 4th International Conference on Computer Systems and Technologies E-Learning - CompSysTech '03*, pages 290–295, 2003. doi: 10.1145/973620.973668.

Koplan B. A., Stevenson W. G., and Cardiovascular O. N. Ventricular Tachycardia and Sudden Cardiac Death. *Mayo Clinic Proceedings*, 84(3):289–297, 2009. ISSN 0025-6196. doi: 10.4065/84.3.289.

Kreipke R. E. and Birren S. J. Innervating sympathetic neurons regulate heart size and the timing of cardiomyocyte cell cycle withdrawal. *The Journal of physiology*, 593(23): 5057–73, 2015. ISSN 1469-7793. doi: 10.1113/JP270917.

Lacinová L. and Hofmann F. Ca2+- and voltage-dependent inactivation of the expressed L-type Cav1.2 calcium channel. *Archives of Biochemistry and Biophysics*, 437(1):42–50, 2005. ISSN 00039861. doi: 10.1016/j.abb.2005.02.025.

Langendorff O. Untersuchungen am uberlebenden Saugethierherzen. *Pflügers Archiv*, 61:291–332, 1895.

Lanner J. T., Georgiou D. K., Joshi A. D., and Hamilton S. L. Ryanodine receptors: structure, expression, molecular details, and function in calcium release., 2010. ISSN 19430264.

Laughner J. I., Ng F. S., Sulkin M. S., Arthur R. M., and Efimov I. R. Processing and analysis of cardiac optical mapping data obtained with potentiometric dyes. *American journal of physiology. Heart and circulatory physiology*, 303(7):H753–65, 2012. ISSN 1522-1539.

Leenhardt A., Denjoy I., and Guicheney P. Catecholaminergic polymorphic ventricular tachycardia. *Circulation: Arrhythmia and Electrophysiology*, 5(5):1044–1052, 2012. ISSN 19413149. doi: 10.1161/CIRCEP.111.962027.

Lewis A. *Clinical translation of hyperpolarised magnetic resonance for cardiovascular and metabolic disease*. Dphil thesis, University of Oxford, 2017.

Liao J., Li H., Zeng W., Sauer D. B., Belmares R., and Jiang Y. Structural insight into the ion-exchange mechanism of the sodium/calcium exchanger. *Science*, 335(6069): 686–690, 2012. ISSN 10959203. doi: 10.1126/science.1215759.

Lindner M., Brandt M. C., Sauer H., Hescheler J., Böhle T., and Beuckelmann D. J. Calcium sparks in human ventricular cardiomyocytes from patients with terminal heart failure. *Cell calcium*, 31(4):175–82, 2002. ISSN 0143-4160. doi: 10.1054/ceca.2002.0272.

Linnenbank A. C., de Bakker J. M. T., and Coronel R. How to measure propagation velocity in cardiac tissue: A simulation study. *Frontiers in Physiology*, 5 JUL, 2014.

Linz K. W. and Meyer R. Profile and kinetics of L-type calcium current during the cardiac ventricular action potential compared in guinea-pigs, rats and rabbits. *Pflugers Archiv European Journal of Physiology*, 439(5):588–599, 2000. ISSN 00316768. doi: 10.1007/s004240050982.

Livshitz L. M. and Rudy Y. Regulation of Ca2+ and electrical alternans in cardiac myocytes: role of CAMKII and repolarizing currents. *American journal of physiology. Heart and circulatory physiology*, 292(6):H2854–66, 2007. ISSN 0363-6135. doi: 10.1152/ajpheart.01347.2006.

Lopez-Perez A., Sebastian R., and Ferrero J. M. Three-dimensional cardiac computational modelling: methods, features and applications. *BioMedical Engineering OnLine*, 14(1): 35, 2015. ISSN 1475-925X. doi: 10.1186/s12938-015-0033-5.

Luke R. A. and Saffitz J. E. Remodeling of ventricular conduction pathways in healed canine infarct border zones. *Journal of Clinical Investigation*, 87(5):1594–1602, 1991. ISSN 00219738. doi: 10.1172/JCI115173.

Luo C. H. and Rudy Y. A Model of the Ventricular Cardiac Action Potential. *Circulation Research*, 68(6):1501–1526, 1991. ISSN 00097330. doi: 10.1161/01.RES.68.6.1501.

MacLennan D. H., Rice W. J., and Green N. M. The mechanism of Ca2+ transport by sarco(endo)plasmic reticulum Ca2+-ATPases, 1997. ISSN 00219258.

Maier L. S., Zhang T., Chen L., DeSantiago J., Brown J. H., and Bers D. M. Transgenic CaMKIIδc overexpression uniquely alters cardiac myocyte Ca2+ handling: Reduced SR Ca2+ load and activated SR Ca2+ release. *Circulation Research*, 92(8):904–911, 2003. ISSN 00097330. doi: 10.1161/01.RES.0000069685.20258.F1.

Malhotra S., Fernandez S. F., Fallavollita J. A., and Canty J. M. J. Prognostic Significance of Imaging Myocardial Sympathetic Innervation. *Current cardiology reports*, 17(8):62, 2015. ISSN 1534-3170 (Electronic). doi: 10.1007/s11886-015-0613-9.

Manfredini R., Portaluppi F., Grandi E., Fersini C., and Gallerani M. Out-of-hospital sudden death referring to an emergency department. *Journal of Clinical Epidemiology*, 49(8):865–868, 1996. ISSN 08954356. doi: 10.1016/0895-4356(96)00114-X.

Marban E., Yamagishi T., and Tomaselli G. F. Structure and function of voltage-gated sodium channels. *The Journal of physiology*, 508(Pt 3):647–57, 1998. ISSN 0022-3751. doi: 10.1111/j.1469-7793.1998.647bp.x.

Martins J. and Zipes D. Epicardial phenol interrupts refractory period responses to sympathetic but not vagal stimulation in canine left ventricular epicardium and endocardium, 1980. ISSN 0009-7330.

Marx S. O. Requirement of a Macromolecular Signaling Complex for beta Adrenergic Receptor Modulation of the KCNQ1-KCNE1 Potassium Channel. *Science*, 295(5554): 496–499, 2002. ISSN 00368075. doi: 10.1126/science.1066843.

Mayer A. *Rhythmical pulsations is scyphomedusae*. Publication 47 of the Carnegie Institute, Washington, DC, 1906.

Meyer C., Rana O. R., Saygili E., Gemein C., Becker M., Nolte K. W., Weis J., Schimpf T., Knackstedt C., Mischke K., Hoffmann R., Kelm M., Pauza D., and Schauerte P. Augmentation of left ventricular contractility by cardiac sympathetic neural stimulation. *Circulation*, 121(11):1286–1294, 2010. ISSN 00097322. doi: 10.1161/CIRCULATIONAHA.109.874263.

Milting H., Lukas N., Klauke B., Körfer R., Perrot A., Osterziel K. J., Vogt J., Peters S., Thieleczek R., and Varsányi M. Composite polymorphisms in the ryanodine receptor 2 gene associated with arrhythmogenic right ventricular cardiomyopathy. *Cardiovascular Research*, 71(3):496–505, 2006. ISSN 00086363. doi: 10.1016/j.cardiores.2006.04.004.

Miragoli M., Gaudesius G., and Rohr S. Electrotonic modulation of cardiac impulse conduction by myofibroblasts. *Circulation Research*, 98(6):801–810, 2006. ISSN 00097330. doi: 10.1161/01.RES.0000214537.44195.a3.

Moens A. L., Claeys M. J., Timmermans J. P., and Vrints C. J. Myocardial ischemia/reperfusion-injury, a clinical view on a complex pathophysiological process, 2005. ISSN 01675273.

Myles R. C., Burton F. L., Cobbe S. M., and Smith G. L. Alternans of action potential duration and amplitude in rabbits with left ventricular dysfunction following myocardial infarction. *Journal of Molecular and Cellular Cardiology*, 50(3):510–521, 2011. ISSN 00222828. doi: 10.1016/j.yjmcc.2010.11.019.

Narayan S. M., Bayer J. D., Lalani G., and Trayanova N. A. Action Potential Dynamics Explain Arrhythmic Vulnerability in Human Heart Failure. A Clinical and Modeling Study Implicating Abnormal Calcium Handling. *Journal of the American College of Cardiology*, 52(22):1782–1792, 2008. ISSN 07351097. doi: 10.1016/j.jacc.2008.08.037.

Narayan S. M., Franz M. R., Clopton P., Pruvot E. J., and Krummen D. E. Repolarization alternans reveals vulnerability to human atrial fibrillation. *Circulation*, 123(25):2922–2930, 2011. ISSN 00097322. doi: 10.1161/CIRCULATIONAHA.110.977827.

Nerbonne J. M. and Kass R. S. Molecular physiology of cardiac repolarization. *Physiological reviews*, 85(4):1205–1253, 2005. ISSN 0031-9333. doi: 10.1152/physrev.00002.2005.

Nieminen T., Lehtimäki T., Viik J., Lehtinen R., Nikus K., Kööbi T., Niemelä K., Turjanmaa V., Kaiser W., Huhtala H., Verrier R. L., Huikuri H., and Kähönen M. T-wave alternans predicts mortality in a population undergoing a clinically indicated exercise test. *European Heart Journal*, 28(19):2332–2337, 2007. ISSN 0195668X. doi: 10.1093/eurheartj/ehm271.

Nivala M., Song Z., Weiss J. N., and Qu Z. T-tubule disruption promotes calcium alternans in failing ventricular myocytes: Mechanistic insights from computational modeling. *Journal of Molecular and Cellular Cardiology*, 79:32–41, 2015. ISSN 10958584. doi: 10.1016/j.yjmcc.2014.10.018.

Niwa N. and Nerbonne J. M. Molecular determinants of cardiac transient outward potassium current (Ito) expression and regulation, 2010. ISSN 00222828.

Noble D. Cardiac Action and Pacemaker Potentials based on the Hodgkin-Huxley Equations. *Nature*, 188(4749):495–497, 1960. ISSN 0028-0836. doi: 10.1038/188495b0.

Nolasco J. B. and Dahlen R. W. A graphic method for the study of alternation in cardiac action potentials. *J.Appl.Physiol*, 25(2):191–196, 1968. ISSN 0021-8987.

Oehmen C. S., Giles W. R., and Demir S. S. Mathematical model of the rapidly activating delayed rectifier potassium current I(Kr) in rabbit sinoatrial node. *Journal of cardiovascular electrophysiology*, 13(11):1131–1140, 2002. ISSN 10453873.

O'Hara T., Virág L., Varró A., and Rudy Y. Simulation of the undiseased human cardiac ventricular action potential: Model formulation and experimental validation. *PLoS Computational Biology*, 7(5):e1002061, 2011. ISSN 1553734X. doi: 10.1371/journal.pcbi.1002061.

Opthof T., Misier A. R., Coronel R., Vermeulen J. H. J., Frank R. G., Moulijn A. C., van Capelle F. J., and Janse M. J. Dispersion of refractoriness in canine ventricular myocardium. Effectsof sympathetic stimulation. *Circ Res*, 68(5):1204–1215, 1991.

Opthof T., Remme C. A., Jorge E., Noriega F., Wiegerinck R. F., Tasiam A., Beekman L., Alvarez-Garcia J., Munoz-Guijosa C., Coronel R., and Cinca J. Cardiac activation–repolarization patterns and ion channel expression mapping in intact isolated normal human hearts. *Heart Rhythm*, 14(2):265–272, 2017. ISSN 15563871. doi: 10.1016/j.hrthm.2016.10.010.

Ostman A., Hellberg C., and Böhmer F. D. Protein-tyrosine phosphatases and cancer. *Nature reviews. Cancer*, 6(4):307–320, 2006. ISSN 1474-175X. doi: 10.1038/nrc1837.

Passini E., Britton O., Lu H., Rohrbacher J., Hermans A., Gallacher D., Greig R., Bueno-Orovio A., and Rodriguez B. Human in silico drug trials demonstrate higher accuracy than animal models in predicting clinical pro-arrhythmic cardiotoxicity. *Frontiers in Physiology*, in press, 2017.

Pastore J. M., Girouard S. D., Laurita K. R., Akar F. G., and Rosenbaum D. S. Mechanism linking T-wave alternans to the genesis of cardiac fibrillation. *Circulation*, 99(10): 1385–1394, 1999. ISSN 0009-7322. doi: 10.1161/01.CIR.99.10.1385.

Paul M., Wichter T., Kies P., Gerss J., Wollmann C., Rahbar K., Eckardt L., Breithardt G., Schober O., Schulze-Bahr E., and Schäfers M. Cardiac sympathetic dysfunction in genotyped patients with arrhythmogenic right ventricular cardiomyopathy and risk of recurrent ventricular tachyarrhythmias. *Journal of nuclear medicine : official publication, Society of Nuclear Medicine*, 52(10):1559–65, 2011. ISSN 1535-5667. doi: 10.2967/jnumed.111.088997.

Payandeh J., Scheuer T., Zheng N., and Catterall W. A. The crystal structure of a voltage-gated sodium channel. *Nature*, 475(1476-4687 (Electronic)):353–358, 2011. ISSN 1476-4687. doi: nature10238[pii]\r10.1038/nature10238.

Persoon-Rothert M., van der Wees K. G. C., and van der Laarse A. Mechanical overload-induced apoptosis: A study in cultured neonatal ventricular myocytes and fibroblasts. *Molecular and Cellular Biochemistry*, 241(1-2):115–124, 2002. ISSN 03008177. doi: 10.1023/A:1020860209333.

Picht E., DeSantiago J., Blatter L. A., and Bers D. M. Cardiac alternans do not rely on diastolic sarcoplasmic reticulum calcium content fluctuations. *Circulation research*, 99(7):740–8, 2006. ISSN 1524-4571. doi: 10.1161/01.RES.0000244002.88813.91.

Pinto J. M. B. and Boyden P. A. Electrical remodeling in ischemia and infarction. *Cardiovascular Research*, 42(2):284–297, 1999. ISSN 00086363. doi: 10.1016/S0008-6363(99)00013-9.

Potse M., Dube B., Vinet A., and Cardinal R. A comparison of monodomain and bidomain propagation models for the human heart. In *Annual International Conference of the IEEE Engineering in Medicine and Biology - Proceedings*, pages 3895–3898, 2006. ISBN 1424400325. doi: 10.1109/IEMBS.2006.259484.

Pruvot E. J., Katra R. P., Rosenbaum D. S., and Laurita K. R. Role of Calcium Cycling Versus Restitution in the Mechanism of Repolarization Alternans. *Circulation Research*, 94(8):1083–1090, 2004. ISSN 00097330. doi: 10.1161/01.RES.0000125629.72053.95.

Pueyo E., Dangerfield C. E., Britton O. J., Virág L., Kistamás K., Szentandrássy N., Jost N., Varró A., Nánási P. P., Burrage K., and Rodríguez B. Experimentally-based computational investigation into beat-to-beat variability in ventricular repolarization and its response to ionic current inhibition. *PLoS ONE*, 11(3), 2016. ISSN 19326203. doi: 10.1371/journal.pone.0151461.

Pueyo E., Corrias A., Virág L., Jost N., Szél T., Varró A., Szentandrássy N., Nánási P. P., Burrage K., and Rodríguez B. A multiscale investigation of repolarization variability and its role in cardiac arrhythmogenesis. *Biophysical Journal*, 101(12):2892–2902, 2011. ISSN 00063495. doi: 10.1016/j.bpj.2011.09.060.

Qu Z., Garfinkel A., Chen P.-S., and Weiss J. N. Mechanisms of Discordant Alternans and Induction of Reentry in Simulated Cardiac Tissue. *Circulation*, 102(14):1664–1670, 2000. ISSN 0009-7322, 1524-4539. doi: 10.1161/01.CIR.102.14.1664.

Qu Z., Xie Y., Garfinkel A., and Weiss J. N. T-wave alternans and arrhythmogenesis in cardiac diseases. *Frontiers in Physiology*, 1 NOV, 2010. ISSN 1664042X. doi: 10.3389/fphys.2010.00154.

Qu Z., Liu M. B., and Nivala M. A unified theory of calcium alternans in ventricular myocytes. *Scientific Reports*, 6, 2016.

Ramay H. R., Liu O. Z., and Sobie E. A. Recovery of cardiac calcium release is controlled by sarcoplasmic reticulum refilling and ryanodine receptor sensitivity. *Cardiovascular Research*, 91(4):598–605, 2011. ISSN 00086363. doi: 10.1093/cvr/cvr143.

Richardson W. J., Clarke S. A., Alexander Quinn T., and Holmes J. W. Physiological implications of myocardial scar structure. *Comprehensive Physiology*, 5(4):1877–1909, 2015. ISSN 20404603. doi: 10.1002/cphy.c140067.

Rogers J. M., Usui M., KenKnight B. H., Ideker R. E., and Smith W. M. A quantitative framework for analyzing epicardial activation patterns during ventricular fibrillation. *Annals of biomedical engineering*, 25(5):749–760, 1997. ISSN 0090-6964. doi: 10.1007/BF02684159.

Rohr S. Role of gap junctions in the propagation of the cardiac action potential, 2004. ISSN 00086363.

Ruchat P., Dang L., Virag N., Schlaepfer J., von Segesser L. K., and Kappenberger L. A biophysical model of atrial fibrillation to define the appropriate ablation pattern in modified maze. *European Journal of Cardio-thoracic Surgery*, 31(1):65–69, 2007. ISSN 10107940. doi: 10.1016/j.ejcts.2006.10.015.

Saitoh H., Bailey J. C., and Surawicz B. Alternans of action potential duration after abrupt shortening of cycle length: differences between dog Purkinje and ventricular muscle fibers. *Circulation Research*, 62(5):1027–1040, 1988. ISSN 0009-7330. doi: 10.1161/01.RES.62.5.1027.

Salerno-Uriarte J. A., De Ferrari G. M., Klersy C., Pedretti R. F., Tritto M., Sallusti L., Libero L., Pettinati G., Molon G., Curnis A., Occhetta E., Morandi F., Ferrero P., and Accardi F. Prognostic Value of T-Wave Alternans in Patients With Heart Failure Due to Nonischemic Cardiomyopathy. Results of the ALPHA Study. *Journal of the American College of Cardiology*, 50(19):1896–1904, 2007. ISSN 07351097. doi: 10.1016/j.jacc.2007.09.004.

Sato D., Bers D. M., and Shiferaw Y. Formation of spatially discordant alternans due to fluctuations and diffusion of calcium. *PLoS ONE*, 8(12), 2013. ISSN 19326203. doi: 10.1371/journal.pone.0085365.

Scherrer-Crosbie M., Liel-Cohen N., Otsuji Y., Guerrero J. L., Sullivan S., Levine R. A., and Picard M. H. Myocardial perfusion and wall motion in infarction border zone: assessment by myocardial contrast echocardiography. *J Am Soc Echocardiogr*, 13(5):353–357, 2000. doi: S0894731700043613[pii].

Schlemmer A., Berg S., Shajahan T., Luther S., and Parlitz U. Entropy Rate Maps of Complex Excitable Dynamics in Cardiac Monolayers. *Entropy*, 17(3):950–967, 2015a. ISSN 1099-4300. doi: 10.3390/e17030950.

Schlemmer A., Berg S., Shajahan T. K., Luther S., and Parlitz U. Quantifying spatiotemporal complexity of cardiac dynamics using ordinal patterns. In *Proceedings of the Annual International Conference of the IEEE Engineering in Medicine and Biology Society, EMBS*, volume 2015-Novem, pages 4049–4052, 2015b. ISBN 9781424492718. doi: 10.1109/EMBC.2015.7319283.

Schroedl N. and Hartzell C. Myocytes and fibroblasts exhibit functional synergism in mixed cultures of neonatal rat heart cells. *Journal of Cellular Physiology*, 117(3): 326–332, 1983.

Sham J. S., Jones L. R., and Morad M. Phospholamban mediates the beta-adrenergic-enhanced Ca2+ uptake in mammalian ventricular myocytes. *Am J Physiol*, 261(4 Pt 2):H1344–9., 1991. ISSN 0002-9513.

Shampine L. F. and Reichelt M. W. The MATLAB ODE Suite. *SIAM Journal on Scientific Computing*, 18(1):1–22, 1997. ISSN 1064-8275. doi: 10.1137/S1064827594276424.

Shannon T. R., Ginsburg K. S., and Bers D. M. Potentiation of fractional sarcoplasmic reticulum calcium release by total and free intra-sarcoplasmic reticulum calcium concentration. *Biophysical Journal*, 78(1):334–343, 2000. ISSN 0006-3495. doi: 10.1016/S0006-3495(00)76596-9.

Shao Y., Redfors B., and Omerovic E. Modified technique for coronary artery ligation in mice. *Journal of visualized experiments : JoVE*, 29(73), 2013. ISSN 1940-087X.

Shen M. J. and Zipes D. P. Role of the autonomic nervous system in modulating cardiac arrhythmias, 2014.

Shi J., Dai W., Hale S. L., Brown D. A., Wang M., Han X., and Kloner R. A. Bendavia restores mitochondrial energy metabolism gene expression and suppresses cardiac

fibrosis in the border zone of the infarcted heart. *Life Sciences*, 141:170–178, 2015. ISSN 18790631. doi: 10.1016/j.lfs.2015.09.022.

Shkryl V. M., Maxwell J. T., Domeier T. L., and Blatter L. A. Refractoriness of sarcoplasmic reticulum Ca2+ release determines Ca2+ alternans in atrial myocytes. *AJP: Heart and Circulatory Physiology*, 302(11):H2310–H2320, 2012. ISSN 0363-6135. doi: 10.1152/ajpheart.00079.2012.

Shlosman I., Marinelli F., Faraldo-Gómez J. D., and Mindell J. A. The prokaryotic Na+/Ca2+ exchanger NCX_Mj transports Na+ and Ca2+ in a 3:1 stoichiometry. *The Journal of general physiology*, page jgp.201711897, 2017. ISSN 1540-7748. doi: 10.1085/jgp.201711897.

Silva J. and Rudy Y. Subunit interaction determines IKs participation in cardiac repolarization and repolarization reserve. *Circulation*, 112(10):1384–1391, 2005. ISSN 00097322. doi: 10.1161/CIRCULATIONAHA.105.543306.

Skrzypiec-Spring M., Grotthus B., Szelag A., and Schulz R. Isolated heart perfusion according to Langendorff-Still viable in the new millennium. *Journal of Pharmacological and Toxicological Methods*, 55(2):113–126, 2007. ISSN 10568719. doi: 10.1016/j.vascn.2006.05.006.

Smith A. F. and Wood J. Can some in-hospital cardio-respiratory arrests be prevented? A prospective survey. *Resuscitation*, 37(3):133–137, 1998.

Song L. S., Wang S. Q., Xiao R. P., Spurgeon H., Lakatta E. G., and Cheng H. beta-Adrenergic stimulation synchronizes intracellular Ca(2+) release during excitation-contraction coupling in cardiac myocytes. *Circ Res*, 88(8):794–801, 2001.

Spach M. S. and Kootsey J. M. The nature of electrical propagation in cardiac muscle. *The American journal of physiology*, 244(1):H3–H22, 1983. ISSN 0090-6964. doi: 10.1007/BF02363287.

Stary V., Puppala D., Scherrer-Crosbie M., Dillmann W. H., and Armoundas A. A. SERCA2a Upregulation Ameliorates Cellular Alternans Induced by Metabolic Inhibitions. *Journal of Applied Physiology*, 120(8):865–875, 2016. ISSN 1522-1601. doi: 10.1152/japplphysiol.00588.2015.

Steinberg B. E., Glass L., Shrier A., and Bub G. The role of heterogeneities and intercellular coupling in wave propagation in cardiac tissue. *Philosophical transactions. Series A, Mathematical, physical, and engineering sciences*, 364(1842):1299–1311, 2006. ISSN 1364-503X. doi: 10.1098/rsta.2006.1771.

Stevenson W. G. and Soejima K. Catheter ablation for ventricular tachycardia. *Circulation*, 115(21):2750–2760, 2007. ISSN 00097322. doi: 10.1161/CIRCULATIONAHA.106.655720.

Su Z., Li F., Spitzer K., Yao A., Ritter M., and Barry W. Comparison of sarcoplasmic reticulum Ca2+-ATPase function in human, dog, rabbit, and mouse ventricular myocytes. *Journal of Molecular and Cellular Cardiology*, 35(7):761–7, 2003.

Sutherland F. and Hearse D. the Isolated Blood and Perfusion Fluid Perfused Heart. *Pharmacological Research*, 41(6):613–627, 2000. ISSN 10436618. doi: 10.1006/phrs.1999.0653.

Sweadner K. J. and Donnet C. Structural similarities of Na,K-ATPase and SERCA, the Ca(2+)-ATPase of the sarcoplasmic reticulum. *The Biochemical journal*, 356:685–704, 2001. ISSN 02646021. doi: 10.1042/0264-6021:3560685.

Szabo B., Sweidan R., Rajagopalan C. V., and Lazzara R. Role of Na+:Ca2+ Exchange Current in Cs+-Induced Early Afterdepolarizations in Purkinje Fibers. *Journal of Cardiovascular Electrophysiology*, 5(11):933–944, 1994. ISSN 15408167. doi: 10.1111/j.1540-8167.1994.tb01133.x.

Szentesi P., Pignier C., Egger M., Kranias E. G., and Niggli E. Sarcoplasmic reticulum Ca2+ refilling controls recovery from Ca2+-induced Ca2+ release refractoriness in

heart muscle. *Circulation Research*, 95(8):807–813, 2004. ISSN 00097330. doi: 10.1161/01.RES.0000146029.80463.7d.

Szumowski L., Sanders P., Walczak F., Hocini M., Jaïs P., Kepski R., Szufladowicz E., Urbanek P., Derejko P., Bodalski R., and Haïssaguerre M. Mapping and ablation of polymorphic ventricular tachycardia after myocardial infarction. *Journal of the American College of Cardiology*, 44(8):1700–1706, 2004. ISSN 07351097. doi: 10.1016/j.jacc.2004.08.034.

Taggart P., Sutton P., Chalabi Z., Boyett M. R., Simon R., Elliott D., and Gill J. S. Effect of adrenergic stimulation on action potential duration restitution in humans. *Circulation*, 107(2):285–289, 2003. ISSN 00097322. doi: 10.1161/01.CIR.0000044941.13346.74.

Taqueti V. R. and O 'Gara P. T. Beta-Blocker Therapy After Myocardial Infarction More Questions Than Answers. *Journal of the American College of Cardiology*, 66(13):1442–1444, 2015. ISSN 0735-1097. doi: 10.1016/j.jacc.2015.08.007.

Ten Tusscher K. H. W. J., Hren R., and Panfilov A. V. Organization of ventricular fibrillation in the human heart. *Circulation Research*, 100(12), 2007. ISSN 00097330. doi: 10.1161/CIRCRESAHA.107.150730.

Tomek J. and Bub G. Hypertension-induced remodelling: on the interactions of cardiac risk factors. *Journal of physiology*, 595(12):4027–4036, 2017.

Tomek J., Novak O., and Syka J. Two-Photon Processor and SeNeCA - A freely available software package to process data from two-photon calcium imaging at speeds down to several ms per frame. *Journal of neurophysiology*, 110(1):jn.00087.2013–, 2013. ISSN 1522-1598. doi: 10.1152/jn.00087.2013.

Tomek J., Rodriguez B., Bub G., and Heijman J. β-adrenergic receptor stimulation inhibits proarrhythmic alternans in post-infarction border zone cardiomyocytes: a computational analysis. *American Journal of Physiology: Heart and Circulatory Physiology*, 2017. doi: 10.1152/ajpheart.00094.2017.

Trayanova N. A. and Chang K. C. How computer simulations of the human heart can improve anti-arrhythmia therapy. *The Journal of physiology*, 00(November 2014):1–20, 2015. ISSN 1469-7793 (Electronic). doi: 10.1113/JP270532.

Tse G. Mechanisms of cardiac arrhythmias, 2016. ISSN 18832148.

Tung L. and Zhang Y. Optical imaging of arrhythmias in tissue culture. *Journal of Electrocardiology*, 39(4 SUPPL.), 2006.

Turner N. A. and Porter K. E. Function and fate of myofibroblasts after myocardial infarction. *Fibrogenesis & tissue repair*, 6(1):5, 2013. ISSN 1755-1536. doi: 10.1186/1755-1536-6-5.

van den Bos E. J., Mees B. M. E., de Waard M. C., de Crom R., and Duncker D. J. A novel model of cryoinjury-induced myocardial infarction in the mouse: a comparison with coronary artery ligation. *American journal of physiology. Heart and circulatory physiology*, 289(3):H1291–300, 2005. ISSN 0363-6135. doi: 10.1152/ajpheart.00111.2005.

Varró A., Lathrop D. A., Hester S. B., Nánási P. P., and Papp J. G. Y. Ionic currents and action potentials in rabbit, rat, and guinea pig ventricular myocytes. *Basic Research in Cardiology*, 88(2):93–102, 1993. ISSN 03008428. doi: 10.1007/BF00798257.

Vaseghi M., Lux R. L., Mahajan a., and Shivkumar K. Sympathetic stimulation increases dispersion of repolarization in humans with myocardial infarction. *AJP: Heart and Circulatory Physiology*, 302(9):H1838–H1846, 2012. ISSN 0363-6135. doi: 10.1152/ajpheart.01106.2011.

Vaseghi M., Gima J., Kanaan C., Ajijola O. A., Marmureanu A., Mahajan A., and Shivkumar K. Cardiac sympathetic denervation in patients with refractory ventricular arrhythmias or electrical storm: Intermediate and long-term follow-up. *Heart Rhythm*, 11(3):360–366, 2014. ISSN 15475271. doi: 10.1016/j.hrthm.2013.11.028.

Vassilev P. M., Scheuer T., and Catterall W. A. Identification of an intracellular peptide segment involved in sodium channel inactivation. *Science (New York, N.Y.)*, 241(4873):1658–61, 1988. ISSN 0036-8075. doi: 10.1126/science.2458625.

Väyrynen T., Boyd J., Sorsa M., Määttä T., and Kuisma M. Long-term changes in the incidence of out-of-hospital ventricular fibrillation. *Resuscitation*, 82(7):825–829, 2011. ISSN 03009572. doi: 10.1016/j.resuscitation.2011.02.030.

Verrier R. L., Klingenheben T., Malik M., El-Sherif N., Exner D. V., Hohnloser S. H., Ikeda T., Martínez J. P., Narayan S. M., Nieminen T., and Rosenbaum D. S. Microvolt T-wave alternans: Physiological basis, methods of measurement, and clinical utility: consensus guideline by international society for Holter and noninvasive Electrocardiology. *Journal of the American College of Cardiology*, 58(13):1309–1324, 2011. ISSN 07351097. doi: 10.1016/j.jacc.2011.06.029.

Walcott G. P., Kroll M. W., and Ideker R. E. Ventricular fibrillation threshold of rapid short pulses. In *Proceedings of the Annual International Conference of the IEEE Engineering in Medicine and Biology Society, EMBS*, pages 255–258, 2011. ISBN 9781424441211. doi: 10.1109/IEMBS.2011.6090049.

Wang L., Myles R. C., De Jesus N. M., Ohlendorf A. K. P., Bers D. M., and Ripplinger C. M. Optical mapping of sarcoplasmic reticulum Ca2+ in the intact heart: Ryanodine receptor refractoriness during alternans and fibrillation. *Circulation Research*, 114(9): 1410–1421, 2014. ISSN 15244571. doi: 10.1161/CIRCRESAHA.114.302505.

Wang W. and MacKinnon R. Cryo-EM Structure of the Open Human Ether-à-go-go-Related K+Channel hERG. *Cell*, 169(3):422–430.e10, 2017. ISSN 10974172. doi: 10.1016/j.cell.2017.03.048.

Watanabe H. and Knollmann B. C. Mechanism underlying catecholaminergic polymorphic ventricular tachycardia and approaches to therapy. *Journal of Electrocardiology*, 44(6):650–655, 2011. ISSN 00220736. doi: 10.1016/j.jelectrocard.2011.07.025.

Weber F. M., Schilling C., Seemann G., Luik A., Schmitt C., Lorenz C., and Dössel O. Wave-direction and conduction-velocity analysis from intracardiac electrograms-a single-shot technique. *IEEE Transactions on Biomedical Engineering*, 57(10 PART 1): 2394–2401, 2010.

Weiss J. N., Chen P.-S., Qu Z., Karagueuzian H. S., and Garfinkel A. Ventricular Fibrillation : How Do We Stop the Waves From Breaking? *Circulation Research*, 87(12): 1103–1107, 2000. ISSN 0009-7330. doi: 10.1161/01.RES.87.12.1103.

Weiss J. N., Karma A., Shiferaw Y., Chen P. S., Garfinkel A., and Qu Z. From pulsus to pulseless: The saga of cardiac alternans, 2006. ISSN 00097330.

Wilson L. D. and Rosenbaum D. S. Mechanisms of arrythmogenic cardiac alternans. *Europace : European pacing, arrhythmias, and cardiac electrophysiology : journal of the working groups on cardiac pacing, arrhythmias, and cardiac cellular electrophysiology of the European Society of Cardiology*, 9 Suppl 6:77–82, 2007. ISSN 15322092. doi: 10.1093/europace/eum210.

Wilson L. D., Jeyaraj D., Wan X., Hoeker G. S., Said T. H., Gittinger M., Laurita K. R., and Rosenbaum D. S. Heart failure enhances susceptibility to arrhythmogenic cardiac alternans. *Heart Rhythm*, 6(2):251–259, 2009. ISSN 15475271. doi: 10.1016/j.hrthm.2008.11.008.

Wit A. L., Allessie M. A., Bonke F. I. M., Lammers W., Smeets J., and Fenoglio J. J. Electrophysiologic mapping to determine the mechanism of experimental ventricular tachycardia initiated by premature impulses. Experimental approach and initial results demonstrating reentrant excitation. *The American Journal of Cardiology*, 49(1): 166–185, 1982. ISSN 00029149. doi: 10.1016/0002-9149(82)90292-2.

Wu J., Naiki N., Ding W.-G., Ohno S., Kato K., Zang W.-J., Delisle B. P., Matsuura H., and Horie M. A Molecular Mechanism for Adrenergic-Induced Long QT Syndrome. *Journal of the American College of Cardiology*, 63(8):819–827, 2014. ISSN 07351097. doi: 10.1016/j.jacc.2013.08.1648.

Xie Y., Grandi E., Puglisi J. L., Sato D., and Bers D. M. Beta-adrenergic stimulation activates early afterdepolarizations transiently via kinetic mismatch of PKA targets. *Journal of Molecular and Cellular Cardiology*, 58(1):153–161, 2013. ISSN 00222828. doi: 10.1016/j.yjmcc.2013.02.009.

Xie Y., Izu L. T., Bers D. M., and Sato D. Arrhythmogenic transient dynamics in cardiac myocytes. *Biophysical Journal*, 106(6):1391–1397, 2014. ISSN 15420086. doi: 10.1016/j.bpj.2013.12.050.

Xing D. and Martins J. B. Myocardial ischemia-reperfusion damage impacts occurrence of ventricular fibrillation in dogs. *Am J Physiol Heart Circ Physiol*, 280(2):H684–92, 2001. ISSN 03636135.

Yang J. H. and Saucerman J. J. Computational models reduce complexity and accelerate insight into cardiac signaling networks, 2011. ISSN 00097330.

Yoshioka K., Gao D. W., Chin M., Stillson C., Penades E., Lesh M., O'Connell W., and Dae M. Heterogeneous sympathetic innervation influences local myocardial repolarization in normally perfused rabbit hearts. *Circulation*, 101(9):1060–6, 2000. ISSN 1524-4539. doi: 10.1161/01.CIR.101.9.1060.

Yu H., Pi-Hua F., Yuan W., Xiao-Feng L., Jun L., Zhi L., Sen L., and Zhang S. Prediction of sudden cardiac death in patients after acute myocardial infarction using T-wave alternans: A prospective study. *Journal of Electrocardiology*, 45(1):60–65, 2012. ISSN 00220736. doi: 10.1016/j.jelectrocard.2011.07.015.

Zhou P., Zhao Y.-T., Guo Y.-B., Xu S.-M., Bai S.-H., Lakatta E. G., Cheng H., Hao X.-M., and Wang S.-Q. Beta-adrenergic signaling accelerates and synchronizes cardiac ryanodine receptor response to a single L-type Ca2+ channel. *Proceedings of the National Academy of Sciences of the United States of America*, 106(42):18028–18033, 2009. ISSN 1091-6490. doi: 10.1073/pnas.0906560106.

Zhou X., Bueno-Orovio A., Orini M., Hanson B., Hayward M., Taggart P., Lambiase P., Burrage K., and Rodriguez B. In Vivo and In Silico Investigation Into Mechanisms of Frequency Dependence of Repolarization Alternans in Human Ventricular Cardiomyocytes. *Circulation research*, 118:266–278, 2016.

Zipes D. P. and Wellens H. J. J. Sudden Cardiac Death, 1998. ISSN 0009-7322.

Zipes D. P. and Jalife J. *Cardiac Electrophysiology: From Cell to Bedside: Sixth Edition*. Saunders, 2013. ISBN 9781455728565. doi: 10.1016/C2011-0-06826-6.

A

Appendix:Experimental

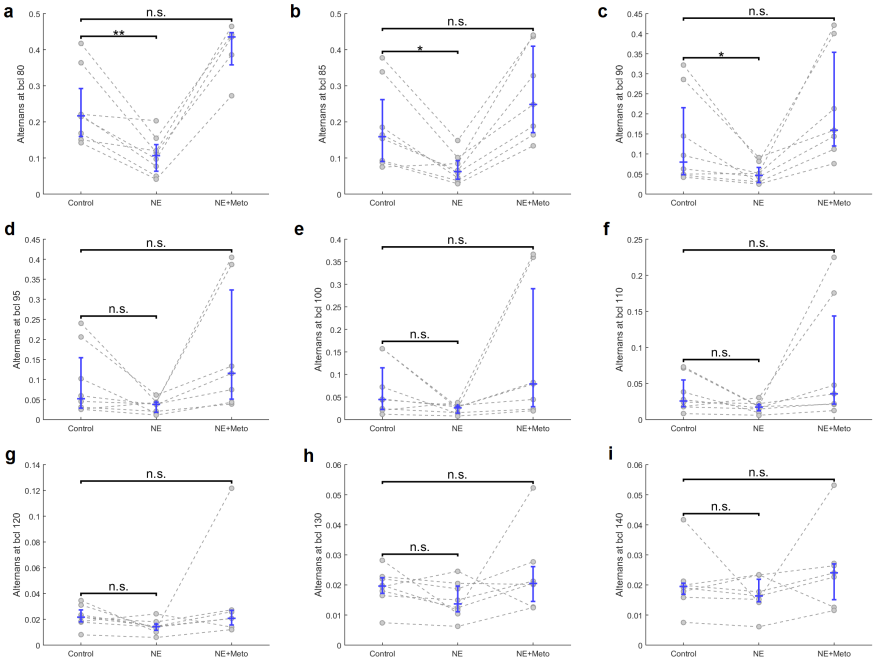


Figure A.1: Normalised alternans magnitude for tested hearts at various pacing frequencies. The subpanels show normalised alternans at all the tested bcls (bcl is indicated on the y axis in each plot), showing that for each of three fastest pacing frequencies, norepinephrine (NE) perfusion significantly attenuated alternans and this was reverted with the beta-blocker metoprolol. For the other frequencies, alternans was attenuated with NE provided that the baseline alternans was large enough. The blue lines with whiskers show median and 25 and 75 percentiles. Asterisks represent statistical significance at the level of 0.01 (**), or 0.1 (*).

B

Appendix:Computational investigation of alternans

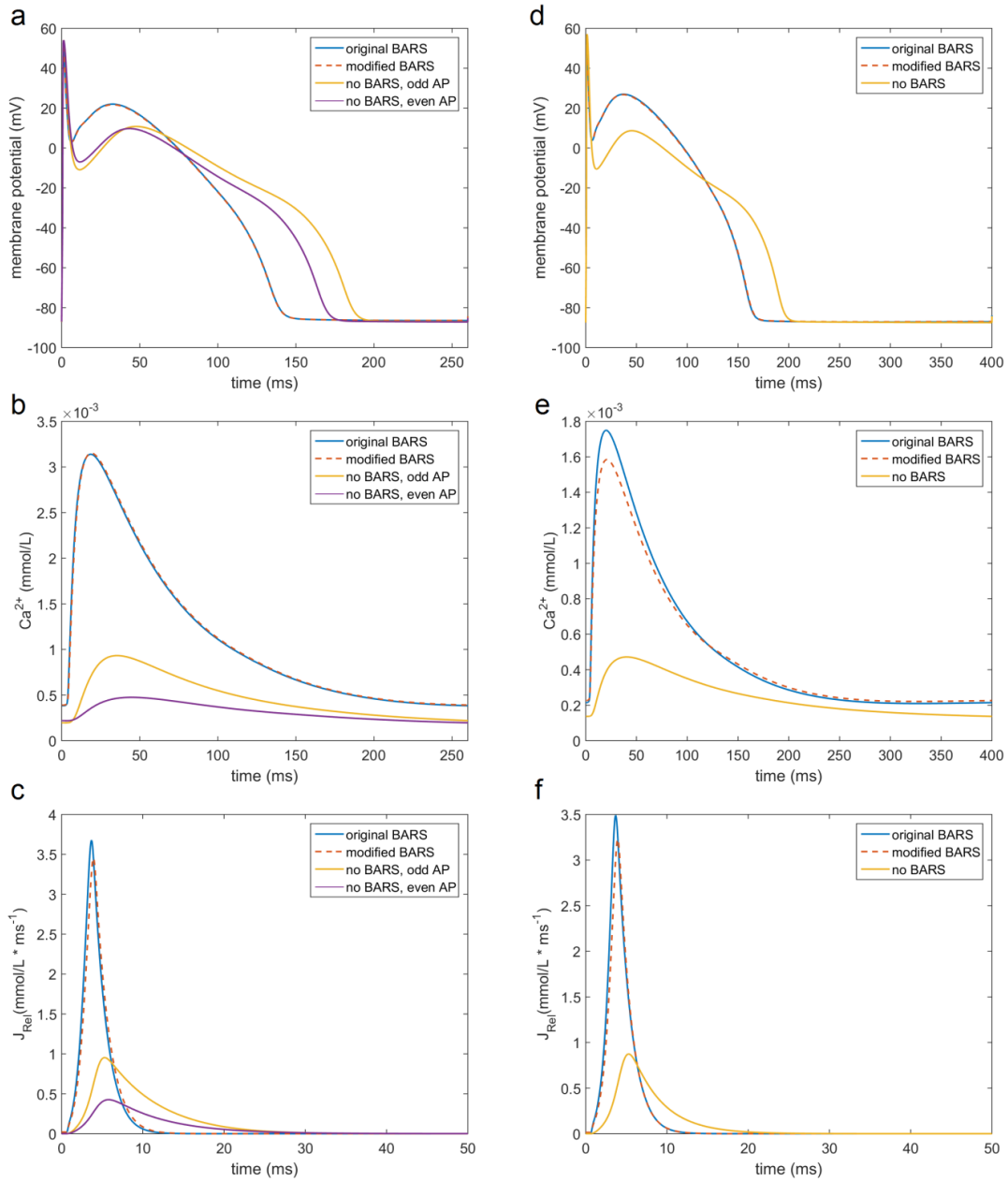


Figure B.1: Similarity of original and modified RyR modulation via βARS in a NZ cell. Beyond modulation of RyR, no other βARS effects were simulated here. Panels a, b, c contain traces of membrane potential, free intracellular calcium, and calcium release flux from the SR (having different x-axis) in a cell paced at bcl 260 ms. As the cell without βARS manifests alternans, both alternating beats are shown. Panels d,e,f then show the same variables as a, b, c, but at bcl 400 ms, when no alternans is present.

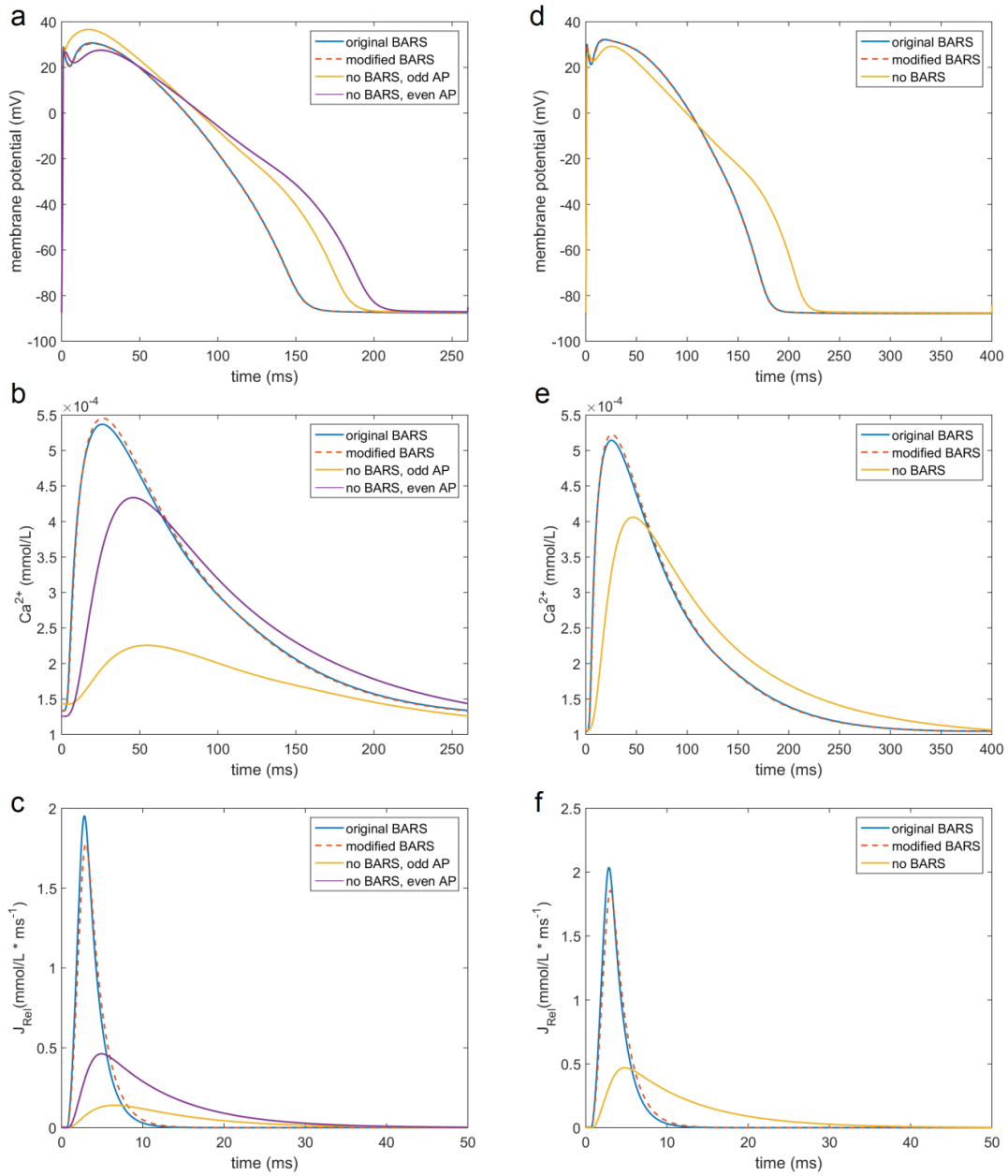


Figure B.2: Similarity of original and modified RyR modulation via βARS in a BZ cell. Beyond modulation of RyR, no other βARS effects were simulated here. Panels a, b, c contain traces of membrane potential, free intracellular calcium, and calcium release flux from the SR (having different x-axis) in a cell paced at bcl 260 ms. As the cell without βARS manifests alternans, both alternating beats are shown. Panels d,e,f then show the same variables as a, b, c, but at bcl 400 ms, when no alternans is present.

C Appendix:Ccoffinn

C.1 Parameter values

Name	Description
$frameRate$	The frame rate of the recording in frames per second.
$mimps$	The upper limit of speed of waves in micrometres per ms.
$pixelMicroMetres$	How many micrometres does a side of a pixel measure (based on the resolution of the recording).

Table C.1: An overview of input constants. These numbers can be different for each video processed in a batch (e.g., all videos of cell cultures created and imaged using a fixed protocol, before and after addition of a drug).

Table C.1 shows a list of constants given by physical conditions of the experiment, Table C.2 contains the free parameters of the methods used in our toolkit, and Table C.3 contains the computed parameters, values of which are based on constants and free parameters. The table C.4 contains an overview of switches that control the behaviour of the software.

Name	Description	Value
hlt, llt, cws	The parameters of the SeNeCA segmentation algorithm for the case when blob-based segmentation is used.	1.4, 1.3, 8
$binningfactor$, $minimumSNR$	The parameters of the filtered binning segmentation algorithm: the video is binned into squares with side length $binningfactor$, ignoring squares traces of which have SNR lower than $minimumSNR$ (these are used only if filtered binning is used for blob segmentation). $minimumSNR$ is 0 by default, meaning that no filtering is performed.	3, 0
$smoothingFactor$	Used to compute $smoothingParameter$; the larger it is, the shorter the filter. E.g., for the default value and 100fps, smoothing width is 100ms	10
$activityThreshold$	Used to determine which segments of dIS (as obtained in Section 5.2.1.2) are labelled as containing an AP upstroke	2
$apdN$	The N determines the APD level measured; scaled to 0-1. I.e., 0.5 represents APD50. The default value used is suited for data with relatively high amount of noise and disorder.	0.3
$minAPD, maxAPD$	The minimum/maximum duration of an action potential in ms. If a candidate action potential does not fit within this range, it is discarded.	25, 800
$distanceThreshold$	If two blobs are closer than this (in pixels), they are considered to belong to the same wave. This parameter may be either given exactly as a number, or as 'auto', being estimated heuristically as $4\cdot$ median distance of each blob to its nearest non-self neighbours.	'auto'
$minDensity$	If a blob considered active based on $activityThreshold$ does not contain at least this many other blobs considered active within $distanceThreshold$, it is relabelled as not active to keep focus on non-sparse activity.	5
$maxArrows$	The maximum number of arrows starting and ending in each blob; used in MCMF tracking. This may be an integer value or 'auto'.	1
usm	Used in feature extraction, determines the radius (in micrometres) around a start point of a tracking arrow in which other arrows are considered for computing roughness of wavefront.	750

Table C.2: An overview of free parameters that must be specified as a part of input. These numbers are expected to be the same for all the videos processed in a batch. The third column contains values that we used in experiments described in this text, included in order to improve the reproducibility of our results.

Name	Description	Formula
$uniformitySurroundings$	usm in pixels	$\frac{usm}{pixelMicroMetres}$
$maxSpeed$	Maximum speed of waves in pixels per frame	$\frac{1000 \cdot mimpms}{frameRate \cdot pixelMicroMetres}$
$smoothingParameter$	Size of averaging filter (in frames) used in smoothing intensity traces of blobsA. It set to make a single cardiac action potential smooth, but not to merge two separate ones.	$\frac{frameRate}{smoothingFactor}$

Table C.3: An overview of parameters computed using constants and free parameters.

Name	Description	Values
$isDebug$	If 1, traces of all the blobs segmented in the processed recording are stored in tmp subfolder, along with their smoothed version and segmentation of activity.	0/1
$isDoubleHump$	If 1, additional smoothing is applied in spike-mining to connect "double-humps" resulting from preprocessing of dye-free imaged data.	0/1
$segmentationMethod$	This switch selects between SeNeCA cell segmentation (for recordings with blobs) and binningSNR segmentation (for continuously activated recordings)	'seneca'/'binningSNR'
$toPlot$	If 1, the segmentation and tracking progress is visualised on-screen	0/1
$trackingMethod$	This determines whether the default minimum-cost-maximum-flow approach or Bayly's method is used for tracking wavefronts.	'MCMF'/'Bayly'
$useZeroArrows$	If 1, zero-length arrows are considered in CV estimation. This is to be used in cases of low pixels-per-frame conduction.	0/1
$verbose$	If 1, progress of computation is output to the console and progress bars are displayed to track the progress of time-consuming steps.	0/1

Table C.4: An overview of switches used in Ccoffinn.